UAB
Universitat Autònoma de Barcelona

Optothermal Studies of Heat in van derWaals Materials

David SALETA REIG

TU/e EINDHOVEN UNIVERSITY OF TECHNOLOGY

UAB Universitat Autònoma de Barcelona

ICN2 Institut Català de Nanociència i Nanotecnologia

UNIVERSITAT AUTÒNOMA DE BARCELONA

Doctoral Thesis

Optothermal Studies of Heat in van der Waals Materials

Author:
David
SALETA REIG

Advisor:
Prof. Dr. Klaas-Jan
TIELROOIJ

A thesis submitted in fulfillment of the requirements
for the degree of Doctor of Philosophy

in the

Ultrafast Dynamics in Nanoscale Systems
INSTITUT CATALÀ DE NANOCIÈNCIA I NANOTECNOLOGIA

Advanced Nanomaterials & Devices
EINDHOVEN UNIVERSITY OF TECHNOLOGY

2025

Thesis Advisor:

Prof. Dr. Klaas-Jan Tielrooij
Catalan Institute of Nanoscience and Nanotechnology (ICN2), Spain
Eindhoven University of Technology (TU/e), the Netherlands

Thesis Tutor:

Prof. Dr. Javier Rodríguez-Viejo
Catalan Institute of Nanoscience and Nanotechnology (ICN2), Spain
Universitat Autonòma de Barcelona (UAB), Spain

Thesis Committee:

Prof. Dr. Andrés Castellanos-Gómez
Instituto de Ciencia de Materiales de Madrid (ICMM-CSIC), Spain

Prof. Dr. Aitor Lopeandia Fernández
Catalan Institute of Nanoscience and Nanotechnology (ICN2), Spain
Universitat Autonòma de Barcelona (UAB), Spain

Prof. Dr. Eric Pop
Stanford University, USA

The research work presented in this thesis, carried out between October 2020 and September 2025, was funded by the Spanish Ministry of Economy through the FPI-SO2019 (SEV-2017-0706-19-1) grant; by Spanish MCIN/AEI project PID2022-142730NB-I00 ("HYDROPTO"); by FLAG-ERA grant ENPHOCAL, from MICIN with No. PCI2021-122101-2A (Spain); and by the European Union's Horizon 2020 research and innovation program under grant agreement No. 804349 (ERC starting grant CUHL).

To my family, friends and colleagues for your unconditional love and support...

"I was born not knowing and have had only a little time to change that here and there."

— Richard P. Feynman

Acknowledgements

This PhD has been a long and often challenging journey, and I feel deeply fortunate to have had so many people walking alongside me.

First and foremost, I want to thank my family. Your love, patience, and belief in me have been a constant source of strength, especially during moments when I doubted myself.

To my friends, thank you for surrounding me with encouragement, laughter, and perspective whenever I needed it most. I am especially grateful to DCB, AvDL, BAG, ATB, JSB, ABI, AS (and many others) for standing by my side during my brief cancer journey. My love and gratitude for you go beyond words. Please know that, just as you were there for me, I will always be there for you.

I am also deeply grateful to my colleagues, who made the work environment not only stimulating but also genuinely supportive. The conversations we shared, the challenges we faced together, and the spirit of teamwork enriched this journey far beyond the pages of this thesis. I cannot imagine this PhD without SV, SG, BL, LM, NS, RF, ROBC, AN and RML (nor without JDM and AB). Each of you has left a lasting mark on me, one that I will carry with me wherever I go.

To my supervisor, KJT, I extend my heartfelt gratitude for your guidance, advice, and encouragement over the years. Your insight and support have shaped not only this work but also my growth as a researcher.

I would also like to thank those who generously gave their time to read, review, and help me improve this thesis: SV, BL, LM, and KJT. Your careful feedback, thoughtful suggestions, and encouragement made this work clearer, stronger, and more complete.

Finally, I want to acknowledge all those —friends, peers, and mentors— who have shared their experiences with me, both academic and personal. I am especially grateful to my past mentors and supervisors, particularly MS, CST, BG and GF whose guidance and encouragement have shaped my path and made this possible.

I would also like to sincerely thank the reviewers of this thesis for dedicating their time and expertise to carefully evaluating my work. Your contributions are invaluable, and I greatly appreciate your efforts.

Resum

A mesura que la tecnologia del silici avança cap a components cada cop més petits —on el gruix del canal en transistors moderns ja ronda ∼5 nm per mantenir la trajectòria prevista per la llei de Moore— la gestió tèrmica esdevé un repte crític. A nanoescala, materials 3D com el silici mostren degradació del rendiment per una major dispersió superficial (més àtoms exposats i enllaços penjants). Per seguir miniaturitzant i afegir funcions als xips de silici, els materials bidimensionals (2D) ofereixen una via prometedora. El seu gruix atòmic i la seva anisotropia tèrmica afavoreixen la integració híbrida 3D–2D, amb potencial per a sensat, fotònica i dispositius memristius per a computació neuromòrfica. En aquest treball aportem comprensió fonamental de les propietats dels materials 2D mitjançant un estudi experimental del transport de calor mediat per fonons en dicalcogenures de metalls de transició (TMDs), centrant-nos en com el gruix i l'entorn afecten les seves conductivitats interfacial i tèrmica. Primer, desenvolupem un sistema de transferència i manipulació amb el qual preparem làmines suspeses de mida rècord fins a monocapa [Capítol 3]. Segon, construïm un muntatge òptic versàtil per explorar el transport tèrmic a nanoescala [Capítols 4 i 5]. Tercer, amb termoreflectància en el domini del temps, mostrem indicis preliminars de transport de calor coherent fora del pla en MoS_2 de diversos gruixos i temperatures, discutint possibles efectes de fonons i fotons coherents [Capítols 6 i 7]. Finalment, mitjançant termometria Raman sense contacte, determinem la conductivitat tèrmica intrínseca en el pla de $MoSe_2$ en funció del gruix i observem una major dissipació cap a molècules ambientals en les làmines més primes [Capítol 8]. Aquests resultats reforcen la comprensió fonamental de la dissipació tèrmica en materials de van der Waals i donen suport a la seva integració en tecnologies emergents.

Paraules clau: *Dinàmica ultrarràpida, transport de calor, propietats tèrmiques, materials 2D, membranes, transferècia en sec, termoreflectància en el domini del temps, termometria Raman*

Resumen

A medida que la tecnología del silicio avanza hacia componentes cada vez más pequeños —donde el grosor del canal en transistores modernos ya ronda ∼5 nm para mantener la trayectoria prevista por la ley de Moore— la gestión térmica se vuelve un desafío crítico. A nanoescala, materiales 3D como el silicio muestran degradación del rendimiento por mayor dispersión superficial (más átomos expuestos y enlaces colgantes). Para seguir miniaturizando y añadir funciones a los chips de silicio, los materiales bidimensionales (2D) ofrecen una vía prometedora. Su espesor atómico y su anisotropía térmica favorecen la integración híbrida 3D–2D, con potencial para sensado, fotónica y dispositivos memristivos para computación neuromórfica. En este trabajo aportamos comprensión fundamental de las propiedades de los materiales 2D mediante un estudio experimental del transporte de calor mediado por fonones en dicalcogenuros de metales de transición (TMDs), centrándonos en cómo el espesor y el entorno afectan sus conductividades interfacial y térmica. Primero, desarrollamos un sistema de transferencia y manipulación con el que preparamos láminas suspendidas de tamaño récord hasta monocapa [Capítulo 3]. Segundo, construimos un montaje óptico versátil para explorar el transporte térmico en nanoescala [Capítulos 4 y 5]. Tercero, con termoreflectancia en el dominio del tiempo, mostramos indicios preliminares de transporte de calor fuera del plano en MoS_2 de distintos espesores y temperaturas, discutiendo posibles efectos de fonones y fotones coherentes [Capítulos 6 y 7]. Por último, mediante termometría Raman sin contacto, determinamos la conductividad térmica intrínseca en el plano de $MoSe_2$ en función del espesor y observamos mayor disipación hacia moléculas ambientales en las láminas más delgadas [Capítulo 8]. Estos resultados refuerzan la comprensión fundamental de la disipación térmica en materiales de van der Waals y respaldan su integración en tecnologías emergentes.

Palabras clave: *Dinámica ultrarrápida, transporte de calor, propiedades térmicas, materiales 2D, membranas, transferencia en seco, termoreflectancia en el dominio del tiempo, termometría Raman*

Abstract

As silicon technology continues its drive toward ever-smaller electronic components —where the channel thickness in modern field-effect transistors is already reduced to ∼5 nm to sustain the trajectory predicted by Moore's law— thermal management emerges as a critical challenge. Conventional three-dimensional materials like silicon suffer performance degradation at the nanoscale, primarily due to enhanced surface scattering from a higher proportion of surface atoms and an increased density of dangling bonds. To sustain miniaturization while adding new functions to silicon chips, two-dimensional (2D) materials offer a compelling path forward. Because they are atomically thin and exhibit anisotropic thermal properties, 2D materials are well suited to hybrid 3D–2D integration, potentially adding sensing, photonic and memristive capabilities for neuromorphic computing in future electronic and optoelectronic platforms. In this work, we contribute to the fundamental understanding of 2D material properties with an experimental investigation of phonon-mediated heat transport in transition metal dichalcogenides (TMDs). We focus on how thickness and environmental conditions influence their interfacial and thermal conductivities. First, we develop a system to transfer and manipulate 2D materials, with which we prepare record-large suspended flakes down to the monolayer thickness [Chapter 3]. Second, we build a versatile optical setup specifically designed to explore thermal transport in nanoscale systems [Chapters 4 and 5]. Third, using our ultrafast time-domain thermoreflectance setup, we present preliminary insights into coherent out-of-plane heat transport in MoS_2 flakes with varying thicknesses down to the monolayer and at varying temperatures. We discuss the results in terms of possible effects of coherent phonons and coherent photons [Chapters 6 and 7]. Finally, using non-contact, steady-state Raman thermometry we determine the intrinsic in-plane thermal conductivity of $MoSe_2$ across various thicknesses, and find an enhanced heat dissipation capabilities to environmental molecules for the thinnest flakes [Chapter 8]. Our findings contribute to the fundamental understanding of heat dissipation in van der Waals materials and support their integration into emerging technologies.

Keywords: *Ultrafast dynamics, heat transport, thermal properties, 2D materials, membranes, dry-transfer, time-domain thermoreflectance, Raman thermometry*

List of Publications

Publications Described in this Thesis

[∗] S. Varghese[†], **D. Saleta Reig**[†], J. D. Mehew, A. Block, A. El Sachat, E. Chávez-Ángel, M. Sledzinska, B. Ballesteros, C. M. S. Torres, and K.-J. Tielrooij, "Fabrication and characterization of large-area suspended $MoSe_2$ crystals down to the monolayer", *Journal of Physics: Materials* **4**(4), 046001 (2021), see Chapter 3.
[†]Equally contributing authors.

[∗] **D. Saleta Reig**, S. Varghese, R. Farris, A. Block, J. D. Mehew, O. Hellman, P. Woźniak, M. Sledzinska, A. El Sachat, E. Chávez-Ángel, S. O. Valenzuela, N. F. van Hulst, P. Ordejón, Z. Zanolli, C. M. Sotomayor Torres, M. J. Verstraete, and K.-J. Tielrooij, "Unraveling heat transport and dissipation in suspended $MoSe_2$ from bulk to monolayer", *Advanced Materials* **34**(10), 2108352 (2022), see Chapter 8.

[∗] **D. Saleta Reig**, B. Liu, et al., "On-demand supression of transient thermoreflectance in gold superstrates via few-layer interfacial MoS_2", *In preparation* (2025), see Chapters 6 and 7.

[∗] B. Liu[‡], **D. Saleta Reig**[‡], et al., "Ultrafast thermalization dynamics of gold superstrates using adhesion layers and interfacial MoS_2", *In preparation* (2025), see Chapters 6 and 7.
[‡]Equally contributing authors.

Related Publications by D. Saleta Reig

[∗] M. Sledzinska, B. Graczykowski, M. Placidi, **D. Saleta Reig**, A. E. Sachat, J. S. Reparaz, F. Alzina, B. Mortazavi, R. Quey, L. Colombo, S. Roche, and C. M. Sotomayor Torres, "Thermal conductivity of MoS_2 polycrystalline nanomembranes", *2D Materials* **3**(3), 035016 (2016).

[∗] M. Sledzinska, R. Quey, B. Mortazavi, B. Graczykowski, M. Placidi, **D. Saleta Reig**, D. Navarro-Urrios, F. Alzina, L. Colombo, S. Roche, and C. M. Sotomayor Torres, "Record low thermal conductivity of polycrystalline MoS_2 films: tuning the thermal conductivity by grain orientation", *ACS Applied Materials & Interfaces* **9**(43), 37905–37911 (2017).

[∗] V. Babacic, **D. Saleta Reig**, S. Varghese, T. Vasileiadis, E. Coy, K.-J. Tielrooij, and B. Graczykowski, "Thickness-dependent elastic softening of few-layer free-standing $MoSe_2$", *Advanced Materials* **33**(23), 2008614 (2021).

[∗] S. Varghese, J. D. Mehew, A. Block, **D. Saleta Reig**, P. Woźniak, R. Farris, Z. Zanolli, P. Ordejón, M. J. Verstraete, N. F. van Hulst, and K.-J. Tielrooij, "A pre-time-zero spatiotemporal microscopy technique for the ultrasensitive determination of the thermal diffusivity of thin films", *Review of Scientific Instruments* **94**(3), 034903 (2023).

[∗] J. D. Mehew, M. Y. Timmermans, **D. Saleta Reig**, S. Sergeant, M. Sledzinska, E. Chávez-Ángel, E. Gallagher, C. M. Sotomayor Torres, C. Huyghebaert, and K.-J. Tielrooij, "Enhanced thermal conductivity of free-standing double-walled carbon nanotube networks", *ACS Applied Materials & Interfaces* **15**(44), 51876–51884 (2023).

[∗] R. Farris, O. Hellman, Z. Zanolli, **D. Saleta Reig**, S. Varghese, P. Ordejón, K.-J. Tielrooij, and M. J. Verstraete, "Microscopic understanding of the in-plane thermal transport properties of 2H transition metal dichalcogenides", *Physical Review B* **109**(12), 125422 (2024).

[∗] G. Lo Gerfo Morganti, R. Rosati, G. D. Brinatti Vazquez, S. Varghese, **D. Saleta Reig**, E. Malic, N. F. van Hulst, and K.-J. Tielrooij, "Transient ultrafast and negative diffusion of charge carriers in suspended $MoSe_2$ from multilayer to monolayer", *Nature Communications* **16**(1), 5184 (2025).

[∗] S. Varghese, J. Tur-Prats, J. D. Mehew, **D. Saleta Reig**, R. Farris, J. Camacho, J. A. Haibeh, A. Sokolov, P. Ordejón, S. Huberman, A. Beardo, F. X. Alvarez, and K.-J. Tielrooij, "Controllable hydro-thermoelastic heat transport in 2D semiconductors at room temperature", *Under review* (2025).

[∗] E. Tornero Gasca[§], M. van Hemert[§], B. Liu[§], S. Ippolito, H. Ramsden, Y. Gogotsi, K. Klinar, **D. Saleta Reig**, K.-J. Tielrooij[¶], and M. Muñoz Rojo[¶], "In- and out-of-plane thermal conductivity of $Ti_3C_2T_x$-based MXene flakes", *In preparation* (2025).
[§,¶]Equally contributing authors.

Other Publications by D. Saleta Reig

[∗] B. Graczykowski, M. Sledzinska, M. Placidi, **D. Saleta Reig**, M. Kasprzak, F. Alzina, and C. M. Sotomayor Torres, "Elastic properties of few nanometers thick polycrystalline MoS_2 membranes: a nondestructive study", *Nano Letters* **17**(12), 7647–7651 (2017).

[∗] **D. Saleta Reig**, P. Hummel, Z. Wang, S. Rosenfeldt, B. Graczykowski, M. Retsch, and G. Fytas, "Well-defined metal-polymer nanocomposites: the interplay of structure, thermoplasmonics, and elastic mechanical properties", *Physical Review Materials* **2**(12), 123605 (2018).

[∗] **D. Saleta Reig**, B. Grauel, V. A. Konyushkin, A. N. Nakladov, P. P. Fedorov, D. Busko, I. A. Howard, B. S. Richards, U. Resch-Genger, S. V. Kuznetsov, A. Turshatov, and C. Würth, "Upconversion properties of SrF_2:Yb^{3+},Er^{3+} single crystals", *Journal of Materials Chemistry C* **8**(12), 4093–4101 (2020).

[∗] S. Kovalev, H. A. Hafez, K.-J. Tielrooij, J.-C. Deinert, I. Ilyakov, N. Awari, D. Alcaraz, K. Soundarapandian, **D. Saleta Reig**, S. Germanskiy, M. Chen, M. Bawatna, B. Green, F. H. L. Koppens, M. Mittendorff, M. Bonn, M. Gensch, and D. Turchinovich, "Electrical tunability of terahertz nonlinearity in graphene", *Science Advances* **7**(15), eabf9809 (2021).

[∗] K.-J. Tielrooij, A. Principi, **D. Saleta Reig**, A. Block, S. Varghese, S. Schreyeck, K. Brunner, G. Karczewski, I. Ilyakov, O. Ponomaryov, et al., "Milliwatt terahertz harmonic generation from topological insulator metamaterials", *Light: Science & Applications* **11**(1), 1–8 (2022).

[∗] I. Ilyakov, A. Ponomaryov, **D. Saleta Reig**, C. Murphy, J. D. Mehew, T. V. de Oliveira, G. L. Prajapati, A. Arshad, J.-C. Deinert, M. F. Craciun, et al., "Ultrafast tunable terahertz-to-visible light conversion through thermal radiation from graphene metamaterials", *Nano Letters* **23**(9), 3872–3878 (2023).

[∗] R. Omar De La Bastida Chiza, E. F. Rongione, K. P. Soundarapandian, A. Nivedan, I. Vangelidis, **D. Saleta Reig**, K. Watanabe, T. Taniguchi, E. Lidorikis, F. H. L. Koppens, S. Castilla, and K.-J. Tielrooij, "Graphene-enabled coherent terahertz wave detection and interferometry", *In preparation* (2025).

Contents

List of Figures

Chapter 1

Introduction

Modern electronic and photonic technologies have advanced rapidly by making components smaller and more densely packed. This trend, in electronics described by Moore's law [1], has led to extraordinary improvements in speed, efficiency, and functionality [2]. However, as devices approach dimensions of just a few nanometers, the materials that have long supported this progress begin to face serious limitations [3]. At these scales, conventional three-dimensional (3D) materials, like silicon, exhibit degraded performance [4]. Electrical resistance increases, thermal conductivity decreases, and interfaces begin to dominate heat and charge transport. A detrimental consequence of using highly dense integrated circuits is the generation of excess heat that must be carried away from the devices at an ever increasing rate. These effects lead to significant challenges in managing heat, as high power densities drive rapid temperature rises that compromise performance and reliability. To address this, low-dimensional materials —systems that are only a few atoms thick or confined to nanoscale structures— could offer the solution. Note that this is only a sketch of a far more intricate reality. The hard-to-anticipate potential of low-dimensional materials underscores the need for deeper fundamental knowledge of their thermophysical properties.

Layered two-dimensional (2D) van der Waals (vdW) materials stand out among low-dimensional systems for being lithography-compatible and thus easily patterned and integrated into devices using established semiconductor manufacturing workflows [5–7]. These materials offer an enhanced tunability and unique properties that are not accessible by conventional 3D materials [8]. They are promising candidates for use in emerging technologies, either by complementing or replacing traditional materials. However, understanding heat transport in these systems is essential for continued progress [9]. In nanoscale devices, thermal

transport is no longer a secondary consideration: it often sets the limits of device performance. In this thesis, we contribute to this understanding through fundamental studies of the strongly anisotropic heat transport in two-dimensional van der Waals materials. In particular, we provide experimental investigations of the in- and out-of-plane heat transport properties of transition metal dichalcogenides (TMDs), a semiconducting 2D vdW materials family that has received significant research attention during the last two decades. Additionally, we explore how thickness and the surrounding environment influence heat dissipation, offering pathways to intentionally tune the thermal behaviour of these materials.

1.1 Two-Dimensional van der Waals Materials

Two-dimensional vdW materials are a unique class of crystalline solids composed of atomically thin layers. Within each layer, atoms are bonded strongly via covalent interactions, while the layers themselves are held together by much weaker van der Waals forces. This distinctive layered structure allows the isolation of individual monolayers or few-layer sheets, making 2D vdW materials highly relevant for research and technology. Their layered structure and reduced dimensionality gives rise to remarkable anisotropic mechanical, electronic, and thermal properties, often exhibiting diverse unprecedented characteristics when isolated as monolayer and few-layer materials. The initial breakthrough in isolating graphene [10] —*i.e.* an individual monolayer of graphite— came through mechanical exfoliation, wherein adhesive tapes were used to peel off single or few atomic layers from bulk 2D crystals.

While some bulk 2D crystals, like graphite and molybdenite, occur naturally [11], most high-quality ultrathin flakes of 2D crystals are obtained via mechanical exfoliation of synthetic materials. Scalable techniques such as molecular beam epitaxy and chemical vapor deposition (CVD) are now employed to produce large-area monolayers, but typically yielding lower quality and/or polycrystalline materials. Once produced, dry- and wet-transfer processes are typically utilized to position the 2D vdW materials onto desired substrates, enabling integration into devices and/or further characterization. Recent demonstrations of selective growth [12] and wafer-scale synthesis of single-crystalline mono- and few-layer materials [13] are expected to greatly accelerate their application landscape.

The ever-growing catalog of 2D vdW materials displays a broad spectrum of unique physical properties, which in turn provides a wide range of potential applications. Graphene, the most renowned example, is a semi-metallic single

atomic layer of carbon arranged in a honeycomb lattice and demonstrates extraordinary mechanical strength, flexibility, and high electron mobility [10, 14]. Other important materials include insulating hexagonal boron nitride (h-BN), semiconducting TMDs like molybdenum disulfide (MoS_2) and molybdenum diselenide ($MoSe_2$), and even superconducting compounds such as niobium diselenide (see **Figure 1.1**). Initially, graphite and molybdenite were mainly used as solid lubricants [15]. However, their atomically thin nature, combined with exceptional electrical, optical, and mechanical properties, positions them as promising candidates for next-generation devices and systems.

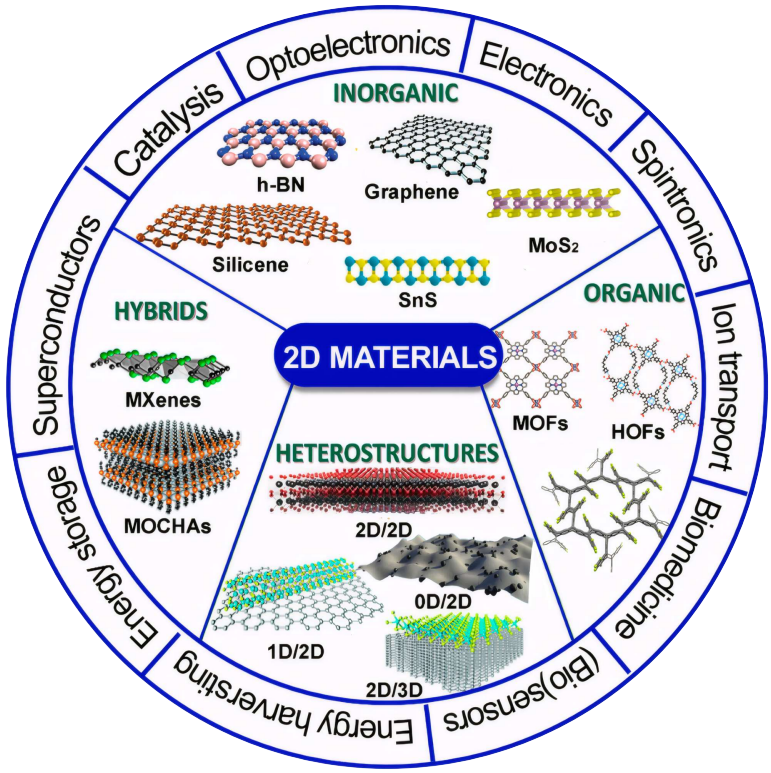

FIGURE 1.1: **Classification of 2D materials and some of their applications.** In this thesis we exclusively focus on inorganic 2D materials, in particular on semiconducting MoS_2 and $MoSe_2$ from the TMD family. Reprinted from Ref. [16], licensed under CC BY 4.0.

One of the most prominent applications lies in the field of nanoelectronics, where the sub-nm thickness of monolayer 2D vdW materials makes them potentially useful in advancing the miniaturization limit of (opto)electronic devices. The high

carrier mobility and flexibility of graphene, for example, have enabled the development of ultrathin transistors [10, 17], flexible and wearable electronics [18], transparent conductive electrodes [19], and supercapacitors [20], among others. Similarly, semiconducting TMDs offer thickness-controllable bandgaps [21], making them superior to graphene for digital electronics, logic computing [22], or flexible field-effect transistors [23]. As a result, they have already been included in the IMEC logic scaling roadmap [3]. Optoelectronics represents another major area of application. Here, graphene excels because of the ultrafast hot carrier dynamics and the ultra-broadband absorption. The strong light-matter interaction in 2D materials, especially for semiconductors like TMDs, gives them the ability to absorb [24], emit [25], and convert light [26] efficiently, enabling the realization of high-performance optoelectronic devices such as photodetectors [27, 28], light-emitting diodes (LEDs) and solar cells [29].

Thanks to the absence of dangling bonds and atomically flat surfaces, these materials can be thinned to the monolayer limit without introducing surface defects. Achieving this is rarely possible with traditional 3D materials, as dangling bonds create imperfect surfaces with increased roughness. Thinning 2D vdW materials, down to mono- or few-layers, modifies their electronic and phononic dispersion relations with respect to their bulk counterparts, given the one-dimensional quasi-particle confinement in the 2D plane. Thus, their electronic, optical, and thermal characteristics can be systematically tuned by controlling the number of layers. Another consequence of quasi-particle confinement is the reduced Coulomb screening in 2D systems, which results in stronger interactions between electrons and holes enabling not only to fabricate room-temperature excitonic devices, but also to observe high-temperature excitonic quantum behaviors [8]. Importantly, mono- and few-layer 2D vdW materials provide among the highest surface-to-volume ratio in the realm of materials science, which makes them extremely sensitive to their surroundings. As a result, they have also become especially valuable in areas like sensing and catalysis, where maximizing surface interactions is crucial.

This enhanced sensitivity to the material's surroundings also implies that it is much more convenient to modulate the material properties of 2D systems by mechanical, electronic, optical, and magnetic modulations than in conventional 3D materials, which is advantageous for device control [23, 30]. Additionally, it implies that their properties can be dramatically affected just by placing them

over a substrate, stacking into 2D heterostructures, encapsulating them or assembling them into periodic vertical superlattices (SLs). In these situations, proximity effects —arising from interfacial coupling to adjacent materials— can strongly modify the intrinsic properties of the 2D layer and enable functionalities absent in the isolated system. Furthermore, introducing a twist angle between layers creates a new, controllable length and interaction scale through long-wavelength moiré (in-plane) SLs, offering an additional means to modulate electronic interactions. A striking example is magic-angle twisted bilayer graphene, which exhibits a rich spectrum of electronic [31] and correlated [32] states —from insulating to superconducting— simply by setting the twist angle between two graphene layers at $\sim$1.1^{o}. This great variety of applications mainly arises from extensive knowledge of the optical and electronic properties of 2D vdW materials, and the ability to precisely control them by external stimuli [30]; by material thickness [21]; by introducing nanoscale patterns [33]; or by assembling them into artificial heterostructures [34]. Altogether, the possibilities unlocked by 2D van der Waals materials promise to redefine the boundaries of what is achievable in materials science.

1.2 Towards Control of Heat Flow in 2D Materials

The thermal properties of 2D van der Waals materials, however, remain less explored than their electrical and optical counterparts. This limited knowledge hinders the development of related (thermal) applications. Understanding how to study heat transport in nanoscale structures has been (and still represents) a great challenge, but offers opportunities to actively or passively control the flow of heat at the nanoscale. Over the past decade, lasers have become essential tools for heating and sensing the temperature of nanomaterials, thanks to (now) well-established optothermal methods like Raman thermometry and thermoreflectance techniques. These techniques enabled researches to shine light on the strongly anisotropic thermal transport properties of 2D vdW materials, which naturally arise from their layered crystal structure. However, comprehensive experimental (and theoretical) studies that examine how thickness affects heat transport in 2D van der Waals materials —especially across a wide range of thicknesses and down to the monolayer limit— remain scarce [9, 35–40]. As a result, it is challenging to draw meaningful conclusions, since comparisons across different measurement techniques or sample geometries are often compromised. In this thesis, we will contribute to this understanding by performing time-domain thermoreflectance

(TDTR) and Raman thermometry measurements on TMD flakes with systematic control of flake thickness.

The anisotropic layered structure in 2D vdW materials causes suppressed heat conduction in the stacking direction —due to the weak vdW interactions— as compared to heat conduction within the covalent plane. Consequently, 2D vdW materials are attractive to be used as heat guides, heat spreaders and thermal interface materials, contributing to a versatile platform for designing efficient heat management solutions. Thermoelectric applications exploiting 2D vdW materials have also received significant attention. Because the thermoelectric figure of merit is proportional to the electrical conductivity and inversely proportional to the thermal conductivity [41], 2D systems may enhance technologies aimed at recycling waste heat into electricity. For thermoelectric applications, these materials benefit from suppressed thermal transport in the stacking direction, and some even exhibit negative correlation between thermal and electrical conductivities with material thickness [41].

Beyond conventional, incoherent phonon transport —where heat is carried diffusively through random phonon scattering— there exists the possibility of harnessing coherent phonon heat flow. This was first demonstrated in 3D conventional materials using epitaxial GaAs/AlAs periodic SLs [42]. In this regime, phase relationships between phonons are preserved over extended distances, allowing wave-like interference effects to influence heat transport. Such coherence could enable a degree of control over thermal currents analogous to photonic control in optical systems, opening the door to phononic crystals and superlattices that guide, filter, or even localize heat. Using SLs made of stacked 2D vdW materials, it should be possible to produce atomically flat interfaces in favor of specular rather than diffuse interfacial scattering (see **Figure 1.2**), thus helping to preserve the phase of phonons that contribute to heat transport [43]. Thanks to the weak interlayer coupling of 2D vdW materials and tunable stacking sequences, coherent phonon heat offers a promising route to engineer thermal transport far beyond what is achievable through diffuse scattering alone. Potential applications would include nanoscale thermal waveguides, thermal switches with ultrafast modulation, and tailored thermal barriers for thermoelectric enhancement. All these applications rely on the deliberate design of phonon interference to steer heat with unprecedented precision.

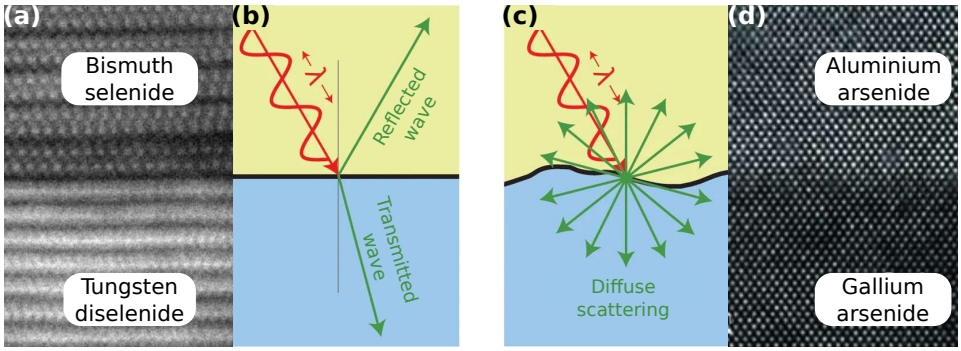

FIGURE 1.2: **Specular and diffuse phonon scattering**. **(a)** Cross-section TEM image of 2D/2D interface. **(b)** When a wave scatters at flat interfaces, specular reflection occurs. **(c)** For rough interfaces, as those between conventional 3D materials, diffuse scattering tends to occur, randomizing the phase of the scattered phonons. **(d)** Cross-section TEM image of a 3D/3D interface. Adapted from (a) Ref. [44] with permissions from Elsevier; (b,c) Ref. [43] with permissions from Springer Nature; and (d) Ref. [42] with permissions from AAAS.

Realizing the full potential of 2D van der Waals materials for (thermal) applications thus remains elusive. Achieving this goal requires a deeper understanding of their thermal properties and effective strategies for tuning them. Particularly, experimental and theoretical studies systematically investigating the effects of thickness on the thermal properties of 2D vdW materials remain scarce. Moreover, the possibility of harnessing coherent phonon heat with 2D vdW materials remains absent in the literature. To the best of our knowledge, only a single theoretical work to date discusses the effects of coherent phonon heat in vertical graphene/h-BN vdW SLs [45]; and two experimental works explored (incoherent) heat transport in periodic stacks of alternating 2D vdW materials [46, 47], but using structures that remain too thin to observe effects due to coherent phonon heat transport. Other interesting works include the use of electrical heaters and optical thermometers to measure the thermal boundary conductances of 2D/2D and 2D/3D interfaces in vdW heterostructures [48]; and the use of interlayer rotation in stacked MoS_2 films to produce extremely anisotropic heat spreaders [49]; although they do not discuss the coherent nature of heat. This thesis is concerned with advancing the current understanding of how heat flows in 2D vdW materials —and how to control it— by studying the effects of thickness and the surrounding environment on the (opto)thermal properties of prototypical TMDs. Importantly, we explore (for the first time) the possibility of coherent phonon heat, and coherent phonon heat interference to contribute to the flow of heat within a single 2D

vdW material.

1.3 Organization of the Thesis

This thesis is essentially comprised of four parts. First, we design a home-built dry-transfer setup to manipulate and transfer 2D materials onto arbitrary substrates. We use this system to fabricate thickness-controlled MoS_2 flakes supported on substrates; and $MoSe_2$ flakes suspended over circular apertures, which we later exploit for our heat transport measurements. Second, we design and build an ultrafast optothermal setup specifically designed to track heat with high spatial and temporal resolution in nanoscale systems. Third, we use our optothermal setup to perform time-domain thermoreflectance measurements aimed at exploring out-of-plane heat transport phenomena across our supported MoS_2 flakes. This is, perpendicular to the stacking direction. Fourth, we exploit our suspended $MoSe_2$ flakes to investigate in-plane heat transport using conventional Raman thermometry measurements, as implemented in a well-established optical setup. The contents of each chapter are the following:

- Chapter 2 provides a general overview of two-dimensional materials; the basics of phonon heat transport; some strategies currently used to manipulate phonons; and the optothermal techniques used to explore heat transport at the nanoscale, relevant in this thesis.
- Chapter 3 details the design and construction of our home-built dry-transfer system; the procedures we employed to transfer thickness-controlled 2D flakes onto arbitrary substrates, with which we prepare supported MoS_2 and suspended $MoSe_2$ samples; and a thorough characterization of our suspended $MoSe_2$ flakes.
- Chapter 4 explains the design and construction of a versatile, ultrafast optical setup, capable of performing multiple heat transport experiments; and details the main components and alignment procedures, focusing on time-domain thermoreflectance measurements.
- Chapter 5 summarizes the theory of time-domain thermoreflectance; and provides all the tools needed to simulate the signals that would be read by a lock-in amplifier in a TDTR experiment.
- Chapter 6 exploits our TDTR setup to present a complete exemplary data analysis using our control experiments (*i.e.*, the bare substrate, and a thick

MoS_2 flake); and reviews the data post-processing and fitting routines used for the TDTR analysis reported throughout the thesis.

- Chapter 7 shows our room-temperature TDTR results of the ***out-of-plane*** heat transport experiments on thickness-controlled supported MoS_2 flakes; and, using temperature-dependent TDTR measurements, explores the possibility of coherent phonon heat interference to occur.
- Chapter 8 gives a unified physical picture of the influence of thickness on the intrinsic ***in-plane*** thermal conductivity κ_r of $MoSe_2$, thanks to a combined experimental-theoretical approach based on Raman thermometry and *ab initio* calculations; and explores the effects of environment and substrate properties by means of an apparent thermal conductivity κ_{app}.
- Chapter 9 presents an overview of the main results and contributions of this thesis and outlines possible avenues for future research.

Chapter 2

Heat Transport in 2D vdW Materials

2.1 Electronic and Phononic Band Structures of Transition Metal Dichalcogenides

Transition metal dichalcogenides, with the general formula MX_2 (where M is a transition metal like molybdenum and tungsten, and X is a chalcogen like sulfur and selenium), represent a diverse class of typically semiconducting 2D vdW materials. As we have seen before, these materials exhibit strong in-plane covalent bonding and weak van der Waals coupling between adjacent layers. Each TMD monolayer consists of a hexagonally packed plane of transition metal atoms sandwiched between two planes of chalcogen atoms covalently bonded to the transition metal, forming a trigonal prismatic or octahedral coordination depending on the polytype. Each polytype exhibits distinct properties, with the most common coordination being trigonal prismatic (displaying hexagonal symmetry, typically referred as 2H) and octahedral (with tetragonal symmetry, referred as 1T) or other less common polymorphs such as the rhombohedral phase (which break the inversion symmetry, referred as 3R) [50]. These phases typically exhibit semiconducting (2H- and 3R-TMDs) or semi-metallic (1T-TMDs) characteristics. In this thesis, we focus solely on 2H-MoS_2 and 2H-$MoSe_2$, as representative semiconducting 2D vdW materials from the TMD family. We show their crystal structure and Brillouin zone in **Figure 2.1**, which display space group symmetry $P6_3/mmc$ [51]. Other families —such as Re-, Pt/Pd-, Zr/Hf-, or Sn-based compounds— can have different structures, dispersion relations, and transport behavior.

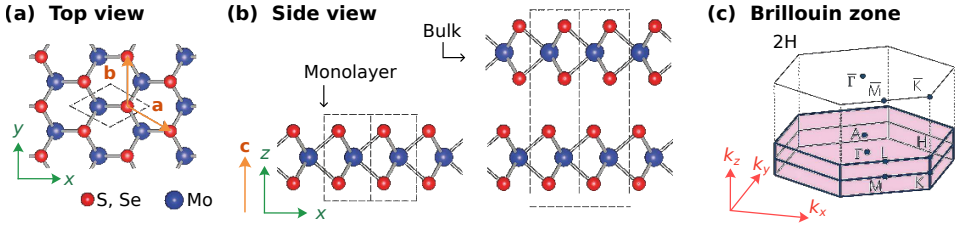

FIGURE 2.1: **Unit cell and Brillouin zone of 2H-TMDs.** **(a)** Top and **(b)** side view representations of the crystal structure and unit cells for monolayer and bulk 2H-TMDs; with the **(c)** Brillouin zone represented in the reciprocal space. Adapted from Ref. [52] with permissions from Springer Nature.

The electronic band structure of TMDs is highly sensitive to both their composition and layer number. Many semiconducting TMDs, including MoS_2 and $MoSe_2$, exhibit an indirect-to-direct band gap transition at the monolayer limit [21, 53], resulting in dramatically enhanced light–matter interactions. **Figure 2.2** shows the exemplary electronic band structures of monolayer [Fig. 2.2**a**] and bulk [Fig. 2.2**b**] $MoSe_2$. In bulk TMDs, the conduction band minimum and valence band maximum are located at different points in momentum space, making optical transitions indirect. These require both a photon and a phonon to conserve energy and momentum, and are thus relatively inefficient. By contrast, monolayer TMDs possess a direct band gap at the K point of the Brillouin zone, allowing electrons to recombine with holes through purely radiative transitions that do not require phonon assistance. This direct band structure leads to a sharp increase in photoluminescence (PL) quantum yield, making monolayer TMDs particularly efficient as light emitters. As the number of layers increases, the band gap becomes indirect. This results in a broader and red-shifted PL spectra whose intensity drops by several orders of magnitude (see Fig. 2.2**c**), due to the lower energy (indirect) transitions from Γ to K. Thus, the optical properties of TMDs, including their photoluminescence, are extremely sensitive to thickness and layer number. In Chapter 3, we will exploit this layer-sensitive PL emission to confirm the exact thickness of mono-, bi- and trilayer $MoSe_2$ flakes.

Nevertheless, we are interested in the thermal properties of 2D vdW materials, where several remarkable and exotic thermal transport phenomena have been observed. Interesting observations are the ultrahigh in-plane thermal conductivity of graphene [56, 57] and hexagonal boron nitride (hBN) [58], the highly anisotropic thermal transport of TMDs [59] and stacked TMD films [48, 49], and the occurrence of second sound in graphite [60]. When starting this thesis work,

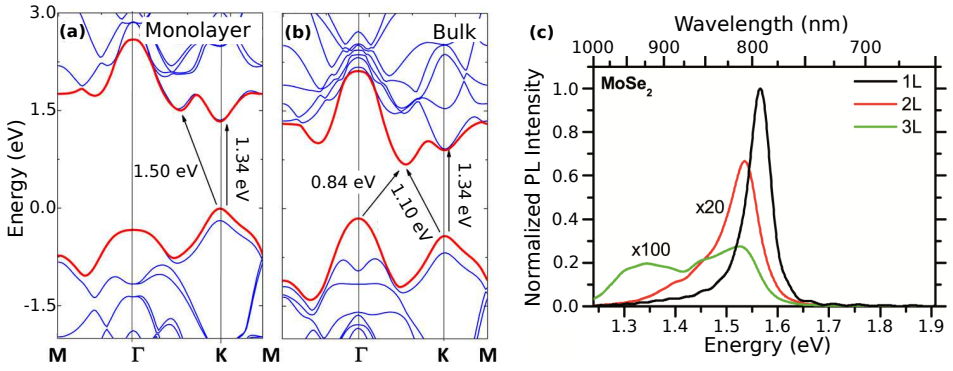

FIGURE 2.2: **Electronic band structure and PL emission for $MoSe_2$.** Calculated electronic band structure for **(a)** monolayer and **(b)** bulk $MoSe_2$; with the measured photoluminescence emission from mono-, bi- and trilayer flakes. Adapted from (a,b) Ref. [54] and (c) Ref. [55].

there were still many open questions concerning the very basic, yet critical, thermal transport properties of TMDs at room temperature [9].

The phononic band structures of bulk TMDs (see **Figure 2.3** for $MoSe_2$) reveal a broad spectrum of optical and acoustic modes. These exhibit significantly lower frequencies as compared to graphite or graphene, given the higher atomic mass in TMDs. For most 2D vdW materials, pronounced layer-dependent changes can be expected, as thinning down the material implies removing interlayer interactions, which are absent at the monolayer limit. Increasing the thickness of the material towards the bulk introduces additional modes because of the interactions between layers, and their relative vibration phase (see Fig. 2.3**b**). The weak interlayer coupling leads to distinct shear and layer-breathing phonon modes at low frequencies, while strong in-plane bonds result in high-velocity acoustic phonons. The combined effects of strong anisotropy and quantum confinement result in highly direction-dependent thermal transport: heat transport is an order of magnitude more efficient in the in-plane (r) direction as compared to the out-of-plane (z) direction due to efficient propagation of acoustic phonons within the layers.

For monolayer TMDs, their three-atom unit cells give rise to a total of 9 vibrational modes: three acoustic and six optical modes (see Fig. 2.3**a**). Acoustic modes are those in which all atoms move in phase with respect to the neighbouring unit cell. In this case, we have longitudinal acoustic (LA), or compression waves along the propagation direction (*i.e.*, sound waves); transverse acoustic (TA), or in-plane shear waves along the propagation direction; and out-of-plane acoustic (ZA), or

flexural waves with typically lower frequencies [Fig. 2.3**c**]. We will see in Chapter 8 that these low-frequency out-of-plane ZA modes significantly contribute to in-plane heat transport in suspended monolayer $MoSe_2$. On a separate note, monolayer TMDs do not show dispersion relations for acoustic phonons from Γ to A (*i.e.*, along the out-of-plane direction) given the lack of repetitions of the unit cell in this direction.

Optical modes are those in which the atoms move with opposite phases within the unit cell. These are often classified based on their symmetry and activity in Raman and/or infrared (IR) spectroscopies. A mode is Raman-active if it causes a change in the material's polarizability, allowing incident photons to scatter inelastically and exchange energy with the lattice vibration. In contrast, a mode is IR-active if it produces a change in the dipole moment of the unit cell, enabling direct absorption of infrared radiation. Whether a particular optical phonon mode is active in Raman, infrared, or both is determined by the crystal symmetry and the selection rules that follow from it. Among the available optical modes in TMDs (see Fig. 2.3**d**), the A'_1, E′ and E″ modes are Raman-active, although backscattering Raman experiments typically suppress the E″ mode due to polarization selection rules. We will see in the following sections that, while acoustic modes typically dominate heat transport in TMDs, optical modes also serve as sensitive experimental probes for studying their thermal properties.

2.2 Phonon Heat Transport in 2D Systems

At the macroscale, heat conduction in solids is described phenomenologically by Fourier's law. It states that the heat flux $\boldsymbol{q}$ is proportional to the negative temperature gradient ∇T:

$$\boldsymbol{q} = -\kappa \nabla T \tag{2.1}$$

where κ is the thermal conductivity (with units of W m^{-1} K^{-1}). This equation captures the everyday fact that heat flows from hot regions to cold regions.

To go beyond the phenomenological constant κ, we need to connect it to the microscopic quasi-particles that carry heat. For most solids like semiconductors and insulators, heat is mainly carried by phonons, the quanta of lattice vibrations. Electrons only contribute significantly to heat transport in metals, where the free electron density is high; or at very low absolute temperatures, where lattice vibrations are frozen. This is because at room temperature the heat capacity (*i.e.*, the ability to store heat) is around two orders of magnitude smaller for electrons C_e

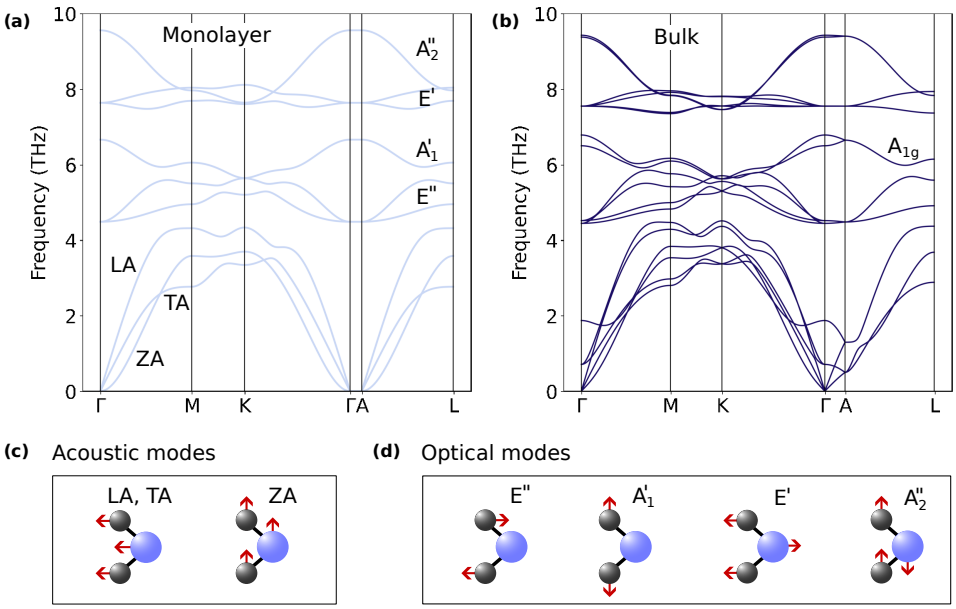

FIGURE 2.3: **Phonon band structure of $MoSe_2$.** Phonon dispersion relations for **(a)** monolayer and **(b)** bulk $MoSe_2$, with the schematic representations of **(c)** acoustic and **(d)** optical modes for the monolayer structure.

than for phonons C_{ph}:

$$C = \frac{1}{V}\left(\frac{\partial U}{\partial T}\right) \tag{2.2}$$

with U the internal energy per volume V and per unit change in temperature.

Phonons also have a typical group velocity v_g, closely related to the sound velocity in the material, that tells us how fast a wavepacket of lattice vibrations moves in the crystal. The group velocity of a phonon mode corresponds to the slope of its dispersion relations along a given direction in momentum space (see Fig. 2.3). It is now clear that acoustic phonons travel much faster than optical phonons, and are thus responsible for sound propagation. Because phonons scatter from defects, other phonons, and boundaries, they travel only a limited distance before they scatter and exchange energy. This is quantified by the phonon mean free path (MFP):

$$\ell = v_g\,\tau \tag{2.3}$$

where τ is the phonon relaxation time, *i.e.*, the average time between successive scattering events.

The Boltzmann transport equation (BTE) provides a statistical framework for describing how the phonon distribution function $f(\boldsymbol{k}, t)$ evolves in response to a temperature gradient. Within the relaxation time approximation, the deviation of f from equilibrium decays over a timescale τ, thereby linking scattering processes to heat transport. Solving the BTE for a small temperature gradient leads to a microscopic expression for the lattice thermal conductivity. In general, it can be written as a sum (or integral) over all phonon modes k:

$$\begin{aligned} \kappa &= \frac{1}{N_{\mathbf{dim}}} \sum_k C_k \, v_{\mathrm{g},k}^2 \, \tau_k \\ &= \frac{1}{N_{\mathbf{dim}}} \sum_k C_k \, v_{\mathrm{g},k} \, \ell_k \end{aligned} \tag{2.4}$$

with C_k the mode-resolved heat capacity, and N_{dim} the dimensionality of the system (*e.g.*, $N_{\mathrm{dim}} = 3$ for 3D-bonded materials like silicon, and $N_{\mathrm{dim}} = 2$ for 2D vdW materials). For a phonon mode k to effectively carry heat and contribute to heat transport, it should possess a high frequency (energy), a large group velocity $v_{\mathrm{g},k}$ and a large MFP ℓ_k.

Acoustic phonons are typically the main carriers of heat in crystalline solids. This dominance arises from two key factors: they possess higher group velocities than optical phonon modes, and their lower frequencies make them less likely to scatter, thereby extending their MFPs [61, 62]. In contrast, optical phonons lie at higher frequencies, where anharmonic scattering processes are more probable and lifetimes are correspondingly shorter [63]. As a result, their contribution to the lattice thermal conductivity is generally small, except in specific cases where low-frequency optical branches can contribute non-negligibly [64]. Although optical modes contribute little to heat conduction —mainly due to their lower group velocities, shorter MFPs, and lower occupation at room temperature and below— their activity in Raman and/or infrared spectroscopies makes them highly valuable for probing lattice temperature dynamics. For example, the temperature-dependent frequency and linewidths of Raman-active phonon modes (as is the case for the $A_{1\mathrm{g}}$ mode in TMDs, see Chapter 8) are commonly exploited to extract information about local heating and thermal transport [65, 66].

Out-of-plane thermal conductivity of TMDs. Studying out-of-plane heat flow and quantifying heat transport capabilities of anisotropic TMDs requires designing experiments where the temperature gradient is defined along the c-axis of the

2D vdW material crystal. For this, flakes supported on substrates, or flakes vertically encapsulated between a heater and a heat sink are often employed. For relatively thick flakes, the out-of-plane thermal conductivity of TMDs is in the order of $\kappa_z \approx 1-5$ W m^{-1} K^{-1} [39, 59]. When these materials are much thinner than the phonon mean free path along the *c*-axis, their impact on heat transport is usually described in terms of the thermal interfacial resistance R_{thermal} of the flake and its contacts with neighboring materials. However, heat flow in thin films is largely governed by surface and size effects, leading to a quasi-ballistic heat transport in this direction [39]. Nevertheless, the total thermal resistance provided by these flakes largely depends on the preparation methods, the interfacial conductances with heater and substrate, stacking order, and the crystalline quality of the material. Therefore, literature values are scattered and thermal boundary conductances ($G = 1/R_{\text{thermal}}$) of 2D vdW materials with glasses and dielectric materials is typically ∼20 MW m^{-2} K^{-1} as for MoS_2 on SiO_2 (G_{MoS_2/SiO_2}) [67], but vary significantly in range $5-50$ MW m^{-2} K^{-1} when considering thickness variations [37], exfoliated and synthetic materials, more specific sample geometries or different techniques [68].

In-plane thermal conductivity of TMDs. Experimental values reported in the literature for the in-plane lattice thermal conductivity κ_r of TMDs also vary substantially. At room temperature, from 6 W m^{-1} K^{-1} [69] to 59 W m^{-1} K^{-1} [70] for $MoSe_2$. Moreover, it is not clear how κ_r changes with the thickness of TMD flakes [9, 38, 40, 71]. A systematic experimental study with a broad range of thicknesses was lacking when starting this thesis work. Moreover, the calculated thermal conductivities extracted from atomistic simulations (typically considering phonons at 0 K) also gave scattered results, with values ranging from 17.6 [72] to 54 W m^{-1} K^{-1} [73] for monolayer $MoSe_2$. In the theoretical approaches, a systematic thickness variation is also lacking, as most studies focused either on monolayer or bulk $MoSe_2$ systems. The effect of the environment on heat transport in TMDs has furthermore not received much attention, despite that a significant effect was observed for graphene [74]. This situation for $MoSe_2$ is representative for all layered materials in the TMD family [9], and indicates that a proper physical understanding of thermal transport in TMDs —and in particular the effect of material thickness and environment in the limit toward monolayer— is missing.

2.3 Strategies for Phonon Control at the Nanoscale

The ability to understand and control heat transport is central to diverse applications. Efficient thermoelectric materials require low lattice thermal conductivity to enhance conversion efficiency, while modern nanoelectronics and optoelectronics demand efficient heat removal to ensure stability and performance. Two-dimensional transition metal dichalcogenides, with their reduced dimensionality and layered structure, provide a unique platform to explore and engineer thermal transport at the nanoscale.

Heat conduction is typically governed by the random motion of thermal energy carriers, these being phonons, electrons, or molecules. Over the past decades, researchers have devoted significant attention to the size-dependent effects on phonon heat transport, which can lead to departures from this purely diffusive (incoherent) behavior [75]. Most experimental evidence for these phonon size effects can be understood within the Casimir framework, where phonons propagate ballistically or quasi-ballistically through a material and scatter primarily at boundaries and interfaces [76]. These classical size effects play a crucial role in fields such as thermoelectric energy conversion and the thermal management of microelectronic devices. In this diffusive regime, the phase information that phonons carry is rapidly lost due to diffuse boundary scattering and internal scattering mechanisms. However, it is possible to move beyond this incoherent heat conduction and achieve control over heat flow by manipulating coherent phonon heat waves (see **Figure 2.4**). Examples include engineering stop-bands in periodic structures [77], generating soliton waves [78], or phonon localization [79]. Realizing these phenomena requires that heat-carrying phonons retain their phase coherence throughout the conduction process.

Using conventional 3D-bonded materials, coherent phonon heat transport was first experimentally observed [42] in metal-organic chemical vapor deposition (MOCVD)-grown superlattices (SLs) made of gallium and aluminum arsenide GaAs/AlAs, with 12/12 nm periods. Here, the authors increased the number of periods and observed an increasing effective thermal conductivity, implying that long MFP phonons (*i.e.*, those with ℓ_k larger than the period thickness of 24 nm) retain their phase information as they travel across the entire superlattice. This means that the additional interfaces modify the dispersion relations of the entire structure, which behaves as a homogeneous material. This is in contrast with the incoherent picture, where the material behaves like a composite material and diffuse scattering at the interfaces dominates heat transport, effectively limiting the

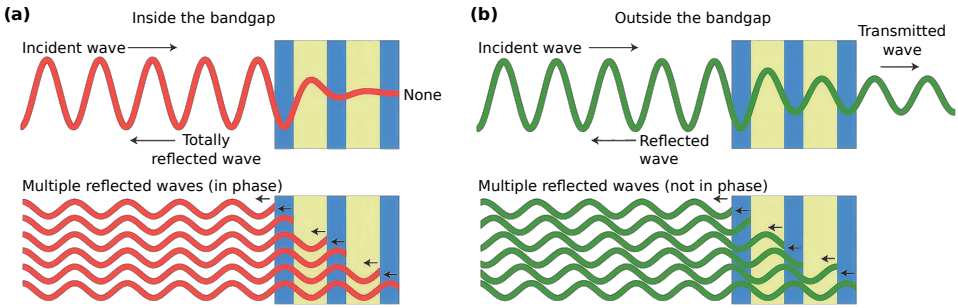

FIGURE 2.4: **Schematic representation of coherent phonon interference.** **(a)** When a wave is incident on a periodic material, multiple reflected waves are created at the interfaces. If these waves are in phase, they interfere constructively and thus prevent the original wave from propagating within the structure. **(b)** If the multiple reflected waves are not in phase, they do not interfere constructively and the original wave is allowed to propagate. The range of frequencies for which the original wave is forbidden from propagating within the structure is known as the bandgap. Reprinted Fig. 1 from Ref. [43], with permissions from Springer Nature.

MFP. Layered 2D materials are also expected to support coherent phonon heat conduction, and developing methods to probe and control it would have relevant implications in phonon engineering and an array of applications.

We note that the quality and abruptness of the interfaces that can be achieved using 2D vdW materials is unprecedented in conventional 3D-bonded materials (see Fig. 1.2). For example, interfaces of the superlattices grown in Ref. [42] have more than three atomic layers of chemical intermixing, implying smooth transitions between the thermal properties of the two superlattice constituents. These intermixed interfaces represent diffusive boundaries for high-frequency phonons, overall decreasing the thermal conductivity of the superlattice by an order of magnitude as compared to its isolated constituent materials. Using 2D vdW materials instead, it is possible to achieve atomically sharp interfaces in favour of specular rather than diffuse scattering (see Fig. 1.2) upon phonon reflection (or transmission) [43, 80]. This effect could significantly contribute in retaining the phase information of phonons during heat transport.

With only four studies reported to date [45–47, 81], the exploration of periodic vertical superlattices made of two-dimensional van der Waals materials (vdW-SLs) as platforms for coherent heat conduction remains in its infancy. Notably, only a theoretical work was published prior to the start of this thesis [81], positioning our experimental work described in Chapter 7 at the forefront of the field and underscoring the promise of 2D vdW materials as ideal systems for phonon

engineering [82]. One reason for this is that any 2D vdW material can be vertically stacked without the need for lattice matching, to create heterostructures [48]. This introduces additional tuning knobs such as the twist-angle or dielectric environment. Moreover, it is well established that, when atomically thin 2D materials are brought into intimate contact, their individual optical, mechanical, and electronic properties merge via interlayer coupling, yielding a hybrid system with emergent dispersion relations distinct from those of the isolated materials [83]. By analogy, similar hybridization effects are expected in thermal transport: when 2D vdW materials are assembled into periodic superlattices, their phonon dispersions and mean free paths should become modified, potentially giving rise to collective thermal properties that differ from those of their constituent mono- or few-layer materials [81]. **Figure 2.5** summarizes the results of a theoretical work using molecular dynamics, where varying the interface density (or period thickness) in graphene/h-BN SLs [45] results in a minimum effective thermal conductivity. This is the expected behavior during the crossover from coherent (at very large interface density) to incoherent (at small interface density) phonon heat transport. These observations are equivalent to the behavior of conventional SLs [84, 85].

However, experimental works of coherent phonon heat transport in 2D vdW-SLs are scarce, and currently limited to the use of CVD-grown graphene/MoS_2 monolayers assembled into stacks no thicker than five layers [46]; or synthetic $(SnS)_{1.17}(NbS_2)_n$ vdW-SLs [47], only up to 3-periods thick. Both studies provide extremely low effective thermal conductivity values, given their extremely high interface density. While not purely diffusive, an increased thermal resistance is observed in Ref. [46] with the number of alternately stacked layers of graphene and MoS_2. This diffusive-like behavior is attributed to the stacking disorder and impurities introduced with the assembling process. In Ref. [47], the authors claim heat conduction is incoherent with their results being dominated by interface scattering, even when using extremely small period thickness. In both experiments, the situation seems to be that the picture of coherent phonon heat transport cannot be resolved for two reasons: due to the small overall thickness variations in relation to the MFP; or due to the almost invariant interface density.

Conceptually, 2D vdW materials already represent superlattice-like structures, at the highest available interface densities, being made of alternating covalent 2D layers and van der Waals gaps. Importantly, they do not behave as composite materials with alternating properties of the monolayer material and air (vacuum), but they act like a uniform, homogeneous material. This is, similarly to conventional superlattices supporting coherent heat conduction. In turn, controlling the

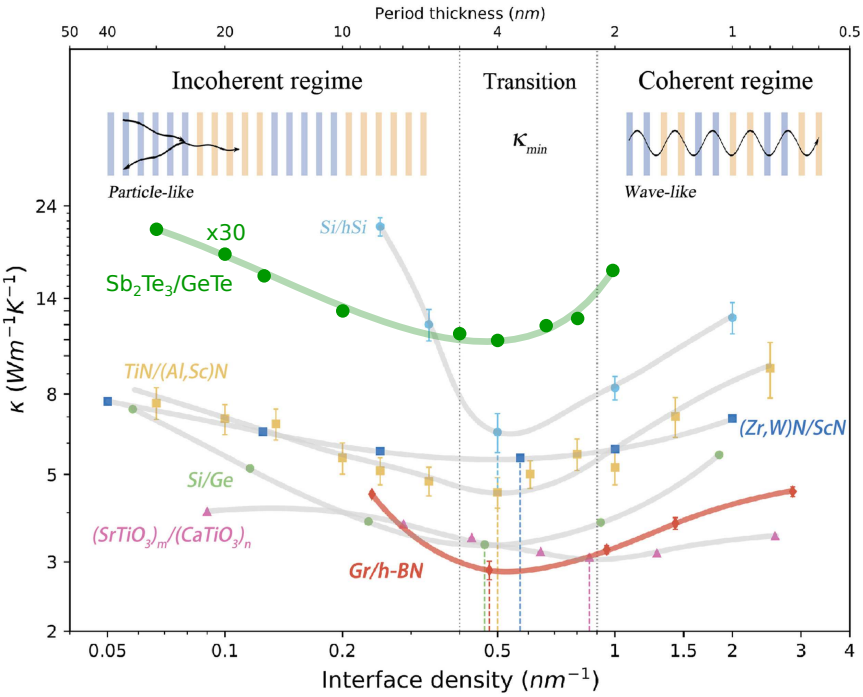

FIGURE 2.5: **Coherent to incoherent heat transport crossover in vdW-SLs.** The out-of-plane thermal conductivity of Gr/h-BN superlattices, compared to that of conventional SLs, as a function of interfacial density at 300 K. The inset depicts a schematic diagram of phonon thermal transport, which consists of three parts divided by interface density: the coherent regime, the incoherent regime, and the transition regime between the former two where there exists a thermal conductivity minimum. The vertical dashed lines in the transition regime correspond to the locations where the six superlattice thermal conductivity minimum occur. Adapted from Ref. [45], licensed under CC BY 4.0, including the data of Ref. [86] (*green circles*).

overall material thickness of 2D vdW materials is known to modify its phonon dispersion relations rather than introducing (removing) thermal resistance channels when increasing (decreasing) their number of layers. Effectively, this means that thickness-control could be sufficient to investigate coherent phonon heat and phonon interference effects within a single 2D vdW material, without the need to fabricate complicated vdW-SLs.

Other strategies for phonon engineering and manipulation of heat flow using 2D vdW materials include the introduction of nanopatterns to create phononic crystals with phonon stop bands; assembling into heterostructures, or encapsulating to control the dielectric environment; and introducing twist angles to tune the

coupling between layers.

2.4 Optical Thermometers at the Nanoscale

Several techniques —such as the 3ω method [87], micro-thermal bridge [88], or scanning thermal microscopy (SThM) [89]— have been developed to measure temperature and thermal properties, but they often requires complex sample fabrication, electrical or physical direct contact with the system, or can perturb the measurement itself, which limits their applicability at the nanoscale. The study of heat transport at the nanoscale requires thermometry methods that are both non-contact and capable of probing heat with high spatial and/or temporal resolution. Optical approaches provide unique advantages in this regard: they offer rapid data acquisition, minimize disturbance of the system under study, and can be integrated into a wide variety of experimental platforms. Among these, two families of techniques have become particularly powerful tools. Raman-based thermometers exploit the temperature-dependent vibrational fingerprint of a material to extract local thermal information with sub-micrometer resolution. Complementary to this, pump–probe thermoreflectance techniques use ultrafast laser pulses and changes in optical reflectivity to track heat flow with sub-picosecond temporal resolution. Together, these approaches enable a detailed, non-invasive view of nanoscale thermal transport, though each comes with its own challenges in calibration, interpretation, and sensitivity to the sample geometry.

2.4.1 Raman-based thermometers

Raman spectroscopy is a light-scattering technique used to retrieve a material's vibrational fingerprint. Typically, a continuous-wave (CW) monochromatic laser source is focused on a sample, and the backscattered light is collected and analyzed by a Raman spectrometer. Most light elastically scatters from the sample (*i.e.*, without energy exchange with the lattice) in a process called Rayleigh scattering. However, a small fraction of photons —around one in ten million— inelastically scatter either losing energy (Stokes) or gaining energy (anti-Stokes), in what is referred to as Raman scattering (see **Figure 2.6**). We present a schematic Raman spectrum [Fig. 2.6**a**] and energy-level diagram illustrating the transitions underlying Rayleigh, Stokes, and anti-Stokes scattering processes, as well as infrared absorption (*i.e.*, the basis of infrared spectroscopy) [Fig. 2.6**b**].

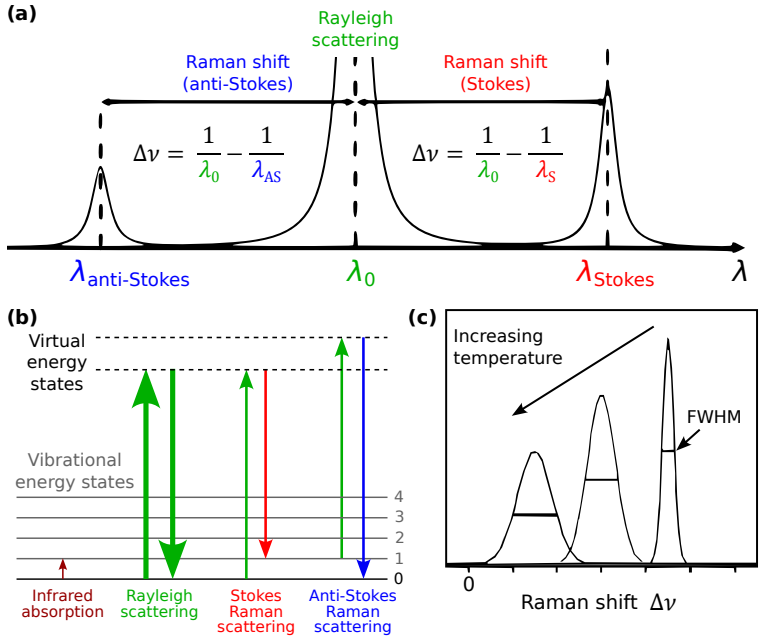

FIGURE 2.6: **Raman scattering and Raman thermometry. (a)** Schematic Raman spectra at low temperature showing the Rayleigh (elastic) scattering, and Stokes and anti-Stokes Raman (inelastic) scattering features, with λ_0 the excitation wavelength and $\Delta\nu$ the Raman shift of the Stokes (S) and anti-Stokes (AS) processes. **(b)** Energy level diagram showing the available transitions (also including the infrared absorption in IR spectroscopy). **(c)** Upon increasing the temperature, the Raman intensity decreases and its full width at half maximum (FWHM) typically broadens, while (red-)shifting to lower frequencies. Adapted panel (c) from Ref. [90].

Experimentally, the elastically scattered (reflected) laser line (Rayleigh scattering) is filtered using a notch or edge filter, while the inelastically scattered light (Raman scattering) is focused on the slit of a spectrometer diverging to a concave mirror, which re-collimates the light and directs it to a grating. The grating disperses the signal onto a CCD detector by reflecting each wavelength at a different angle. The resolution of the spectrometer is determined by the groove density (g/mm) of the grating and the distance of the second mirror and the CCD camera (typically fixed by the manufacturer) [90]. A larger groove density implies a higher resolution at the expense of collection efficiency and, thus, increased acquisition time. Finally, a CCD sensor records the Raman signal and presents it in terms of relative energy ($E_{\text{Raman}} = E_{\text{laser}} \pm E_{\text{vibration}}$), typically expressed in wavenumbers (cm^{-1}).

The Raman probe can be used as a sensitive thermometer thanks to a (first calibrated) temperature-dependent property, most typically the phonon population and/or phonon frequency. Temperature dictates the available phonon population, with lower temperatures favouring phonons to be in the ground state and higher temperatures implying more phonons are thermally excited. In turn, Stokes (S) processes are more likely to occur at higher temperatures and anti-Stokes (A) processes at lower temperatures.

The ratio of the Raman intensities $I_{A,S}$ of both processes thus becomes a sensitive probe of the local temperature:

$$\frac{I_A}{I_S} = A\,\frac{n}{n+1} = A\exp\left(-\frac{\hbar\omega}{k_B T}\right) \tag{2.5}$$

with n the phonon population; A a calibration constant, measured at the time of experiment by changing the absolute temperature T; ω the phonon frequency; k_B the Boltzmann constant; and $\hbar$ the reduced Planck constant ($h/2\pi$).

Additionally, the phonon frequency is commonly used as a thermometer, given that the Raman peak position and linewidth vary with temperature [Fig. 2.6**c**]. As the lattice expands and interatomic forces change due to anharmonicity, the Raman signal red-shifts to lower wavenumbers, while increased phonon–phonon scattering shortens phonon lifetimes and broadens the linewidth. With prior calibration, fitting the peak position while varying both the absolute temperature (calibration) and laser power thus provides a straightforward way to determine the local temperature under the laser spot. In Chapter 8 we will use this approach to study in-plane heat transport in $MoSe_2$.

The thermal conductivity is ultimately derived from the experimental sample geometry, and often require finite-element simulations [65, 66, 90]. For a bulk isotropic material, this can be simply expressed on the temperature increase ΔT produced by a given absorbed laser power P_{abs} within the laser spot size σ:

$$\kappa = \frac{P_{abs}}{4\sqrt{\pi}\,\Delta T\,\sigma} \tag{2.6}$$

We will see in Chapter 8 that this expression slightly changes when considering a thin-film material suspended over a circular hole, thus involving the film thickness and the hole size. In our case, as the material is sufficiently thin, we homogeneously heat the suspended membrane along the c-axis such that heat flow is

restricted to the in-plane direction along the membrane, thus retrieving the intrinsic in-plane thermal conductivity of the material.

2.4.2 Pump-probe thermometry

The advantage of using ultrafast lasers is the possibility to study heat flow with high temporal resolution, and —more importantly— to gain sensitivity by differential measurements. In this case, a signal containing thermal information is monitored while varying the time of arrival between the pump (exciting and introducing heat in the system) and probe (monitoring the temperature) laser pulses, as we depict in **Figure 2.7**. The most common example is time-domain thermoreflectance (TDTR), in which the temperature-dependent reflectivity of a metal transducer deposited on the sample of interest serves as the local thermometer. We will give more details about TDTR in Chapters 5, 6 and 7. Another relevant example is transient grating spectroscopy (commonly, TGS), in which the interference of two pulsed laser beams generates a spatially periodic heating pattern, and the decay of this "thermal grating" is monitored to extract the thermal diffusivity and related properties of the sample [91]. Recently, we have also developed a spatiotemporal method that exploits the temperature-dependent exciton linewidth of suspended TMD flakes to retrieve their in-plane thermal diffusivity, and observed signs of non-diffusive heat transport (see Refs. [92–94]). Time-resolved Raman-based thermometries could also enable spatiotemporal heat transport experiments —importantly, with material selectivity— at the expense of dealing with signals dominated by non-equilibrium phonon dynamics (see Section B.2).

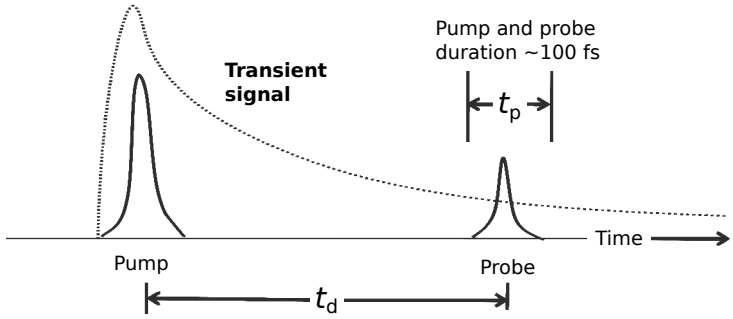

FIGURE 2.7: **Pump-probe sampling of a transient signal.** A pump pulse photoexcites the sample creating a transient response. A time-delayed probe pulse evaluates the transient response to retrieve the signal.

We must note that probing temperature changes with high temporal resolution can result in the observation of coherent phonons with different natures, depending on the experimental conditions and sample geometry (see **Figure 2.8**). For example, the pump can excite optical phonons that are sensed by modulating the probe beam matching the frequency and phase of the optical phonons, with the pump beam overlapped spatially with the probe [Fig. 2.8**a**]. In a different scenario, the pump pulse can generate propagating acoustic phonons that travel through the sample and reach the probed region after a delay, producing discrete changes in the signal [Fig. 2.8**b**]. This occurs when both pump and probe beams have a spatial offset and coherent phonons travel towards the probed region; or when propagative phonons arrive back at the probed region after specular phonon reflections within the sample. Nevertheless, if the thickness of the material is similar or smaller than the phonon wavelength, coherent phonons cannot propagate and are typically observed as resonant phonons. These would thus produce a signal oscillating at the phonon frequency in the time-domain [Fig. 2.8**c**].

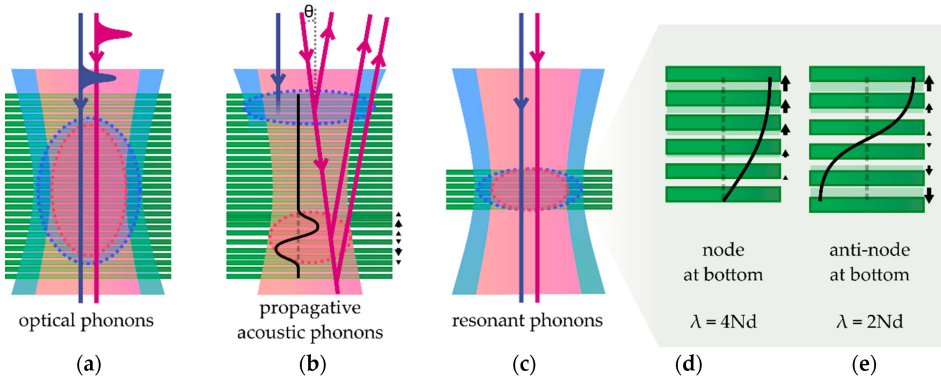

FIGURE 2.8: **Schematic representations of the time-domain probing of coherent phonons.** The coherent phonons can have different nature in a layered material, namely **(a)** optical phonons, **(b)** propagative phonons, and **(c−e)** resonant phonons when the film is reduced to the nanoscale. Pump and probe pulsed beams are presented with blue and pink solid lines, respectively, as well as the respective pumped and probed regions with dashed circles in (a−c). Scattered beams at the top and bottom interfaces, and at the propagative strain wavefront with a resulting different optical paths are shown in (b). The spatial acoustic waveform is presented with a solid black line in (b,d,e) along with black arrows indicating the corresponding out-of-plane displacement. Reprinted from Ref. [95], licensed under CC BY 4.0.

In our TDTR experiments of Chapter 7 we observe oscillations in the spatial domain —this is, while varying the thickness of our material— which we explore

as potential signs of resonant coherent phonon heat within our TMD flakes, as a result of standing wave formation producing a specific spatial waveform (see Fig. 2.8**d,e**). The main drawback of such techniques is that complex processes can dominate the signal at different timescales. These typically require comparing the experimental data to thermal models that simulate heat flow in the specific sample geometry, to reproduce the measured signal which typically involve many input thermophysical parameters. We will see this is the case for the modelling of TDTR signals (see Chapter 5). Nevertheless, we will see that fabricating samples with carefully chosen geometries enables the design of thermal transport experiments that selectively probe anisotropic heat flow along specific crystal orientations. It is therefore important to advance our ability to precisely handle 2D vdW materials. In this thesis, we employ sample design (see Chapter 3) as a key tool to study heat transport in TMDs, both along the in-plane and out-of-plane directions.

Chapter 3

Fabrication and Characterization of Large-Area Suspended $MoSe_2$ Crystals Down to the Monolayer

This chapter is based on Ref. [96]:

S. Varghese,[†] **D. Saleta Reig**,[†] J. D. Mehew, A. Block, A. El Sachat, E. Chávez-Ángel, M. Sledzinska, B. Ballesteros, C. M. Sotomayor Torres, and K.-J. Tielrooij, "Fabrication and characterization of large-area suspended $MoSe_2$ crystals down to the monolayer." *J. Phys. Mater.* **4**(4), 046001 (2021).

[†] *Equally contributing authors*

In this chapter, I describe the procedure we employed to fabricate all TMD-based samples used in this thesis. I describe the home-built transfer stage with which we prepared both, suspended $MoSe_2$ flakes, and MoS_2 flakes supported on standard substrates. We will use the supported MoS_2 flakes to study out-of-plane thermal transport (see Chapters 6 and 7). I then present a thorough characterization of the thickness-controlled suspended $MoSe_2$ flakes and, finally, exploit them for accurate optical absorption measurements. We will use the suspended $MoSe_2$ flakes to study in-plane thermal transport (see Chapter 8).

3.1 Motivation

Flakes of layered materials are highly sensitive to their surrounding environment due to proximity effects and various coupling mechanisms, including long-range Coulomb scattering [97], dielectric interactions [98], phonon scattering [99], and near-field energy transfer [100]. These interactions influence the electrical, optical, thermal, and mechanical properties of 2D flakes, whether they are supported on a substrate, underneath a superstrate, or fully encapsulated between two materials. For a broad range of applications and scientific studies —like the heat transport experiments presented in Chapter 8— it is essential to avoid these effects induced by the material's environment. This can be achieved by using freely suspended crystals, such as flakes placed over holes or trenches, enabling direct access to the intrinsic thermal properties of these materials. Suspended systems are interesting because of their electrical, optical, thermal and mechanical properties, and often exhibit improved figures of merit. Moreover, suspended 2D materials can be used in thermal management and gas sensing applications [101].

Using a simple approach based on mechanical exfoliation and dry-transfer, we fabricate a series of large-area, thickness-controlled, suspended $MoSe_2$ flakes [Section 3.2]. We take $MoSe_2$ as a representative 2D material of the TMD family, as we are interested in studying its in-plane heat transport properties as a function of flake thickness (see Chapter 8). Nevertheless, the fabrication and characterization presented in this chapter for $MoSe_2$ is applicable to any other TMD material, as in the MoS_2 samples supported on standard substrates we prepared to study the out-of-plane heat transport using time-domain thermoreflectance (see Chapter 7). We then provide a thorough characterization using a combination of techniques that report on the suspended samples quality and potential contamination [Section 3.3]. Importantly, our suspended flakes enable transmission and reflection measurements, which we exploit to accurately determine their optical absorption [Section 3.3.3]. We will use these accurate absorption measurements as an important input parameter for the Raman thermometry measurements in Chapter 8.

3.2 Sample Fabrication

The sample fabrication essentially consists of exfoliating thin $MoSe_2$ flakes (in the range of $0.7 - 50$ nm) onto viscoelastic stamps [Section 3.2.1], which are then used to deterministically transfer the desired flake onto standard substrates and holey substrates with a large (15 μm) circular aperture [Section 3.2.2]. **Figure 3.1** shows

a schematic of our fabrication procedure. The exfoliation and transfer is based on the method of Ref. [102], while our home-built transfer is a modified version of the design from Ref. [103].

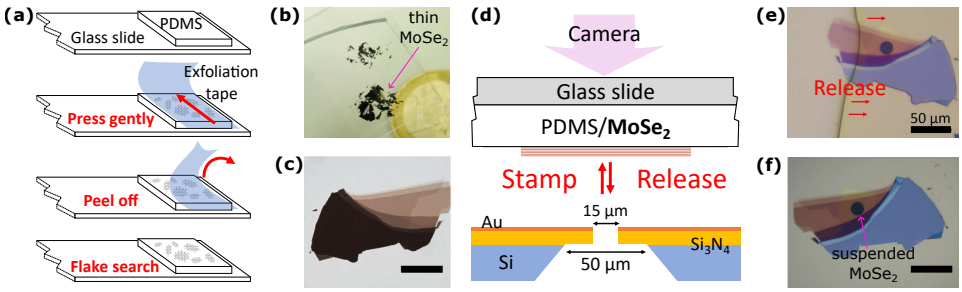

FIGURE 3.1: **Fabrication of few-layer $MoSe_2$ fakes suspended over a circular aperture. (a)** Exfoliation procedure. **(b)** Flakes sitting on PDMS ready for inspection next to a 1€ coin for scale comparison with a mm-sized region of ultrathin $MoSe_2$. **(c)** Optical transmission image of a typical few-layer flake, with darker regions corresponding to thicker material. **(d)** Schematic of the transfer procedure, where the flake is brought in contact with the substrate deterministically with the aid of a camera and micromanipulators. **(e)** A flake being released over a circular aperture. **(f)** Optical image of the transferred flake with a region suspended over the 15 µm hole. The scale bars in panels (c,e,f) are 50 µm.

3.2.1 Exfoliation of few-layer $MoSe_2$

The first step in sample fabrication is preparing viscoelastic stamps that we use to transfer our flakes on the target substrates, followed by a mechanical exfoliation from bulk $MoSe_2$. Prior to transfer we estimate the thickness of our flakes by comparing their optical contrast to a calibration sample with known thickness.

Preparation of the viscoelastic stamp

For the preparation of the viscoelastic polydimethylsiloxane (PDMS) stamps, we mix silicone elastomer curing agent and silicone elastomer base (SYLGARD 184, Sigma Aldrich) in 1:10 wt% proportions. We stir the mixture and place it in a vacuum desiccator to force the release of air bubbles until it appears transparent. We then spread the mixture in a Petri dish in order to achieve a bubble-free, homogeneous ∼1 mm thick PDMS film with a smooth surface. We close the Petri dish while allowing it to degas. It is then left drying for ∼48 h in air. When it is dry, we seal the Petri dish to avoid dust and loss of stickiness. Finally, we cut the PDMS in $\sim 1 \times 2$ cm^2 pieces at the moment of use, selecting PDMS from the center of the

Petri dish, where it has the highest flatness. We control the stickiness of the PDMS by varying the ratio between elastomer and curing agent, with more curing agent producing harder, less sticky PDMS.

Mechanical exfoliation from a bulk $MoSe_2$ crystal

For exfoliation, we sandwich a flat piece of bulk $MoSe_2$ crystal (2H-$MoSe_2$, HQ-graphene) between two strips of Scotch tape (Magic Tape, Scotch). We thin down and spread the crystals over an area of $\sim 1 \times 2$ cm^2 by bringing the two tapes in contact a few times at different, yet close, positions. We use both these strips as parent tapes, from which we produce exfoliation tapes by peeling the thin crystals with a fresh piece of Scotch tape. We immediately bring the exfoliation tapes in contact with a home-made PDMS bed, placed on the edge of a clean glass slide, as schematically shown in Fig. 3.1**a**. Rubbing gently with a cotton swab typically ensures good contact between the crystals and PDMS, yielding larger flakes. Additionally, fast peeling of the exfoliation tapes results in increased presence of thin flakes.[1] Figure 3.1**b** shows a typical PDMS slide with large, thick pieces of $MoSe_2$ supported on the PDMS bed. Thin flakes are typically small ($10 - 50$ μm) and can be located under a microscope. Surprisingly, this particular slide contains a mm-sized region of few-layer $MoSe_2$, visible to the naked eye. Figure 3.1**c** shows a transmission optical image of an exemplary few-layer $MoSe_2$ flake.

Flake search and thickness estimation

Using an optical microscope, we first identify the flakes we intend to dry-transfer onto circular apertures. We specifically search for flakes that are highly crystalline, flat, and feature a uniform thickness area larger than the target aperture. We inspect the flakes under transmission and reflection illumination, looking for flat flakes with sharply defined edges. Transmission images reveal information about their thickness and homogeneity (useful for thin, semitransparent flakes), while reflection images reveal details about the surface quality such as the presence of wrinkles (or the flatness of opaque, thick flakes). Note that a flake may appear flat and homogeneous under transmission illumination, but can turn out to be wrinkled upon inspection in reflection. Before we proceed with transferring the flakes, we first obtain an estimation of flake thickness by comparing the optical contrast

[1] Mechanical exfoliation is not a deterministic process, but with a bit of practice, patience, and luck, it is relatively easy to obtain mono- and few-layer TMD flakes with lateral dimensions up to hundreds of microns.

under transmission illumination with that of a flake with known thickness, as shown in **Figure 3.2**.

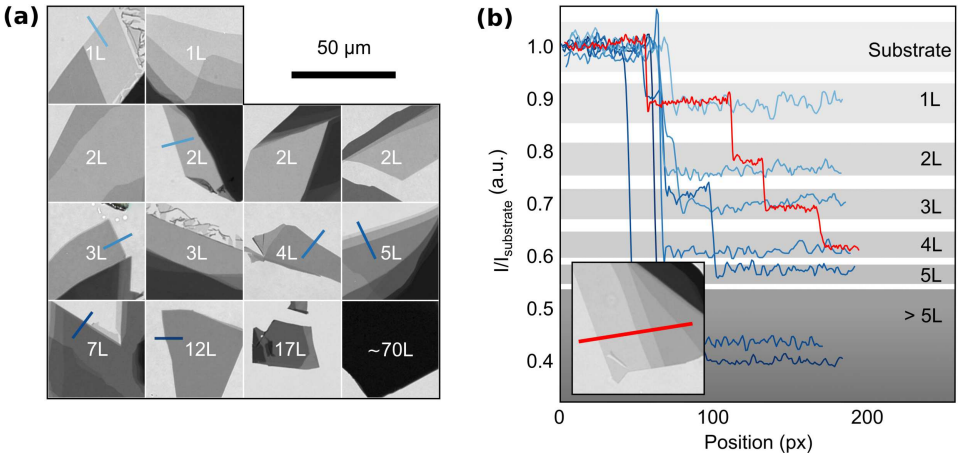

FIGURE 3.2: **Thickness estimation based on optical contrast. (a)** Green-channel transmission optical images of several $MoSe_2$ flakes whose thickness range from 1L to ∼70L. **(b)** The substrate-normalized intensity can be used to estimate the thickness by comparison with the calibration sample shown in the inset. The scale bar of 50 µm is valid for panels (a,b).

This approach was proposed in Ref. [104] and works well for thin TMD flakes because of their large, layer-dependent optical absorption. Using ImageJ software, we split the RGB color channels of our transmission images. We obtain best results when the microscope is set for Köhler illumination, which ensures a uniform lighting across the entire field of view.[2] We find the green channel to have an optimal contrast to determine the thickness of few-layer TMDs, while the red channel can be used to estimate the thickness of thicker flakes. Fig. 3.2**a** shows the green channel for a series of flakes on PDMS. In Fig. 3.2**b**, we compare their intensity contrasts, while normalizing to the substrate values, to that of a flake with known thickness [inset of Fig. 3.2**b**]. For the calibration flake, we use a terrace-like few-layer flake, whose thicknesses have been confirmed using photoluminescence (PL) measurements. The wavelength and linewidth of the PL emission strongly depends on the number of layers (see Section 3.3.1), as TMD flakes become direct bandgap semiconductors at the monolayer thickness [21].

[2]In practice, the light source is focused onto the plane of the condenser diaphragm, which in turn is conjugate to the specimen plane, and the field diaphragm and condenser aperture are adjusted to achieve uniform illumination.

3.2.2 Dry-transfer of TMD flakes

For transferring the previously selected PDMS-supported $MoSe_2$ flakes, we employ a home-built dry-transfer setup [**Figure 3.3**], following the procedure detailed in Fig. 3.1**d**. As target substrates, we use commercial silicon nitride membranes with a circular 15 µm aperture (NTPR005D-C15, Norcada) and, crucially, we metalize their surface with titanium (5 nm) and gold (50 nm) using an electron-beam evaporator (ATC-8E Orion, AJA International Inc.). Gold-coating the substrates prior to transfer significantly enhances the transfer yield thanks to the strong adhesion between gold and chalcogen atoms [105].

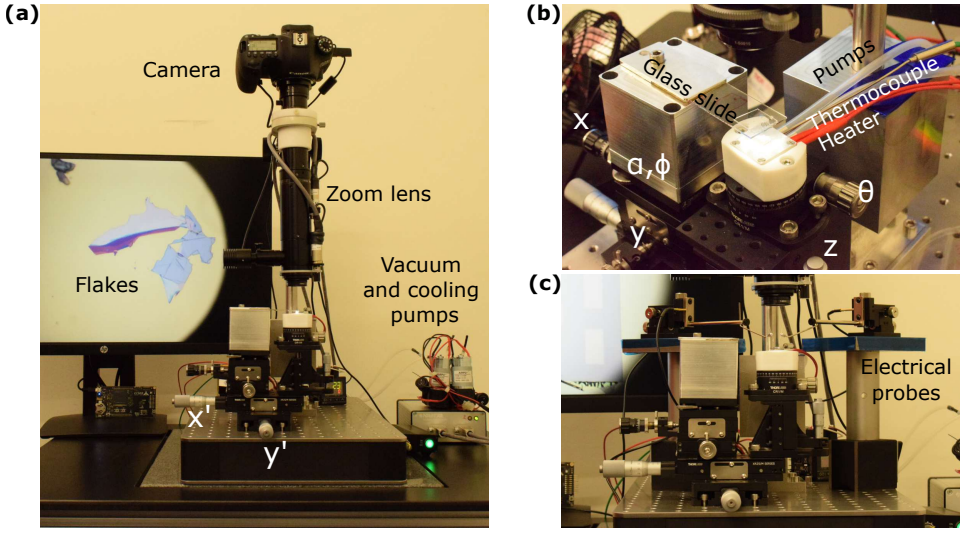

FIGURE 3.3: **Home-built setup for the deterministic transfer of 2D flakes. (a,b,c)** Pictures of our home-built dry-transfer stage. **(b)** Zoom showing the glass slide holder, micromanipulators, and vacuum chuck with temperature control. **(c)** Electrical probes on magnet mounts add probe station capabilities.

A home-built dry-transfer setup

In our dry-transfer setup (see Fig. 3.3**a**), the target substrate mounts on a vacuum chuck, which has the possibility to vary the temperature up to 200ºC using a heating cartridge and a thermocouple for feedback (see Fig. 3.3**b**). Temperature control is particularly useful for hot pick-up transfer strategies typically used to fabricate, for example, hexagonal boron nitride encapsulated graphene [106]. An inverted pump blows air into a microchannel when faster cooling is required. The substrate holder sits on a rotational θ-stage, and a linear z-stage will be used to

bring the substrate in contact with the desired flake from the PDMS slide. The slide is held upside down with the flakes facing the target substrate, while sitting on a micromanipulator stack with 4 degrees of freedom: x, y to adjust the position of the flake with respect to the substrate; and α, ϕ to adjust the angle between the flake and substrate. In addition, two linear stages at the bottom of the entire manipulator stack (x' and y') allows us to inspect the sample away from the region of interest without losing alignment, even when it is already in contact. The alignment of the flakes is performed from the top, through the glass slide and PDMS stamp, with the aid of a camera. A zoom lens with motorized magnification and focus allows for continuously tune the magnification up to $\sim$50X.

Moreover, three micromanipulator-assisted electrical probes can be mounted on magnetic bases to add probe station functionality to our setup, in combination with a source measure unit (see Fig. 3.3**c**). All these features make our dry-transfer setup a powerful system to manipulate, transfer, assemble and electrically test a wide range of 2D materials. Our setup has enabled the successful transfer of various 2D materials on a broad range of substrates using multiple techniques, such as the pick-up [107] and hot pick-up [106] transfer methods, and the micro-dome PDMS approach [108], among others [102]. Although its full potential remains under exploration, our setup has already demonstrated a remarkable ability to produce and electrically test a wide range of samples including the suspended $MoSe_2$ samples presented here and the supported MoS_2 samples used in Chapter 7, the suspended samples studied in Ref. [109] and Ref. [110], but also homo- and heterostructures, encapsulated and twisted devices, hybrid 2D-1D systems, and more. Additional details on the dry-transfer setup components can be found in Table A.1.

Transfer procedure for suspended flakes

In order to transfer a flake onto a gold-coated holey substrate, we use the z-stage to bring the substrate toward the viscoelastic PDMS stamp supporting the flake of interest, as schematically depicted in Fig. 3.1**d**. Prior to stamping, we align the flake over the target aperture on the substrate and adjust the α- and ϕ-stages to define the contact and release directions. We obtain the best results when releasing the flake onto the substrate starting from the thinner and sharper edge of the flake toward thicker or less ideal regions, see Fig. 3.1**e** as an example. The flake is being released if the optical contrast of the flake on both sides of the PDMS-flake contact interface is similar (*i.e.*, the flake remains flat on the substrate). If not, this indicates

that the flake is still on PDMS (*i.e.*, the flake bends and less reflected light reaches the camera).

A PDMS-flake contact interface that is not straight means that the flake has more affinity to either substrate or PDMS. In the exemplary transfer of Fig. 3.1**e**, the flake sticks better to Au and the retracting PDMS-flake contact interface moves faster on the flake than on gold, thus simplifying the transfer. The reason for this is a low adhesion energy for TMDs to PDMS (18 mJ m^{-2} for MoS_2) [111] compared to that for TMDs to gold (1207.26 mJ m^{-2} for MoS_2) [112]. The most critical step comes at the moment of releasing the flake over the suspended region, where the PDMS-flake contact interface moves very slowly, because the flake is more inclined to stay supported on PDMS rather than suspended in air. We control this critical step by using an extremely slow release, and achieving a straight PDMS contact interface. The optical microscope image in Fig. 3.1**f** shows an example of a transferred $MoSe_2$ flake. With this technique, we have achieved the successful fabrication of various monolayers, and few-layer TMD flakes suspended over holes with large areas (177 μm^2), which we will use in Chapter 8 to study the in-plane thermal conductivity of $MoSe_2$.

Wrinkle removal

We observe that fabricating suspended flakes sometimes produces wrinkles due to strain during dry-transfer or changes in ambient conditions (see **Figure 3.4a**). Interestingly, an annealing step at 150ºC for roughly 30 minutes easily removes these wrinkles (see Fig. 3.4**b**). Figure 3.4 shows a $MoSe_2$ flake before and after this "ironing" step, which can conveniently be performed immediately after transfer on the heating stage. Additionally, even initially flat flakes that wrinkle from temperature or humidity changes can later be flattened on a hot plate. This demonstrates the high stability of our suspended $MoSe_2$ flakes, which remain suspended for several years [96].

Transfer procedure for supported flakes

To transfer supported flakes, we follow the same procedure described for suspended flakes. The only difference is that we directly stamp the desired flake on standard substrates such as SiO_2/Si wafers. The main goal of fabricating TMD flakes supported on substrates is to study the out-of-plane thermal conductivity of TMDs using time-domain thermoreflectance. For this, we prepare a series of terrace-like MoS_2 flakes on SiO_2/Si substrates with thickness ranging from 1L to

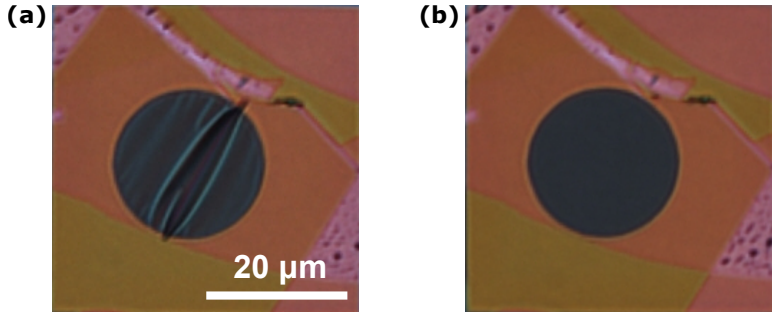

FIGURE 3.4: **Wrinkle removal by thermal annealing. (a)** Optical image of the flake showing a wrinkled suspended area which we **(b)** flattened by annealing the sample at 150°C for 30 min.

12L (see Chapter 7). The MoS_2 supported flakes are then coated with 50 nm gold and 2 nm Ti adhesion layer using an electron-beam evaporator. The thin gold layer covering our flakes will serve as a transducer to translate a transient reflectivity into a transient temperature in the TDTR experiments reported in Chapter 7.

3.3 Characterization of Large-Area Suspended Flakes

In this section, we detail the characterization of our suspended $MoSe_2$ flakes, for which we use a combination of techniques that report on the flake thickness and its residual strain [Section 3.3.1], the sample roughness and crystallinity [Section 3.3.2]. Most characterization techniques reported here for $MoSe_2$ are also applicable to other suspended TMDs. Finally, we leverage our large-area suspended $MoSe_2$ membranes for accurate optical absorption measurements [Section 3.3.3].

3.3.1 Thickness confirmation, strain and surface roughness

We first confirm the flake thickness previously estimated from optical contrast analysis. For this, we perform PL measurements (for $1-3$L flakes), Raman spectroscopy (for $1-5$L flakes), and atomic force microscopy (for $>$10L flakes) measurements on suspended and supported regions of the transferred flakes.

Photoluminescence

Figure 3.5 shows images of the $MoSe_2$ flakes transferred over 15 µm diameter circular apertures [Fig. 3.5**a**] and the corresponding PL measurements for exemplary mono-, bi- and trilayer $MoSe_2$, which we use to confirm the thickness of the

thinnest flakes [Fig. 3.5**b**]. We use a CW laser with a wavelength of 532 nm to excite the center of the suspended flake. The PL emission is collected, dispersed with a grating-spectrometer, and detected by a nitrogen-cooled charged-coupled device (CCD). Figure 3.5**b** shows the PL intensity of the suspended flakes marked in Fig. 3.5**a**, normalized to the monolayer intensity. Our PL studies on monolayer $MoSe_2$ show a relatively intense emission peak centered at 790 nm (1.57 eV), in agreement with the literature values of the exciton peak in monolayer $MoSe_2$ [55, 113]. The PL spectrum of a bilayer $MoSe_2$ flake shows reduced intensity and the emission peak is red-shifted toward 805 nm (1.55 eV) compared to the monolayer. For a trilayer flake, the PL emission peak further red-shifts, broadens and its intensity drops significantly, also in agreement with observations reported in the literature [53, 114].

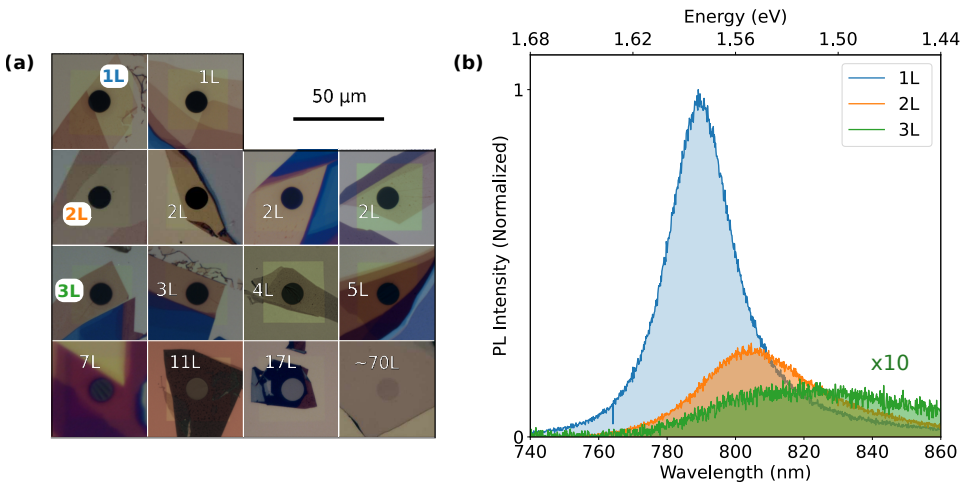

FIGURE 3.5: **Suspended $MoSe_2$ samples and thickness confirmation via PL measurements. (a)** Optical images of the thickness-controlled $MoSe_2$ flakes transferred over circular apertures. **(b)** Photoluminescence spectra of the mono-, bi-, and trilayer $MoSe_2$ flakes marked in panel (a).

Raman spectroscopy

We characterize the suspended $MoSe_2$ flakes by Raman spectroscopy with a spectral resolution of 0.25 cm^{-1}, in order to extract information about strain in the suspended flake. The relative shifts in peak position of different Raman modes (*i.e.*, the A_{1g} mode in $MoSe_2$) also provide information about the thickness of TMDs [115] (see **Figure 3.6**). We use the same setup that we used for the PL measurements (described elsewhere [116]), and study the occurrence of strain-induced changes in the Raman spectra of our suspended and supported $MoSe_2$

flakes. Figure 3.6**a** shows the A_{1g} mode in the Raman spectra of suspended $MoSe_2$ flakes with thicknesses in the range $1-4$ layers, and bulk. The spectra for supported and suspended $MoSe_2$ are very similar (see Ref. [96]). For bulk $MoSe_2$, the A_{1g} peak position is located at 242 cm^{-1}, in agreement with previously reported values of 243 cm^{-1} [54] and 242 cm^{-1} [30]. The A_{1g} mode shifts to lower frequency upon reducing the flake thickness, and reaches a value of 239.7 cm^{-1} for monolayer $MoSe_2$, also consistent with the reported values of 240.5 cm^{-1} [55]. The Raman measurements again confirm the flake thicknesses we extracted from optical contrast analysis and PL measurements.

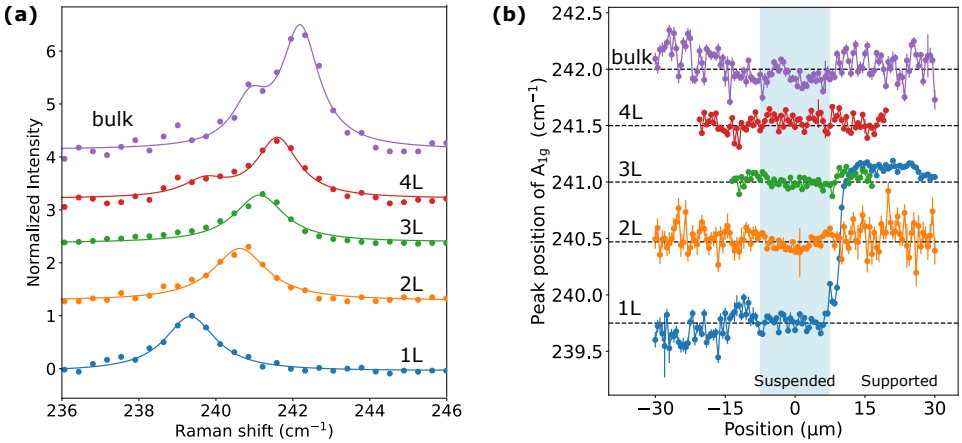

FIGURE 3.6: **Raman spectroscopy of suspended $MoSe_2$ flakes. (a)** Experimental Raman spectra (*scatters*) and corresponding Lorentzian fits (*solid lines*) of suspended $1-4$L flakes and bulk ($\sim$50 nm) $MoSe_2$, zoomed in to visualize the A_{1g} mode. **(b)** Fitted peak position of the A_{1g} across the suspended $MoSe_2$ flakes using 3 μW incident laser power. The *blue-shaded* area indicates the suspended region. The peak position of the monolayer data suddenly "jumps", as the flake thickness changes from 1L to 3L in the scanning direction.

To investigate potential strain, we acquire Raman spectra at different sample positions across the supported and suspended regions of our flakes, and extract the peak position of the A_{1g} mode of $MoSe_2$ as a function of sample position (see Fig. 3.6**b**). We used very low incident power (3 μW at the sample plane) to avoid temperature-induced Raman shifts. The frequency of the A_{1g} mode barely varies in the suspended region of the sample, while it fluctuates in the supported part of the sample. These fluctuations arise due to the small SNR given the low laser powers used and are within, or very close to, the resolution limit of the spectrometer. Thus we conclude that our Raman measurements are more sensitive to the number of layers than any potential strain related effects, as the variability in peak

positions between supported and suspended regions (*blue-shaded* area in Fig. 3.6) are within the resolution limit of the spectrometer. This is also supported by the relatively small values of residual stress we found for these membranes using Brillouin light scattering measurements in Ref. [109].

Atomic force microscopy

We employ atomic force microscopy (AFM) imaging in tapping mode to confirm the thickness of those flakes for which the optical contrast analysis, PL, and Raman spectroscopy fail to provide an unambiguous thickness determination. We show the AFM topography maps of the three thickest flakes we transferred onto gold-coated substrates in **Figure 3.7(a,b,c)**. Using Gwyddion software, we extract height profiles across an edge of the flake (in particular, at the thickness region that is also suspended over the circular aperture), as shown in Fig. 3.7**d.e.f**. The measured thickness values for these thick flakes are 7.7 ± 0.7, 11.9 ± 1.4 and 46.9 ± 2.1 nm, corresponding to 11 ± 1, 17 ± 2 and 67 ± 3 layers, respectively.

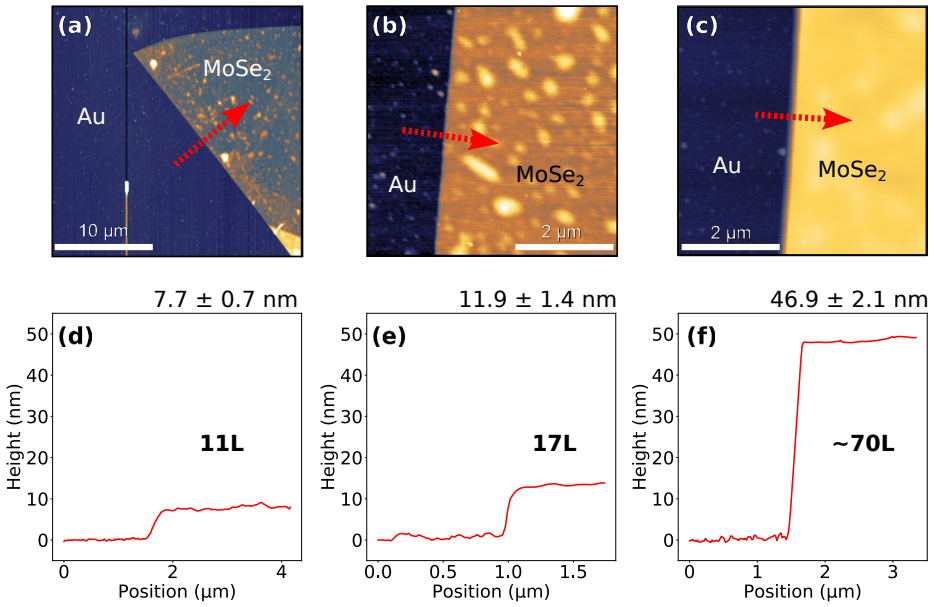

FIGURE 3.7: **AFM thickness measurements of transferred $MoSe_2$ flakes. (a,b,c)** AFM topography images of the three thickest flakes from Fig. 3.5**a**; with **(d,e,f)** the height profiles along the red dashed arrow of each panel.

In order to quantify the roughness and surface quality of our samples we perform AFM imaging at the edge of a suspended region (see **Figure 3.8**). Figure 3.8**a**

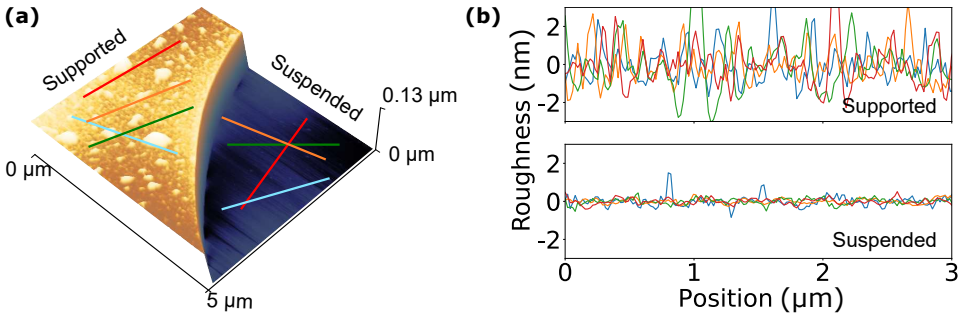

FIGURE 3.8: **AFM roughness measurements of transferred $MoSe_2$ flakes. (a)** 3D AFM topography image of the edge of a suspended 2L flake, with the **(b)** roughness profiles along the colour lines for both supported (*top panel*) and suspended (*bottom panel*) regions.

shows the 3D topography AFM image of a suspended bilayer $MoSe_2$ flake at the hole edge. Interestingly, we observe an abrupt "sagging" of the membrane at the edge of the suspended region of the sample. Similar effects were reported previously [117], and come from the exceptional ability of atomically thin materials to conform to the nano/microstructures of the substrate underneath [118]. Therefore, it is not surprising that the flakes show increased roughness on the supported region, as it is susceptible to the substrate's roughness. The RMS roughness (Rq) of the flake in the supported region (see top panel in Fig. 3.8**b**) is 2.8 ± 1.0 nm, which corresponds to the roughness of the gold-coated substrate. However, in the suspended region (see bottom panel in Fig. 3.8**b**), the surface quality is significantly higher: we find an Rq of 0.75 ± 0.25 nm over a 2×2 µm^2 area. This is similar to the thickness of a molecular monolayer ($\sim$0.7 nm), which suggests that the flake is atomically flat. The sub-nanometer roughness over several micrometers further demonstrates the absence of small wrinkles on the suspended region and absence of residue.

3.3.2 Crystallinity

After confirming that our thickness-controlled suspended flakes have excellent surface quality, we next use transmission electron microscopy (TEM) to assess their crystallinity, and energy-dispersive X-ray spectroscopy (EDX) to analyze the chemical composition and potential polymer contamination from the transfer process. For details on the EDX characterization, see Ref. [96].

Transmission electron microscopy

We characterize our $MoSe_2$ samples using a high-resolution transmission electron microscope (ARM-200f, JEOL). The high-resolution TEM images were collected at 80 kV [109]. Such images (see an example in **Figure 3.9a**) provide important information about the structure and quality of our suspended $MoSe_2$ flakes. In all our TEM images, the flake appears to be defect- and/or dislocation-free over tens of nanometers (see Ref. [109]). The high-magnification TEM image in Fig. 3.9**a** depicts a honeycomb arrangement of atoms, with the $MoSe_2$ molecular structure superimposed on the lattice, indicating a single-crystalline structure with an interplanar distance of ∼0.28 nm, which perfectly agrees with the literature [119]. The fast Fourier transform (FFT) pattern in Fig. 3.9**b** displays symmetric hexagonal patterns, indicating the hexagonal lattice structure of the $MoSe_2$ single-crystals. Thus, we conclude that our flakes are highly crystalline.

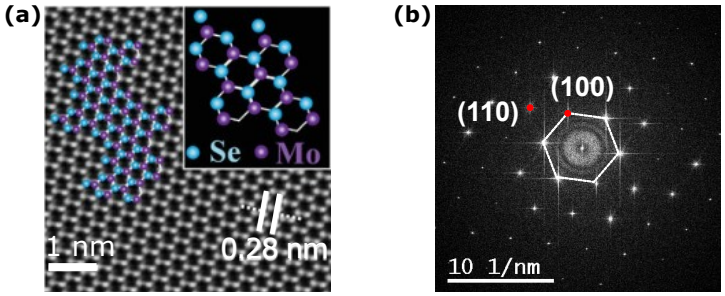

FIGURE 3.9: **Transmission electron microscopy of suspended $MoSe_2$ flakes. (a)** High-resolution TEM image of a representative suspended $MoSe_2$ flake with its molecular structure overlaid. **(b)** FFT of the TEM image displaying symmetric hexagonal patterns, indicating single-crystalline $MoSe_2$.

3.3.3 Optical absorption measurements

We now present optical absorption measurements for the suspended $MoSe_2$ flakes fabricated and characterized in this chapter. Our exfoliated, few-layer, large-area, suspended, single-crystalline, unstrained, clean flakes benefit from the fact that the holey substrates are open windows, suitable for transmission measurements where light only interacts with the flake. We first perform a systematic study of the laser absorption at 532 nm as a function of flake thickness in ambient conditions. Then, we perform optical absorption measurements using a commercial FTIR/Vis-NIR microspectrometer with a broadband light source. Finally, we compare the PL spectra from supported and suspended regions of our flakes.

Laser absorption at 532 nm

Using a home-built optical setup based on a CW laser diode centered at 532 nm, we isolate the absorption of the flake by measuring the transmitted P_T and reflected P_R laser powers, with respect to the incident power P_{inc}. For this, we use a calibrated power head (S130C, Thorlabs) and both, a pristine holey substrate and a perfect mirror as reference. **Figure 3.10** shows the laser transmission and reflection measurements performed for a series of suspended $MoSe_2$ flakes. We obtain the optical absorption A of the suspended flakes as a function of number of layers from the following relation:

$$\begin{aligned} A &= 1 - T - R \\ &= 1 - \frac{P_T}{P_{T,100}} - \left(\frac{P_R - P_{R,0}}{P_{R,100}} \right) \end{aligned} \tag{3.1}$$

where P_T and P_R represent the transmitted and reflected power slopes with incident laser power, obtained from the linear fits in Fig. 3.10**a**; with $P_{T,100}$ and $P_{R,0}$ the transmitted and reflected power slopes through a bare holey substrate [*black lines* and *scatters* in Fig. 3.10**a**]; and $P_{R,100}$ the reflected power slope from a perfect mirror; used as reference to account for collection losses.

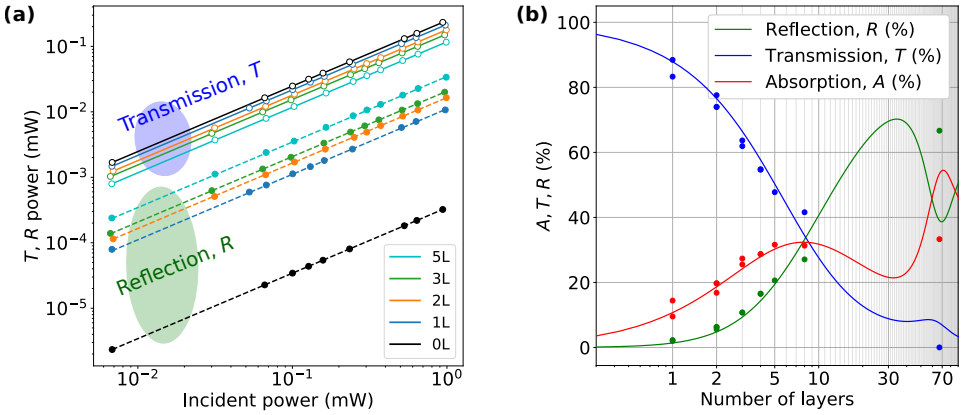

FIGURE 3.10: **Laser absorption measurements of suspended $MoSe_2$ flakes at 532 nm. (a)** Transmitted (*solid lines* and *empty scatters*) and reflected (*dashed lines* and *solid scatters*) laser power as a function of incident laser power. The black data set labelled as "0L" corresponds to T and R power measurements performed through the aperture of a bare holey substrate, used as a reference. **(b)** Measured reflection R and transmission T values, with the resulting absorption $A = 1 - T - R$ for suspended $MoSe_2$ flakes as a function of thickness. The solid lines are fits of the refractive index n and extinction coefficient k using the transfer matrix method.

Figure 3.10**a** shows a log-log plot of the reflected and transmitted powers as a function of incident laser power. The vertical offset thus represents the slope from a linear fit, with an expectedly decreasing (increasing) transmittance (reflectance) with flake thickness as they become optically opaque. Figure 3.10**b** shows the resulting absorption A, transmission T and reflection R values obtained for the $MoSe_2$ flakes as a function of number of layers. We observe that the absorption increases with thickness and saturates quickly after 5 layers (5L). The material becomes quite strongly reflective as thickness increases toward the bulk. We measured multiple samples in the $1-3$ layer regime, and obtained very reproducible R values of $2 \pm 0.2\%$ and $6 \pm 0.2\%$ for 1L and 2L $MoSe_2$, respectively, showing minimal sample-to-sample variations. The reflectivity of TMDs has also been shown to effectively reveal the thickness of each flake [120], which we find to increase from 2% to 20% from 1 to 5 layers. For the monolayer and bulk $MoSe_2$, we obtained an absorption of $10 \pm 3\%$ and $33 \pm 3\%$, respectively. From a transfer matrix method (TMM) analysis (see Section A.2), we obtain a refractive index of $n = 5.42$ and extinction coefficient $k = 1.36$ for $MoSe_2$ by fitting to the experimental data. These values are close to the literature values of $n = 5.24$ and $k = 1.16$ for bulk $MoSe_2$ [121]. We note that for thicker flakes, internal reflections inside the material occur, giving rise to non-monotonous behavior of the optical properties as a function of thickness, and that n and k could also be thickness-dependent.

Available absorption values for mono- and few-layer TMDs in the literature are scarce and scattered. For monolayer $MoSe_2$ supported on SiO_2/Si, an absorption of $23 \pm 8\%$ has been estimated for a wavelength of 514 nm [55]. Others have determined values of 5.6% and 9.7% at 633 nm for suspended mono- and bilayer $MoSe_2$ [70], respectively. We note that most of the values found in the literature are obtained either on supported flakes or flakes suspended over small holes with sizes comparable to the laser spot, or shallow, well-like holes. In these cases, the absorption is calculated using an analysis that relies on knowledge of the complex permittivities of materials in the sample, which introduces potential uncertainties in the obtained absorption values. In contrast, our large-area suspended flakes allow for direct optical absorption measurements that do not require knowledge of any dielectric properties of the substrate.

FTIR/Vis-NIR spectroscopy of suspended flakes

The second optical absorption experiment we perform is in the range from 500 to 1000 nm using a commercial FTIR/Vis-NIR microspectrometer (Hyperion 2000,

Bruker), which we summarize in **Figure 3.11**. Here, we show the absorption spectra in the visible to near-infrared range for $1-5$ layers suspended $MoSe_2$ flakes.

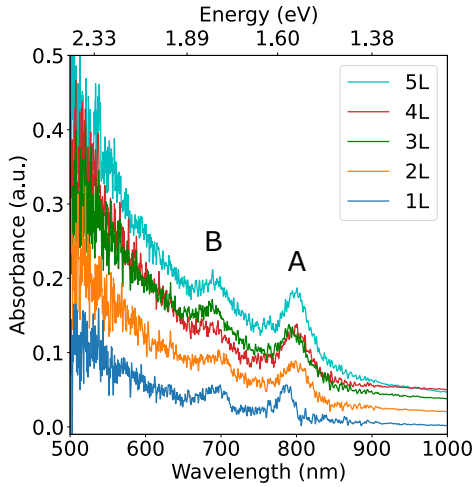

FIGURE 3.11: **FTIR/Vis-NIR spectroscopy of suspended $MoSe_2$.** Spectra in the visible to NIR range acquired for $1-5$ layers $MoSe_2$ flakes.

Absorption and excitonic features for bulk TMD crystals are well known since they have been studied since several decades [122, 123]. We find exciton peaks around 805 nm (A-peak) and 690 nm (B-peak), in agreement with previous studies on $MoSe_2$ [55, 124]. We also observe that the A-exciton peak exhibits a sudden blue-shift at the monolayer thickness, similar to early findings in TMDs [125, 126]. The energy difference between the A and B peaks, which is an indication of the strength of spin-orbit interaction, is $\sim$220 meV for $MoSe_2$, in agreement with the literature [53, 126]. This shows that we can use our large-area, clean, suspended flakes for both quantitative absorption measurements at a single wavelength, and spectrally resolved absorption measurements.

3.3.4 Suspended and supported photoluminescence

As a final demonstration of the usefulness of suspended crystals, we compare PL measurements on supported and suspended regions of mono-, bi-, and trilayer $MoSe_2$ flakes, which we show in **Figure 3.12**.

We clearly observe that suspended TMDs lead to brighter PL emission, in agreement with the results of Ref. [70]. The PL signal of the trilayer $MoSe_2$ flake is only detectable in the suspended regions in these experimental conditions (*i.e.*, using

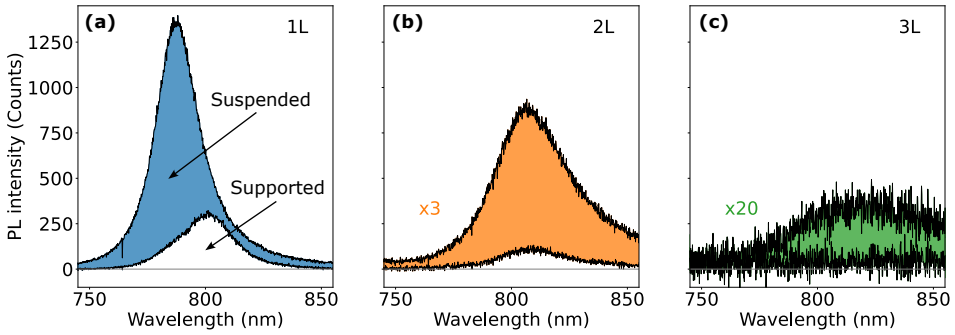

FIGURE 3.12: **Suspended and supported photoluminescence of $MoSe_2$.** PL emission from **(a)** 1L, **(b)** 2L, and **(c)** 3L $MoSe_2$ flakes as measured on supported and suspended regions around one year after their fabrication. The shaded areas represent the PL enhancement on the suspended regions. Data sets presented in panels (b) and (c) are scaled by a factor 3 and 20, respectively.

very low laser power to avoid laser-induced heating effects). Moreover, we performed these PL measurements on samples that were more than one year old, which also confirms that their optical properties do not significantly degrade over time. These results demonstrate an exceptional quality and stability of the suspended flakes prepared in this thesis.

3.4 Summary and Outlook

In summary, we have developed a fabrication procedure to obtain large-area, suspended TMD flakes, based on standard PDMS-assisted dry-transfer, combined with gold-coated, commercial substrates with 15 μm-diameter holes. We have prepared a set of suspended $MoSe_2$ samples ranging from monolayer to ∼70 layers. Careful characterization of the suspended flakes using PL, AFM, TEM, EDX, and Raman scattering measurements shows that they are single-crystalline, clean, and minimally strained. We also found that the wrinkles on the suspended region can be removed through thermal annealing, and that samples do not degrade during a time period of >20 months. Finally, we showed two optical absorption experiments performed on the suspended $MoSe_2$ flakes, which are exempt from any artefacts or errors induced by their environment. Beyond optical measurements, we envision broad use of our suspended TMD structures for electrical, thermal and mechanical studies and potential applications requiring an isolated response from environment-free thin flakes, in addition to applications and studies requiring photon emission with minimal losses.

The suspended $MoSe_2$ flakes fabricated and characterized in this chapter (together with additional flakes suspended over smaller hole sizes and flakes transferred over pristine substrates without the gold-coating) will be used to study the in-plane thermal conductivity of $MoSe_2$ as a function of number of layers using Raman thermometry in Chapter 8 [Ref. [127]]. We prepared additional suspended $MoSe_2$ flakes for mechanical studies using Brillouin light scattering [Ref. [109]] and exciton diffusion studies using spatiotemporal microscopy [Ref. [110]]. We also fabricated mono- and few-layer flakes of various TMDs to study the layer-dependent in-plane thermal diffusivity using our home-built spatiotemporal microscopy setup (which we described in Ref. [92]), revealing non-diffusive heat transport at room temperature [Ref. [94]]. More details on the room temperature observation of non-diffusive heat transport in suspended TMDs can be found in Ref. [93].

The supported MoS_2 flakes transferred on standard SiO_2/Si substrates will be employed to study its thermal transport properties in the out-of-plane direction using time-domain thermoreflectance in Chapter 7. These supported flakes are coated with a thin gold film (50 nm), using 2 nm Ti adhesion layers, to act as a transducer in TDTR experiments.

Contributions

I designed and built the transfer setup, and fabricated the suspended $MoSe_2$ samples with together with Sebin Varghese. I fabricated the supported MoS_2 samples with assistance from Dr. Bohai Liu. I performed most sample characterization measurements with help from Sebin Varghese, including Raman and PL measurements using the Raman setup of Prof. Clivia Sotomayor Torres. I built the laser absorption setup and performed the optical absorption measurements in the laboratory of Prof. Klaas-Jan Tielrooij.

Chapter 4

Multifunctional Optothermal Pump-Probe Setup

In this chapter, I explain the design and construction of a multi-purpose pump-probe optical setup to explore thermal transport phenomena in two-dimensional materials and nanoscale systems. I review the main aspects of the time-domain thermoreflectance setup design, construction, and alignment; including the possibility to perform other types of measurements by changing the probe wavelength, its bandwidth, the pump-probe modulation scheme and/or the detection strategy. The TDTR setup described in this chapter will be employed for the experimental work reported in Chapters 6 and 7.

4.1 Motivation

The rapid progress in 2D material research has unlocked promising opportunities for next-generation electronic and photonic devices [8, 9]. However, while their electronic and optical properties have been widely studied, understanding the thermal behavior of atomically thin materials remains a significant challenge. Effective heat management is essential to maintain device performance, reliability and longevity —especially in high-power and/or high-frequency applications where overheating can lead to device failure. This calls for the development of a versatile ultrafast optical setup capable of probing thermal properties of 2D materials with high spatial and temporal resolution to uncover the underlying heat transfer mechanisms, potentially guiding innovations in device design.

The optical setup presented in this chapter has been designed to perform three complementary types of measurements: time-domain thermoreflectance (TDTR), time-resolved Raman scattering (trRS), and time-resolved photocurrent (trPC). Each technique provides distinct perspectives into the thermal dynamics of 2D materials. TDTR precisely measures thermal conductivity and interfacial thermal conductance; trRS captures phonon dynamics and thermalization processes; and trPC provides insight into the photoexcited (hot) carrier dynamics. Together, these techniques enable a unified framework to study heat flow and energy dissipation at the nanoscale, aimed at facilitating the design of materials and devices that could assist in addressing the thermal management challenges faced by emerging technologies [9].

In this chapter we will only review the TDTR setup, as it is the only setup configuration used for the experiments reported in this thesis (see Chapters 6 and 7). However, most of its features are shared between all three setup configurations, and we describe the unique features of the trRS and trPC setup configurations in Section B.2.

4.2 Setup Design and Construction

Our versatile ultrafast optical setup has been specifically designed to explore the thermal behaviour of nanoscale materials with high spatial and temporal resolution. The aim of time-domain thermoreflectance implementation is to provide information on how heat is transported across 2D material systems, in particular in the out-of-plane direction. As we have seen in Section 2.4.2, time-domain thermoreflectance uses short pump pulses to periodically heat a metal transducer,

deposited on the material of interest, in a modulated fashion. The transducer's reflectivity linearly changes with the temperature fluctuations introduced by the modulated train of pump pulses. A second train of time-delayed probe pulses evaluates these heat-induced reflectivity fluctuations at the modulation frequency of the pump beam using a photodiode and a lock-in amplifier.

Figure 4.1 shows a detailed schematic of our TDTR setup, which we implemented on a $3 \times 1.5\ \mathrm{m}^2$ optical table that sits on pneumatic vibration isolators. A cryostat chamber integrated within the optical table is equipped with low-temperature (LT) piezo-scanners, sensors and electrical connections; and has optical access from the front and from the back of the sample (see Section 4.2.1). This allows us to perform optical and (opto)electronic measurements both in reflection and transmission configurations, from room temperature down to 4 K. The high spatial resolution of our setup is given by the LT piezo-scanners that allow us to move the sample with sub-micrometer precision.

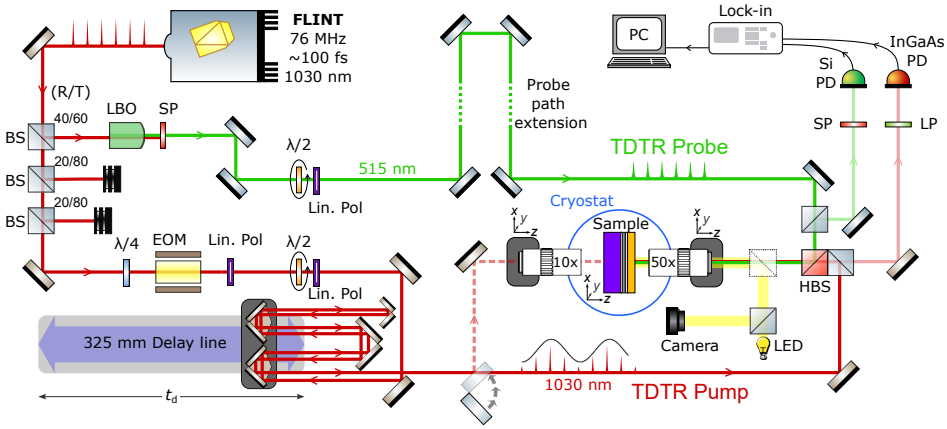

FIGURE 4.1: **Detailed schematic of the time-domain thermoreflectance setup.** BS: beamsplitter, LBO: lithium triborate crystal, SP: short-pass filter, LP: long-pass filter, $\lambda/2$: half-waveplate, $\lambda/4$: quarter-waveplate, Lin. Pol: linear polarizer, EOM: electro-optic modulator, PD: photodiode, LED: white light-emitting diode, HBS: harmonic beamsplitter. The dotted beamsplitter represents a drop-in cube. Focusing elements other than objective lenses are not shown for clarity reasons.

The high temporal resolution of our setup is enabled by the short duration of our laser pulses. Our fundamental laser (FLINT, Light Conversion) emits ~100 fs laser pulses centered at 1030 nm, at a repetition rate f_{rep} of 76 MHz. The total output power is ~14 W, but only 20% of the output power is used to generate four parallel pump and probe beams (*i.e.*, three probes for the three setup configurations

and a shared pump), using beamsplitters for the first three beams (the probes) and a dielectric mirror for the last beam (the shared pump). The rest of the fundamental laser power (80%, not depicted in Fig. 4.1) feeds a series of non-linear stages, the output of which serves as the probe beam in a separate spatiotemporal thermometry setup (described in detail in Ref. [92]) on the same optical table.

The TDTR pump [*red line* in Fig. 4.1] is modulated at $0.1 - 20$ MHz frequencies using an electro-optic modulator [more details in Section 4.3.1]. It then passes over a variable delay line that elongates the pump's optical path, introducing a controlled time delay between pump and probe pulses [more details in Section 4.3.1]. A non-polarizing beamsplitter (BS) directs the pump light towards the objective lens, as it passes through a harmonic beamsplitter (HBS),[1] and focuses on the sample. The non-polarizing BS also allows for collecting the reflected pump light on a biased InGaAs photodiode connected to the lock-in amplifier to, for example, diagnose the modulation (see Section 4.3.1), or measure its spot size (see Section 4.3.2). Additionally, our setup has the possibility to direct the pump beam at the back of the sample thanks to a flip-mirror that brings the pump beam to a second (back-)objective lens (10X), collinear with the front-objective (50X) (see Section B.2). This back-pump, front-probe configuration will be used in TDTR and trRS setup configurations to study samples on transparent substrates (see Chapter 7).

The TDTR probe [*green line* in Fig. 4.1] is the second-harmonic (515 nm) of our fundamental laser, which we obtain by focusing light through a non-linear lithium triborate crystal (LBO-603H, Eksma Optics) on a rotator mount for phase-matching. A short-pass filter blocks the unconverted light at the fundamental wavelength. The probe path is extended with silver mirrors to compensate for the longer optical path of the pump beam. The probe beam eventually recombines with the pump at the HBS, where it is reflected before being focused on the sample by the same objective lens. The probe light reflected from the sample is collected by the objective lense and then guided to a fast-response, cathode-grounded Si photodiode (SM05PD2A, Thorlabs) connected to our lock-in amplifier (HF2LI, Zurich Instruments), which we use to demodulates the signal at the modulation frequency of the pump beam (see Section 4.2.1).

[1] The harmonic beamsplitter provides >99% reflection for 515 nm and >95% transmission for 1030 nm allowing us to recombine the pump and probe beams.

4.2.1 General setup features

In this section we describe the general features of our setup. Mainly, the sample space, which is essentially our cryostat chamber; the white light imaging system; and the lock-in detection scheme. **Figure 4.2** shows a bird's eye view of the excitation and detection path of our setup, designed in a cage system. The pump and probe beams (*green* and *red lines*, respectively) couple in free-space into the cage system, where they recombine and get focused onto the sample by the main (front-)objective lens. The reflected pump and probe beams are collected with separate photodiodes for lock-in detection. The possibility of directing the pump beam to the back of the sample brings new measurement configurations to the setup (see Section B.2).

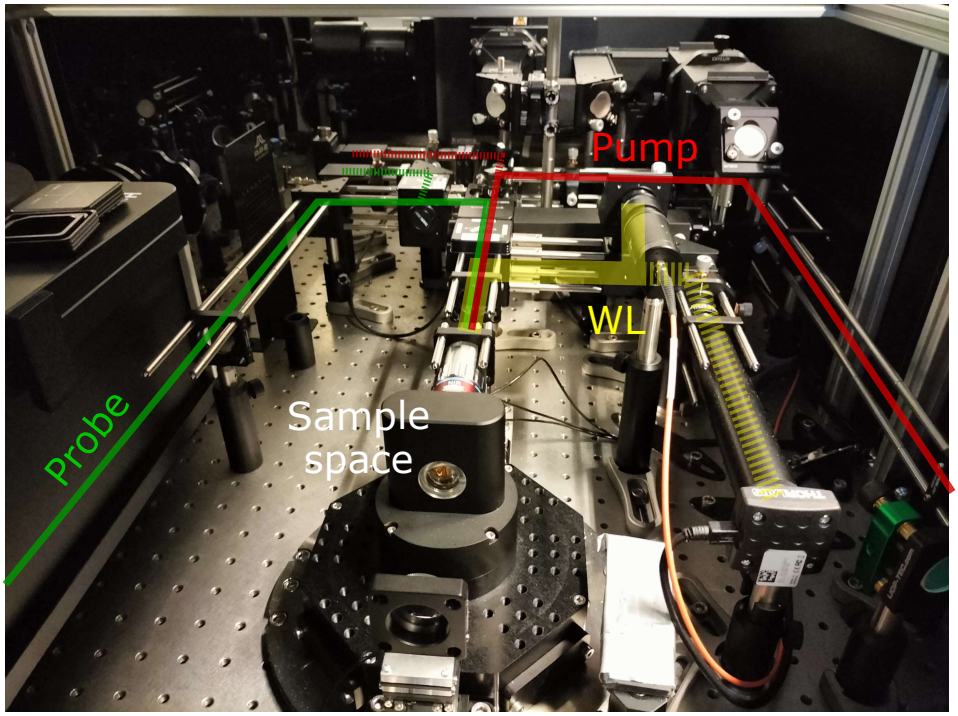

FIGURE 4.2: **Bird's eye view of our optothermal setup.** A cage system allows us to couple the pump (*red line*) and probe (*green line*) beams into the front objective, which focuses them on the sample. The sample is imaged using white light (WL, *yellow line*) and a camera. The reflected lasers (*dashed lines*) are then collected using photodiodes, connected to our lock-in amplifier. The back-objective is unmounted and not shown here.

Sample space

Figure 4.3 shows a picture of the sample space, which has two viewports to access the sample from the front and from the back. In most cases, we use a long working distance (front-)objective lens (50X Plan Apo NIR Infinity Corrected, Mitutoyo) —that sits on room-temperature (RT), closed-loop, *xyz*-nanopositioners (ECS3030/Al/RT, Attocube)— to focus both the laser beams and the white light used for imaging onto the sample [Fig. 4.3**a**]. The sample space is essentially a closed-loop helium cryostat chamber integrated within our optical table (attoDRY800, Attocube), allowing us to measure under high vacuum (10^{-5} mbar) and control the temperature ($4 - 350$ K) of the sample, with uncoupled vibrations from the cryostat compressor (HC-4E, Sumitomo) and vacuum pumps. We open the cryostat chamber to mount our samples on a piezo stack that consists of 3 LT *xyz*-nanopositioners (2× ANPx311/LT and ANPz102/LT, Attocube), 2 LT *xy*-piezo-scanners (2× ANSxyz100/LT, Attocube), 2 thermometers, a heater and a pressure sensor [Fig. 4.3**b**]. The cryostat chamber also includes 20 electrical connectors enabling (opto)electronic measurements, where each connector can be grounded, floated or connected to the sample using a custom-built break-out box.

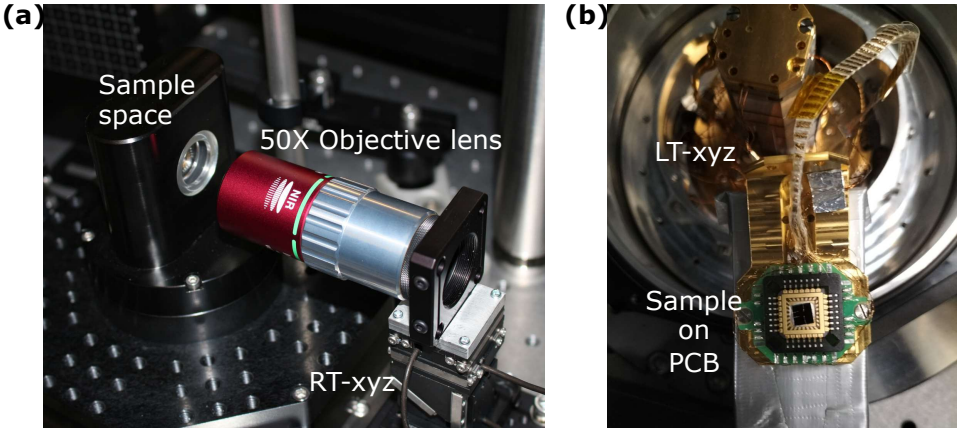

FIGURE 4.3: **Pictures of the sample space.** **(a)** The enclosed cryostat chamber with the front-objective mounted on RT *xyz*-nanopositioners. **(b)** The cryostat chamber is opened to mount the sample (in this case, on a printed-circuit board (PCB) which connects to the electrical pins at the bottom of the chamber). The sample holder then sits vertically on the stack of LT *xyz*-nanopositioners.

Imaging system

To visualize the sample through the front viewport, we use a monochrome CMOS camera (DCC1545M, Thorlabs) which we infinity-correct using a 200 mm plano-convex lens.[2] As white light source, we use a mounted LED (MCWHLP2, Thorlabs) with a diffuser and a lens that focuses the light at the back aperture of the (front-)objective. This is to obtain a large illumination area covering the entire field of view. An "imaging" drop-in BS cube directs the white light onto the sample and back to the camera, and is equipped with a neutral density (ND) 3 filter to attenuate the incoming laser beams and avoid saturating the camera. The infinity-correction of the camera ensures that the attenuated laser beams are imaged at the best optical focus. We remove the "imaging" drop-in BS cube when performing measurements to collect the most reflected probe light (or scattered light, in the case of the trRS setup).

Lock-in detection

In the TDTR setup, the reflected probe light is guided by a non-polarizing beamsplitter after reflecting off the harmonic beamsplitter (HBSY12, Thorlabs), and passes through a short-pass filter (FESH0750, Thorlabs) before reaching the detector. The filtered probe light is then focused onto the active area of a fast-response, cathode-grounded Si photodiode connected to the lock-in amplifier. The combination of the HBS and the short-pass filter ensures sufficient filtering of the modulated pump light on the Si photodiode, which could strongly affect the measured transient signal in TDTR.

The lock-in amplifier is controlled by the LabOne software and/or using Python. Typical time constants (TC) used in our TDTR experiments are always in the $10-200$ ms range, and the polling time (*i.e.*, the amount of time the signal is acquired) is set to $5\times$TC. We included the possibility to collect the pump light with a biased InGaAs photodiode (DET10N2, Thorlabs) to diagnose its modulation (see Section 4.3.1) and measure the pump spot size (see Section 4.3.2). Time- and frequency-domain visualization of the pump beam modulation is achieved using the oscilloscope mode of the lock-in amplifier using LabOne Scope.

[2] In practice, we infinity-correct our camera by optimizing the contrast of an image obtained for a distant object (*e.g.*, an antenna on top of a building or a tree that is as far as possible) by tuning the distance between the lens and the camera.

4.2.2 Additional setup configurations

The simple layout and modular design of our ultrafast optical setup allows for relatively easy switching between three different setup configurations. These include time-domain thermoreflectance [Section 4.2], time-resolved Raman scattering [Section B.2] and time-resolved photocurrent [Section B.2]. The setups mainly differ in the probe wavelength and/or bandwidth, the pump-probe modulation scheme, and the detection strategy. We select the desired probe line, among the three available probes, by blocking the two unwanted probe beams using beam dumps. The three probe lines would travel the same optical path length, by eventually combining into one common path thanks to the use of flip-mirrors. This maintains the relative delay time between pump and probe beams (*i.e.*, the time-zero position on the delay line) in all setups ensuring minimal realignment when changing to another setup configuration.

The detection strategy depends on the setup configuration: TDTR senses the transient temperature via the temperature-dependent reflectivity of metals using a photodiode and lock-in detection; trRS collects the inelastically scattered light from optical phonons using a grating-based spectrometer and a CCD camera; and trPC detects the photo-generated current (or voltage) using lock-in detection. A cage system in the detection path enables the use of alignment-free drop-in BS cubes that we insert, remove or replace to guide the incident light onto the sample, and the reflected light onto either a photodiode (TDTR setup) or a spectrometer (trRS setup). Moreover, the electrical connections in our cryostat chamber enable (opto)electronic measurements using a break-out box and a lock-in amplifier (trPC setup). More details on the trRS and trPC setups can be found in Section B.2.

The possibility to perform electrical measurements also enables for electrically determining the thermal conductivity of our transducer films using the four-probe van der Pauw method. Such electrical measurements reporting on the thermal conductivity of the metal transducer will be employed to reduce the number of unknowns in our TDTR experiments (see Section 6.3.1).

4.3 TDTR Setup Alignment

In this section, we provide guidance on the alignment of our TDTR setup, with some of the considerations potentially applicable to the other configurations of our setup, different TDTR setup designs, and ultrafast optical setups in general.

We mainly review the specific alignment of our electro-optic modulator and alignment of our quadruple-pass delay line (see Section 4.3.1), and the spatial and temporal beam overlap including the measurements of the pump and probe spot sizes (see Section 4.3.2).

4.3.1 Aligning the EOM and delay line

To visualize the laser path at the fundamental wavelength (1030 nm), we use a laser viewing card (VRC4, Thorlabs). Whenever possible, we align the setup using minimum laser powers, which we adjust using half-waveplates (WPH05M-1030 and WPH05M-514, Thorlabs) mounted on motorized rotators (K10CR2/M, Thorlabs), in combination with linear polarizers (LPNIR050-MP2 and LPVISA050-MP2, Thorlabs). The half-waveplate [$\lambda/2$ in Fig. 4.1] rotates the incident polarization and the linear polarizer defines the output polarization state. This allows us to adjust the laser power of both beams in range $\sim 0.2 - 10$ mW at the sample plane. In a typical experiment, we calibrate the laser power with the angle of the rotator to adjust the laser power at will, as in the automated power-dependent experiments shown in Chapter 6. We use a power meter kit (PM130D, Thorlabs) consisting of a digital console and a photodiode power sensor to measure the laser power at any position of the setup.

Alignment procedures for our electro-optic modulator

To sinusoidally modulate the intensity of the pump beam at MHz frequencies, we use a Pockels cell-type modulator consisting of two matched lithium niobate crystals (EO-AM-NR-C2, Thorlabs). Our EOM can modulate the intensity of the pump beam up to 100 MHz. However, due to the Nyquist criterion, the modulation frequency must stay below half the laser repetition rate (*i.e.*, 38 MHz) [128]. We drive the EOM using the triangular output of a function generator (AFG-2112, GW INSTEK), amplified by either a high-power amplifier (VBA-100-30, Vectawave) or a voltage amplifier (HVA200, Thorlabs). The amplifier applies a time-varying voltage along the z-cut axis of the non-linear $LiNbO_3$ crystals changing its refractive index and creating retardance between the polarization components parallel and perpendicular to the crystal axis. This changes the polarization state at the output of the EOM, and a linear polarizer modulates the intensity of the pump beam as the polarization changes.

For convenience, our EOM is mounted on a 5-axis stage (PY005/M, Thorlabs), where two actuators control the yaw and Y axes, two actuators adjust the pitch

and Z axes, and a single actuator adjusts the X axis. This makes it possible to place the EOM in the beam path and achieve maximum transmission through its 2 mm aperture. Once this is achieved, we mark the position of the transmitted beam on a card (a laser viewing card for IR wavelengths) at a distance of a $\sim$10 cm from the EOM's output. A linear polarizer perpendicular to the incident polarization is placed between the card and the EOM and, using a diffuser at the entrance of the EOM (*e.g.*, a piece of translucent Scotch tape), a closed isogyre pattern will be projected on the viewing card (see **Figure 4.4a**). This occurs because lithium niobate crystals are birefringent and have a fixed principal axis. Misalignment between the incident polarization and crystal axis gives rise to a four-lobed interference pattern (the isogyre) [129]. We adjust this pattern using the degrees of freedom of the EOM mount such that the minimum transmission is centered with the transmitted beam's position previously marked on the card. If the pattern is not fully closed (*i.e.*, minimum transmission at the center), the EOM needs to be biased.

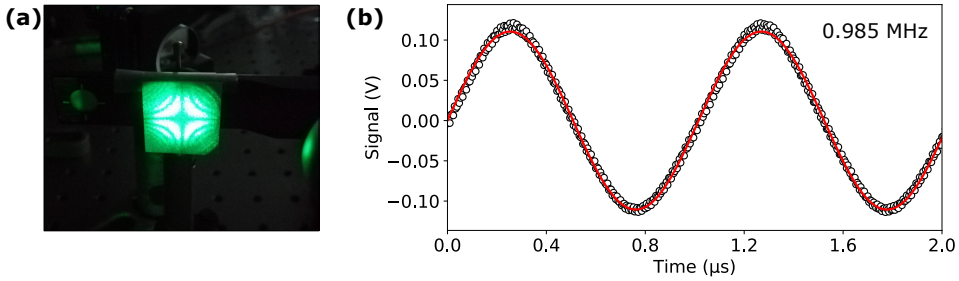

FIGURE 4.4: **Electro-optic modulation of the pump beam. (a)** Closed isogyre pattern shown for a green EOM for clarity. The EOM is optically biased using the quarter-waveplate technique. **(b)** Typical amplitude modulation of the pump beam as read by LabOne Scope (*empty scatters*) with a fitted sine wave for reference (*red line*).

Typical half-wave voltages V_π required to drive an EOM (defined as the voltage required to shift the retardance by π radians) are in the order of hundreds of volts, and increase with the wavelength of light. While amplitude modulators utilize a triangular wave with a peak-to-peak voltage $V_{pp} = V_\pi$ and an electrical bias of $V_\pi/2$ for full sinusoidal modulation, commercial voltage amplifiers able to drive an EOM at long wavelengths are scarce. We note that resonant EOMs benefit from much smaller half-wave voltages, with the disadvantage that they operate at a single, fixed frequency. In our experiments, we modulate the pump beam ($\lambda_\mathrm{p} = 1030$ nm) between 1 and 10 MHz, and take advantage of the quarter-waveplate technique to optically bias the EOM. In practice, a quarter-waveplate

[$\lambda/4$ in Fig. 4.1] set at 45° with respect to the incident polarization produces circular polarization at the entrance of the EOM, eliminating the need for electrically biasing the modulator. We can therefore use the entire output of the high-power amplifier to sufficiently amplify the triangular wave provided by the function generator. We synchronize the function generator with the lock-in amplifier ensuring that the reference signal used for demodulation is phase-locked to the actual modulation of the pump beam. We show an example of the typical amplitude modulation of the pump beam in Figure 4.4**b**.

Alignment of a retroreflector-based delay line

Our setup contains a 325 mm quadruple-pass delay line equipped with two silver-mirror retroreflectors (DL-BKIT4U-S-M, Newport) which we use to achieve a maximum time delay between pump and probe pulses of ∼8.7 ns. In practice, we typically vary the time delay between −1 ns and 7.7 ns to fine-sample the zero time delay, when both beams coincide in time. This is important in TDTR experiments, as we will need to determine the phase offset of the reference modulation (see Section 6.2.1). These long delays in nanosecond timescales are crucial for TDTR measurements and other heat transport experiments. The time delay in picoseconds between two delay line positions $\Delta x = x_1 - x_0$ is then given by:

$$\Delta t = 2 \times 4 \times \frac{\Delta x}{c} \times 10^{12} \tag{4.1}$$

with $c \simeq 3 \times 10^8$ m/s the speed of light, and the factor 2 accounting for the optical path introduced by the incident and reflected beam at each of the 4 passes in the delay line (see Fig. 4.5**b**). The time delay rate we achieve with our delay line is ∼26.7 ps/mm, with an accuracy of ∼70 fs.

In our setup, we delay the pump beam while keeping the probe fixed during measurements. Two plano-convex lenses arranged as a telescope collimate and expand the pump beam waist to $w_\mathrm{p} \approx 1.5$ mm in diameter before it enters the delay line. The magnification relationship is $M = f_2/f_1$, with f_1 and f_2 the focal lengths of the first and second lenses. We choose this waist size to ensure that the pump beam stays collimated until the next focusing element, as determined by its Rayleigh length (calculated using $z_R = \pi w_\mathrm{p}^2/\lambda_\mathrm{p} > 6$ m) at the pump wavelength of $\lambda_\mathrm{p} = 1030$ nm. We extended the optical path of the probe beam to compensate for the additional optical path of the pump introduced by the delay line.

In a retroreflector-based delay line, the alignment is achieved by ensuring the incident beam is collinear with the delay line movement. A retroreflector essentially reflects a light beam perpendicular to the incident beam, while introducing lateral and vertical offsets relative to the position of the incident beam with respect to the center of the retroreflector (see Fig. 4.5**a**).

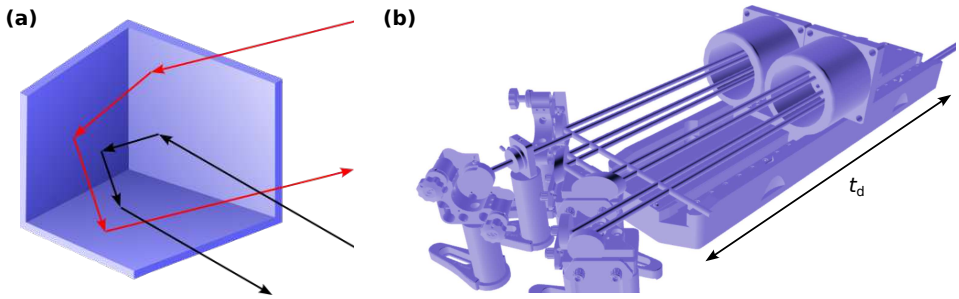

FIGURE 4.5: **Retroreflector-based 325 mm quadruple-pass delay line. (a)** Schematic of a retroreflector mirror, where the incident rays reflect three times to produce an output ray which is parallel to the incident beam. **(b)** 3D CAD drawing (DL-BKIT4U-S-M, Newport) of our retroreflector-based quadruple-pass delay line, used to introduce a time delay t_d between pump and probe pulses.

4.3.2 Spatial and temporal beam overlap

Once the amplitude of the pump beam is modulated at MHz frequencies and the delay line is aligned, we proceed with the spatial alignment of the pump and probe beams on the sample. To achieve this, we use our infinity-corrected camera to visualize the beams and align them to the same spot by adjusting the last two mirrors that direct each beam toward the objective lens.[3] The goal is to transmit both beams through the center of the objective lens. Once the beams illuminate the same xy position on the sample, we must ensure they are also focused on the same z plane. To achieve spatial overlap in the z-axis (*i.e.*, the direction normal to the sample), we slightly decollimate the pump beam before the objective lens to adjust its focus at the same plane as the probe beam focus. We perform this alignment with visual aid from our camera, and finally verify it by measuring both laser spot sizes using the knife-edge technique with our optical focus as reference.

[3]Each of these two mirrors has two independent degrees of freedom, and combined, allow for lateral beam translation without tilting the beam, commonly referred to as "walking the beam", while maintaining collinearity with the objective.

Spatial beam overlap using the knife-edge technique

The knife-edge technique determines a beam spot size by translating a sharp edge (*e.g.*, a lithographically defined metal pad) through the beam while recording the reflected power and fitting the resulting intensity profile to obtain the beam width. To perform knife-edge measurements on the probe beam we insert an optical chopper in the beam path, rotating at few-hundred Hz, while for the pump we modulate the beam at MHz frequencies using our EOM. We modulate the beams in order to increase the accuracy of our knife-edge measurements.

Figure 4.6 shows a summary of typical knife-edge measurements using our setup, which we perform as a function of the z-position of the objective lens. We first zeroed the objective's z-position at the optical focus of the camera (see Fig. 4.6**a**). Moving the z-position of the objective effectively moves the focal plane across the sample surface. By scanning the sample from the region of low reflectivity (SiO_2) to the region of high reflectivity (gold), we obtain step-like profiles at various z-positions of the objective lens (see Fig. 4.6**b**). The sharpness of the step is given by the convolution of the beam profile and the step size of the scanned edge, the latter being typically much smaller than the laser spot. The sharpest step-like profile appears at the best laser focus, and we fit its derivative to a Gaussian function [Equation 4.2] to retrieve the laser spot size (see Fig. 4.6**c**):

$$f(x) = A \exp\left[-\frac{(x-x_0)^2}{2\sigma^2}\right] \tag{4.2}$$

with A the amplitude, x_0 the center of the profile, and σ the standard width. The Gaussian fits performed on the reflectivity derivatives yield the standard widths σ at each objective position (see Fig. 4.6**d,e**). However, in TDTR experiments, the relevant spot size w_0 is the root mean square average of the pump and probe laser spot radii $r = \sqrt{2}\,\sigma$ using the $1/e^2$ definition (see Fig. 4.6**e**):

$$w_0 = \sqrt{\frac{r_{\text{pump}}^2 + r_{\text{probe}}^2}{2}} \tag{4.3}$$

Figure 4.6**e** shows the average standard widths of the pump σ_{pump} and probe σ_{probe} beams, which have been measured in x and y directions to diagnose the beam ellipticity. The pump beam has also been measured at the initial and final positions of the delay line to diagnose its collimation. The symmetric V-shaped profiles suggest both beams are centered and collinear with the objective lens. The standard width of the probe beam σ_{probe} reaches a smaller value, as it focuses

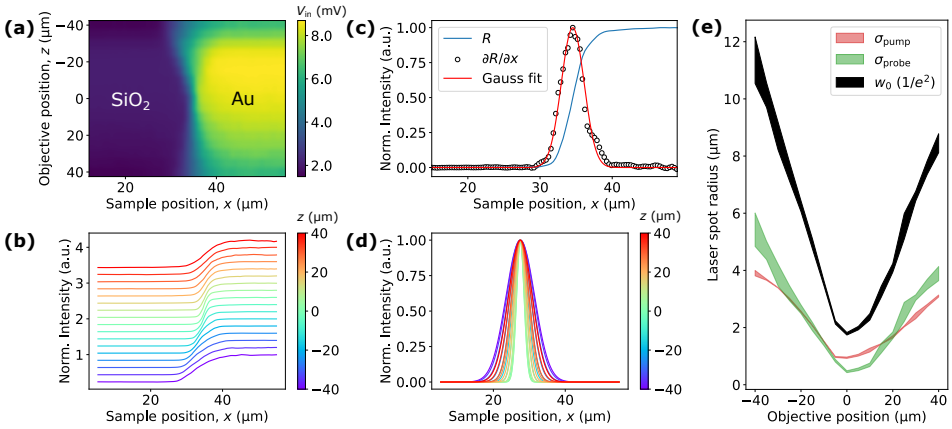

FIGURE 4.6: **Laser spot size determination: the knife-edge method.** **(a)** Colormap of the reflectivity linescans across the edge of a gold pad on SiO_2/Si wafer, performed at different z-positions of the objective lens. **(b)** Step-like profiles obtained at each objective position. **(c)** Exemplary Gaussian fit on the reflectivity derivative, from which we extract the standard width of our laser profile. **(d)** Summary of the Gaussian fits at each objective position, showing the narrowest profile at the optical focus ($z = 0$ µm). **(e)** Standard widths of pump σ_{pump} (*red*) with $\lambda = 1030$ nm, probe σ_{probe} (*green*) with with $\lambda = 515$ nm, and calculated RMS average spot size w_0 (*black*) of both beams.

more tightly due to its smaller wavelength and also because we decided not to fill the back aperture of the objective with the pump beam. The errors in the measured standard widths mainly arise from small deviations from perfect optical alignment, while the errors shown for the average spot sizes w_0 have been calculated using error propagation of Eq. 4.3. Overall, our knife-edge measurements suggest that the laser focus of both beams coincides with the optical focus, thanks to the infinity-correction of our camera, and that we can vary the spot size w_0 from 2 to 10 µm in TDTR experiments with an uncertainty of ∼5%.

Temporal beam overlap

To find the position of the delay line at which both, pump and probe beams, arrive simultaneously at the sample (*i.e.*, the zero time delay $t_{\text{d}} = 0$), we use the time-domain thermoreflectance configuration (more details in Chapter 5). Here, we use our pump beam modulated at MHz frequencies (f_{mod}) to produce temperature fluctuations on a gold surface, we use sufficient laser power to produce detectable reflectivity changes at the probe wavelength. We should be able to detect these changes by monitoring the reflection of our probe beam, spatially overlapped (in

xzy) with our pump laser and demodulating it at the frequency f_{mod} using our lock-in amplifier.

In our setup, all of this is simplified when using low modulation frequencies of $\sim$1 MHz (we will see some of these reasons in Section 6.2.2). In this situation, unless using a high thermal conductivity substrate, the signal should be detectable in the entire time delay accessible by our delay line, even at negative time delays. This is, when the probe pulse arrives before the pump pulse, effectively evaluating the previous pump pulse at a time delay given by the repetition rate of our laser ($1/f_{\text{rep}} \approx 13$ ns). The reason is because heat introduced by consecutive pump pulses has not fully dissipated upon the arrival of the next pulse (*i.e.*, the pulse accumulation regime already considered by the TDTR model, see Chapter 5). In this configuration, it is relatively straightforward to find the delay line position at which both beams coincide temporally at the sample surface (*i.e.*, where we expect the maximum thermoreflectance signal) and is a matter of scanning the delay line.

It is possible that the zero time delay does not fall on the delay line range. In this case, the signal would not jump from a maximum value expected when the beams coincide in time ($\Delta t = 0$) to a minimum value when pump pulses arrive after probe pulses ($\Delta t < 0$). At negative time delays we expect the minimum thermoreflectance signal, as the probe evaluates the effect of the previous pump pulse at an effective time delay of $\Delta t = 1/f_{\text{rep}} \approx 13$ ns, and the temperature induced by the pump has been significantly dissipated. Therefore, the probe path extension should be enlarged or shortened relative to the optical path of the pump beam. As path lengths are difficult to measure precisely, it is convenient to use a fast oscilloscope fed with the reference signal from our fundamental laser, and compare the time delay of both beams with respect to this reference. We achieve this by connecting the photodiode that monitors the reflection of the beams to the oscilloscope. If the probe pulses arrive earlier (later) than the pump, the probe path needs to be extended (shortened). Finally, we fine-tune the spatial overlap to optimize the TDTR signal magnitude, which we can estimate beforehand considering how the optical signal is converted into an electrical current by our photodiode, and into a voltage by our lock-in amplifier (see Section B.1).

4.4 Summary and Outlook

In this chapter, we have detailed the design and construction of a versatile ultrafast pump-probe optical setup, optimized to investigate the thermal properties of 2D and low-dimensional materials with high spatial and temporal resolution.

The modular architecture of the setup allows for easily switching between different experimental techniques, including time-domain thermoreflectance, time-resolved Raman spectroscopy, and time-resolved photocurrent measurements. By integrating these capabilities, the system provides a powerful platform for studying thermal transport, dissipation, and related phenomena in a wide range of materials. Beyond its flexibility, this setup enables a wide range of approaches to thermal characterization by looking at heat-related phenomena from various perspectives. Focusing on the TDTR setup, we have discussed the critical aspects of its operation, including alignment procedures and key performance considerations. This setup will be employed in Chapters 6 and 7 to conduct TDTR measurements, demonstrating its effectiveness in probing out-of-plane thermal transport across flakes of 2D materials.

Contributions

Dr. Alexander Block drafted the early TDTR setup design and implemented the hardware-Python interfacing. I rebuilt and upgraded this early setup and assisted Nupur Sontakey in developing the trRS setup. I assisted Dr. Jake D. Mehew in designing and implementing the early version of the trPC setup. I coordinated the disassembly of the optical setup and the move of the UDNS laboratory from ICN2 (Barcelona, Spain) to TU/e (Eindhoven, The Netherlands) with assistance from Sebin Varghese and Dr. Bohai Liu. I redesigned the optical setup to simplify its layout and make the three experimental setups compatible. I rebuilt the TDTR, trRS and trPC setups in TU/e with assistance from Dr. Loïc Moczko and Dr. Bohai Liu.

Chapter 5

Time-Domain Thermoreflectance: Background and Theory

In this chapter, I explain the basic principles of time-domain thermoreflectance, and I give all the necessary tools to model the signals acquired in TDTR experiments using a lock-in amplifier. I show an example of the simulated lock-in signals for a simple 2-layer system consisting of a gold transducer on bulk MoS_2, and explain how to estimate the sensitivities of the lock-in signals to the different parameters. Mathematical derivations in this chapter are based on those reported in Refs. [130–133]. The notation may differ to bring consistency and to bridge the various derivations reported in the Literature. The mathematical tools needed to understand this chapter can be found in Appendix C.1. The contents of this chapter will serve as theoretical and experimental backgrounds for Chapters 6 and 7.

5.1 Basics of Time-Domain Thermoreflectance

During the 1970s and 1980s, the thermoreflectance technique initially employed continuous-wave (CW) light sources [134]. The later introduction of picosecond and femtosecond pulsed lasers enabled the exploration of ultrafast phenomena such as non-equilibrium electron-phonon interactions and coherent phonon transport. Early researchers, including Paddock, Eesley, and Maris, demonstrated the method's potential by measuring thermal diffusivity of thin films using picosecond ultrasonics [135, 136]. Over the past two decades, the approach has been refined to investigate anisotropic thermal transport [133, 137–139] and the spectral behavior of phonons [140, 141]. In early versions of TDTR, data reduction methods relied on simplified assumptions until Cahill incorporated the "pulse accumulation" effect by solving the three-dimensional heat diffusion equation for multilayer structures [130]. This is, the response of a new laser pulse takes into account the remanent response of the previous pulse, which has not yet decayed to a negligible value. Subsequent extensions by Schmidt *et al.* to include anisotropic conduction have led to the development of a widely adopted thermal model that assumes axisymmetric laser profiles, top-surface heating and sensing, and thermal equilibrium among phonon modes [133].

In essence, time-domain thermoreflectance measurements determine the thermal properties by monitoring how a material's reflectance changes with temperature. In practice, a thin metal film is deposited on the sample of interest to act as a transducer. The transducer linearly translates small lattice temperature changes, given by the heat flux Q and the lattice heat capacity C_l ($\Delta T_l = Q/C_l < 10$ K), into measurable differences in reflectance:

$$\Delta R/R = \left(\frac{1}{R}\frac{\partial R}{\partial T}\right)\Delta T = \chi\,\Delta T \tag{5.1}$$

with χ its thermoreflectance coefficient, which is the amount of reflectivity change per unit Kelvin. Note that, upon arrival of a pump laser pulse, the electron system —with a much smaller heat capacity of $C_e \approx 0.02$ MJ m^{-3} K^{-1}— heats up significantly more ($\Delta T_e = Q/C_e \gg 10$ K), as $C_l/C_e > 100$. This also implies that the electrons quickly transfer the energy to the phonons, increasing the lattice temperature by just a few kelvins. The hot surface then cools due to heat diffusion driven by the temperature gradient. Thus, the transducer's temperature depends on the thermal properties of the materials underneath, which act as a heat sink.

In a typical TDTR experiment, an electro-optic modulator (EOM) modulates the

intensity of the pump beam at $0.1 - 20$ MHz frequencies to periodically heat the sample. A probe beam captures the transient reflectance changes induced by the pump beam, thus revealing the material's dynamic thermal response. The probe wavelength and the metal transducer are typically chosen to maximize the thermoreflectance coefficient [142, 143]. We show the wavelength dependence of χ for some exemplary metal films used as transducers in TDTR (see Figure C.1). The reflected probe light is collected by a fast-response photodiode to convert the optical signals into electrical signals. A lock-in amplifier isolates the signal at the modulation frequency f_{mod} of the pump beam. This signal is then recorded at various time delays of arrival between the pump and probe pulses, mapping the dynamics of the thermal response up to $\sim$10 ns.

The thermal transport properties are obtained by fitting the data to a thermal transport model, adjusting the unknown parameters to match experimental observations (see Chapter 6). While TDTR can be used to study non-equilibrium [140] phenomena and electron-phonon coupling [144], most studies report effective thermal conductivity to describe nanoscale systems. However, we will see that caution must be taken when using Fourier's law in systems where heat is significantly carried by phonons with long mean-free paths (MFP) [138]. In this case, heat transport may not be purely diffusive, and ballistic effects could significantly contribute to the cooling of the transducer.

In this chapter, we review the extended TDTR model by solving the heat equation in a multilayer stack. We then model the lock-in amplifier operation to simulate the signals that would be obtained in typical TDTR experiments. Finally, we reproduce a sensitivity analysis from the literature, for relatively thin MoS_2 on a substrate ($Al/MoS_2/SiO_2/Si$), to validate our model implementation.

5.2 Thermal Transport Model and Signal Processing in TDTR

Understanding TDTR measurements requires understanding both thermal transport and signal sampling. It requires developing a model that describes heat diffusion through a multilayer sample while recording the transient thermal response. This model involves two key steps: first, solving the heat diffusion equation in a multilayer stack [Section 5.2.1], and second modelling the corresponding TDTR

signals acquired using a lock in amplifier [Section 5.2.2]. **Figure 5.1** shows the typical multilayer sample geometry, with the top layer representing the metal transducer (*e.g.*, Au or Al). Immediately below is (are) the material(s) of interest, which in the context of this thesis typically consists of flakes (or stacks) of 2D materials from the TMD family. When the material of interest is not a bulk material, TDTR experiments require using a substrate (*e.g.*, a SiO_2/Si wafer) to ensure sufficient heat sinking, represented by the bottom layer. Therefore, most of the samples studied in this thesis consist of Au/TMD/SiO_2/Si, unless specified. The thermal model then takes into account the thicknesses (L_n) and the thermal parameters ($\kappa_{z,n}$, $\kappa_{r,n}$ and C_n) of each layer (n) in the multilayer stack, and the interfacial conductances (G_n) between them.

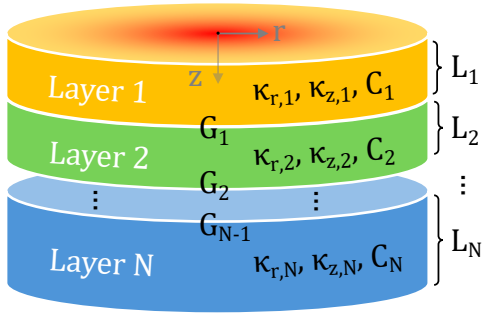

FIGURE 5.1: **TDTR sample geometry.** Multilayer sample geometry for the thermal model of TDTR experiments, with $\kappa_{r,n}$ and $\kappa_{z,n}$ the thermal conductivities in the radial r and cross-plane z directions, respectively; C_n the heat capacity; G_n the interfacial thermal conductance; and L_n the thickness. Every layer n has z coordinates from its top surface $z = 0$ to its bottom surface $z = L_n$ at a distance of the layer thickness L_n.

5.2.1 Solving the heat diffusion equation in a multilayer stack

Several publications have addressed the solution of the one-dimensional heat diffusion equation through a multilayer system [145–147]. In Ref. [130], Cahill expanded Feldman's algorithm [146, 147] to three-dimensional heat conduction for modelling thermal responses in TDTR experiments. The approach described in Ref. [145] was extended to account for three-dimensional and anisotropic in- and out-of-plane heat conduction [132]. Here, we summarize the solution of the anisotropic heat diffusion equations in cylindrical coordinates for a multilayer stack while using the quadrupole approach [148] as in Ref. [131].

The governing equation for the temperature T evolution is based on Fourier's law of heat conduction for each layer of the stack (see Figure 5.1) and reads

$$C_n \frac{\partial T}{\partial t} = \kappa_{r,n} \frac{1}{r} \frac{\partial}{\partial r} \left(r \frac{\partial T}{\partial r} \right) + \kappa_{z,n} \frac{\partial^2 T}{\partial z^2} \tag{5.2}$$

where C_n is the volumetric heat capacity of each layer n, while $\kappa_{r,n}$ and $\kappa_{z,n}$ are their in-plane and out-of-plane thermal conductivities, respectively. Applying the Fourier transform on Eq. 5.2 over the time variable t

$$-i\omega C_n \hat{T} = \kappa_{r,n} \frac{1}{r} \frac{\partial}{\partial r} \left(r \frac{\partial \hat{T}}{\partial r} \right) + \kappa_{z,n} \frac{\partial^2 \hat{T}}{\partial z^2} \tag{5.3}$$

and the Hankel transform on Eq. 5.3 over the radial coordinate r

$$-i\omega C_n \hat{\hat{T}} = \kappa_{r,n} (4\pi^2 k^2) \hat{\hat{T}} + \kappa_{z,n} \frac{\partial^2 \hat{\hat{T}}}{\partial z^2} \tag{5.4}$$

we reach an expression that can be simplified into an ordinary differential equation as:

$$\frac{\partial^2 \hat{\hat{T}}}{\partial z^2} = \lambda_n^2 \hat{\hat{T}} \tag{5.5}$$

with $\hat{\hat{T}}$ the temperature in the frequency domain, and $\lambda_n^2 = 4\pi^2 k^2 \eta_n + i\omega C_n / \kappa_{z,n}$; where k is the Hankel transform variable, $\eta_n = \kappa_{r,n} / \kappa_{z,n}$ is the anisotropy ratio of each layer, and $\omega = 2\pi f$ is the angular frequency.

The general solution of Equation 5.5 can be written as:

$$\hat{\hat{T}} = \underbrace{D_n^+ \exp\left[\lambda_n z\right]}_{B_n^+} + \underbrace{D_n^- \exp\left[-\lambda_n z\right]}_{B_n^-} \tag{5.6}$$

where D_n^+ and D_n^- are complex constants to be determined based on the boundary conditions between the different layers, and B_n^+ and B_n^- are the "state vectors" that specify the temperature at a particular point of the system. The heat flux Q can be obtained from the temperature [Eq. 5.6] and Fourier's law of heat conduction:

$$\begin{aligned} \hat{\hat{Q}}_n = -\kappa_{z,n} \frac{\partial \hat{\hat{T}}}{\partial z} &= -\kappa_{z,n} (\lambda_n B_n^+ - \lambda_n B_n^-) \\ &= -\gamma_n \left(D_n^+ \exp\left[\lambda_n z\right] - D_n^- \exp\left[-\lambda_n z\right] \right) \end{aligned} \tag{5.7}$$

where $\gamma_n \equiv \kappa_z \lambda_n = \kappa_z \sqrt{4\pi^2 k^2 \eta_n + i\omega C_n / \kappa_{z,n}}$.

It is convenient to re-write Equations 5.6 and 5.7 in matrices (quadrupoles) as:

$$\begin{bmatrix} \hat{\hat{T}} \\ \hat{\hat{Q}} \end{bmatrix}_{n,z=L_n} = \underbrace{\begin{bmatrix} 1 & 1 \\ -\gamma_n & \gamma_n \end{bmatrix} \begin{bmatrix} \exp\left[\lambda_n L_n\right] & 0 \\ 0 & \exp\left[-\lambda_n L_n\right] \end{bmatrix}}_{[\mathcal{N}]_n} \begin{bmatrix} D^+ \\ D^- \end{bmatrix}_n \tag{5.8}$$

The constants D^+ and D^- can be calculated by setting $z = 0$ and performing the matrix inversion in Equation 5.8:

$$\begin{bmatrix} D^+ \\ D^- \end{bmatrix}_n = \underbrace{\frac{1}{2\gamma_n} \begin{bmatrix} \gamma_n & -1 \\ \gamma_n & 1 \end{bmatrix}}_{[\mathcal{M}]_n} \begin{bmatrix} \hat{\hat{T}} \\ \hat{\hat{Q}} \end{bmatrix}_{n,z=0} \tag{5.9}$$

Thus, the bottom surface of a layer is related to the top surface via the $[N]_n$ and $[M]_n$ matrices from Equations 5.8 and 5.9 as:

$$\begin{bmatrix} \hat{\hat{T}} \\ \hat{\hat{Q}} \end{bmatrix}_{n,z=L_n} = [\mathcal{N}]_n [\mathcal{M}]_n \begin{bmatrix} \hat{\hat{T}} \\ \hat{\hat{Q}} \end{bmatrix}_{n,z=0} \tag{5.10}$$

The product $[N]_n \cdot [M]_n$ can be simplified into a 2×2 matrix relating the temperature at the top and bottom surfaces of a single slab:[1]

$$\begin{bmatrix} \hat{\hat{T}} \\ \hat{\hat{Q}} \end{bmatrix}_{n,z=L_n} = \begin{bmatrix} \cosh\left[\lambda_n L_n\right] & -\frac{1}{\gamma_n}\sinh\left[\lambda_n L_n\right] \\ -\gamma_n \sinh\left[\lambda_n L_n\right] & \cosh\left[\lambda_n L_n\right] \end{bmatrix} \begin{bmatrix} \hat{\hat{T}} \\ \hat{\hat{Q}} \end{bmatrix}_{n,z=0} \tag{5.11}$$

For heat flow across an interface, the original derivation in Ref. [130] does not consider thermal boundary (Kapitza) resistances. In Ref. [130], interfaces are modelled using a layer with sufficiently small thickness and thermal conductivity values. Assuming a constant heat flow across the interface ($\hat{\hat{Q}}_{n+1,z=0} = \hat{\hat{Q}}_{n,z=L_n}$) it is possible to introduce an interfacial thermal conductance G that produces a finite temperature difference $\Delta T = Q/G$ at the interface, thus accounting for the thermal boundary resistance. In this case, the temperature at the top surface of the underlayer is $\hat{\hat{T}}_{n+1,z=0} = \hat{\hat{T}}_{n,z=L_n} - \frac{1}{G}\hat{\hat{Q}}_{n,z=L_n}$, which allows us to build another matrix $[\mathcal{R}]_n$ to relate the temperature and heat flux at the interfaces between two

[1] We use the definitions of the hyperbolic $\cosh(x)$ and $\sinh(x)$ functions:

$$\cosh(x) = \frac{\exp(x) + \exp(-x)}{2} \qquad \sinh(x) = \frac{\exp(x) - \exp(-x)}{2}$$

consecutive layers:

$$\begin{aligned}\begin{bmatrix}\hat{\hat{T}}\\ \hat{\hat{Q}}\end{bmatrix}_{n+1,z=0} &= \underbrace{\begin{bmatrix}1 & -1/G\\ 0 & 1\end{bmatrix}}_{[\mathcal{R}]_n}\begin{bmatrix}\hat{\hat{T}}\\ \hat{\hat{Q}}\end{bmatrix}_{n,z=L_n}\\ &= [\mathcal{R}]_n[\mathcal{N}]_n[\mathcal{M}]_n\begin{bmatrix}\hat{\hat{T}}\\ \hat{\hat{Q}}\end{bmatrix}_{n,z=0}\end{aligned} \tag{5.12}$$

This allows us to relate non-consecutive layers as:

$$\begin{aligned}\begin{bmatrix}\hat{\hat{T}}\\ \hat{\hat{Q}}\end{bmatrix}_{n+2,z=0} &= [\mathcal{R}]_{n+1}[\mathcal{N}]_{n+1}[\mathcal{M}]_{n+1}\begin{bmatrix}\hat{\hat{T}}\\ \hat{\hat{Q}}\end{bmatrix}_{n+1,z=0}\\ &= [\mathcal{R}]_{n+1}[\mathcal{N}]_{n+1}[\mathcal{M}]_{n+1}[\mathcal{R}]_n[\mathcal{N}]_n[\mathcal{M}]_n\begin{bmatrix}\hat{\hat{T}}\\ \hat{\hat{Q}}\end{bmatrix}_{n,z=0}\end{aligned} \tag{5.13}$$

The temperature T and heat flux Q on the top surface of the multilayer stack can thus be related to those at the bottom of the substrate such that:

$$\begin{aligned}\begin{bmatrix}\hat{\hat{T}}\\ \hat{\hat{Q}}\end{bmatrix}_{n=N,z=L_N} &= [\mathcal{N}]_N[\mathcal{M}]_N\cdots[\mathcal{R}]_1[\mathcal{N}]_1[\mathcal{M}]_1\begin{bmatrix}\hat{\hat{T}}\\ \hat{\hat{Q}}\end{bmatrix}_{n=1,z=0}\\ &= \begin{bmatrix}A & B\\ C & D\end{bmatrix}\begin{bmatrix}\hat{\hat{T}}\\ \hat{\hat{Q}}\end{bmatrix}_{n=1,z=0}\end{aligned} \tag{5.14}$$

Because of the high modulation frequencies used in TDTR experiments, the heat flux at the bottom of the substrate layer ($n = N$, $z = L_N$) is zero: $\hat{\hat{Q}}_{z\to\infty} = 0$. This yields $0 = C\hat{\hat{T}}_{n=1,z=0} + D\hat{\hat{Q}}_{n=1,z=0}$. The Green's function $\hat{\hat{G}}$, which is essentially the thermal response function due to the applied heat flux of unit strength [130], can be solved as (see details in Section 5.2.2):

$$\hat{\hat{G}}(k,\omega) = \frac{\hat{\hat{T}}_{n=1,z=0}}{\hat{\hat{Q}}_{n=1,z=0}} = -\frac{D}{C} \tag{5.15}$$

5.2.2 Modelling of signals acquired in TDTR experiments

The next step is to understand and simulate the signals acquired in TDTR experiments. Here, a modulated train of pump pulses excites the electron system

of the metal transducer. Each pulse first increases the temperature of the transducer's electron system and these scatter with the phonons within picosecond timescales [144], thus increasing the lattice temperature. The heat then diffuses radially and across the layers of the stack, eventually reaching the heat sink provided by the bulky substrate. Heat diffusion occurs in nanosecond timescales, contributing to the pulse-to-pulse cooling of the laser-heated surface of the transducer. The heat introduced by each pulse may not completely dissipate upon arrival of the next pump pulse, leading to the "pulse accumulation" regime [133]. Modulating the pump beam at frequencies (f_{mod}) of a few MHz implies periodically tuning the laser power that arrives at the sample within microsecond timescales ($1/f_{\mathrm{mod}}$). The surface temperature then starts to oscillate at the modulation frequency, as cycles of intense lasing lead to an increasing temperature, and cycles of weak lasing allows for cooling the sample surface, alternately. The transient surface temperature at this particular frequency can be probed with a second pulsed laser (the probe beam). The dynamic thermal response at f_{mod} is then retrieved by monitoring the reflectivity of the probe beam while delaying the pump and probe pulses in time. We depict the signal detection mechanism in **Figure 5.2**.

Assuming Dirac delta functions δ for the laser pulses, which is a valid assumption considering the ultrashort pulse duration (typically ~100 fs) compared to the interval between pulses $T_{\mathrm{rep}} = 1/f_{\mathrm{rep}} = 2\pi/\omega_{\mathrm{s}}$ (typically several nanoseconds), the intensity of the modulated pump beam in real space and time domain is expressed as

$$p(r,t) = p_0(r)\left(\sum_{m=-\infty}^{\infty}\delta\left(t - mT_{\mathrm{rep}}\right)\right)\exp\left[i2\pi f_{\mathrm{mod}}t\right] \tag{5.16}$$

where $p_0(r) = 2A_{\mathrm{p}}/(\pi w_{\mathrm{p}}^2)\exp\left[-2r^2/w_{\mathrm{p}}^2\right]$; with A_p the average laser power of the pump beam, which has a Gaussian distribution in space with a $1/e^2$ radius of w_{p}; and $2\pi f_{\mathrm{mod}} = \omega_0$ the sinusoidal modulation frequency of the train of laser pulses, as we show in Figure 5.2**a**.

To convert the intensity of the pump beam $p(r,t)$ to the frequency domain, we perform the Hankel transform on space and the Fourier transform on time of Equation 5.16:[2]

$$\hat{\hat{P}}(k,\omega) = \hat{P}_0(k)\sum_{m=-\infty}^{\infty}\delta\left(\omega - \omega_0 - m\omega_{\mathrm{s}}\right) \tag{5.17}$$

[2]We use the frequency shift property of Fourier transforms, where:

$$\mathcal{F}\{y(t)\cdot\exp\left[i2\pi f_{\mathrm{mod}}t\right]\} = \hat{Y}(f - f_{\mathrm{mod}})$$

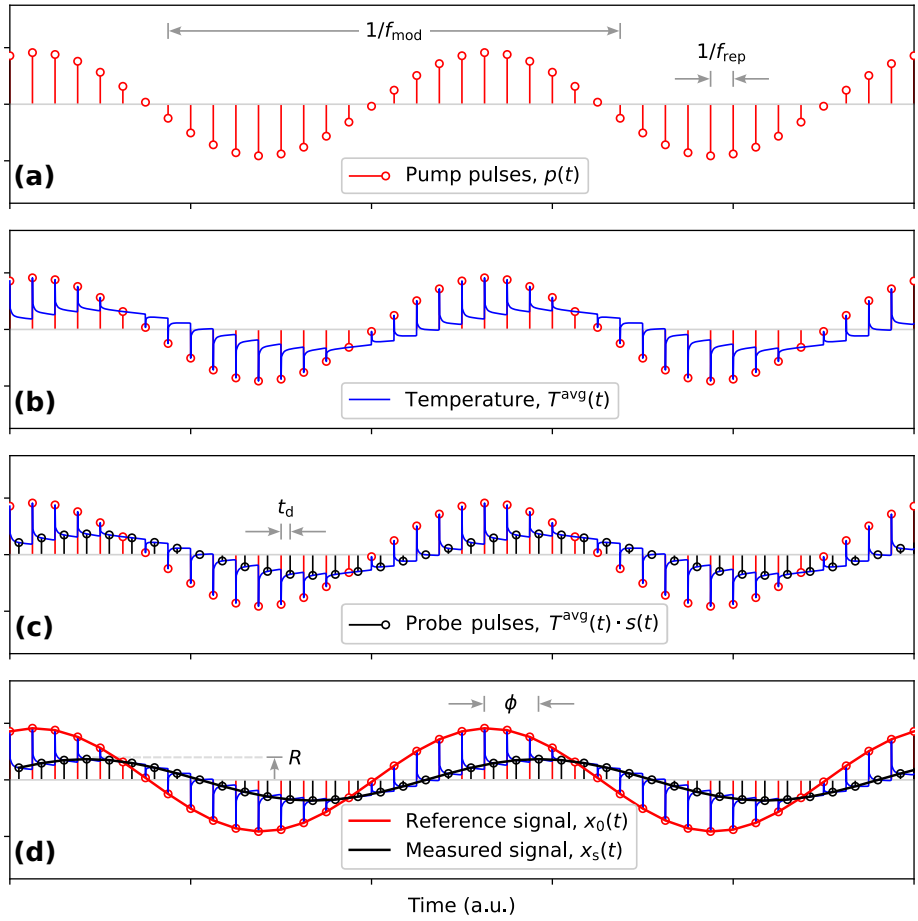

FIGURE 5.2: **Signal detection mechanism in the time domain. (a)** A train of pump pulses in the time-domain $p(t)$ with a repetition rate f_{rep} is modulated by a sine wave at a modulation frequency f_{mod}. **(b)** The pump beam induces a surface temperature response $T^{avg}(t)$. **(c)** A train of probe pulses $s(t)$ evaluates the surface temperature at a fixed time delay t_d. **(d)** The amplitude R and phase difference ϕ between the reference $x_0(t)$ (*red curve*) and measured $x_S(t)$ (*black curve*) signals are recorded by the lock-in amplifier at each time delay.

where $\hat{P}_0(k) = A_\mathrm{p} \exp\left[-\pi^2 k^2 w_\mathrm{p}^2/2\right]$ is the Hankel transform of $p_0(r)$.

The surface temperature response (in Hankel space and frequency domain) is the product between the heat input $\hat{\hat{P}}(k,\omega)$ [Eq. 5.17] and the thermal response function of the system $\hat{\hat{G}}(k,\omega)$ [Eq. 5.15]:

$$\hat{\hat{T}}(k,\omega) = \hat{\hat{P}}(k,\omega)\hat{\hat{G}}(k,\omega) \tag{5.18}$$

Inverse Hankel transform of Equation 5.18 corresponds to the temperature distribution on the surface as a result of the modulated pump heating as in Eq. C.1:

$$\hat{T}(r,\omega) = 2\pi \int_0^\infty \hat{\hat{P}}(k,\omega)\hat{\hat{G}}(k,\omega) J_0(2\pi k r) k dk \tag{5.19}$$

while inverse Fourier transform of $\hat{T}(r,\omega)$ is the temperature response $T(r,t)$.

A second train of laser pulses evaluates the temperature change due to the pump-induced AC heating. The intensity of the probe beam also has a Gaussian distribution in space, and is time-delayed by t_d with respect to the pump beam:

$$s(r,t) = s_0(r) \sum_{m=-\infty}^{\infty} \delta\left(t - mT_\mathrm{rep} - t_\mathrm{d}\right) \tag{5.20}$$

with $s_0(r) = 2A_\mathrm{s}/(\pi w_\mathrm{s}^2) \exp\left[-2r^2/w_\mathrm{s}^2\right]$ the Gaussian distribution of the probe beam, with a $1/e^2$ radius of w_s; normalized ($A_\mathrm{s} = 1$) so that we can use it as a probability distribution. Applying the Hankel and Fourier transforms on Eq. 5.20:

$$\hat{\hat{S}}(k,\omega) = \hat{S}_0(k) \sum_{m=-\infty}^{\infty} \delta\left(\omega - m\omega_\mathrm{s}\right) \exp\left[-i\omega_\mathrm{s} t_\mathrm{d}\right] \tag{5.21}$$

where $\hat{S}_0(k) = \exp\left[-\pi^2 k^2 w_\mathrm{s}^2/2\right]$ is the Hankel transform of $s_0(r)$.

Knowing the expression of the probe beam, we can now compute the Fourier transform of the weighted average of the surface temperature $\mathcal{F}\{T^\mathrm{avg}(t)\}$, which is essentially the temperature integrated over the probed area given by the laser spot size of the probe beam:

$$\begin{aligned} \mathcal{F}\{T^\mathrm{avg}(t)\} &= \mathcal{F}\left\{\int_0^\infty T(r,t) s_0(r) r dr\right\} \\ &= 2\pi \int_0^\infty \hat{T}(r,\omega) s_0(r) r dr \end{aligned} \tag{5.22}$$

Using the expression of the surface temperature $\hat{T}(r,\omega)$ [Eq. 5.19] and the expression of the pump beam $\hat{\hat{P}}(k,\omega)$ [Eq. 5.17] in Equation 5.22:

$$\begin{aligned}\hat{T}^{\text{avg}}(\omega) &= 2\pi\int_0^\infty \hat{\hat{P}}(k,\omega)\hat{\hat{G}}(k,\omega)\left(2\pi\int_0^\infty s_0(r)J_0(2\pi kr)rdr\right)kdk \\ &= 2\pi\int_0^\infty \hat{\hat{P}}(k,\omega)\hat{\hat{G}}(k,\omega)\hat{S}_0(k)kdk \\ &= 2\pi\int_0^\infty \left(\hat{\hat{P}}_0(k,\omega)\sum_{m=-\infty}^{\infty}\delta\left(\omega-\omega_0-m\omega_s\right)\right)\hat{\hat{G}}(k,\omega)\hat{S}_0(k)kdk\end{aligned} \tag{5.23}$$

We can now define the weighted average of the surface transient temperature due to harmonic heating at a frequency ω as

$$\begin{aligned}\Delta\hat{T}(\omega) &\equiv 2\pi\int_0^\infty \hat{\hat{P}}_0(k,\omega)\hat{\hat{G}}(k,\omega)\hat{S}_0(k)kdk \\ &= A_p 2\pi\int_0^\infty \hat{\hat{G}}(k,\omega)\exp\left[-\pi^2k^2w_0^2\right]kdk\end{aligned} \tag{5.24}$$

with $w_0 = \sqrt{(w_p^2+w_s^2)/2}$ the root mean square (RMS) average of the pump and probe radii using the $1/e^2$ definition. Then,

$$\hat{T}^{\text{avg}}(\omega) = \Delta\hat{T}(\omega)\sum_{m=-\infty}^{\infty}\delta\left(\omega-\omega_0-m\omega_s\right) \tag{5.25}$$

Figure 5.2**b** shows a representation of the weighted average surface temperature (in time domain) induced by the pump beam $T^{\text{avg}}(t)$ for a 2-layer system (*e.g.*, a transducer on a semi-infinite substrate). Note that some pulses appear to have a negative contribution to the surface temperature. The reason is that we neglected the DC component of the pump heating for simplicity (similar to Refs. [131–133]). In practice, the lock-in amplifier rejects the DC component, which justifies this mathematical simplification.

The probe beam samples a weighted average of the temperature distribution in real space $\hat{T}_S^{\text{avg}}(\omega)$ [Fig. 5.2**c**] as a convolution between the temperature profile $\hat{T}^{\text{avg}}(\omega)$ and the probe beam profile $\hat{S}(\omega)$. According to the Nyquist sampling theorem [Eq. C.2]:

$$\begin{aligned}\hat{T}_S^{\text{avg}}(\omega) &= \sum_{n=-\infty}^{\infty}\hat{T}^{\text{avg}}\left(\omega-n\omega_s\right)\exp\left[-in\omega_s t_d\right] \\ &= \sum_{n=-\infty}^{\infty}\Delta T(\omega-n\omega_s)\sum_{m=-\infty}^{\infty}\delta\left(\omega-(n+m)\omega_s-\omega_0\right)\exp\left[-in\omega_s t_d\right]\end{aligned} \tag{5.26}$$

which is non-zero only when $n = -m + (\omega - \omega_0)/\omega_s$. Therefore,

$$\hat{T}_S^{avg}(\omega) = \sum_{m=-\infty}^{\infty} \Delta\hat{T}(m\omega_s + \omega_0) \exp\left[-i(-m\omega_s + \omega - \omega_0)t_d\right] \tag{5.27}$$

In practice, as f_{rep} (76 MHz) is $4 - 400$ times larger than f_{mod} ($0.2 - 20$ MHz), the only frequency allowed by the lock-in band-pass filter is the modulation frequency of the pump beam ω_0. Thus, evaluating Eq. 5.27 at $\omega = \omega_0$, we reach an expression for the sampled weighed average surface temperature:

$$\hat{T}_S^{avg}(\omega) = \delta(\omega - \omega_0) \sum_{m=-\infty}^{\infty} \Delta\hat{T}(m\omega_s + \omega_0) \exp\left[im\omega_s t_d\right] \tag{5.28}$$

The inverse Fourier transform of Eq. 5.28 is the probed signal $T_S^{avg}(t)$ in time domain at a time delay t_d:

$$T_S^{avg}(t) = \exp\left[i\omega_0 t\right] \sum_{m=-\infty}^{\infty} \Delta\hat{T}(m\omega_s + \omega_0) \exp\left[im\omega_s t_d\right] \tag{5.29}$$

This is a sinusoidal function as we illustrate with a *black curve* in Fig. 5.2**d**. Its amplitude is the sum of all frequency responses $\Delta\hat{T}(\omega)$ at the multiple frequencies $\omega_0 + m\omega_s$. The real and imaginary parts of $T_S^{avg}(t)$ are then proportional to the in- and out-of-phase signals read by the lock-in amplifier, respectively:

$$\begin{aligned} V_{in} &\propto \mathrm{Re}\{T_S^{avg}(t)\} \\ &= \frac{1}{2} \sum_{m=-\infty}^{\infty} \left[\Delta\hat{T}(m\omega_s + \omega_0) + \Delta\hat{T}(m\omega_s - \omega_0)\right] \exp\left[im\omega_s t_d\right] \end{aligned} \tag{5.30}$$

$$\begin{aligned} V_{out} &\propto \mathrm{Im}\{T_S^{avg}(t)\} \\ &= -\frac{i}{2} \sum_{m=-\infty}^{\infty} \left[\Delta\hat{T}(m\omega_s + \omega_0) - \Delta\hat{T}(m\omega_s - \omega_0)\right] \exp\left[im\omega_s t_d\right] \end{aligned} \tag{5.31}$$

5.3 Components of the Lock-In Amplifier Signal

The lock-in amplifier mixes the signal $T_S^{avg}(t)$ [Eq. 5.29], at ω_0 and at a fixed time delay t_d, with two reference waves at ω_0 with a phase offset of $\pi/2$, while using low-pass filters to remove the AC components of the outputs of the multipliers [131]. The lock-in returns two readings, the in-phase signal V_{in}, composed of

the cosine components, and the out-of-phase signal V_{out}, composed of the sine components.

The V_{in} signal is related to the surface temperature change caused by the pump pulse heating, while the V_{out} signal is mainly due delayed thermal response at the modulation frequency f_{mod} given the finite thermal diffusion times. The decay rate of V_{in} represents the cooling process of the sample surface due to heat dissipation, and reports on the thermal diffusivity of the sample. The length scale that is affected by the pulsed heating is characterized by a thermal diffusion length d_d:

$$d_d = \sqrt{\kappa_z t_d / C} \tag{5.32}$$

with κ_z and C the thermal conductivity and heat capacity of the sample, respectively. Similarly, the thermal penetration depth d_p due to modulated continuous heating can be estimated as:

$$d_p = \sqrt{\kappa_z / (\pi f_{mod} C)} \tag{5.33}$$

Finally, the lock-in amplifier extracts the amplitude $R = \sqrt{V_{in}^2 + V_{out}^2}$ and phase $\phi = \tan^{-1}(V_{out}/V_{in})$ of the measured signal, relative to the reference wave [*red curve* in Fig. 5.2**d**].

5.3.1 Sensitivity analysis

The sensitivity of TDTR measurements to a given parameter can be evaluated by means of a sensitivity analysis [75, 149]. This makes it possible to use a tandem fitting approach, where a parameter is extracted from the most sensitive measurement configuration and is later fixed to evaluate other parameters in a configuration less sensitive to the first parameter, as in Ref. [39]. For example, given that the thermal penetration depth d_p decreases at higher modulation frequencies (see Section 5.3), the sensitivity to the upper layers and interfaces increases at higher f_{mod}. This means that one could use measurements at high modulation frequency to extract G_1, and then fix the fitted value of G_1 to extract $\kappa_{z,2}$ and G_2 from measurements at lower f_{mod} [39].

The ability to accurately measure an unknown thermal property from TDTR experiments can be quantitatively assessed using the definition of a sensitivity coefficient $\mathcal{S}_\xi$, as introduced in Ref. [75]:

$$\mathcal{S}_\xi = \frac{\partial \ln X}{\partial \ln \xi} = \frac{\xi}{X}\frac{\partial X}{\partial \xi} \tag{5.34}$$

where the sensitivity coefficient $\mathcal{S}_\xi$ represents how sensitive is the measured signal X ($= R$, ϕ, V_{in}, V_{out}, or $-V_{\text{in}}/V_{\text{out}}$) to a given parameter ξ. A positive (negative) $\mathcal{S}_\xi$ implies that a 1% increase in the parameter ξ will result in $\mathcal{S}_\xi \times 1\%$ increase (decrease) in the measured signal X. A larger (smaller) $\mathcal{S}_\xi$ indicates a stronger (weaker) dependence of the signal X on the parameter ξ, with $\mathcal{S}_\xi = 0$ meaning that the signal is unaffected by this parameter.

Reproducing a sensitivity analysis from the literature

To verify that our implementation of the thermal model described in Section 5.2.2 works, we reproduce the sensitivity analysis of Ref. [39] for an $Al/MoS_2/SiO_2/Si$ sample geometry. **Figure 5.3** shows the sensitivity analysis performed for 20 nm MoS_2 [Fig. 5.3**a,b**] and 200 nm MoS_2 [Fig. 5.3**c,d**] on a SiO_2/Si substrate with a 100 nm aluminum transducer layer, while using two different modulation frequencies ($f_{\text{mod}} = 4$, 10 MHz). Our results are comparable to those reported in Ref. [39] as we obtain the same qualitative trends for all evaluated parameters. However, it is challenging to reproduce the exact magnitude of the sensitivity coefficients for this and other works, as very rarely all the parameters involved in the thermal model are reported in the literature [39, 75, 130, 140, 144, 149–152].

As a general trend, increasing the modulation frequency enhances the sensitivity to parameters that are closer to the top most layer (*i.e.*, the transducer). In the same way, decreasing the modulation frequency enhances the sensitivity to parameters that are closer to the bottom most layer (*i.e.*, the substrate). This is because the thermal penetration depth d_{p} can be conveniently tuned by the modulation frequency [Eq. 5.33]. However, it is difficult to predict the trend and magnitude of the sensitivity coefficients, because adjusting one parameter may have a strong impact on the sensitivity of the rest of parameters. Therefore, it is advisable to perform sensitivity analysis not only for the feasible sample geometries and experimental configurations, but also as a function of the magnitude of the parameters of interest (see Chapters 6 and 7). Prior knowledge on how the TDTR signals are influenced by the different parameters is crucial to properly design a TDTR experiment and to estimate the uncertainties of the fitted parameters.

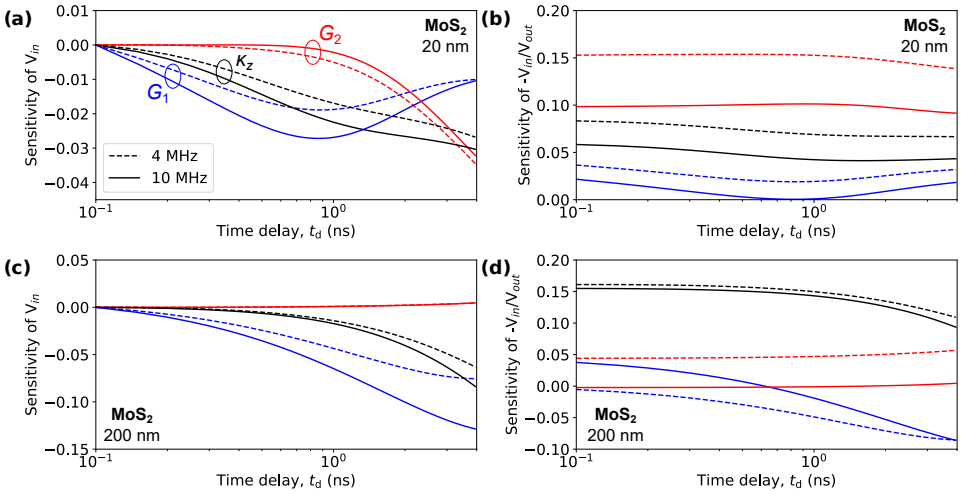

FIGURE 5.3: **Sensitivity analysis for Al/MoS_2/SiO_2/Si.** Calculated sensitivity coefficients of **(a,c)** in-phase V_{in} signals (normalized at a time delay of $t_{\text{d}} = 100$ ps) and **(b,d)** ratio $-V_{\text{in}}/V_{\text{out}}$ signals for **(a,b)** thin MoS_2 with $L = 20$ nm, $G_1 = 70$ MW m^{-2} K^{-1}, $G_2 = 25$ MW m^{-2} K^{-1}, and $\kappa_z = 0.9$ W m^{-1} K^{-1}; and for **(c,d)** thick MoS_2 with $L = 200$ nm, $G_1 = 34$ MW m^{-2} K^{-1}, $G_2 = 21$ MW m^{-2} K^{-1}, and $\kappa_z = 2$ W m^{-1} K^{-1}. **Legend:** κ_z of MoS_2 (*black curves*), G_1 of Al/MoS_2 (*blue curves*), and G_2 of MoS_2/SiO_2 (*red curves*); at two modulation frequencies: $f_{\text{mod}} = 4$ MHz (*dashed lines*) and $f_{\text{mod}} = 10$ MHz (*solid lines*). Reproduced Figure S1 from Ref. [39] using our thermal model implementation.

5.4 Summary and Outlook

In this chapter, we have reviewed the solution of the heat diffusion equation in a multilayer stack, which we will use to model the signals produced in the time-domain thermoreflectance experiment using our lock-in amplifier-based optothermal setup described in Chapter 4. Additionally, we have implemented our thermal model in Python and reproduced a sensitivity analysis reported in the literature. We will use this model to understand the effect of different parameters on our TDTR signals, and to fit the experimental data for both our control experiments (see Chapter 6) and for the substrate-supported few-layer MoS_2 samples prepared in Chapter 3 (see Chapter 7).

Contributions

I assisted Dr. Alexander Block to implement the thermal model in Python. I refined the Python codes and performed all the simulations reported in this chapter.

Chapter 6

Data Post-Processing and Setup Validation for TDTR

In this chapter, I create a reproducible workflow for TDTR data analysis. First, I show our approach at post-processing the TDTR data. For this, we use exemplary TDTR measurements on our Au/SiO_2/Si control sample, using the TDTR setup described in Chapter 4. I then explain all the steps we take to reduce the unknown parameters before we proceed to compare it with our thermal model, which we described in Chapter 5. As a first control experiment, and a validation of our TDTR setup, I show our results for the Au/SiO_2/Si sample, from which we extract the thermal conductivity of SiO_2 and the interfacial conductance of Au/SiO_2. As our second and last control experiment, I show the results we obtained on two thick MoS_2 interlayer samples, which we use to extract the out-of-plane thermal conductivity of MoS_2 and interfacial conductance of Au/MoS_2. This chapter is meant to walk the reader step-by-step through the time-domain thermoreflectance data analysis, to simplify the analysis and discussion of the results reported in Chapter 7.

6.1 Introduction

In this chapter, we focus on the steps involved in TDTR data analysis, using a standard SiO_2/Si substrate as our example. We use this sample and a similar sample that includes a thick MoS_2 flake transferred on SiO_2/Si as our control experiments to provide a solid reference for the TDTR experiments discussed in Chapter 7. We first coat both samples with 50 nm gold (including 2 nm titanium adhesion layers) using electron beam evaporation. These thin gold films will serve as our metal transducers that translate temperature fluctuations induced by our pump laser into measurable reflectivity fluctuations at the probe wavelength.

Because many experimental and material parameters affect the measured TDTR signals —such as heat capacities C_n, thermal conductivities κ_n, interface conductances G_n, and layer thicknesses L_n— we take important steps to reduce uncertainties and limit the number of unknowns wherever possible. In previous works, the heat capacities were typically pre-determined from separate measurements using scanning calorimetry [153] or extracted from the literature. The thickness of the metal transducer is often obtained from picosecond acoustics measurements [154], and its thermal conductivity from electrical van der Pauw measurements [155]. The van der Pauw method employs four electrical probes to retrieve the averaged sheet resistivity of thin metal films, which then relates to the thermal conductivity via Wiedemann-Franz law [156] (see Section 6.3.1). The laser spot size of both beams is typically measured using the knife-edge technique (see Section 4.3.2). This way, the unknown parameters are often reduced to κ and G for the layer of interest. For anisotropic materials, like TMDs, we need to consider the in-plane κ_r and out-of-plane κ_z thermal conductivities, or the anisotropy ratio $\eta = \kappa_r/\kappa_z$.

Most TDTR experiments use a large spot size ($w_0 = 5 - 20$ μm) and a high modulation frequency ($f_{\text{mod}} = 1 - 10$ MHz), resulting in a quasi-one-dimensional thermal transport across the multilayer structure [131]. In this case, the TDTR signals are most sensitive to thermal properties in the cross-plane direction (κ_z and G). Therefore, TDTR is commonly used to measure the out-of-plane thermal conductivity beneath the transducer $\kappa_{z,2}$ and the interfacial conductances at the transducer/sample G_1 and sample/substrate G_2 interfaces. In cases where the number of unknowns cannot be further reduced, it is a common practice to perform TDTR measurements at different spot sizes [139] and/or modulation frequencies [39, 150] to allow for tandem or global fitting the parameters of interest. Each measurement configuration may be more or less sensitive to specific parameters, and a proper sensitivity analysis is crucial to effectively plan a TDTR experiment (see

Section 5.3.1).

In the following sections, we describe each stage of the analysis in detail. We start with the data post-processing [Section 6.2]. Then we show all the steps needed to extract κ_{z,SiO_2} and G_{Au/SiO_2} using our $Au/SiO_2/Si$ control sample [Section 6.3]. Finally, we introduce thick MoS_2 interlayers both in our experiment and model, to measure its in-plane thermal conductivity κ_{z,MoS_2} and interfacial thermal conductance with gold G_{Au/MoS_2} by fixing the rest of parameters.

6.2 Data Post-Processing

Before we can proceed with extracting thermal parameters from the sample, we need to take into account some additional considerations such as the need to correct for the phase offset of the signal introduced by the electronics [Section 6.2.1], and background subtraction of signals that were not induced by the pump beam [Section 6.2.2].

The first step is to confirm the stability of our data acquisition process and to ensure that the thermoreflectance signal does not drift over time. For each measurement, we usually perform at least five repetitions and verify that the average of these repeated measurements aligns closely with the individual raw traces. **Figure 6.1** shows five repeated measurements of the V_{in} [Fig. 6.1**a**] and V_{out} [Fig. 6.1**b**] signals obtained from a 50 nm gold transducer on SiO_2/Si. The average of these measurements (*black curve*) closely matches the individual raw traces. Potential reasons for drifting thermoreflectance signals would include ambient temperature changes, laser-induced overheating, laser power fluctuations, loss of laser focus or spatial beam overlap, and sample drifting, among others. This stability check is often omitted, as the ratio signal $-V_{in}/V_{out}$ should be insensitive to laser power fluctuations and loss of beam overlap. However, other reasons such as a changing spot size may influence both the V_{in} and V_{out} signals and, thus, their ratio.

6.2.1 Determining the phase offset of the reference modulation

Ideally, the reference modulation should be perfectly in phase with the signal supplied to the electro-optic modulator. However, the lock-in amplifier, the signal cables, and the photodiode all have their own response, which results in an artificial phase shift ϕ_{inst} introduced by the instrumentation. There are several ways to account for ϕ_{inst}, such as normalizing the data or monitoring the phase of the pump beam directly, each of them with their own limitations and challenges [132].

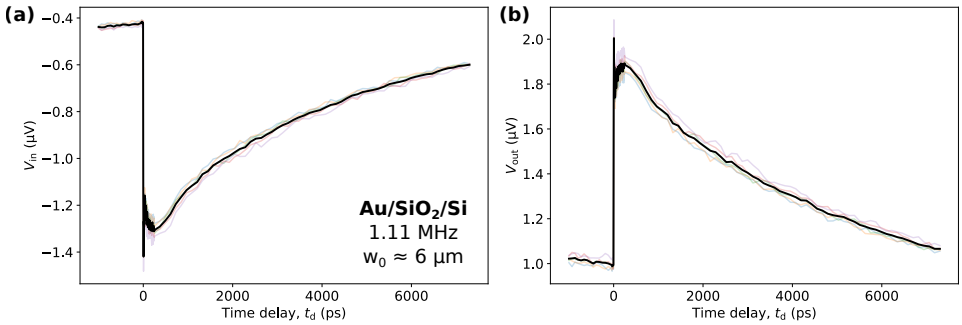

FIGURE 6.1: **Averaging repeated TDTR measurements.** Repeated measurements of **(a)** V_{in} and **(b)** V_{out} for a $Au/SiO_2/Si$ sample at 1.11 MHz and $w_0 \approx 6$ μm (*semitransparent color curves*), and their average (*black curve*). From now on, we will only deal with averaged traces from at least 5 repetitions.

The most common way to correct for phase shifts introduced by the instrumentation is using the fact that the V_{out} signal should be continuous as the delay time crosses $t_{\text{d}} = 0$ [130]. Thus, we conveniently correct the measured V_{in} and V_{out} signals by rotating the signal $V(t)$ in the complex plane [75]:

$$V(t) = V_{\text{in}}(t) + iV_{\text{out}}(t) \tag{6.1}$$

We now express the signal rotated by a phase ϕ_{rad} as $V'(t)$:

$$V'(t) = V(t)\ \exp\left[i\phi_{\text{rad}}\right] \tag{6.2}$$

where $\exp\left[i\phi_{\text{rad}}\right] = \cos\left(\phi_{\text{rad}}\right) + i\sin\left(\phi_{\text{rad}}\right)$ represents a counter-clockwise rotation in the complex plane; and $\phi_{\text{rad}} = \phi_{\text{deg}}\pi/180$ is the phase in radians. Finally, we recompute the rotated lock-in signals V'_{in}, V'_{out}, R' and ϕ':

$$\begin{cases} V'_{\text{in}} = \text{Re}\{V'(t)\} \\ V'_{\text{out}} = \text{Im}\{V'(t)\} \\ R' = |V'(t)| = \sqrt{{V'_{\text{in}}}^2 + {V'_{\text{out}}}^2} \\ \phi'_{\text{deg}} = \dfrac{180}{\pi}\arg\left(V'(t)\right) = \arctan\left(\dfrac{V'_{\text{out}}}{V'_{\text{in}}}\right) \end{cases} \tag{6.3}$$

Figure 6.2 shows the complex rotation performed on the averaged V_{in} and V_{out} signals shown in Fig. 6.1, obtained from our $Au/SiO_2/Si$ sample at 1.11 MHz using a RMS average spot size of $w_0 \approx 6$ μm. In Fig. 6.2**b**, the measured V_{out}

signal spikes at zero time delay, and we correct it using a phase of $\phi_{\text{deg}} = 45.5^{\text{o}}$. Using a Python script we arbitrarily rotate the phase and achieve the best phase by minimizing the residuals of a linear fit across the zero time delay. When the phase is not optimal [*gray curves* in Fig. 6.2**d**], the V_{out} signal is not continuous and the linear fitting error increases. This allows us to determine the phase offset with an accuracy of $\sim$0.1°. The V_{in} signal is also corrected using the optimal phase we find for V_{out} [Fig. 6.2**a**]. After complex rotation, the effect of changing the phase by a few degree seems smaller on V_{in} [Fig. 6.2**c**] than on V_{out} [Fig. 6.2**d**] because the V_{in} signal now shows larger variations with time delay.

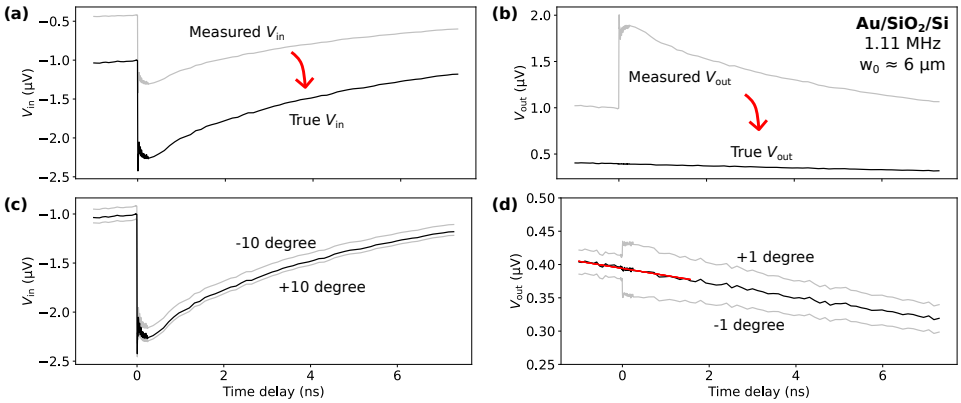

FIGURE 6.2: **Correcting for the instrumentation phase offset.** The measured **(a)** V_{in} and **(b)** V_{out} signals (*gray curves*) need to be corrected, as V_{out} is not continuous around time-zero. We correct the instrumentation phase shift by rotation in the complex plane to retrieve the true signal (*black curves*). We compare the true **(c)** V_{in} and **(d)** V_{out} signals to the signals rotated with **(c)** $\pm$10 degree (for clear visualization) and **(d)** $\pm$1 degree offset from the best phase. We find the best phase to be 45.5° by performing a linear fit across the zero time delay (*red line*) for each test phase. The red arrows indicate the signal transformation upon complex rotation. From now on, we will only deal with offset corrected signals.

6.2.2 Subtracting radiative signals at high f_{mod}

Operating a non-resonant electro-optic modulator at MHz frequencies typically requires input voltages of hundreds of volts. Experimentally, this is achieved using a voltage amplifier that amplifies the output of either a lock-in amplifier or a function generator. However, the amplifier may act as a source of electromagnetic radiation if it is not properly shielded or grounded; the BNC cables may act as antennas, picking up the radiated signals from the amplifier; and improper

grounding may create ground loops which could allow electromagnetic interference to couple into the signal path. All these factors could result in undesired signals not induced by the pump beam to affect the measured signal in the form of a background offset. These signals are unwanted in TDTR measurements, as they would affect the $-V_{\text{in}}/V_{\text{out}}$ signal ratio. Therefore, they must be avoided and/or subtracted from the measured signals. In our setup, this situation occurs, and is clearly depicted by sweeping the modulation frequency of the pump beam but not allowing it to reach the sample or photodiode, while recording and demodulating the signal using the lock-in amplifier (see Figure C.2).

Figure 6.3 shows the importance of measuring and subtracting backgrounds not induced by the pump beam in TDTR experiments. The amplitude R of the measured background signal due to radiative pick-up at high modulation frequencies needs to be subtracted from the measured signal [Fig. 6.3**a**] to obtain a ratio signal that is physical (*i.e.*, always positive). In this thesis, we always measure and subtract backgrounds when the modulation frequency is above 2 MHz (see Figure C.2). We achieve this by subtracting the measured V_{in} and V_{out} components of the background —this is, a repeated measurement after blocking the pump beam— from the actual signal. As we will measure signals from different sample regions in our measurements (see Chapter 7), we do not block the probe beam while measuring backgrounds to potentially account for reflectivity changes. Thus, the only difference between our signal and background is the presence and absence of the pump beam, respectively. The uncorrected ratio signal typically results in a negative or sign-changing signal when the background is large [Fig. 6.3**b**]. However, a small background may not be trivial to identify, and one must always verify that the transient signal is zero when any of the two beams is blocked, prior to data acquisition.

6.2.3 Laser power dependence of TDTR lock-in signals

To verify our approach for subtracting background signals, we perform measurements at a large modulation frequency of our pump beam (10 MHz). We vary the pump P_{pump} and probe P_{probe} laser powers, and use different laser spot sizes w_0. In **Figure 6.4**, we directly show the post-processed TDTR signals for clarity reasons: this is, phase offset corrected and background-subtracted signals. We notice that the V_{in} [Fig. 6.4**a**] and V_{out} [Fig. 6.4**b**] signals strongly depend on laser powers. For both, the signal magnitude increases at higher power. A higher probe power implies collecting more light at the photodiode and, therefore, a larger signal will

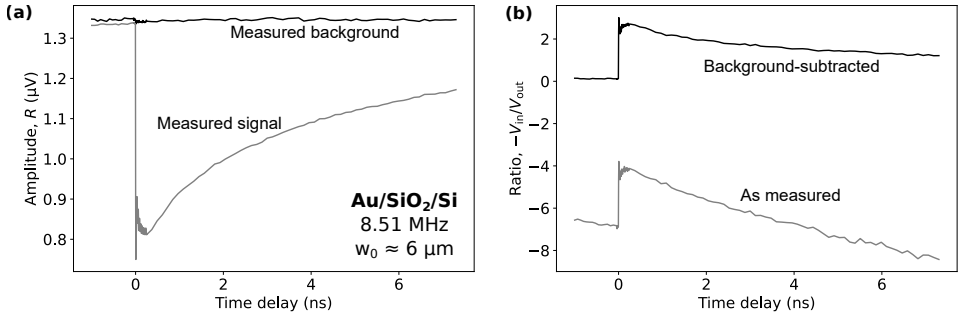

FIGURE 6.3: **Subtracting radiative signals at high frequencies. (a)** The amplitude R (*gray curve*), measured from our 50 nm gold transducer on SiO_2/Si at 8.51 MHz, contains a large background due to radiative pick-up. We measure the background (*black curve*) by repeating the measurement while blocking the pump beam. **(b)** Once we have corrected for the phase offset of the instrumentation, the ratio $-V_{in}/V_{out}$ signal will be analyzed only after background subtraction (*black curve*). If the background is large, the uncorrected signal (*gray curve*) typically produces an unphysical ratio $-V_{in}/V_{out}$ signal which is either negative or changes sign. From now on, we will only deal with background-subtracted signals whenever the modulation frequency is above 2 MHz.

be expected. The signal magnitude also increases with pump power, but the reason for a larger signal is likely an increased transient temperature at higher pump powers.

The TDTR ratio signal $-V_{in}/V_{out}$ [Fig. 6.4**c,d**] is expected to be independent on laser power, as V_{in} and V_{out} have the same dependencies on this parameter and other optical properties of the transducer layer (see Chapter 7). We confirm this picture by plotting the ratio signals [Fig. 6.4**c,d**] of the background-subtracted data we have shown in Figure 6.4**a,b**. As expected, we now see that all ratio signals align when using low [*solid lines*] and high [*dashed lines*] laser powers. This would not be the case for uncorrected signals, and the corrected ratio signals only depend on the laser spot size employed. A log-log plot of the ratio signal [Fig. 6.4**d**] shows three distinctive transport regimes: (*i*) the laser pulse excites the electrons in the transducer, which thermalize via e-e scattering and increase the lattice temperature via e-ph coupling; (*ii*) launching acoustic phonons or sound waves that resonate within the transducer film (picosecond acoustics), while building up the temperature as a result of ph-ph scattering; and eventually (*iii*) starts to decay because of of interfacial thermal (Kapitza) conductance and thermal conductance across the multilayer structure.

We have seen that to correct for the instrumentation phase shift we need to verify

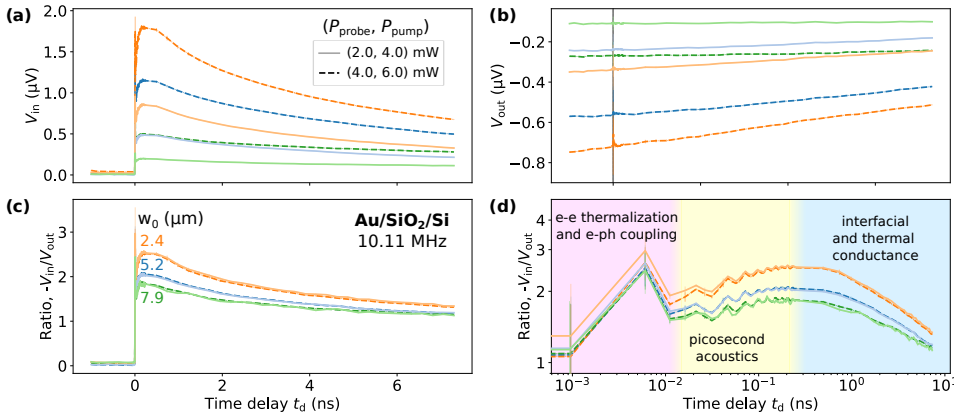

FIGURE 6.4: **Power-independent ratio signals at different spot sizes.** The post-processed **(a)** V_{in} and **(b)** V_{out} show a strong dependence on laser power, while the **(c,d)** ratio signal $-V_{in}/V_{out}$ is independent on laser power. We show data at "low" (*solid lines*) and "high" (*dashed lines*) pump P_{pump} and probe P_{probe} powers; and using three different spot sizes w_0 of 2.4 (*orange*), 5.2 (*blue*) and 7.9 μm (*green*). **(d)** Log-log plot of the ratio signal showing three distinctive transport regimes: the e-e thermalization and e-ph coupling (*pink shade*); the picosecond acoustics (*yellow shade*); and the interfacial (Kapitza) and thermal conductances (*blue shade*).

that V_{out} is smooth and continuous at $t_d = 0$. However, at high powers [*dashed lines* in Fig. 6.4] and/or small spot sizes [*orange lines* in Fig. 6.4], this is not the case and the V_{out} signal still shows a small spike after it has been phase offset corrected, potentially implying that we are starting to overheat the electron system (see Fig. 6.4**b**). This spike only lasts a few picoseconds, and does not seem to affect the linearity of the relevant time delays in TDTR, which start at a few-hundred picoseconds (see Fig. 6.4**d**). In any case, we conclude that it is better to use moderate laser powers and/or large spot sizes.

We also notice an unexpected behaviour of the ratio signals at early time delays: in the picosecond acoustics window the ratio signal increases until ∼200 ps. We attribute it to the fact that we use thin gold transducers and titanium adhesion layers, with our results strongly resembling those reported in Ref. [144]. Here, the authors explain these observations as the reheating process of the transducer layer because the heat is mainly generated at the interface, rather than at the top most surface of the transducer. We understand the picture as follows: the pump beam excites electrons in the gold layer that ballistically travel to the interface —where they scatter and launch acoustic phonons— and the interface temperature starts to increase by means of e-ph scattering and other mechanisms [144]. The acoustic

phonons reflect at the interface and start resonating within the metal transducer generating the oscillations observed in the picosecond acoustics window. At these early timescales, phononic heat has not yet diffused across the interface into the substrate via phonon-phonon scattering as this process occurs at almost an order of magnitude longer timescales of hundreds of ps ($\tau_{\text{int}} = L_{\text{int}}C/G_{\text{int}}$ [157]). This means that the thermal energy from the Ti lattice is transferred back to the relatively colder Au lattice, increasing the thermoreflectance signal, which peaks around ~200 ps. At this time (*i.e.*, the time at which phonon relaxation starts), the temperature starts decaying and we enter the TDTR regime dominated by Kapitza resistance and thermal conductance across the multilayer stack [144].

6.3 Measurements of Out-of-Plane Thermal Conductivity and Interfacial Thermal Conductance

Our cautious data post-processing routine is now complete and the data is ready to be analyzed. We begin by reducing the number of unknown parameters in our experiment [Section 6.3.1]. Next, we explore how sensitive our measurements are to the relevant parameters [Section 6.3.2]. Finally, we move on to the main TDTR measurement of this chapter, using our $Au/SiO_2/Si$ control sample, where we fit the processed data to our thermal model to determine the out-of-plane thermal conductivity $\kappa_z = \kappa_r = \kappa$ of SiO_2 and interfacial conductance G_1 between gold and SiO_2 [Section 6.3.3].

6.3.1 Reducing the number of unknown parameters in TDTR

We notice that the thermal properties of gold, silicon oxide and silicon are well-known, and most TDTR experiments take them from the literature. In our case, we want to verify that our TDTR setup is capable of measuring thermal properties of the material bellow the transducer, which in Chapter 7 will be thin flakes of MoS_2 with varying thickness. Therefore, we use our $Au/SiO_2/Si$ as control sample to measure the thermal properties of silicon oxide by fixing or determining the rest of parameters. In particular, we aim at extracting its interfacial thermal conductance G_1 with gold, and its thermal conductivity κ_{SiO_2}, to compare it with the literature values of $G_{Au/SiO_2} \approx 134 - 152$ MW m^{-2} K^{-1} [158, 159] and $\kappa_{SiO_2} \approx 1.35$ W m^{-1} K^{-1} [160].

Prior to data acquisition, we measured the laser spot sizes using the knife-edge technique, as we described in Section 4.3.2, and found that we can tune the average laser spot size w_0 in range $2-10$ µm. We now perform picosecond acoustics measurements to determine the transducer layer thickness L_{Au}, and van der Pauw measurements to extract the thermal conductivity κ_{Au} of gold. We take the remaining parameters of Au, SiO_2 and Si, and their interfaces, from the literature [160–163], leaving κ_{SiO_2} and G_{Au/SiO_2} as our only "unknown" parameters.

Determining L_{Au} from picosecond acoustics

The pulsed optical excitation of electrons in the metal transducer generates coherent longitudinal acoustic phonons (sound waves) upon e-ph scattering at the interface. These coherent acoustic phonons (CAPs) travel at the speed of sound and reflect at the metal transducer boundaries because of the large acoustic mismatch between Au and both air and SiO_2. The oscillations last hundreds of picoseconds thanks to specular rather than diffuse reflections at the interface. The picosecond acoustics technique consists in sampling these oscillations that occur in the early dynamics ($10-300$ ps) to retrieve the oscillation period T_{osc} or frequency f_{osc}. By using literature values for the sound velocity v_g of the transducer material, the extraction of its thickness L is straightforward. An acoustic phonon travels from the surface through the transducer thickness to the interface and back in one oscillation period, covering twice the thickness L_{Au} at the speed of sound v_{Au}:

$$2L_{Au} = v_{Au}\, T_{osc} = \frac{v_{Au}}{f_{osc}} \tag{6.4}$$

Figure 6.5 shows our procedure for extracting the frequency of the oscillations f_{osc} present in our ratio signals $-V_{in}/V_{out}$ [Fig. 6.5**a**]. We first subtract the baseline, which we obtain from a polynomial fit [*red line* in Fig. 6.5**a**] to isolate the oscillations [Fig. 6.5**b**]. We artificially add zeroes before and after our data to compute the Fast Fourier Transform (FFT) [Fig. 6.5**c**], and observe a peak centered at a frequency of $f_{osc} = 34.42$ GHz, which we retrieved from Lorentzian fitting the FFT data. Using Eq. 6.4 and a sound velocity of $v_{Au} = 3240$ m/s [160], we find a thickness of $L_{Au} = 47.1$ nm, which differs by less than 6% from the evaporated thickness of 50 nm. We note that the accuracy of these measurements could be greatly improved using longer acquisitions and better sampling the oscillations, at the expense of increased measurement time.

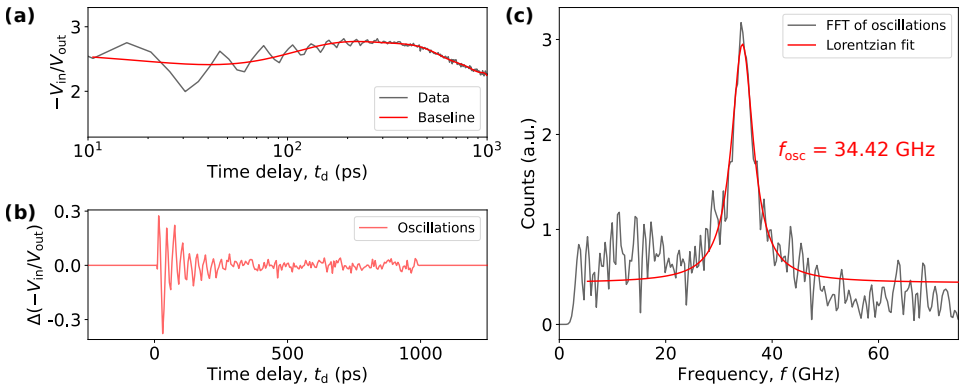

FIGURE 6.5: **Picosecond acoustics measurements of L_{Au}. (a)** The ratio signal shows oscillations from 10 to 250 ps as a result of coherent acoustic phonons resonating within the transducer film. **(b)** We subtract the baseline of the ratio signal to isolate the oscillations. **(c)** We perform FFT of the oscillations and fit the peaks with a Lorentzian function to retrieve a frequency of 34.66 GHz.

Standing wave formation in gold. Because of the smaller thickness of our transducer layer (50 nm) compared to its acoustic wavelength ($\lambda = v/f$) —which is $\lambda \approx 100$ nm using $v_{Au} = 3240$ m/s and the frequency of ~34 GHz we obtained from our ps acoustic measurements— the CAPs no longer propagate but rather form a standing wave due to the boundary conditions [95]. In this case, the resonance frequency of the observed oscillations should decrease with increasing the thickness of the transducer, which we verified with independent picosecond acoustics measurements using 100 nm gold films. This excludes them from being Brillouin oscillations from the silicon oxide underneath [164], and confirms that our setup is capable of probing resonant coherent phonons (RCPs), at least within the metal transducer layer. The RCP modes can be described from their spatial wavelength λ, which is defined by nodes or anti-nodes at each interface (see Figure 2.8). For our gold layer, the absence of an overlay implies that an anti-node is found at the top interface (*i.e.*, the atomic displacement at the surface is maximum and not restricted by another material). This leaves two possibilities for the bottom interface (G_2), either a node [Fig. 2.8**d**] or an anti-node [Fig. 2.8**e**] will be found with distinct allowed wavelengths:

$$\lambda = \frac{4L}{2m-1} \qquad \text{(node at bottom)} \tag{6.5}$$

$$\lambda = \frac{2L}{m} \qquad \text{(anti-node at bottom)} \tag{6.6}$$

where L is the thickness of the slab and m an integer representing the mode index. We immediately notice that the bottom surface of the gold film must be an anti-node to satisfy the frequency we obtain from picosecond acoustics measurements:

$$f = \frac{v}{\lambda} = \frac{(2m-1)v}{4L} \qquad \text{(node at bottom)} \tag{6.7}$$

$$f = \frac{v}{\lambda} = \frac{mv}{2L} \qquad \text{(anti-node at bottom)} \tag{6.8}$$

We will perform this same analysis to evaluate the possibility of standing wave formation in MoS_2 (see Section 7.3.2).

Determining κ_{Au} using the van der Pauw method

The van der Pauw technique is a widely used method for measuring the sheet resistance $R_\square$ (in ohms per square $\Omega/\square$) of thin, flat, and electrically conductive samples with arbitrary shape, provided the sample is uniform, and the electrical contacts are placed along the perimeter. In this method, four electrical probes contact the sample edges. By passing current through different pairs of contacts and measuring the resulting voltages across the other two —and repeating this for the different pairs— the van der Pauw technique enables accurate determination of the sheet resistance of typical metal transducer layers used in TDTR.

We use the van der Pauw technique to measure the sheet resistance $R_\square$ of our gold transducer layer. Knowing the film thickness ($L_{Au} = 47.1$ nm from picosecond acoustics measurements), we calculate its electrical conductivity σ_{Au} as

$$\sigma_{Au} = \frac{1}{R_\square \, L_{Au}} \tag{6.9}$$

To obtain the thermal conductivity κ_{Au} of our gold transducer layer, we apply the Wiedemann-Franz law [156]:

$$\kappa_{Au} = \mathcal{L}_0 \, \sigma_{Au} \, T \tag{6.10}$$

where $\mathcal{L}_0$ is the Lorenz number and T is the absolute temperature. For metals at moderate temperatures, $\mathcal{L}_0 \approx 2.44 \times 10^{-8}$ W Ω K^{-2}. With this, we find a thermal conductivity of our gold transducer of $\kappa_{Au} \approx 100$ W m^{-1} K^{-1}, which we will use as a key input parameter in our TDTR model. We note that this value is quite small as compared to the bulk gold value of $\kappa_{Au} = 318$ W m^{-1} K^{-1} [165], which we attribute to the deposition process producing producing polycrystalline films with grain sizes in the order of electron mean free paths.

Summary of thermal parameters used to model our TDTR signals

Table 6.1 shows a summary of all thermal parameters of all materials used for the modelling of lock-in signals in TDTR experimental analysis. The value of $\kappa_{Si} = 148$ W m^{-1} K^{-1} is valid for undoped silicon. We use silicon substrates that are doped, possibly implying up to ∼30% reduction in thermal conductivity [166]. We later verified that this systematic error does not alter the conclusions we draw.

TABLE 6.1: **Summary of TDTR parameters for the control samples.** Material and setup parameters relevant in our TDTR experiments using our Au/Ti(O_x)/SiO_2/Si and Au/Ti(O_x)/MoS_2/SiO_2/Si control samples. For simplicity, we omit Ti(O_x) throughout the thesis. We give their values, the source or measurement technique employed to determine them, and relevant references. All materials involved except MoS_2 are isotropic ($\eta \equiv \kappa_r/\kappa_z = 1$), so we write $\kappa_z = \kappa_r = \kappa$.

	Param.	Value	Units	Source	Reference
Au	κ_{Au}	∼100	W m^{-1} K^{-1}	Van der Pauw	This work
	C_{Au}	2.49	MJ m^{-3} K^{-1}	Literature	[163]
	L_{Au}	47.1	nm	Picosecond acoustics	This work
Au/SiO_2	G_{Au/SiO_2}	154.8 ± 67.3	MW m^{-2} K^{-1}	TDTR fit A	This work
		$134 - 152$		Literature	[158, 159]
Au/MoS_2	G_{Au/MoS_2}	34.7 ± 1.9	MW m^{-2} K^{-1}	TDTR fit B	This work
		20.8		Literature	[167]
MoS_2	κ_{z,MoS_2}	2.37 ± 0.22	W m^{-1} K^{-1}	TDTR fit B	This work
		2.50		Literature	[39]
	κ_{r,MoS_2}	90	W m^{-1} K^{-1}	Literature	[39, 59]
	C_{MoS_2}	1.99	MJ m^{-3} K^{-1}	Literature	[160]
	L_{MoS_2}	160	nm	AFM	This work
MoS_2/SiO_2	G_{MoS_2/SiO_2}	≈ 18	MW m^{-2} K^{-1}	Literature	[67, 168, 169]
SiO_2	κ_{SiO_2}	1.42 ± 0.02	W m^{-1} K^{-1}	TDTR fit A	This work
		1.35		Literature	[150]
	C_{SiO_2}	1.62	MJ m^{-3} K^{-1}	Literature	[150]
	L_{SiO_2}	285	nm	Wafer supplier	University Wafer
SiO_2/Si	$G_{SiO_2/Si}$	> 600	MW m^{-2} K^{-1}	Literature	[161, 162]
Si	κ_{Si}	148	W m^{-1} K^{-1}	Literature	[160]
	C_{Si}	1.61	MJ m^{-3} K^{-1}	Literature	[160]
	L_{Si}	400	µm	Wafer supplier	University Wafer
Setup	w_0	$2 - 10$	µm	Knife-edge	This work
	f_{mod}	$1 - 10$	MHz	Lock-in amplifier	This work

6.3.2 Sensitivity analysis

To assess the parameter dependencies of our thermal model across varying experimental configurations, we conducted a comprehensive sensitivity analysis for each sample geometry. This analysis quantifies how changes in input parameters affect the thermoreflectance signal, thereby identifying which parameters can be

reliably extracted from the TDTR data. For each control and sample configuration, we computed the partial derivatives of the model signal with respect to relevant thermal properties, normalized by the parameter value and the signal amplitude (see Section 5.3.1). We computed the sensitivities over the full range of time delays for the ratio $-V_{\text{in}}/V_{\text{out}}$ signals in all four combinations of modulation frequencies and laser spot sizes. For example, in the case of the bare substrate, the signal is most sensitive to the thermal conductivity of SiO_2, particularly at low modulation frequencies. Including a thick MoS_2 interlayer increases the sensitivity to the first interface while decreasing the sensitivity to $\kappa_{z,1}$. In Section C.2, we provide the sensitivity plots for all sample geometries and experimental configurations, as a function of time delay.

6.3.3 Fitting procedure

Several fitting procedures have been reported in the literature for TDTR experiments. These methods include fitting different lock-in signals, such as the phase ϕ, the ratio $-V_{\text{in}}/V_{\text{out}}$, or simultaneously fitting normalized in-phase V_{in} and ratio signals [39]. Other techniques involve fitting the entire complex TDTR signal $V = V_{\text{in}} + iV_{\text{out}}$ [170]; analyzing signal ratios from two different modulation frequencies R_{f_1}/R_{f_2} [151, 152]; employing microscopic transfer functions with *ab initio* inputs from the Boltzmann transport equation [171]; and utilizing iterative tandem fitting approaches [39]. Additionally, simultaneous fitting of multiple parameters [139, 150] and machine learning-based neural networks for TDTR data processing have also been explored [172].

In this thesis, we employ a global fitting approach using an objective function that minimizes the sum of squared residuals between data and model predictions. Our Python implementation fits the ratio $-V_{\text{in}}/V_{\text{out}}$ signal while monitoring the normalized the normalized V_{in} as a sanity check. Instead of a tandem fitting approach, we simultaneously optimize two parameters (like G_1 and κ_{SiO_2} in Section 6.4.1, or G_1 and κ_{z,MoS_2} in Section 6.4.2) across multiple data sets with various modulation frequencies, laser spot sizes, or both. This strategy enhances robustness by ensuring consistency across data sets, reducing uncertainty, and preventing overfitting. To systematically explore the parameter space, we use a two-step routine: a brute-force minimization over a coarse grid, followed by a Levenberg-Marquardt algorithm. The initial brute-force step scans a predefined range of parameter values, minimizing the weighted residuals to ensure an unbiased fit. The best-fit values from this step serve as initial guesses for the final least-squares minimization, with updated parameter bounds to $\pm 50\%$ of these

initial guesses. This two-step fitting procedure helps avoid convergence to local minima during parameter optimization.

6.4 Validating our TDTR Setup on Control Samples

To establish a robust experimental baseline for subsequent thermal transport measurements on few-layer MoS_2 [Chapter 7], we first examine two control samples using our TDTR setup. The first involves direct deposition of the gold transducer onto the bare SiO_2/Si substrate [Section 6.4.1], providing a reference to later evaluate the effect of introducing atomically thin MoS_2 interlayers. The second incorporates a mechanically exfoliated, bulk-like MoS_2 ($\sim$160 nm thick) flake [Section 6.4.2], dry-transferred onto the substrate prior to deposition of the transducer layer, as we described in Chapter 3. We use a thick MoS_2 as control with the aim to evaluate the thickness-dependent thermal properties of thin MoS_2 flakes. These two systems bracket the experimental extremes, from the absence of MoS_2 to a thick MoS_2 interlayer, providing a benchmark for interpreting the thermal response of the thickness-dependent TDTR measurements reported in Chapter 7. Table 6.1 summarizes the full set of TDTR parameters, including the results of our global fitting approach applied to both control systems.

6.4.1 TDTR on bare substrate

We now proceed with fitting the experimental ratio signals, for which we perform a global fit using the data sets measured at $f_{mod} = 1.11$ and 10.11 MHz, while using laser spot sizes $w_0 = 2.4$ and 7.9 μm. We simultaneously extract κ_{SiO_2} and G_{Au/SiO_2} for all experimental configurations. **Figure 6.6** shows the normalized V_{in} signals [Fig. 6.6**a**], and ratio $-V_{in}/V_{out}$ signals [Fig. 6.6**b**], together with the thermal model using best fit parameters of $\kappa_{SiO_2} = 1.42 \pm 0.02$ W m^{-1} K^{-1} and $G_{Au/SiO_2} = 154.8 \pm 67.3$ MW m^{-2} K^{-1}. Our results for κ_{SiO_2} and G_{Au/SiO_2} are in good agreement with the literature values of 1.35 W m^{-1} K^{-1} [150] and $134 - 152$ MW m^{-2} K^{-1} [158, 159], respectively. Our thermal model not only describes the experimental data from 0.5 to 7.3 ns, but also the data at negative time delays, where the probe evaluates the effect of the previous pump pulse at an effective time delay of $\sim$13 ns. This data is typically not used in TDTR fitting or shown at all in the literature.

The normalized V_{in} signals, in spite not being in perfect agreement, follow the same trends as the experimental data (see Fig. 6.6**a**). The in-phase signals are

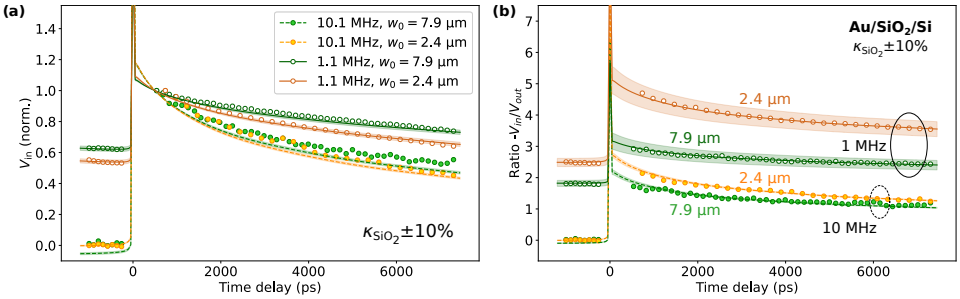

FIGURE 6.6: **Global fitting of TDTR data for Au/SiO_2/Si.** Experimental (*scatters*) and fitted (*lines*) **(a)** in-phase V_{in} signals, normalized at $t_d = 0.5$ ns, and **(b)** ratio $-V_{in}/V_{out}$ signals. The experimental data and model are shown at 1.1 (*empty scatters* and *solid lines*) and 10.1 MHz (*solid scatters* and *dashed lines*), using laser spot sizes of 2.4 (*orange*) and 7.9 µm (*green*). The global fit uses the parameters shown in Table 6.1 for all data sets. The shaded regions correspond to the confidence intervals of $\kappa_{SiO_2} \pm 10\%$.

mostly affected by the heat capacities of the gold and SiO_2 layers, which we fixed in our model and are the main cause for discrepancies. We plot a confidence interval for κ_{SiO_2} by recomputing the model with ±10% of its best fit value [*shaded areas* in Fig. 6.6]. We observe that our thermal model at low modulation frequency is significantly more affected by κ_{SiO_2}, and we confirmed with our sensitivity analysis that this is the most sensitive of all parameters in this experimental configuration (see Figure C.3). The two data sets at small and large spot sizes add robustness and reliability, because the sensitivity of the ratio signal to spot size variations is greatly reduced when using large spot sizes. The data sets at high modulation frequencies are more strongly affected by the interfacial thermal conductance G_{Au/SiO_2}, and allow us to extract a 95% confidence interval from the fitting of ∼56%. We note that this error is quite large, and the reason is that the sensitivity to this parameter dramatically decreases when the parameter magnitude increases: the overall thermal transport becomes dominated by the resistive oxide underneath.

Our TDTR measurements on the bare SiO_2/Si substrate reveal that we have sensitivity —to some extent— to the interfacial thermal conductance of the first interface $G_1 = G_{Au/SiO_2}$. Interestingly, our sensitivity would increase for smaller values of G_1 (see Figure C.4). We expect that, upon introducing few-layer MoS_2 flakes at the interface, the effective interfacial conductance will be reduced, potentially increasing our sensitivity to this parameter. This is, by decoupling the

transducer from the substrate given the van der Waals nature of the 2D flake interactions with both transducer and substrate. However, this might not be necessarily the case for atomically thin MoS_2, as it has been shown to produce less resistive thermal transport across interfaces as compared to thicker flakes [37].

6.4.2 TDTR on thick MoS_2 interlayers

We now proceed with our second control experiment, using a thick MoS_2 flake ($L_{MoS_2} \approx 160$ nm, which we transferred on SiO_2/Si with the procedures described in Chapter 3. For these TDTR measurements, we use modulation frequencies of $f_{mod} = 1.11$ and 8.51 MHz and laser spot sizes of $w_0 = 2.1$ and 4.5 µm. After fixing all parameters for Au, SiO_2 and Si, we now have a total of four unknowns: the interfacial conductances $G_1 = G_{Au/MoS_2}$ and $G_2 = G_{MoS_2/SiO_2}$, and the in-plane κ_{r,MoS_2} and out-of-plane κ_{z,MoS_2} thermal conductivities of MoS_2. As the aim of this work is to study few-layer 2D flakes, we will be mainly dominated by the out-of-plane thermal properties of our flakes. Therefore, in our model we fix the in-plane thermal conductivity of MoS_2 to its literature value of $\kappa_{r,MoS_2} = 90$ W m^{-1} K^{-1} [39, 59]. Also, the interface between 2D materials and SiO_2, particularly for MoS_2, have been well characterized both experimentally [67, 168] and theoretically [169], with values in range $10 - 25$ MW m^{-2} K^{-1}. Thus, we fix this parameter to $G_{MoS_2/SiO_2} = 18$ MW m^{-2} K^{-1}, and proceed to simultaneously extract G_{Au/MoS_2} and κ_{z,MoS_2} by performing a global fit on all the experimental data sets.

In **Figure 6.7** we show our results comparing the experimental data of our thick MoS_2 flake to our thermal model using the best fit parameters. We obtain interfacial and thermal conductivities of $G_{Au/MoS_2} = 34.7 \pm 1.9$ MW m^{-2} K^{-1} and $\kappa_{z,MoS_2} = 2.37 \pm 0.22$ W m^{-1} K^{-1}, respectively. The fitting convergence clearly depicts a properly explored parameter space, with the two variables contributing in the minimization process (see Figure C.6). We note that the value of our interfacial thermal conductance is larger than the one reported for Au/MoS_2 of 20.8 MW m^{-2} K^{-1}, while Au/Ti/MoS_2 interfaces exhibit interfacial thermal conductances of 21.5 MW m^{-2} K^{-1}, only marginally larger than Au/MoS_2 interfaces [167]. Our gold transducers do include a 2 nm titanium adhesion layer and —while this is not ideal because elemental Ti has been shown to react with MoS_2 during deposition [173]— we will later study the influence of this adhesion layer in our measurements (see Section 7.5). Nevertheless, our interfacial conductance value of $G_{Au/MoS_2} = 34.7 \pm 1.9$ MW m^{-2} K^{-1} shows a much smaller error than the one we obtained for the thermal conductance of the Au/SiO_2 interface (see

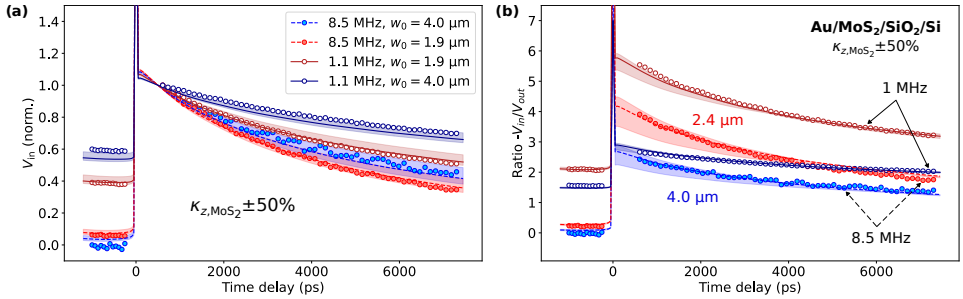

FIGURE 6.7: **Global fitting of TDTR data for Au/SiO_2/Si.** Measured (*scatters*) and fitted (*lines*) **(a)** in-phase V_{in} signals, normalized at a time delay of $t_{\text{d}} = 0.5$ ns, and **(b)** ratio $-V_{\text{in}}/V_{\text{out}}$ signals. The experimental data and model are shown at 1.1 (*empty scatters* and *solid lines*) and 8.5 MHz (*solid scatters* and *dashed lines*), using laser spot sizes of 1.9 (*red*) and 4.0 µm (*blue*). The global fit uses the parameters shown in Table 6.1 for all data sets. The shaded regions correspond to the confidence intervals of $\kappa_{z,\text{MoS}_2} \pm 50\%$.

Table 6.1). We attribute the smaller error to the increased sensitivity to this parameter in this sample geometry, mainly because $G_{\text{Au/MoS}_2}$ is much smaller than $G_{\text{Au/SiO}_2}$.

We observe that the fits are not perfect, but we have only varied G_1 and $\kappa_{z,1}$ —after adjusting the laser spot sizes to their values used for these measurements— while fixing the rest of parameters. Particularly, the data at large modulation frequency and small spot size significantly deviates from our model at long time delays. However, the sensitivity of all ratio signals to both G_1 and $\kappa_{z,1}$ is quite small at long delays as evidenced by the ±50% confidence interval for κ_{z,MoS_2}, depicted as shaded areas in Fig. 6.7 (also, see Section C.2). The fitting quality could be greatly improved by varying other parameters of the transducer layer and substrate. We note that the sensitivity of the ratio signals to κ_{r,MoS_2} and $G_2 = G_{\text{MoS}_2/\text{SiO}_2}$ are very small and, thus, do not affect our determination of $G_1 = G_{\text{Au/MoS}_2}$ or κ_{z,MoS_2}. The out-of-plane thermal conductivity we obtain for thick MoS_2 is in good agreement with the thickness-dependent experimental κ_z of MoS_2 reported in Ref. [39], where the authors use a different metal transducer and different oxide thickness on their substrates. We, thus, conclude that our TDTR setup enables probing the thermal properties of 2D material interlayers present between our gold transducer and substrate, using the analysis workflow reported in this chapter.

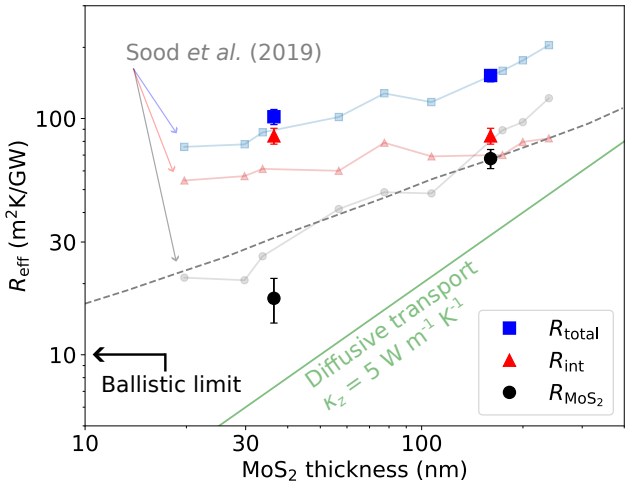

FIGURE 6.8: **Interfacial thermal resistance across thick MoS_2 interlayers.** Out-of-plane thermal resistance of MoS_2 films R_{MoS_2} (*black circles*), combined thermal resistance of G_1 and G_2 interfaces (*red triangles*), and total thermal resistance $R_{total} = R_{MoS_2} + R_{int}$ (*blue squares*). The semi-transparent data sets are the experimental results from Ref. [39], the dashed line their calculations of quasi-ballistic transport, with the ballistic limit at $R \approx 10$ m^2 K GW^{-1}. The solid green line corresponds to the resistance provided by purely diffusive transport with a constant thermal conductivity of $\kappa_z = 5$ W m^{-1} K^{-1}.

6.4.3 Extracting total and interfacial thermal resistances

To further validate the thermal properties we extracted from our thick MoS_2 sample, we compare our results to those reported in Ref. [39]. For this, we plot the interfacial resistance $R_{int} = 1/G_1 + 1/G_2$, the out-of-plane thermal resistance of our MoS_2 interlayers $R_{MoS_2} = L_{MoS_2}/\kappa_{z,MoS_2}$, and the total (effective) thermal resistance $R_{total} = R_{int} + R_{MoS_2}$ (see **Figure 6.8**). We included the measurements of a second, relatively thick (∼36.4 nm), MoS_2 interlayer sample showing similar results in reasonable agreement with the results reported in Ref. [39].

We note that, in our case, the interfacial resistance R_{int} corresponds to the contribution of Au/MoS_2 (G_1) and MoS_2/SiO_2 (G_2) interfaces, while the data from Ref. [39] was obtained using an aluminum transducer thus uses a different G_1. In any case, the trend is clear: the contribution from R_{MoS_2} to the total resistance decreases for thinner MoS_2 flakes, implying that heat transport in thin MoS_2 is dominated by the interfaces rather than by diffusive transport within the TMD itself. Because of quasi-ballistic transport across the film thickness, R_{MoS_2} saturates at a finite value of ∼10 m^2 K GW^{-1} in the limit of $2-3$ layers. In the absence of

quasi-ballistic effects (*i.e.*, in the purely diffusive regime), R_{MoS_2} would have been much smaller and become vanishingly small at the monolayer limit [*green solid line* in Fig. 6.8]. Potentially, this also implies that we could use an effective thermal resistance (conductance) to describe thermal transport across the few-layer MoS_2 flakes studied in Chapter 7 (all of them thinner than 10 nm), without the need to simulate anisotropic heat transport within the TMD itself further reducing the number of unknown parameters in our system.

6.5 Summary and Outlook

In this chapter we have detailed a complete analysis of TDTR data, including all the considerations we need to follow before we proceed with extracting the properties of interest from our sample. We have first measured the laser spot sizes using the knife-edge technique. Then, we measured the thickness of the transducer layer using picosecond acoustics, and its thermal conductivity using electrical van der Pauw measurements. With this, we have reduced the number of unknowns to G_{Au/SiO_2} and κ_{SiO_2} for our first control sample using a bare substrate; and to G_{Au/MoS_2} and κ_{z,MoS_2} for our second control sample using a thick MoS_2 flake dry-transferred onto the bare substrate.

After performing sensitivity analyses in all our experimental configurations for both control samples, we understood which parameters have a stronger influence on the measured ratio signals. On the one hand, we verified that our sensitivity to G_1 is quite low when its magnitude is large and the material underneath is poorly conductive, as in $Au/SiO_2/Si$. Our sensitivity to this parameter significantly increased in $Au/MoS_2/SiO_2/Si$ due to the reduced interfacial conductance of the Au/MoS_2 interface. On the other hand, we found that the ratio signals are quite sensitivity to the thermal conductivities of SiO_2 and MoS_2 in the out-of-plane direction, enabling their extraction with confidence.

Finally, we have shown exemplary TDTR measurements on both our control samples and performed global fitting across multiple data sets. Our obtained parameter set captures all experimental configurations simultaneously, adding robustness and consistency. Our results closely match literature values, except for G_{Au/MoS_2}, which is slightly larger than expected. Nevertheless, this shows that our setup is capable of measuring thermal properties of the material immediately below the transducer layer confidently. With these methods, we have created a reproducible workflow for TDTR data analysis. This workflow will also serve as the foundation for the TDTR measurements reported in Chapter 7, where we use few-layer

MoS_2 flakes dry-transferred onto standard SiO_2/Si substrates, aimed at studying coherent phonon heat transport across MoS_2.

Contributions

I assisted Dr. Bohai Liu with the fabrication of supported MoS_2 samples. I performed the pre-characterization and TDTR measurements with help from Dr. Bohai Liu. I wrote the Python scripts and performed the data analysis.

Chapter 7

Thermoreflectance of Thermally Thin MoS_2

This chapter is based on works in preparation:

D. Saleta Reig, B. Liu, et al., "On-demand suppression of transient thermoreflectance in gold superstrates via few-layer interfacial MoS_2", *In preparation* (2025).

B. Liu,‡ **D. Saleta Reig**,‡ et al., "Ultrafast thermalization dynamics of gold superstrates using adhesion layers and interfacial MoS_2", *In preparation* (2025).

‡*Equally contributing authors*

In this chapter, I present our experimental investigation of out-of-plane heat transport across the few-layer MoS_2 flakes supported on SiO_2/Si substrates we fabricated in Chapter 3. I discuss the effects of flake thickness on the effective interfacial thermal resistance exhibited by our MoS_2 flakes at room temperature. I then explore the possibility of coherent phonon heat and phonon interference effects to occur within our MoS_2 flakes using temperature-dependent time-domain thermoreflectance experiments.

7.1 Introduction

Heat conduction in solids is often dominated by incoherent, diffusive transport, where phonon phase information is quickly lost through scattering. However, under certain conditions, heat-carrying phonons can maintain phase coherence, enabling new ways to control thermal flow through effects like phonon bandgaps, localization, or soliton formation. Two-dimensional van der Waals (vdW) and their superlattices (SLs) offer an unprecedented platform for exploring such coherent phonon heat transport, thanks to their atomically sharp interfaces, tunable stacking configurations, and lack of lattice-matching constraints. Only a single theoretical work [45] has predicted similar coherent-to-incoherent transport crossovers in vdW-SLs, very similar to those reported for conventional SLs (see Fig. 2.5). An experimental work claimed that incoherent phonon transport dominates heat conduction in vdW SLs [47]. Nevertheless, clear experimental demonstrations remain scarce, as most studies are hindered by interface disorder or by limited control over layer thickness [46, 47]. To the best of our knowledge, this chapter constitutes only the second experimental investigation of coherent phonon heat transport and interference in 2D van der Waals materials, placing our work at the forefront of research in this emerging field.

Systematic fabrication of vdW-SLs made of single-crystalline, high-quality mechanically exfoliated 2D flakes represents an enormous, challenging task. This would require the use of tens to hundreds of flakes with the same thickness, stack them without introducing residues or defects, and preferably with twist-angle control. The SLs assembly process would result in an ever decreasing overlapping area of interest, limited by the flake with smallest lateral dimension and the relative orientation with the rest of flakes. Using synthetic films and subsequent stacking would simplify the process at the expense of compromised material quality and increased interfacial disorder. Leaving the only feasible option the direct growth of high-quality vdW-SLs, which is an active field of research as these structures are also interesting for optical applications.

However, our hypothesis is that experimental evidence of coherent phonon heat transport might be observable using a single 2D vdW material, without the need to fabricate complex superlattice-like samples. By changing the material thickness across a wide range of thicknesses, coherent phonon heat interference effects should manifest as resonances and/or as departures from classical behavior as heat transport transitions from coherent to incoherent. For this purpose, it is important to ensure clean and atomically sharp interfaces to facilitate specular rather

than diffuse phonon scattering, while using reproducible fabrication techniques. As a strategy to mitigate these challenges, we use only three mechanically exfoliated terraced-like MoS_2 flakes —that is, flakes containing adjacent regions of different thicknesses within a small area of $\sim$100 μm— to cover the thickness range between 1L and 12L, and study a few additional thicker flakes. The aim of using terraced-like flakes is to study thickness dependencies within a single or few flakes, thus minimizing sample-to-sample variability, and eliminating uncertainties arising from differences in sample preparation or experimental conditions.

In this chapter, we use time-domain thermoreflectance to investigate coherent phonon heat transport across our thickness-controlled MoS_2 flakes. We use a varying effective interfacial thermal conductance G_{eff} in our thermal model (see Chapter 5) to describe the effects of introducing thin MoS_2 flakes at the transducer/substrate interface. We then analyze the TDTR signal magnitudes as in an analogous Fabry-Pérot optical cavity, and perform temperature-dependent TDTR measurements to gain insights into the wave nature of the optothermal response. Additionally, we explore the possibility of optical (and optothermal) effects to affect our TDTR signals and, therefore, our conclusions. Finally, we analyze the early dynamics of our signals to gain understanding of how the MoS_2 flakes affect the heat generation mechanisms in our experiment.

Several works have studied the thermal properties of MoS_2 flakes with systematic thickness variations. However, most works covered either the thick (>20 nm) or the thin (>5L) range of thickness. The intermediate thickness range is only covered by an experimental work using stacked MOCVD-grown polycrystalline randomly-oriented MoS_2 ($rMoS_2$), and therefore includes stacking disorder [49]. We will benchmark our results to those reported in Ref. [39], which used TDTR on exfoliated MoS_2 flakes ranging between 20 and 200 nm. Here, the authors show both a quasi-ballistic transport in the entire studied thickness range —mainly due to very large phonon mean free paths in the cross-plane direction— and a monotonous increase in out-of-plane thermal conductivity with flake thickness. Another work systematically varied the MoS_2 flake thickness in the few-layer range, and reported an enhanced interfacial conductance only for mono- and bilayer MoS_2 using frequency-domain thermoreflectance (FDTR) [37]. Importantly, none of these works using single-crystalline MoS_2 experimentally studied the effects of absolute temperature in the out-of-plane heat transport across these materials [37, 39].

7.2 Thermoreflectance of MoS_2 at Room Temperature

We perform thickness-dependent TDTR measurements using our terraced-like MoS_2 flakes covering the thickness range between 1L and 12L, while using a spot size of $w_0 \approx 2.2$ μm. We use this spot size for a few reasons, the main one being the finite size of our homogeneous thickness regions of ∼10 μm. We have seen that, in these conditions, our sensitivity to the interfacial conductance of the transducer/substrate interface (G_1) significantly increases for smaller values of G_1 (see Figure C.4). Our experimental ratio $-V_{in}/V_{out}$ signals confirm our expectations, showing a strong resemblance to the traces we simulate for changing values of $G_1 \equiv G_{eff}$ in our model using a $Au/SiO_2/Si$ sample geometry (see **Figure C.9**). We observe the same trend independent of the modulation frequency of the pump beam. This means that introducing few-layer MoS_2 flakes between the transducer and substrate results in a more resistive interfacial thermal transport with increasing flake thickness. From now on, we focus on the 1.11 MHz data, as we obtain a better signal-to-noise ratio and do not need to perform background subtraction to our signals (see Section 6.2.2).

7.2.1 Effective interfacial thermal resistance

We thus proceed with fitting our experimental ratio signals by fixing the parameters we previously extracted for $Au/SiO_2/Si$ (*i.e.*, those reported in Table 6.1 not involving MoS_2) while varying $G_1 \equiv G_{eff}$. **Figure 7.1** shows log-log plots of the in-phase V_{in} signals normalized to 500 ps [Fig. 7.1**a**] and ratio $-V_{in}/V_{out}$ signals [Fig. 7.1**b**] from 500 ps to 7.5 ns. For simplicity, we fix the spot size to a value of $w_0 = 2.2$ μm as we obtained all data sets using the best focusing conditions of our setup, even if measured in different days. The experimental trend observed with flake thickness is well-captured by our best fit values of G_{eff} increasing from 2 MW m^{-2} K^{-1} for 9L towards ∼60 MW m^{-2} K^{-1} for monolayer MoS_2 flakes. The values obtained for monolayer MoS_2 are in very good agreement with the G_{eff} obtained in Ref. [37] using FDTR. The results obtained for 11L and 12L suggest extremely low values of $G_{eff} \approx 1$ MW m^{-2} K^{-1} if we would evaluate their ratio signal magnitude at long time delays >4 ns. We show the individual TDTR fits for each thickness as compared to the bare substrate data in **Figures C.10** and **C.11**, with exception of 3L and $10-12$L MoS_2 which we will discuss in the following sections.

Figure 7.2 shows our best fit results for the total resistance $R_{Total} \equiv 1/G_{eff}$ across the interface. As in Section 6.4.3, this is the total resistance R_{Total} introduced by

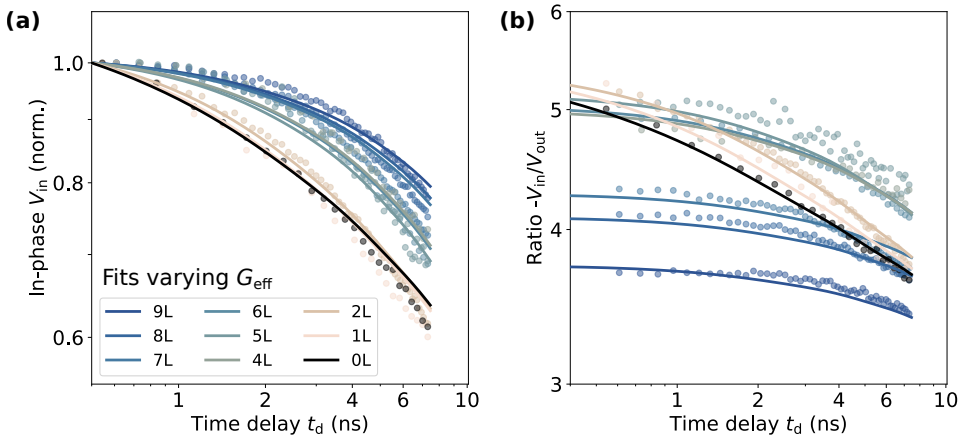

FIGURE 7.1: **Log-log plots of fitted TDTR signals for few-layer MoS_2.** Experimental (*scatters*) and simulated (*lines*) **(a)** normalized in-phase V_{in} and **(b)** Ratio $-V_{in}/V_{out}$ signals. The in-phase signals show an increasingly slow decay and the best fit values of G_{eff} decrease with increasing flake thickness.

both the interfacial resistance ($R_{int} = 1/G_1 + 1/G_2$, with contributions from the two interfaces $G_1 \equiv G_{Au/MoS_2}$ and $G_2 \equiv G_{MoS_2/SiO_2}$), and the resistance provided by heat conduction within the flake ($R_{MoS_2} = L/\kappa_z$). We also show the R_{Total} we extracted using our complete model (*i.e.*, including anisotropic heat transport within MoS_2) for the thick flakes (see Section 6.4.2). The black dashed line represents the quasi-ballistic transport calculated for MoS_2 in Ref. [39], reaching a finite resistance value of $R_{MoS_2} \approx 10$ MW m^{-2} K^{-1} at the limit of $2-3$ layers. Our results for few-layer MoS_2 flakes quantitatively agree with those from Ref. [37], and on thicker flakes with those from Ref. [39]. However, at intermediate thicknesses of $7-12$L we observe an increased resistance, significantly larger than expected based on the trends found in the literature. This resistance is larger than those reported for randomly-oriented rMoS_2 flakes including stacking disorder [49]. This is remarkable considering our superior crystal quality, which preserves the 2H-stacking order and pristine internal vdW gaps of the exfoliated bulk crystal.

A potential scenario is that mono- and bilayer flakes are too thin to manipulate the flow of heat, such that ballistic transport dominates and the overall resistance is mainly governed by the interfaces. For thick flakes (>10 nm), classical behavior also seems to dominate, with size effects showing a quasi-ballistic picture of heat transport. In this case, the flakes are thicker than the phonon wavelength and incoherent phonons behave like particles scattering at the system boundaries

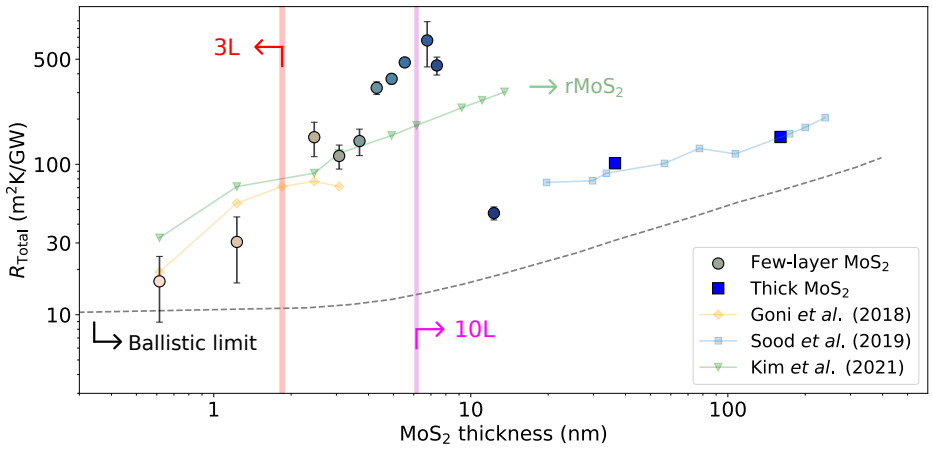

FIGURE 7.2: **Total thermal resistance across few-layer MoS_2 flakes.** Fitting results of G_{eff} converted into a $R_{\text{Total}} = 1/G_{\text{eff}}$ for few-layer MoS_2 (*circles*) and those we obtained in Section 6.4.2 from κ_z and $G_{\text{Au/MoS}_2}$ using thick MoS_2 interlayers (*squares*), as compared to the results from Ref. [39] (*shaded blue squares*), Ref. [37] (*shaded yellow diamonds*), and Ref. [49] (*shaded green triangles*).

(*i.e.*, at both interfaces), because of the large mean free paths in the cross-plane direction [39]. Nevertheless, flakes with intermediate thicknesses in the range of phonon wavelengths (*i.e.*, a few nanometers) seem to manipulate the flow of heat, creating a significant increase in thermal resistance. This unexpected behavior departing from classical expectations could originate from the contribution of coherent phonon heat conduction in these systems. Their atomically sharp interfaces, favoring specular phonon reflection, could facilitate phonon standing wave formation and/or phonon interference effects, potentially creating phonon bandgaps which forbid certain phonons responsible for heat conduction.

7.2.2 Breakdown of diffusive heat transport

In **Figure 7.3**, we show our ratio signals at 1.11 MHz, now including the 3L and $10-12$L data sets. Interestingly, both 3L and 10L exhibit a much faster decay in the TDTR window than any other measurement, with the 10L data also showing a significantly larger ratio signal magnitude. We attribute these deviations from the expected behaviour to the small magnitude of the in- and out-of-phase TDTR signals at these specific thickness values, potentially caused by phonon heat interference. The extremely fast decays observed in 3L and 10L MoS_2 cannot be

reproduced by our diffusive thermal model even if we use extremely large effective interfacial conductances G_{eff}. For 11L and 12L, the ratio signals keep slowly increasing with time delay up to several nanoseconds, also preventing us from applying our thermal model to interpret these experimental data sets (see Fig. C.9).

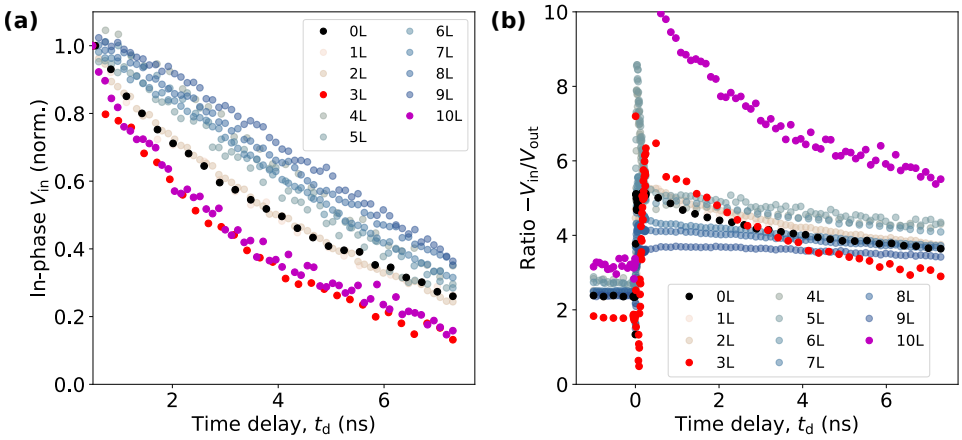

FIGURE 7.3: **Fast decaying ratio signals for 3L and 10L MoS_2.** (a) In-phase V_{in} signal normalized at 500 ps, and **(b)** ratio $-V_{in}/V_{out}$ signals, now including the 3L (*red*) and 10L (*magenta*) data sets. The small in- and out-of-phase signal magnitudes obtained at these specific MoS_2 thicknesses result in fast decaying ratio signals deviating from the expected diffusive behavior.

7.2.3 Thermoreflectance imaging with single-layer resolution

To understand our observations until now we perform optical, reflectivity and thermoreflectance imaging on our flakes, which we summarize in **Figure 7.4**. We had transferred these flakes on ∼1 cm^2 SiO_2/Si substrates and later coated with a 50 nm gold transducer (including a 2 nm titanium adhesion layer), according to the procedures described in Chapter 3. Optical images of our terraced-like flakes prior to the deposition of the gold transducer layer [Fig. 7.4**a**] show well-defined thickness regions ranging from 2L to 12L. We use two other similar terraces to cover the entire range between 1L and 12L, which we show in **Figure C.7**. After the gold transducer has been deposited, the optical contrast decreases and, thus, our ability to distinguish different flake regions. Using the white light imaging system of our setup (see Chapter 4), we can only see the contours of the regions of the flake thicker than ∼10L. To overcome this challenge, we perform both reflectivity (only in this case we chop our probe beam at few hundred Hz) and thermoreflectance imaging (*i.e.*, also using our MHz modulated pump at a fixed time

delay).

We normalize the reflectivity map to the substrate's value and plot the differential substrate-subtracted reflectivity [Fig. 7.4**b**]. We observe a monotonous increase in probe reflectivity with flake thickness, with a very subtle effect for flakes under 5L. This is not the case for the thermoreflectance map of the in-phase V_{in} signal normalized to the substrate's value [Fig. 7.4**c**]. To our surprise, we notice a strongly non-monotonous behaviour of the V_{in} signal magnitude with flake thickness (we observe the same trend for V_{out}). This provides us with an extremely high accuracy at identifying the sample regions and a clear visualization of their imperfections and defects (see **Figure C.8**). Interestingly, the TDTR signal changes sign for 3L, 4L and 5L thicknesses, with the 3L region barely showing any TDTR signal. From our additional samples, we notice that this sign change extends until 9L, with 9L MoS_2 also showing decreased signal magnitude (see Figure C.7).

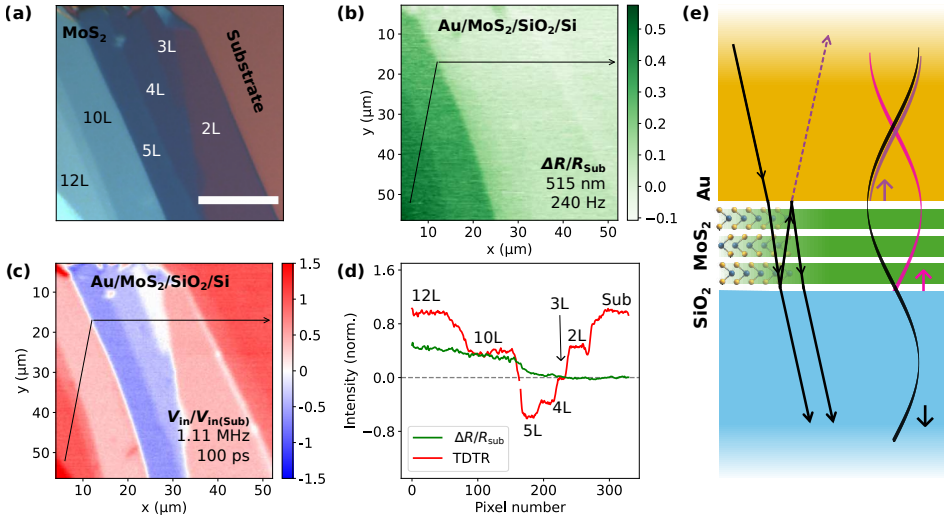

FIGURE 7.4: **Reflectance and thermoreflectance of few-layer MoS_2.** **(a)** Optical image prior to transducer's deposition, with a 20 μm scale bar. **(b)** Probe differential reflectance $\Delta R = R - R_{\text{Sub}}$ map normalized to the substrate reflectance $\Delta R/R_{\text{Sub}}$. **(d)** TDTR map (normalized V_{in}) at 100 ps and 1.11 MHz. **(d)** Intensity profiles along the black arrows of panels (c) and (d). **(e)** Schematic representation of enhanced phonon transmission in 3L MoS_2 due destructive interference in the backward direction as its thickness of 1.85 nm coincides with the quarter-wavelength of the acoustic phonon waves.

We plot the intensity profiles along the black arrows drawn in Fig. 7.4**b,c** for comparison [Fig. 7.4**d**], and conclude that such non-monotonous effect of flake thickness on the TDTR signal magnitude cannot be solely explained by a monotonous increase in reflectivity. With the probe beam blocked, the photodiode monitoring it detects no signal originating from the pump beam, as two stacked colour filters prevent pump light from reaching the detector. This means that our observations could be caused by heat-related effects. A potential scenario could be that —at a specific thickness of 3L and ∼9L— phonon interference occurs, where destructive interference in the backward direction enhances phonon transmission into the substrate. Figure 7.4**e** schematically depicts this process, potentially illustrating the role of coherent phonons in phonon transport across TMD flakes.

7.3 Assessing Coherent Phonon Interference Effects

To evaluate the role of coherent phonon interference in out-of-plane heat transport across our MoS_2 flakes, we analyze the magnitude of the in-phase V_{in} and out-of-phase V_{out} TDTR signals, which we plot in **Figure 7.5**. We observe a decreasing signal until 3L MoS_2, with $4-8$L showing V_{in} [Fig. 7.5**a**] and V_{out} [Fig. 7.5**b**] signals with opposite sign. As we have seen in Figure 7.4, the signals again change sign for thicker flakes. We tentatively ascribe this oscillatory behavior of the signal magnitude with flake thickness to coherent phonon interference, as in a phonon cavity formed along the stacking direction within the MoS_2 flake. The loss of thermoreflectance signal observed at specific thickness values would thus correspond to resonances (interferences) occurring at specific phonon cavity lengths (or flake thicknesses) close to the $1/4$ and $3/4$ phonon wavelengths λ.

For our analysis, we normalize the absolute values of our TDTR signals for all thicknesses to the substrate signal magnitude. We do this at every time delay, such that the normalized substrate data becomes 1, independent of the time delay; and the normalized MoS_2 data shows constant values of V_{in} and $_{out}$ with a thickness-dependent reduction with respect to the bare substrate. We mask the $0-4$ ns time delays, where the in-phase V_{in} signals show stronger variations with time delay. The V_{out} signals should contain information about the delayed thermal response as a result of continuous modulated heating, while the V_{in} signal reports on the heat dissipation due to the pulsed heating. Therefore, we stick to the V_{out} signals, although both signals exhibit the same trends with flake thickness and should not affect our conclusions. Potentially, this could also mean that this effect does

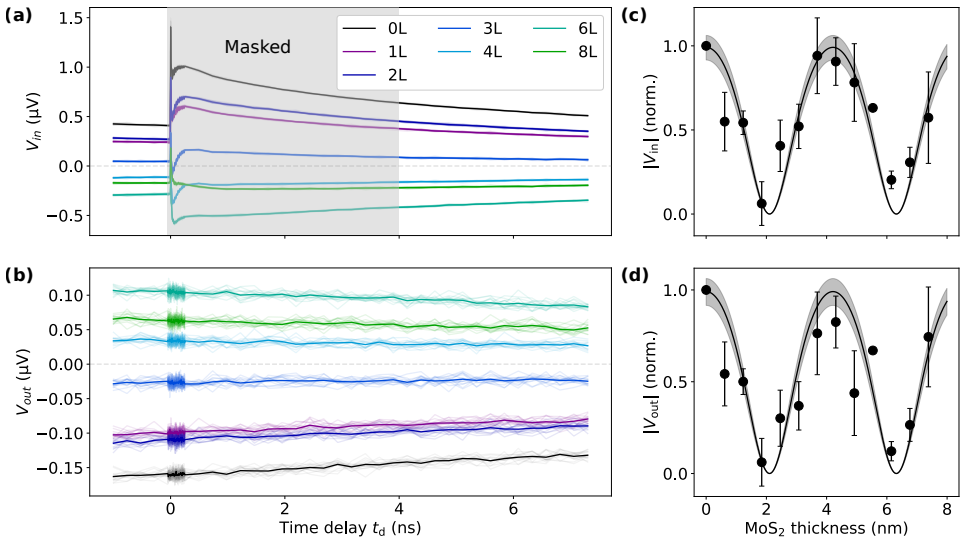

FIGURE 7.5: **Thermoreflectance signal magnitude at room temperature.** **(a)** In-phase V_{in} and **(b)** out-of-phase V_{out} signals for few-layer MoS_2 flakes obtained at room temperature on a single terraced-flake. We mask the $0-4$ ns time delays, and take the absolute values of the **(c)** in-phase and **(d)** out-of-phase signals, normalized to bare substrate signal. The errorbars come from the averaging across multiple TDTR measurements on different samples. The introduction of few-layer MoS_2 flakes underneath the transducer results in the loss of thermoreflectance signal at around 3L and 10L MoS_2. The early dynamics, within the picosecond acoustics window, will be discussed in Section 7.5.

not strongly affect our ratio $-V_{\text{in}}/V_{\text{out}}$ signals, adding confidence to the effective interfacial thermal resistances we obtained in Section 7.2.

By looking at the absolute signal magnitudes [Fig. 7.5**c,d**], we are essentially monitoring the thermoreflectance signal level as we vary our MoS_2 phonon cavity length. This would be somehow equivalent to monitoring the reflectance in an analogous optical Fabry-Pérot cavity. Here, we observe two clear resonances for thicknesses of 3L and ∼10L, at which both the V_{in} and V_{out} signal magnitudes are minimum. We thus proceed with fitting these resonances in the reflectivity of our phonon cavity R_{cavity} using an Airy function to extract the phonon wavelength λ and finesse $\mathfrak{F}$ of the cavity:

$$\begin{aligned} R_{\text{cavity}} &\propto 1 - T_{\text{cavity}} \\ R_{\text{cavity}} &\propto 1 - \frac{1}{1 + \left(\frac{4\mathfrak{F}^2}{\pi^2}\right)\left[\sin^2\left(2\pi\frac{L}{\lambda} + \phi\right)\right]} \end{aligned} \tag{7.1}$$

with T_{cavity} the phonon transmission, and $\phi = \pi/2$ the phase shift introduced upon reflection. Our fitting of the data shown in Fig. 7.5**c,d** using Eq. 7.1 yields a wavelength of $\lambda = 8.42$ nm and a finesse of $\mathfrak{F} \approx 1.5$. The finesse $\mathfrak{F}$ is defined as the ratio between the free spectral range (*i.e.*, the separation between resonances) and the full-width at half maximum (FWHM) of the resonance. Such small values of finesse indicate a leaky cavity, expected for a phonon cavity, as phonon scattering at both interfaces would significantly contribute to their cooling ability.

Simply using the obtained wavelength and the bulk longitudinal sound velocity of $v_{MoS_2,\perp} = 3170$ m/s [174] we obtain a frequency $f = v/\lambda$ of 0.38 THz, which is a reasonable number for the expected range of frequencies for phonon modes contributing to heat transport in the out-of-plane direction. Our results fall within the frequency range reported for longitudinal acoustic modes of $0 - 2$ THz using molecular dynamics [49]. These are also similar to the frequencies reported for the interlayer breathing modes of few-layer $MoSe_2$ [175]. The key aspect of our experiments is that we observe signatures of coherent phonon interference while probing broadband lattice heat involving multiple phonon modes.

7.3.1 Tuning the phonon wavelength with temperature

We now proceed with temperature-dependent TDTR measurements, which we summarize in **Figure 7.6**. We take advantage of our cryostat with optical access to perform TDTR measurements from 120 K up to 300 K, with steps of 30 K. At each temperature, we allow the sample to thermalize for 30 min prior to data acquisition. Before we start collecting traces as a function of time delay, we perform TDTR imaging to correct for potential drifts during the warming process. Once again, the TDTR maps clearly show the regions of our flake with different thicknesses, with no sign of inhomogeneous residues, blisters, or cracks on our flakes. As we already knew, at 300 K the signal is minimal for 3L MoS_2 [Fig. 7.6**a**], but this is not the case at 120 K. At lower temperatures, the phonon wavelength increases and the resonance occurs at a thicker region, specifically in 5L MoS_2 at 120 K [Fig. 7.6**b**]. Moreover, we observe the same resonance in 4L at intermediate temperatures of ~210 K.

Interestingly, plotting the temperature-dependent signal magnitudes of the different layers [Fig. 7.6**c**] reveals an unexpected result: the TDTR signals increase or decreases with temperature depending on the number of layers. For 1L and 2L MoS_2 we observe an increasing signal magnitude at lower temperatures. This trend is

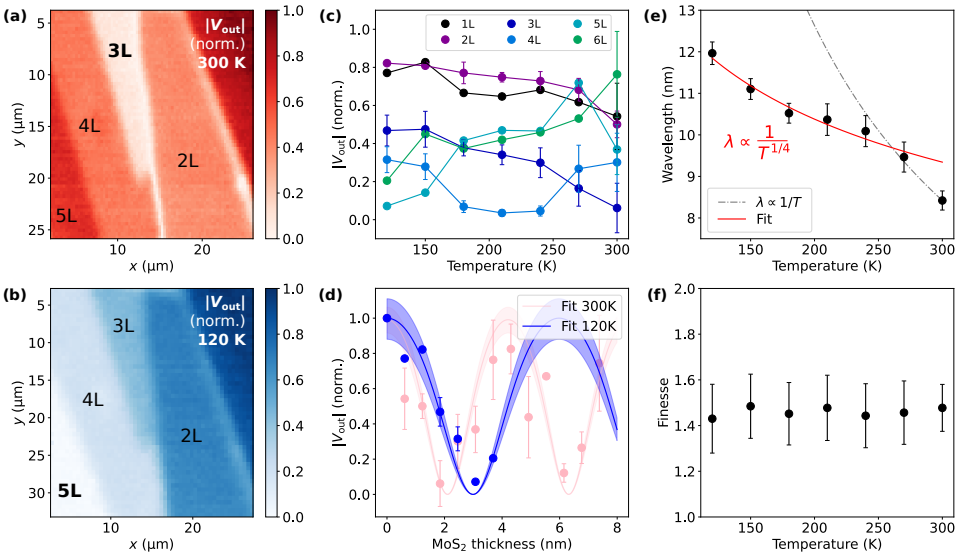

FIGURE 7.6: **Thermoreflectance of few-layer MoS_2 vs temperature.** TDTR maps (normalized V_{out} at $t_d = 100$ *ps*) of few-layer MoS_2, using a spot size of $w_0 = 2.2$ μm obtained at **(a)** 300 K and **(b)** 120 K. At 300 K, the 3L region shows near-zero signal, while at 120 K this is the case for the 5L region. **(c)** Scaling of the V_{out} signal magnitude as a function of temperature for the different number of MoS_2 layers. **(d)** Airy fitting (*solid lines* and *shaded regions*) of the TDTR signal magnitude (*scatters*) as a function of flake thickness, at 300 K (*pink*) and 120 K (*blue*); and retrieved **(e)** wavelengths and **(f)** finesse values.

steeper for 3L MoS_2 which shows a very low signal magnitude at room temperature which increases towards 50% of the bare substrate signal magnitude at 120 K. Now, for 4L MoS_2 the signal shows a minimum in signal (at around 210 K) within our temperature range. Surprisingly, slightly thicker MoS_2 flakes start showing a decreasing signal upon lowering the temperature. We understand these results as follows: at room temperature the conditions for standing wave formation are satisfied for 3L MoS_2 because it closely matches the quarter-wavelength of the resonant wave. Lowering the temperature decreases the frequency (increasing the wavelength) of the resonant wave, and thus, the conditions will be better satisfied in 4L; and further lowering the temperature would likely result in another minimum at around 120 K for 5L and at even lower temperatures for 6L MoS_2.

We show the Airy fits to our TDTR signal magnitude with flake thickness, at 300 K and 120 K [Fig. 7.6**d**] (for the rest of temperatures, see **Figure C.12**). With this, we extract a temperature-dependent wavelength [Fig. 7.6**e**] and a finesse of

$\mathfrak{F} \approx 1.5$ for all temperatures. The obtained phonon wavelengths support our theory, showing an increasing wavelength from 8.4 to ∼12 nm from 300 to 120 K. Interestingly, these results point a $\lambda \propto T^{-1/4}$ scaling at low temperatures, in contrast to the $\lambda \propto T^{-1}$ scaling expected at high temperatures for acoustic phonons with linear dispersion relations. This is because the phonon relaxation time is proportional to T^{-1}. Likely coincidentally, there seems to be a kink in the scaling of λ with the absolute temperature, which appears to occur at around 260 K. A value in fact close to the calculated Debye temperature $\Theta_D = 262.3$ K for MoS_2 [72]. This is the temperature above which most phonons are thermally populated and, thus, a different scaling with temperature is expected for most thermal properties above and below Θ_D.

7.3.2 Standing wave formation in MoS_2

In **Figure 7.7**, we qualitatively compare the ratio signals for 3L, 4L and 5L at 300 K, 210 K and 120 K with those of the bare substrate. This is, at the conditions for which their signals are minimum. Interestingly, we again see a picture where wave-like phonon heat could be responsible for our observations. At room temperature [Fig. 7.7**a**], we observe a much faster decay for 3L MoS_2 than that of the bare substrate, while 4L and 5L MoS_2 show a resistive behaviour. Decreasing the temperature makes 3L MoS_2 behave closer and closer to the bare substrate. At 210 K [Fig. 7.7**b**], 4L MoS_2 shows the fast decay and 5L a resistive behavior. At 120 K [Fig. 7.7**c**], we observe the fast decay on 5L MoS_2 and both 3L and 4L MoS_2 behave similar to the bare substrate. These results seem to suggest that the resonances occur in thicker flakes because of the increasing phonon wavelengths at decreasing temperatures. This would also support our hypothesis that coherent phonon interference, or standing wave formation, within MoS_2 could explain our findings. When flakes are too thin, transport is purely ballistic and their thermal presence can barely be distinguished from the bare substrate. Slightly increasing the thickness (or significantly lowering the temperature) to match 1/4 of the phonon wavelength, produces the conditions for standing wave formation, enhancing phonon transmission into the substrate. Thicker flakes do not satisfy the resonant conditions until 10L (or 3/4 of the phonon wavelength), which also produces a fast decay in the $-V_{in}/V_{out}$ ratio signals (see Figure 7.3).

Performing TDTR fits at temperatures other than room temperature would require prior knowledge of the temperature-dependent thermal properties of all materials in our sample, and thus, are omitted in this thesis. Similarly, we do

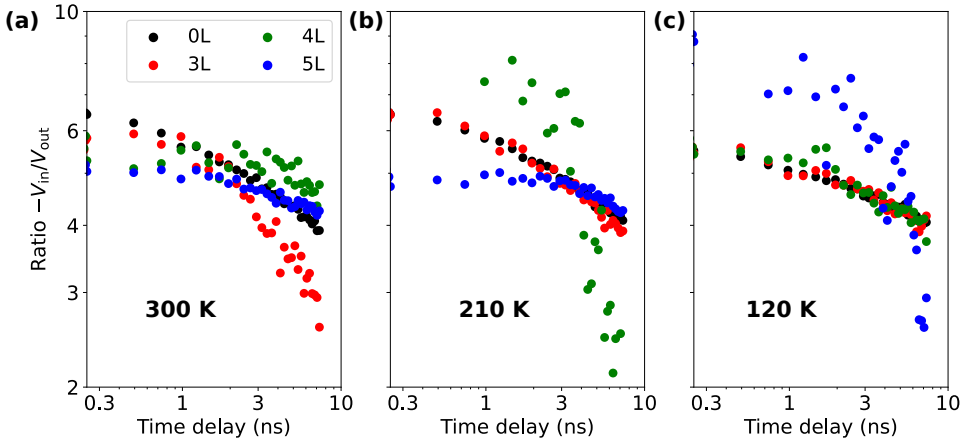

FIGURE 7.7: **Tuning the phonon wavelength with temperature.** Ratio $-V_{in}/V_{out}$ signals for bare substrate (*black*), and 3L (*red*), 4L (*green*) and 5L (*blue*) MoS_2 flake regions obtained at **(a)** 300 K, **(b)** 210 K and **(c)** 120 K. See the corresponding in- and out-of-phase signals in Figure C.14.

not even consider modelling the traces obtained in conditions satisfying standing wave formation, as our model based on diffusive heat transport fails to produce such steep decays in the ratio signals. We conclude that, even if coherent phonon interference effects were present within our few-layer MoS_2 flakes, these phonon cavities would likely be very lossy based on the small finesse values we obtained. In these lossy phonon cavities, standing waves would partially confine vibrational thermal energy while simultaneously dissipating it through scattering and leakage at both interfaces (including cooling to the substrate phonons via ph-ph scattering). This could create specific conditions in which resonant coherent MoS_2 phonons considerably enhance the transfer of thermal energy into substrate phonons, resulting in a tunable switch for the heat transfer capabilities of MoS_2.

If coherent phonons were to be present within the MoS_2 interlayers, we would obviously expect to observe them as RCPs rather than propagating CAPs given the ultrathin nature of our flakes ($0.6 - 10$ nm). This means that we can treat them in the same way as the RCPs we observe in gold. Assuming good interfacial contacts with both transducer and substrate, we hypothesise that an anti-node is found at the top surface (*i.e.*, the same boundary condition as the bottom surface of our transducer, see Section 6.3.1); and a node is found at the interface with the substrate (because of a good mechanical contact with the rigid SiO_2 layer). In this case, we should expect standing waves to form in our vdW layered material at specific thickness values of $L = N\,d = \lambda(2m-1)/4$, with N the number

of layers, $d = 6.15$ Å the interlayer distance, and $1 \leq m \leq (N-1)$ the mode number. We note that the conditions for the mode frequency [Eqs. 6.7 and 6.8] are not necessarily valid in the case of few-layer flakes, as the acoustic sound velocity v may differ from their bulk counterpart. Then, the fundamental standing wave mode ($m = 1$) will be supported at a thickness of $L = \lambda/4$, and its first overtone ($m = 2$) at $L = 3\lambda/4$. Assuming the loss of signal for ~3L MoS_2 to be caused by the fundamental standing wave, we would find a phonon wavelength of $\lambda = 4\,N\,d = 7.4$ nm. This value differs from the one obtained using our Airy fitting ($\lambda_{\text{Airy}} = 8.4$ nm) because at room temperature we retrieve the resonance at a thickness of 2.1 nm instead of the 1.85 nm we use here for 3L MoS_2. Note that using the cross-plane sound velocity of MoS_2 ($v_{MoS_2,\perp} = 3170$ m/s) we would find a frequency of ~0.43 THz.

This situation is analogous to optical thin film interference, exploited in anti-reflective coating applications. Here, light waves reflecting from the various interfaces constructively (destructively) interfere at specific values of film thickness, resulting in minima (maxima) of transmission. For any kind of waves, when the back-reflected waves are in phase they interfere constructively and the wave cannot be transmitted across the material. Whereas waves that are not in phase do not constructively interfere, and the original wave is allowed to propagate in the cavity (see Figure 2.4). For two identical mirrors, the conditions for interference would results in $L = m\lambda/2$. If one of the mirrors induces a π phase shift to the reflected waves, then the resonance happens at odd multiples of quarter-wavelengths $L = (2m-1)\lambda/4$. These are exactly the same conditions as those of asymmetric standing phonon waves, where a node is found at one interface and an anti-node at the other. In a Fabry-Pérot cavity, constructive interference of back-reflected waves would be equivalent to standing wave formation, a process that would contribute to the trapping of energy inside the cavity.

7.4 Assessing Photon Interference Effects

We have seen that our experimental thermoreflectance signal at long delay times $\geq$4 ns are strongly affected by the presence of few-layer MoS_2 interlayers. Although many of our observations are consistent with coherent phonon interference, they could also arise from alternative effects, in particular optical contributions. We note that our probe wavelength (515 nm) is close to the maximum thermoreflectance coefficient for gold. However, at slightly smaller probe wavelengths the thermoreflectance coefficient abruptly changes sign and peaks again,

at around 480 nm (see Figure C.1). This means that the probed thermoreflectance signal could strongly vary if the presence of MoS_2 interlayers affects the effective thermoreflectance coefficient of our transducer. We thus proceed using the transfer matrix method (TMM) to evaluate the effects of introducing MoS_2 on the reflectivity R and thermoreflectance coefficient $\chi = dR/dT$ in our specific sample geometry, at our probe wavelength.

Assuming small lattice temperature changes of $\Delta T \approx 1$ K induced by the modulated pump beam (see Section B.1), we can estimate the room-temperature reflectance and thermoreflectance coefficients, while using literature values for the refractive indexes n_j and extinction coefficients k_j of all materials in our sample [121, 176]. We use the TMM —including an interlayer slab with varying thickness from 0 to 10 nm with the bulk MoS_2 optical properties— to simulate our few-layer MoS_2 flakes. Here, we do not expect optical interference effects to occur within our MoS_2 cavities because of the small flake thickness (<10 nm) compared to the probe wavelength (515 nm). However, the MoS_2 flakes under the transducer layer could potentially affect the effective thermoreflectance coefficient when using thin semitransparent gold films, due to the multiple reflections at the various interfaces in our sample.

We simulate our $Au/Ti/MoS_2/SiO_2/Si$ multilayer structure (see Section A.2) using the literature values summarized in Table C.1 for the refractive indexes and extinction coefficients. We are able to reproduce the abrupt increase in reflectivity for flakes approaching the 10L thickness (see Figure 7.4**b,d**), and a sign-changing thermoreflectance for intermediate flake thicknesses [**Figure 7.8**]. The calculated thermoreflectance crosses the zero value at two points (for $3-4$L and $10-11$L) just slightly thicker than those at which we see suppressed TDTR signals (3L and 10L). Somehow, the internal reflections in our layered sample geometry can result in a sign changing effective thermoreflectance coefficient, which indeed seems a plausible explanation for the loss of signal at specific thickness-temperature combinations. Although convincing, the exact shape we retrieve for the effective thermoreflectance coefficient strongly depends on the specific combination of properties, and slight modifications can produce a very different effect (see **Figure C.13**). In any case, we cannot attribute our observations solely to optical effects, excluding the coherent phonon picture, based on this analysis; and we do not know how intricately interconnected these optothermal effects might be.

Our measured in-phase and out-of-phase signals also seem to support an optical (optothermal) origin of our observations (see **Figure C.14**), as depicted by

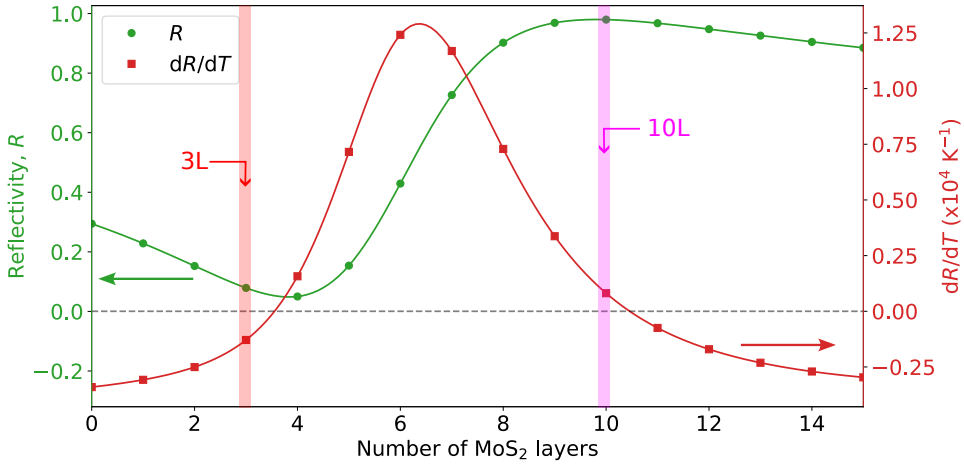

FIGURE 7.8: **Reflectance and thermoreflectance from transfer matrix method.** Left axis corresponds to the reflectivity at the top surface of the transducer affected by all the internal reflections in the sample, with the estimated thermoreflectance coefficient as a function of MoS_2 spacer flake thickness.

their smooth crossing of zero signal levels as we decrease the temperature. Their shape or decay rates do not seem to be strongly affected by the signal magnitude, although they do when normalized or when computing the ratio signal (see Fig. 7.7). We explain our observations as a dramatic increase in the error of our ratio signals, with amplified slopes, when we approach conditions (*i.e.*, thickness-temperature combinations) favouring a small thermoreflectance coefficient. This is because the experimental error is the same for all traces but becomes similar or bigger than the signal magnitude, which approaches zero at long time delays. We visualize this effect in Fig. 7.7 as a decreased signal-to-noise ratio for the fast decaying ratio signals which occur for 3L (300 K), 4L (210 K) and 5L (120 K). Performing these calculations at temperatures significantly lower than 300 K would imply poor assumptions of $n_j(T)$ and $k_j(T)$, given the limited knowledge of temperature influence on all the properties involved. In any case, this means that we can efficiently tune and suppress the thermoreflectance coefficient of thin gold films just by introducing few-layer MoS_2 flakes underneath, which could have strong implications for the design of optothermal applications.

7.5 Consequences of Using Thin Au Transducers with Ti Adhesion Layers

Besides possible phonon and photon interference effects, we consider additional physical effects to occur in our experiments. First, we use thin (50 nm) gold as transducer, with small electron-phonon coupling ($g_{Au} = 2.2 \times 10^{16}$ W m^{-3} K^{-1}) as compared to aluminum ($g_{Al} = 25 \times 10^{16}$ W m^{-3} K^{-1}), which is more typically used as transducer in TDTR [39, 177]; and second, we use 2 nm Ti adhesion layers, which have been shown to react with MoS_2 [173]. The thin gold transducers result in a thickness-dependent reflectivity of our probe beam given the presence of few-layer MoS_2 flakes underneath, particularly for those above ~10L. In principle, the ratio signals in TDTR should be unaffected by the probe reflectivity. However, this could compromise our comparison between the G_{eff} values we find for $Au/MoS_2/SiO_2$ and the one we obtain for Au/SiO_2, and could become an issue to study flakes thicker than ~10L. The use of Ti adhesion layers is also not ideal because it might have chemically modified the surface of our flakes during the deposition of the transducer. Combined, these two reasons are likely responsible for the dramatic effect of introducing few-layer MoS_2 flakes we observe at early time delays (*i.e.*, within the picosecond acoustics window, see Fig. 7.5**a**). The main consequence is, likely, that the presence of our semiconducting flakes alters the heat generation mechanisms and thus, the reheating process of the gold transducer, which we described in Section 6.2.3.

To further explore the origins of our loss of thermoreflectance signal at specific thickness values, we perform TDTR measurements with increased sampling rate within the picosecond acoustics window [**Figure 7.9**]. Here, we notice clear oscillations with a period of ~29.5 ps for most data sets (*i.e.*, the resonant coherent phonons in our gold transducer). Interestingly, very thin flakes show stronger oscillations, and supported for longer times, than the bare substrate. This occurs thanks to the van der Waals interactions of our flakes with both transducer and substrate, which mechanically decouples them. Thicker flakes still show ps oscillations which start to faint or are significantly distorted. For the 6L flake, the oscillation amplitude is minimal, as this is the region showing the largest TDTR signal magnitudes, comparable to the bare substrate. Moreover, the reheating effects seem mitigated for this region. In the coherent phonon interference picture, at this specific thickness of 6L (*i.e.*, in between of the two resonances at 3L and 10L) the back-reflected thermal waves constructively interfere impeding phonon transmission into the substrate. This would imply an increased Au lattice temperature,

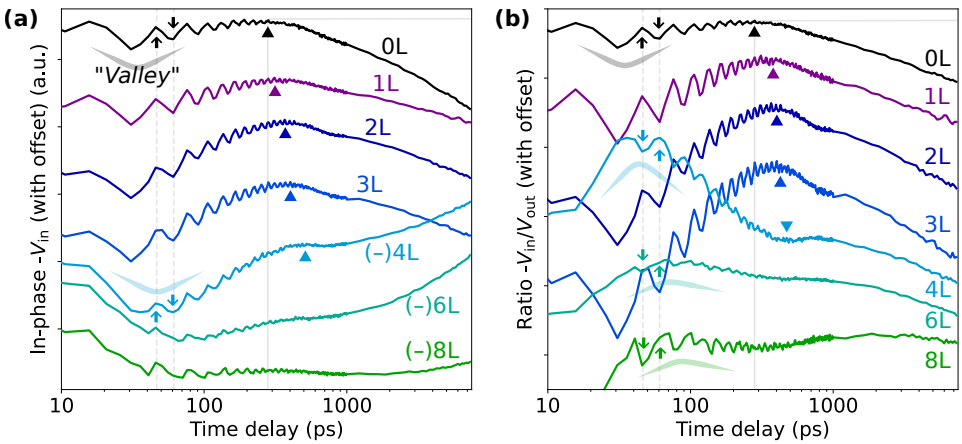

FIGURE 7.9: **Influence of flake thickness on the non-equilibrium dynamics. (a)** In-phase V_{in} and **(b)** ratio $-V_{in}/V_{out}$ signals for 0L to 8L MoS_2, fine-sampled from 0 to 1 ns time delays. The signals include arbitrary offsets for clarity purposes. The sign of the V_{in} signal determines the shape of the ratio signals at early times, with flakes $\leq$3L showing ps oscillations with the same phase as the bare substrate, and a similar reheating process of the transducer. In contrast, flakes >3L show a π-phase shift of the ps oscillations and the entire reheating process with respect to the bare substrate. The two vertical dashed lines highlight a period of 29.5 ps corresponding to a round-trip for the acoustic phonons, with arrows emphasizing the different phase of the oscillations for flakes $\geq$4L. Triangles point to the time phonon temperature starts decaying.

and therefore a lower contrast to the effects of the resonant acoustic phonons. For the 8L flake, the oscillations are recovered, but show signs of acoustic echoes scrambling their oscillatory behavior. These acoustic echoes can provide valuable insight into how phonon reflect at the various interfaces [82, 178], but drawing meaningful conclusions here would require higher temporal sampling and likely longer averaging. We are actively working to build a complete picture of this phenomenon, which we describe in Ref. [179].

The V_{in} signals [Fig. 7.9**a**] progressively turn negative for flakes thicker than 3L (see Fig. 7.5 and Fig. C.14). Because of this, the ps oscillations for flakes within 4L to 9L appear to have the opposite phase as those for the bare substrate (and to those of thinner flakes) when evaluating the ratio $-V_{in}/V_{out}$ signal [Fig. 7.9**b**]. The reversed sign of the in-phase and out-of-phase signals flips both the ps oscillations and the entire reheating process of the transducer when computing their ratio (see Fig. 7.9**b**). The time needed to reheat the gold (*i.e.*, until the temperature starts decaying, marked with *triangles* in Fig. 7.9) increases with flake thickness, at least

for the thinner flakes with the same sign as the bare substrate.

Flakes thinner than 3L exhibit a similar behaviour as the bare substrate: the signal increases until $\sim 200 - 400$ ps and then starts decaying, with an increasingly larger valley-to-peak signal difference. Understand "valley" as the signal after the $t_d = 0$ spike —arising from the hot electron temperature upon photoexcitation— has fully decayed (*i.e.*, at ∼30 ps); and "peak" as the maximum phonon temperature before it starts cooling, at around $t_d \approx 300$ ps. A larger valley-to-peak ratio means a larger contrast in temperature, and a slower rise in gold temperature implies a longer time to reach e-ph equilibrium of the layers underneath the transducer. The main reason is that photoexcited electrons in gold travel to the interface before cooling, and directly scatter with phonons either at the Ti/MoS_2 interface, within MoS_2, or at the MoS_2/SiO_2 interface. They first increase the temperature of the effective interface, which later reheats the transducer [144].

This process takes twice as much time for 3L MoS_2 (∼400 ps) as compared to the bare substrate (∼200 ps). This probably implies that the heat is mainly generated at the MoS_2/SiO_2 interface and needs to flow through resistive MoS_2 before it can reheat the gold. As the thickness of MoS_2 increases, it is more likely that this process occurs at the Ti/MoS_2 interface, resulting in bidirectional heat transfer towards transducer and substrate, thus suppressing the temperature gradient and producing a flat response. These conditions in which heat is generated within or in close vicinity of the semiconductor channel —rather than away from it— are closer to technological applications than standard TDTR measurements using transducers with stronger e-ph coupling like aluminum (*i.e.*, heat generated away from it eventually flows across MoS_2). Interestingly, this situation seems not to play an important role at nanosecond timescales with the exception of 3L and 10L MoS_2, which behave significantly different than the rest of thicknesses. However, it is possible that these reheating effects make us underestimate the effective thermal conductance by artificially flattening the probed thermal response.

In any case, this would not explain the decrease in thermoreflectance signal, unless significant amounts of thermal energy can be removed from the gold (*e.g.*, by standing wave formation and/or efficient heat transfer towards the substrate). In other words, a considerable portion of the energy we inject into the system through photoexcitation of gold electrons is transferred directly to the three-layer MoS_2/SiO_2 interface —and, subsequently, to the SiO_2/Si substrate— without ever reaching the gold as "phonon heat"; making it inaccessible to our measurement. This is consistent with the picture of destructive interference of back-reflected

waves carrying our signal (our probed thermoreflectance), enhancing the transmission of heat-carrying phonon waves into the substrate, as we depicted in Figure 7.4**e**. As the gold remains colder, the ps oscillations are supported for longer times in 3L MoS_2, also suggesting that this thickness provides the greatest decoupling between the gold transducer and the substrate, enabling the efficient manipulation of heat flow (*i.e.*, by reflecting low frequency sound waves while transmitting higher frequency heat-carrying phonons) resembling a thermal rectifier. This argument would be supported by both, the longer time required to reheat the transducer and the fast decaying ratio signals observed for 3L MoS_2 at room temperature. A potential outcome of this capability is the realization of phonon filters or thermal waveguides, which could be integrated into nanoscale devices to selectively control heat transport for thermoelectric enhancement, thermal isolation, or phononic signal processing.

On the one hand, our semitransparent gold transducers are not ideal to study conventional heat transport in thermally thin MoS_2 flakes [144, 177]. Nevertheless, this does not impede us from extracting effective interfacial conductances for most flake thicknesses (see Section 7.2.1), with the exception of 3L and 10L MoS_2. On the other hand, we cannot exclude the possibility that coherent phonon heat transport occurs in our experimental conditions. The presence of thin MoS_2 interlayers has a strong influence in the observed early dynamics. We have seen that many other factors also influence our TDTR signals, such as the thickness, temperature, effective optothermal properties of the transducer, and the non-equilibrium phenomena, as discussed in this chapter. In any case, thin-gold transducers on 2D vdW materials are also beneficial for some applications. As we have shown, for TDTR imaging with unmatched layer-by-layer resolution, enabling the detection of cracks, defects and residues in buried layers; for the precise control of the effective thermoreflectance coefficient; and for providing an enhanced sensitivity to the non-equilibrium dynamics.

7.6 Conclusions

In this chapter, we have studied out-of-plane heat transport across few-layer MoS_2 by means of time-domain thermoreflectance. We have extracted values of the effective total resistance provided by MoS_2 by systematically varying the flake thickness between 1L and 12L. We found a more resistive behavior than we expected for the intermediate thicknesses based on the results reported in the literature [37, 39, 49]. We have studied the possibility of coherent phonons to play

a role in the loss of the thermoreflectance signal we observe at specific thickness values; and extracted a temperature-dependent phonon wavelength, seemingly reasonable for heat-carrying acoustic phonon modes in MoS_2. This is, while probing a transient temperature built from the contribution of multiple phonon modes with diverse frequencies. We have observed a strong temperature dependence of the TDTR signals and, in combination with our control of flake thickness, we have achieved an effective on-demand suppression of the thermoreflectance signals. We conclude that this tunability arises due to a combination of effects that modulate the effective thermoreflectance coefficient in our experimental conditions, making it temperature-dependent and heavily influenced by the presence of few-layer MoS_2 flakes under the gold transducer. We have also observed strong differences in the early dynamics, which we attributed to significant amounts of heat being generated at the interface and transferred back to the transducer in a process highly sensitive to the number of MoS_2 layers.

Our experimental data is extremely rich in non-equilibrium dynamics, electronic and phononic transport information —also including optical and optothermal information— and could potentially reveal signatures of coherent phonon heat in MoS_2. However, our analysis does not provide a unique physical interpretation and further experimental and theoretical inputs would be needed to fully understand our observations. For example, cross-sectional TEM measurements would help identifying the exact type of interface formed on substrate and MoS_2 upon titanium evaporation; also helping to determine potential differences in the granular structure of the gold deposited above. In any case, we have provided all the tools needed to reproduce our analyses on an extensive data set involving TDTR measurements as a function of flake thickness and temperature. Measurements performed at higher modulation frequencies and larger spot sizes (not shown in this chapter) yielded similar observations at the expense of lower signal-to-noise ratios and lower reproducibility because of the large radiative signals from our voltage amplifier (see Figure C.2). Overall, our findings provide valuable insights for the design of optothermal experiments and could have an impact in applications requiring control of thermoreflectance properties of thin metal films. Such control over the effective thermoreflectance coefficient could enable optimized optical transducers for high-sensitivity temperature sensing, non-contact thermal monitoring, and photonic devices where heat-induced changes in reflectivity are exploited for functionality.

Contributions

I assisted Dr. Bohai Liu with the fabrication of supported MoS_2 samples. I performed the TDTR measurements with help from Dr. Bohai Liu. I performed the data analysis and simulations; and interpreted the results with inputs from Dr. Bohai Liu.

Chapter 8

Unraveling Heat Transport and Dissipation in Suspended $MoSe_2$ from Bulk to Monolayer

This chapter is based on Ref. [127]:

D. Saleta Reig, S. Varghese, R. Farris, A. Block, J. D. Mehew, O. Hellman, P. Woźniak, M. Sledzinska, A. El Sachat, E. Chávez-Ángel, S. O. Valenzuela, N. F. van Hulst, P. Ordejón, Z. Zanolli, C. M. Sotomayor Torres, M. J. Verstraete, and K.-J. Tielrooij, "Unraveling heat transport and dissipation in suspended $MoSe_2$ from bulk to monolayer." *Adv. Mater.* **34**(10), 2108352 (2022).

In this chapter, I present our experimental and theoretical investigation of the in-plane thermal conductivity of the suspended $MoSe_2$ flakes fabricated in Chapter 3. I discuss the effects of flake thickness and environment on the thermal properties of $MoSe_2$, as well as common experimental artifacts in these kind of measurements.

8.1 Introduction

As the backbone of the semiconductor industry, silicon has enabled the performance and scalability driving the modern information era. Current state-of-the-art transistors measure only a few nanometers, and substantial research is focused towards the sub-2 nm scaling. At these scales, a large portion of the Si atoms in the transistor channel are surface atoms, with dangling bonds and a crystal structure that deviates from that in bulk silicon. In turn, this degrades the overall properties expected from this material and compromises device performance. Particularly, due to decreased heat dissipation capabilities, creating phonon bottlenecks which lead temperature to accumulate. The degrading thermal properties upon reducing the thickness of silicon, and 3D-bonded materials in general, calls for the exploration of low-dimensional semiconducting materials. For silicon, this situation has been shown experimentally using Raman thermometry measurements on thickness-controlled silicon membranes down to 9 nm, which already exhibit a 15-fold reduction ($\kappa_{Si,9nm} \approx 9$ W m^{-1} K^{-1}) in their in-plane thermal conductivity κ_r (*i.e.*, along the plane of the membrane) with respect to the thermal conductivity of bulk silicon ($\kappa_{Si,bulk} = 148$ W m^{-1} K^{-1}) [4]. This reduction arises from increased scattering at system boundaries, as the thickness falls bellow the dominant phonon mean free paths; and from additional scattering channels given the larger portion of surface atoms contributing to an increased microscopic roughness.

Two-dimensional van der Waals materials offer the possibility to produce sub-nanometer materials (and membranes, see Chapter 3) with atomic flatness, making them particularly relevant to complement or even replace silicon in certain applications. As we have seen in previous chapters exploring the out-of-plane thermal conductivity κ_z of TMDs, the situation is similar for their in-plane thermal conductivity κ_r: very scattered experimental and theoretical values of κ_r have been reported in the literature (see Chapter 2). Moreover, systematic investigations of in-plane thermal transport in TMDs exploring the effects of material thickness —and how environmental factors influence behavior when approaching the monolayer limit— also remain lacking. Performing reliable experimental and theoretical in-plane thermal transport studies over a broad thickness range, and down to the molecular monolayer, is challenging. Experimental approaches can be susceptible to thickness-dependent and substrate-induced artifacts, while requiring reproducible fabrication of a large number of clean samples with thickness control. Theoretical approaches based on molecular dynamics simulations

are limited in accuracy by the choice of empirical interatomic potentials, while *ab initio* simulations often examine phonons at 0 K, rather than at finite temperature. Simulations of thicknesses other than monolayer and bulk are computationally costly, and therefore so far non-existent, with the only exceptions being an *ab initio* study on MoS_2 as a function of thickness limited to the range $1-3$ layers [36] and a molecular dynamics study on monolayer and bilayer MoS_2 [99].

In this chapter, we overcome these technical challenges, which enables us to develop a deep understanding of thermal transport properties of TMD crystals. In particular, we study how the in-plane thermal conductivity (from now on we use $\kappa_r = \kappa$) of $MoSe_2$ is affected by the crystal thickness and its environment. For this, we exploit the thickness-controlled, large-area, single-crystalline, clean suspended flakes we fabricated and characterized in Chapter 3. By using suspended flakes, we avoid contributions from the substrate to access the intrinsic in-plane thermal properties of these materials. We use a combined experimental-theoretical approach to build a unifying physical picture of the intrinsic lattice thermal conductivity of the representative TMD $MoSe_2$. In our experimental approach, we employ the widely used technique of Raman thermometry, where we carefully identified and eliminated important artifacts, such that we obtain the intrinsic thermal conductivity. In our theoretical approach, we perform *ab initio* simulations based on density functional theory (DFT) and Boltzmann transport theory using phonons at finite temperature, including anharmonic renormalization yielding accurate results also at finite temperature. We employ SIESTA [180, 181], which is particularly suitable for atomistic simulations with a large number of atoms, such that we can obtain results up to several molecular layers.

Experimentally, we estimate the in-plane thermal conductivity κ of our suspended flakes using a simple relationship that assumes strictly in-plane, diffusive heat transport with perfect heat sinking at the edge of the hole. Here, we do not consider quasi-ballistic effects to occur given the large lateral sizes of our samples. Also, we do not consider non-diffusive effects to affect our measurements, as we use a continuous wave laser which is not tightly focused on the samples. We will see that our assumptions are not satisfied when performing Raman thermometry measurements in air (or N_2), as ambient molecules introduce an additional cooling channel. In addition to in-plane diffusion from the hot spot to the heat sink, heat dissipation also occurs by transfer to the ambient molecules as a sink (see Section 8.3.3). These assumptions are also not satisfied when using flakes suspended over small holes, and when heat sinking is not highly efficient as for samples on

gold-coated substrates (see Section 8.3.4). In these cases, we use an apparent in-plane thermal conductivity κ_{app} to study the effects of these experimental artifacts in our measurements. We note that it has so far not been possible to experimentally produce suspended materials with (sub-)nanometer thickness and a lateral size of several microns, such as our $MoSe_2$ films.

Theoretically, we find that the main contribution to the in-plane thermal conductivity in few-layer $MoSe_2$ comes from phonon modes centered around $\sim$1 THz. Toward the monolayer limit, the contribution of these modes decreases substantially, as there are fewer modes and the phonon lifetimes decrease. These effects are counteracted by the appearance of "surface" modes around $\sim$0.1 THz with an exceptionally long mean free path (MFP) of several micrometers, which contribute substantially to thermal transport. This results in an in-plane thermal conductivity that progressively increases from a value of $\kappa \approx 20$ W m^{-1} K^{-1} for the thinnest films, toward $\kappa \approx 32$ W m^{-1} K^{-1} for the thickest films, at a temperature of $\sim$400 K. This behavior originates from the layered nature of 2D-bonded $MoSe_2$ and similar TMDs, and is different from the behavior of non-layered materials, such as 3D-bonded silicon. In such materials, the thermal conductivity keeps decreasing for thinner films, due to increased boundary scattering at the surfaces [4].

Finally, we find that thermal transport in $MoSe_2$ is strongly affected by the material's environment, in particular for monolayer crystals, where more than 80% of the thermal power is lost through out-of-plane heat dissipation to surrounding air molecules. We extract a remarkably large heat transfer coefficient up to $h_c \approx 50\,000$ W m^{-2} K^{-1} for monolayer $MoSe_2$, and an apparent thermal conductivity above 250 W m^{-1} K^{-1}. This is larger than the 140 W m^{-1} K^{-1} of bulk crystalline silicon [4]. Moreover, we point to the importance of identifying and eliminating substrate-related experimental artifacts, providing guidance for thermal characterization of atomically thin suspended materials. Our results highlight the highly promising applicability of TMDs in (opto-)electronic applications, where material thicknesses of a few nanometers, or less, are required.

8.2 Methods

In this section, we detail the procedures we employ in our combined experimental [Section 8.2.1] and theoretical [Section 8.2.2] study.

8.2.1 Experimental approach

We perform Raman thermometry measurements on suspended $MoSe_2$ flakes of systematically varied thickness from monolayer (1L) up to ∼70 layers (70L), fully covering the 1L to 5L range (see **Figure 8.1**). This corresponds to a thickness ranging from 0.7 nm up to ∼50 nm. Importantly, we use more than one sample with the same thickness in the 1L to 3L regime —including two monolayer, four bilayer and two trilayer samples— in order to assess the reproducibility of both our samples and our experimental technique. We perform Raman experiments in vacuum and air, and both on supported and suspended regions of our flakes.

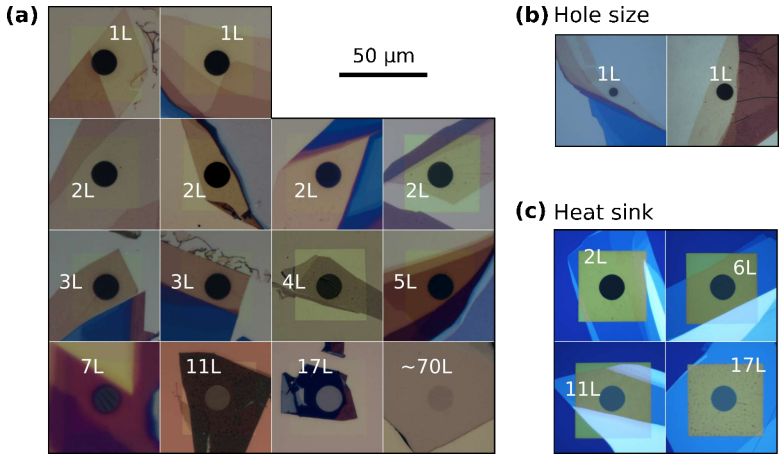

FIGURE 8.1: **Suspended $MoSe_2$ flakes investigated using Raman thermometry. (a)** Thickness-controlled (1L to 70L) $MoSe_2$ flakes transferred over artifact-minimized substrates. This is, flakes transferred over gold-coated Si_3N_4 substrates with large holes ($R = 7.5$ μm). **(b)** Monolayer $MoSe_2$ flakes suspended over smaller holes ($R = 2.5$ μm and $R = 5$ μm). **(c)** Thickness-controlled $MoSe_2$ flakes suspended over large holes on non-coated substrates (Si_3N_4). Scale bar of 50 μm is valid for all panels.

Suspended $MoSe_2$ sample fabrication

The sample fabrication, based on PDMS-assisted dry transfer of mechanically exfoliated $MoSe_2$ flakes, is described in detail in Chapter 3 (also, see Ref. [96]). As substrates, we used gold-coated holey Si_3N_4 membranes for the study of the effect of $MoSe_2$ crystal thickness and the effect of the environment (see Figure 8.1**a**). Those substrates have a single hole with a radius of 7.5 μm. For the study of the effect of hole size, we dry-transfer monolayer $MoSe_2$ flakes over gold-coated silicon-on-insulator wafers with back-thinned membranes with holes. We used focused ion beam to perforate holes with a radius of 2.5 and 5 μm prior to transfer

(see Fig. 8.1**b**). We deposited gold coatings using electron-beam evaporation, consisting of 50 nm gold with 5 nm titanium adhesion layer, prior to flake transfer. Gold-coating the substrate facilitates sample fabrication [96], and importantly ensures efficient heat sinking at the edge of the hole. We also study flakes with varying thickness, transferred on Si_3N_4 substrates without the gold coating, aimed at understanding and eliminating possible artifacts affecting the extracted thermal conductivity (see Fig. 8.1**c**).

Raman thermometry

One of the most popular methods to study thermal properties of thin films is Raman thermometry [38, 40, 70, 71], where a laser beam serves both as a heater and a thermometer [**Figure 8.2**]. The thermometer works via Raman scattering of the laser light, where the frequency shift of a temperature-calibrated Raman active mode serves as a probe of the local temperature of a sample. This technique benefits from a relatively simple implementation, contactless nature, and no stringent sample requirements, apart from the presence of a temperature-sensitive Raman mode (*e.g.*, the A_{1g} mode in $MoSe_2$). We collect Raman spectra using a Raman spectrometer (T64000, Horiba) and a CW laser beam, with a wavelength centered at $\lambda = 532$ nm, focused to a $1/e$ spot radius ($r_0 = 2\sigma \approx 1$ μm). For "stage heating" measurements (see Fig. 8.2**a**), we place the samples in a temperature-controlled vacuum stage (Linkam). We use silver paste to glue the samples on a copper holder, for a good thermal link with the stage. We leave the samples to thermalize for 20 min at each temperature. We perform these as calibration measurements to obtain the shifting rates of the A_{1g} mode both in the supported and suspended regions, giving comparable results (see Table S1 in Ref. [127]). The temperature increase in the "laser heating" measurements (see Fig. 8.2**b**) is defined as $\Delta T = (\nu_P - \nu_{P=0})/\chi_T$, with $\nu_{P=0}$ the intercept from the linear fit of Raman shift with laser power. We perform Raman experiments both in vacuum (5×10^{-3} mbar) and air (1 bar), as depicted in Fig. 8.2**c** and Fig. 8.2**d**, respectively.

We independently pre-determined the absorbances of our suspended $MoSe_2$ crystals using a home-built optical setup by measuring reflectance and transmittance through the suspended region (see Section 3.3.3). For all thicknesses, we assume homogeneous heating in the c-axis of the flake. We obtain the error bars in the experimental thermal conductivity from the uncertainty in absorption, flake thickness (only for the thicker flakes), and Raman laser spot size, as well as statistical errors in the fitted Raman shifts, accumulating to ∼30% for the thinnest flakes and ∼20% for the thicker flakes. Multiple measurements on different samples

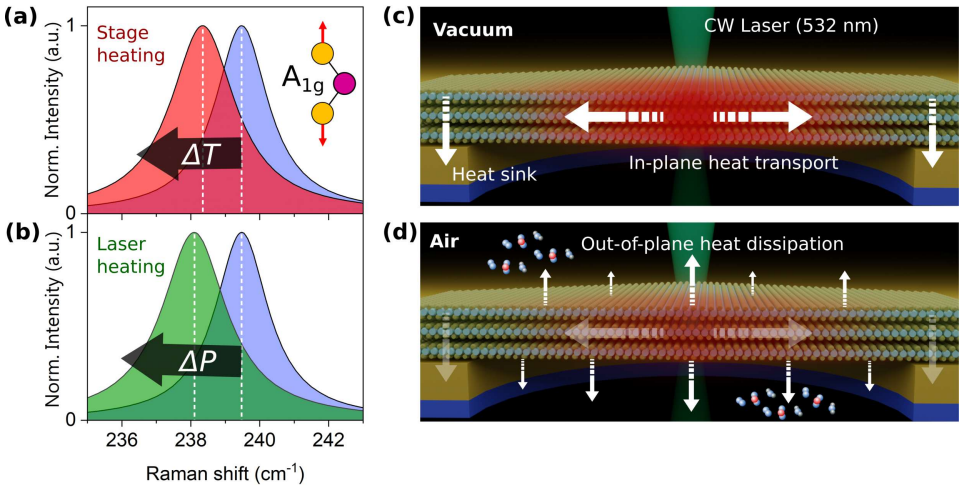

FIGURE 8.2: **Raman thermometry on suspended $MoSe_2$. (a)** The A_{1g} Raman mode of $MoSe_2$ (*inset*) red-shifts with increasing the temperature of the sample stage (*red profile*). **(b)** This mode also red-shifts when increasing the laser power (*green profile*) with respect to its peak position at room temperature at very low incident power (*blue profile*). **(c)** 3D representation of the Raman experiment in vacuum, where the laser induces a hotspot that cools via radial in-plane diffusion towards the heat sink. **(d)** 3D representation of the experiment performed in ambient air, where out-of-plane heat dissipation also occurs by transfer to environmental molecules.

with the same thickness, for example, the four bilayer samples, demonstrate that sample-to-sample variations fall within this experimental uncertainty.

8.2.2 Theoretical approach

We compare our experimental results reporting on the intrinsic in-plane thermal conductivity of our flakes (*i.e.*, the measurements performed in vacuum conditions, using our artifact-minimized substrates) with the computed thermal properties of $MoSe_2$. For this, we use density functional theory (DFT), as implemented in SIESTA [181], in combination with the temperature-dependent effective potential (TDEP) method that allows us to take into account phonons at a non-zero temperature [182, 183]. Additionally, we simulate our Raman experiment considering additional cooling channels, such as heat dissipation to environmental molecules and thermal radiation. The aim is to validate our experimental approach and to estimate the out-of-plane heat transfer coefficients h_c to air molecules.

Density functional theory simulations

The computational approach is based on first-principles calculations. We study thermal transport properties using the density functional theory as implemented in the SIESTA program [180, 181] and employing LMKLL functionals [184] to take into account van der Waals interactions. We consider structures with different number of layers, from monolayer up to 6L, with 17 Å of vacuum to eliminate the interaction between periodically repeated images. More details on the DFT simulations for $MoSe_2$ can be found in Ref. [127], and an in-depth theoretical analysis of the microscopic parameters influencing the thermal conductivity of TMDs, such as the phonon dispersion and the phonon lifetimes, can be found in Ref. [185].

Thermal transport simulations

We simulate the thermal transport in our Raman thermometry experiment by solving the 2D (in-plane) steady state thermal model, *i.e.* Fourier's law, including a heat exchange at the sample's surfaces, *e.g.* due to convection and/or conduction to the environment, as well as thermal radiation. In polar coordinates with radial symmetry, the time-dependent temperature rise above ambient temperature $\Delta T(r,t)$ evolves according to [74]

$$\frac{\partial \Delta T}{\partial t} = \underbrace{\frac{1}{r}\frac{\partial}{\partial r}\left(r \cdot \frac{\kappa}{C_v}\frac{\partial \Delta T}{\partial r}\right)}_{\text{in-plane conduction}} + \underbrace{\frac{S}{C_v}}_{\text{source}} - \underbrace{\frac{N_{\text{surf}} \cdot h_c \cdot \Delta T}{d \cdot C_v}}_{\text{out-of-plane dissipation}} - \underbrace{\frac{N_{\text{surf}} \cdot \sigma_{\text{SB}} \cdot \Delta T^4}{d \cdot C_v}}_{\text{radiation}} \tag{8.1}$$

with C_v the $MoSe_2$ sample's volumetric heat capacity ($C_v = 1.87$ MJ m^{-3} K^{-1}, the bulk value) [72], κ its in-plane thermal conductivity, d its thickness, and $N_{\text{surf}} = 2$ the number of surfaces (top and bottom). We assume perfect heat sink conditions $\Delta T(R,t) = 0$ at the hole boundaries, with $R = 7.5$ µm the hole radius. We set the out-of-plane heat transfer coefficient to zero ($h_c = 0$) to simulate the experiment in vacuum, and then we adjust it to simulate the experiment in air. Similarly, we only include the radiative term, with the Stefan-Boltzmann constant $\sigma_{\text{SB}} = 5.67 \times 10^{-8}$ W m^{-2} K^{-4}, to study the effects of thermal radiation, which has been found to affect the extracted κ by only 0.1%.

The Gaussian volumetric heating source $S(r)$ depends on the total absorbed heating laser power P_{abs} and the $1/e$ spot size r_0 via [56]

$$S(r) = \frac{P_{\text{abs}}}{d\pi r_0^2} \exp\left[-\frac{r^2}{r_0^2}\right] \tag{8.2}$$

We evolve Eq. 8.1 in the time-domain until steady state is reached, and we extract the average temperature from the area between $r = 0$ and $r = r_0$ for comparison with the experimental data. More details can be found in the Supplementary Information of Ref. [127].

8.3 Results and Discussion

In our experiments (see Section 8.2.1), we use CW light with a wavelength of 532 nm to heat a local spot with a $1/e$ spot size $r_0 \approx 1$ μm in the center of a suspended $MoSe_2$ crystal (see Figure 8.2**c**,**d**). Subsequent cooling occurs —in the ideal situation— by radial, diffusive flow of heat toward the edge of the suspended region of the crystal, where the substrate acts as a heat sink. We probe the temperature at the location of the laser spot, corresponding to the steady-state situation where laser-induced heating is compensated by cooling through heat flow and subsequent heat sinking. Thus, a higher (lower) steady-state temperature indicates less (more) efficient cooling, which in turn implies a lower (higher) κ. For thin exfoliated TMD flakes, the obtained κ corresponds to in-plane transport, as the out-of-plane thermal conductivity is typically more than an order of magnitude lower [59].

We perform Raman thermometry measurements [**Figure 8.3**] on all the suspended $MoSe_2$ samples shown in Figure 8.1, exploiting the temperature-sensitive A_{1g} Raman mode (see inset of Fig. 8.2**a**). We first calibrate the red-shifting rates of the A_{1g} mode with temperature. We collect Raman spectra while varying the temperature of the crystal using a controlled heating stage, using very low incident power to avoid laser-induced heating (see Fig. 8.3**a** for monolayer $MoSe_2$ and the Supporting Information of Ref. [127] for the results for other thicknesses). We find that the temperature coefficients $\chi_T = \partial\nu/\partial T$ change from -0.007 cm^{-1} K^{-1} for bulk to -0.015 cm^{-1} K^{-1} for monolayer $MoSe_2$. This allows us to correlate the red-shift $\Delta\nu$ of the A_{1g} mode, with the increase in temperature ΔT (as depicted in Fig. 8.2**a**). We exploit these results in our "laser heating" experiment (see Fig. 8.3**b** for monolayer $MoSe_2$ and Ref. [127] for the other thicknesses): a higher laser power at the sample P induces a larger temperature increase ΔT, and therefore a larger red-shift $\Delta\nu$, enabling our Raman probe to act as both a local heater and thermometer (as depicted in Fig. 8.2**b**).

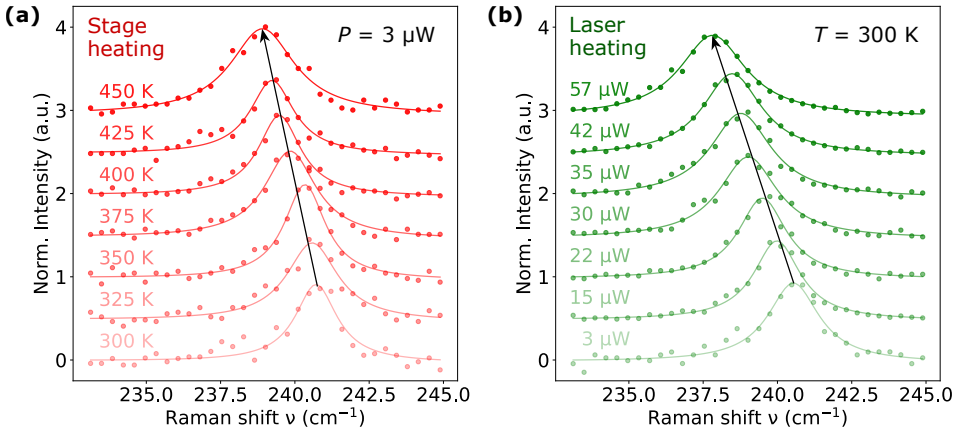

FIGURE 8.3: **Raman thermometry of a suspended monolayer $MoSe_2$. (a)** Calibration measurements of Raman spectra at 532 nm for increasing temperature of the sample stage, showing an increasing red-shift. The laser power was kept very low to avoid laser-induced heating. **(b)** Raman spectra at room temperature for increasing laser power P, showing an increasing red-shift of the A_{1g} mode due to laser-induced heating.

8.3.1 Intrinsic in-plane thermal conductivity of $MoSe_2$

We extract the in-plane thermal conductivity by performing linear fits on the obtained temperature increase ΔT as a function of absorbed laser power $P_{abs} = A \cdot P$, which we obtain from the optical absorption A of the sample. The fits yield the slope $\partial T / \partial P_{abs}$, from which we calculate the in-plane thermal conductivity using the following equation [56]:

$$\kappa = \alpha \cdot \frac{1}{2\pi d} \cdot \left(\frac{\partial T}{\partial P_{abs}} \right)^{-1} \cdot \ln \left(\frac{R}{r_0} \right) \tag{8.3}$$

where R is the hole radius, r_0 is the laser spot radius, d is the flake thickness, and α is a prefactor that is a function of the ratio R/r_0. For our experimental conditions, $\alpha \approx 1$ [56]. Equation 8.3 for κ is valid when the only cooling channel is in-plane diffusive heat transport to the edge of a circular suspended material, where perfect heat-sinking occurs, such that the crystal is at ambient temperature. The accurate extraction of κ relies on knowledge of the laser spot size r_0 and the optical absorption A of each of the flakes, which we measured independently (see Chapter 3). We confirmed the validity of Equation 8.3 using a numerical simulation of the Raman thermometry experiment (more details in Section 8.2.2). Importantly, this numerical model allows for including additional physical processes, such as

out-of-plane heat dissipation (see Section 8.3.3).

Before presenting the results, we point out the importance of eliminating artifacts that can occur in Raman thermometry measurements on such ultrathin samples, in particular related to the substrate and environmental conditions. After considering several substrate designs, we concluded that using gold-coated substrates with a hole radius of 7.5 μm leads to the elimination of several important artifacts, as illustrated in **Figure 8.8**. We will explore each of these potential artifacts in detail in Sections 8.3.3 and 8.3.4. We thus study the effect of crystal thickness on the thermal conductivity using our experimental approach of Raman thermometry, crucially performing these measurements under vacuum conditions [**Figure 8.4**].

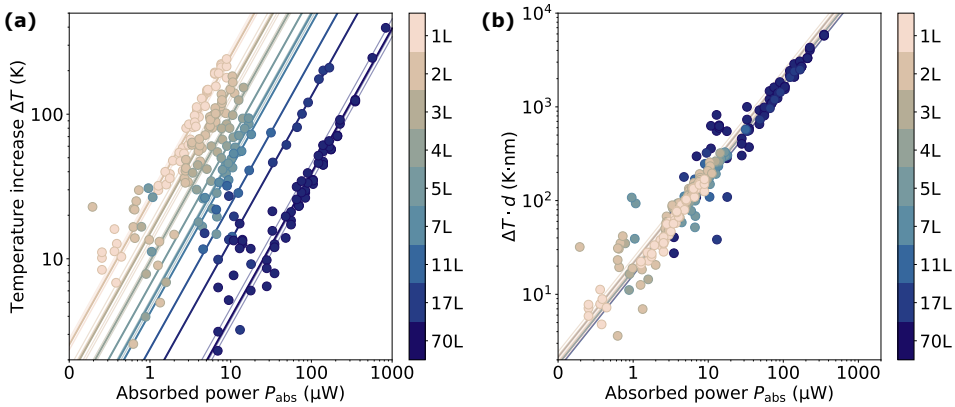

FIGURE 8.4: **Raman thermometry of $MoSe_2$ as a function of crystal thickness. (a)** Temperature rise ΔT as a function of absorbed power P_{abs} for $MoSe_2$ crystals of varying thickness. **(b)** The same data as in panel (a), now multiplied by the thickness of each crystal, such that the slope is representative of κ. Each layer thickness has its own corresponding color (see color bars). Solid lines are linear fits to the data.

We plot ΔT as a function of absorbed power P_{abs} [Fig. 8.4**a**], and observe a clear trend with the thickness of the samples: thinner crystals heat up more significantly for the same absorbed power. This is intuitive, as thinner crystals have a smaller volume in which the same amount of heat is deposited, and thus a smaller thermal capacitance. Plotting $\Delta T \cdot d$ as a function of P_{abs} [Fig. 8.4**b**] gives a slope that is directly representative of the thermal conductivity κ (see Equation 8.3). We now see that all data points fall on almost the same slope, suggesting that the intrinsic in-plane κ of $MoSe_2$ is not dramatically affected by crystal thickness. A quantitative analysis of the experimental data using Equation 8.3 results in a weakly decreasing thermal conductivity for crystals with a thickness of 70L down to 1L.

Figure 8.5 shows our results for the in-plane thermal conductivity κ of $MoSe_2$ with the available experimental values in the literature [59, 69, 70, 186]. Most strikingly, our systematic thickness variation demonstrates a relatively weak effect of crystal thickness. The thermal conductivity is smaller for the thinnest samples than for the thickest sample (∼70L), whereas some experimental literature values suggest the opposite trend (see Fig. 8.5). We ascribe this discrepancy to the fact that not all measurements in the literature were performed under the same conditions nor with similar substrates, and often using non-coated substrates with rather small hole sizes, which can all lead to an overestimation of the thermal conductivity, in particular for monolayer samples. Besides, if any contamination would be present on a monolayer sample, this could also act as a thermal dissipation channel, giving rise to an increased apparent thermal conductivity. In our case, we used artifact-minimized substrates and well-characterized, clean samples [96].

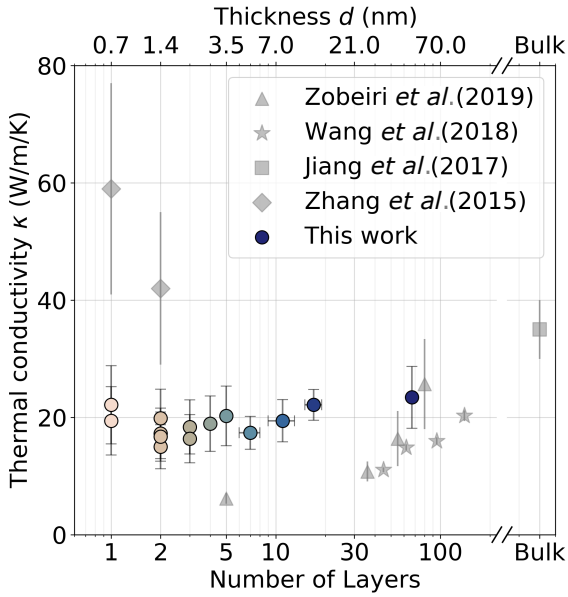

FIGURE 8.5: **In-plane thermal conductivity of $MoSe_2$ vs literature.** Comparison of the experimentally measured κ of $MoSe_2$ (*coloured circles*) with values reported in the literature (*gray symbols*): [70] (◆); [59] (■); [186] (★); and [69] (▲).

8.3.2 Theoretical results and discussion of thickness effect

We compute the thermal properties of $MoSe_2$ using density functional theory, as implemented in SIESTA, in combination with the TDEP method, allowing us to

account for phonons at a finite temperature. In brief (see Section 8.2.2), with this method we identify harmonic and anharmonic force constants taking into account atomic displacements and forces of a canonical ensemble at a given temperature. We compute the phonon dispersions and the anharmonic terms of the interatomic potential, in order to obtain the in-plane lattice thermal conductivity κ. With this method, we compute κ for bulk $MoSe_2$, and for thin crystals with thicknesses from 6L down to monolayer, and between 300 and 500 K [127] (see Ref. [185] for results on other bulk and monolayer TMDs as compared to silicon and silicene).[1]

We compare the theoretically obtained in-plane thermal conductivity of $MoSe_2$ crystals with varying thicknesses to our experimental results [**Figure 8.6a**]. For the thinnest crystals, we see that the first-principles-based results at 400 K yield a κ of 15 W m^{-1} K^{-1} for 1L, weakly increasing to 21 W m^{-1} K^{-1} for 6L, and then increasing further to 32 W m^{-1} K^{-1} for bulk. The experimental values similarly increase from a value below 20 W m^{-1} K^{-1} for bilayer sample, to a value above 20 W m^{-1} K^{-1} for 17L and 70L. Considering the experimental uncertainty and the temperature range of the theoretical results, our results are in quantitative agreement. Importantly, both results show that there is a weak effect of crystal thickness on the thermal conductivity. Furthermore, if there is any effect, it is opposite to the effect in suspended graphite, which shows an increase in thermal conductivity upon decreasing crystal thickness, with monolayer graphene exhibiting the largest thermal conductivity [35, 56, 57].

The results of our first-principles calculations provide important physical insights for the observed weak effect of crystal thickness on κ for TMDs: we examine which phonons contribute to the total thermal conductivity by plotting the spectrally decomposed thermal conductivity κ_{spec} of $MoSe_2$ (see Fig. 8.6**b**). We find that for bulk crystals, the largest contribution comes from modes around 1 THz. This contribution gradually decreases with the crystal thickness. However, toward the monolayer limit, modes with a frequency well below 1 THz start playing an important role. We show the cumulative thermal conductivity as a function of MFP (see Fig. 8.6**c**), and observe that in the monolayer case, an increased fraction of heat is carried by low-frequency modes with a relatively long MFP. These results also highlight the importance of using large hole sizes, as a significant fraction of κ is carried by phonons with a MFP of several microns, and confirm that our experimental hole size is not significantly affecting the extracted κ through boundary scattering: phonons with a MFP <7.5 μm contribute to >90% of the total κ.

[1] Silicene is the two-dimensional allotrope of silicon.

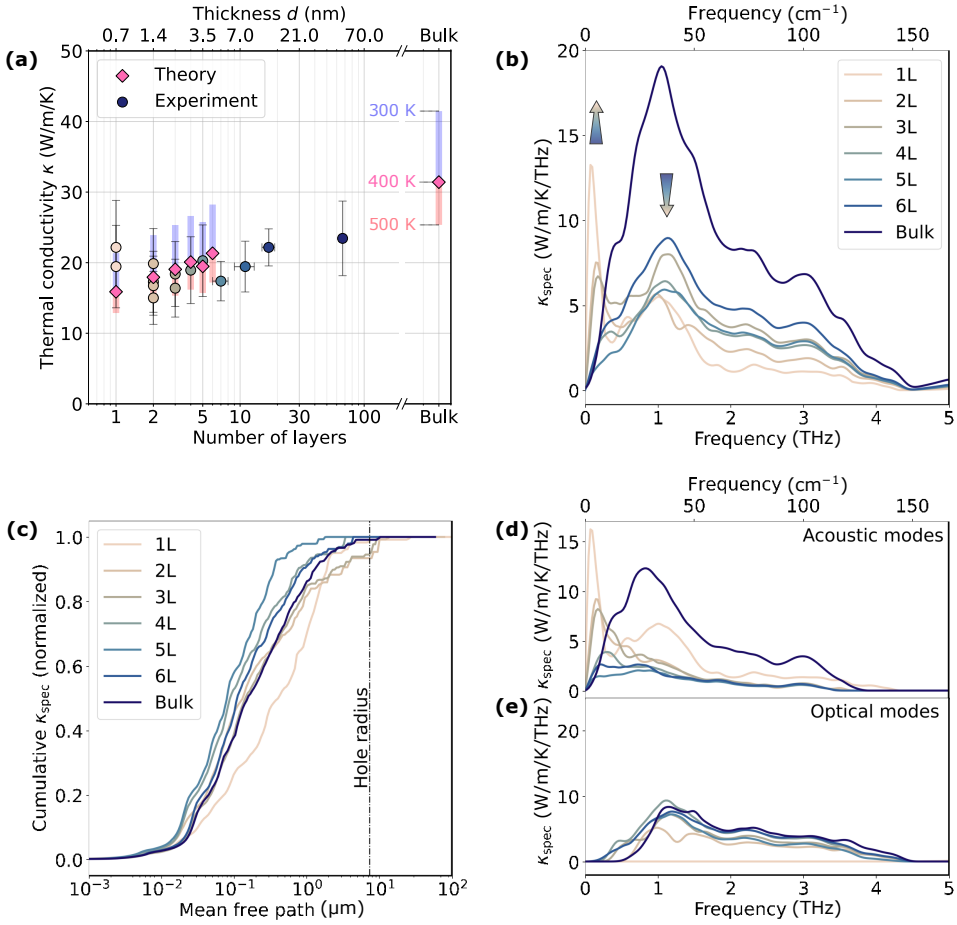

FIGURE 8.6: **Microscopic understanding of heat transport in $MoSe_2$.** **(a)** In-plane thermal conductivity of $MoSe_2$ crystals as a function of thickness, using our experimental (*circles*) and theoretical (*diamonds*) approach. The experimental error bars represent the 70% confidence interval, while the theoretical conductivities show how the values vary between a temperature of 300 and 500 K. **(b)** Spectrally decomposed thermal conductivity κ_{spec} as a function of phonon frequency indicating how, toward thinner films, an increasing contribution from a sub-THz mode compensates the decreasing contribution from modes around 1 THz. **(c)** Decomposed in-plane thermal conductivity as a function of phonon MFP. The cumulative thermal conductivity is normalized by the overall in-plane thermal conductivity. **(d,e)** Spectrally decomposed thermal conductivity κ_{spec} for (d) acoustic-like modes and (e) optical-like modes.

In order to gain more understanding of the key phonon modes, we decompose the spectral contribution into acoustic modes (see Fig. 8.6**d**) and low-frequency optical modes (see Fig. 8.6**e**). For the latter, we only take into account modes below 4 THz: the thermal conductivity of higher optical modes is negligible. The contribution of the optical modes, which are centered slightly above 1 THz and have an interlayer character, weakly decreases with decreasing crystal thickness. The acoustic contribution that is centered below 1 THz exhibits stronger thickness effects, with the most striking effect being the increasingly strong contribution of the flexural mode situated at $\sim$0.1 THz for ultrathin $MoSe_2$. Thus, from the simulation results in Figure 8.6**b-e** we understand that toward the monolayer limit, the decreasing contribution to κ from modes around 1 THz is rather effectively compensated by the increasing contribution of modes with a much lower frequency, in particular a low-energy flexural mode, resulting in an overall weak effect of material thickness.

This is a surprising result, because both the phonon dispersions and the phonon lifetimes (see Ref. [127]) change drastically with thickness, as is also clear from the spectrally decomposed thermal conductivity in Figure 8.6. Moreover, it is remarkable that significant amounts of heat are carried by modes with a MFP of several micrometers in a material with sub-nanometer thickness. This shows that out-of-plane boundary scattering does not play any role for the in-plane thermal conductivity of 2D van der Waals bonded TMDs. This is in large contrast with thin films of 3D bonded materials, where the thermal conductivity is typically thought to be limited by boundary scattering at the film surface, limiting the out-of-plane MFP to an effective scattering thickness. For 2D materials this is not the case: the very long lifetimes of low energy modes in thin $MoSe_2$ are made possible by the weakness of the van der Waals interlayer scattering, which is generic for all 2D materials, and leads to the well-known thermal transport anisotropy of an order of magnitude [59]. In our theoretical simulations, the full physical thickness is taken into account: surface vibrations are distinguished explicitly, and the scattering between bulk-localized and surface-localized modes is included in the anharmonic three-phonon interatomic force constants. The simulated surface does not contain additional sources of scattering (strain, residues, defects, etc.) which would also limit the mean free path. The agreement with experiments is a further confirmation of the very clean and ideal nature of the experimental samples.

8.3.3 Out-of-plane heat dissipation to the environment

Many properties of thin, layered materials have been shown to be sensitive to the environment [99]. In the case of thermal properties, a relatively small effect caused by heat transport to gas molecules was observed for suspended graphene [74]. We examine the effect of the surrounding environment on thermal transport in our $MoSe_2$ crystals on gold-coated substrates, by performing Raman thermometry experiments both in vacuum and in air, for several samples with different thicknesses. In **Figure 8.7a**, we show the obtained apparent thermal conductivity κ_{app} as a function of flake thickness in the case of air, instead of vacuum. We find a thermal conductivity that is slightly higher in air than in vacuum for thick flakes, whereas it is almost an order of magnitude higher for monolayer $MoSe_2$. We repeated this experiment with a monolayer sample in nitrogen atmosphere, and found an even larger κ_{app}. The reason for this large effect is likely that the presence of air or nitrogen introduces an additional cooling channel: the out-of-plane heat dissipation which occurs by transfer to the environmental molecules as a sink (as schematically depicted in Fig. 8.8**a**). The relative effect of this competing dissipation channel is much larger than in the case of graphene, because the in-plane thermal conductivity of monolayer $MoSe_2$ is much smaller than that of graphene. We note that Equation 8.3 is not valid if there is an additional cooling channel, which means that the obtained apparent thermal conductivity κ_{app} in air is not an intrinsic material property of $MoSe_2$. However, it can be seen as an effective parameter describing heat transport in the combined air-$MoSe_2$ system. Thus, the obtained κ_{app} above 250 W m^{-1} K^{-1}, which is larger than the 140 W m^{-1} K^{-1} of bulk crystalline silicon [4], is a promising result.

In order to understand the observed effect of the environment in more detail, we include additional cooling channels in our simulation of the Raman thermometry experiment (see Section 8.2.2). We first consider radiative cooling, estimating its maximum possible contribution by using a ΔT of 200 K, which is the largest value we used in our experiment (see Figure 8.4**a**). The results can be found in Supporting Information of Ref. [127], and indicate a negligible effect of $<$0.1% for radiative cooling at such temperatures. Due to the T^4-scaling, this cooling channel will likely only start playing a role at significantly higher temperatures ($\Delta T \gg 200$ K). The next cooling channel we consider is that of out-of-plane heat dissipation from $MoSe_2$ to the surrounding air molecules. We plot the experimentally obtained loss fraction, defined as $\xi = 1 - \kappa_{vac}/\kappa_{app,air}$, as a function of surface-to-volume ratio of the crystal (see Figure 8.7**b**), and compare it to our simulation of the Raman thermometry experiment that includes an out-of-plane heat transfer term. We

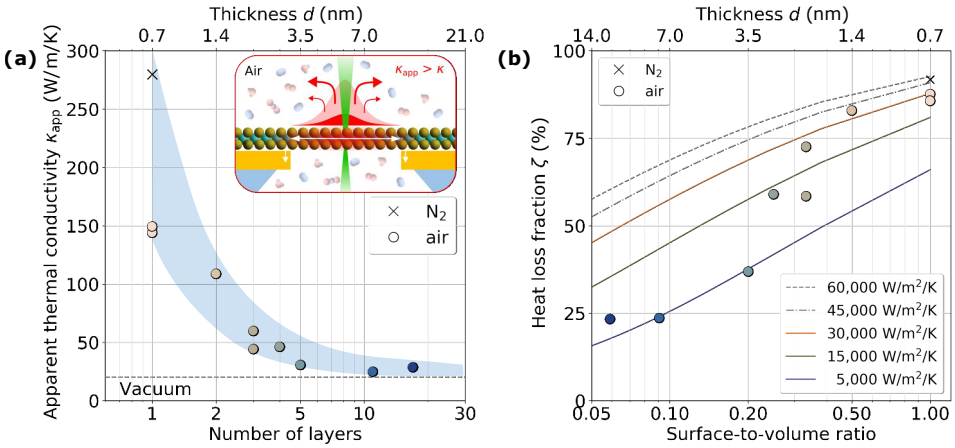

FIGURE 8.7: **Air-mediated losses in suspended $MoSe_2$. (a)** Apparent in-plane thermal conductivity of suspended $MoSe_2$ flakes on large, gold-coated holes as measured in air and nitrogen environments. **(b)** Relative power losses to air, extracted by comparing measurements performed in vacuum with those performed in air. Solid lines represent the simulated power losses for different heat transfer coefficients (see Section 8.2).

find a heat loss fraction $\xi \approx 20\%$ for the lowest surface-to-volume ratio, which we can reproduce with a heat transfer coefficient $h_c \approx 5\,000$ W m^{-2} K^{-1}. For monolayer $MoSe_2$ in air, on the other hand, we find >80% loss, which we can reproduce with a $h_c \approx 30\,000$ W m^{-2} K^{-1}. For the monolayer in nitrogen environment, we estimate a slightly larger coefficient $h_c \approx 50\,000$ W m^{-2} K^{-1}. These are much larger values than the typical values for the convective heat transfer coefficient found in the literature [40, 70], even for forced convection by gases: $h_c = 25 - 250$ W m^{-2} K^{-1} [187]. Our result, however, is very close to the value observed for monolayer graphene (2.9×10^4 W m^{-2} K^{-1}) [74], and close to the ideal h_c to air at ambient pressure and temperature with an ideal molecular accommodation coefficient of 10^5 W m^{-2} K^{-1} [74]. The larger heat transfer coefficient for nitrogen, compared to air, could be related to the absence of humidity. Importantly, these results provide clear evidence that out-of-plane heat dissipation to air plays a significant role in the cooling dynamics of suspended ultrathin materials, and that cooling is significantly more efficient for atomically thin crystals than for thicker crystals. When such thin crystals are placed in air, their overall cooling ability is enhanced by their efficient interaction with air molecules. The mechanism for this is likely the coupling of phonon modes in $MoSe_2$ to various degrees of motion of the surrounding molecules, including their vibrational modes [188]. This is very relevant and beneficial for designing applications where the thermal

management of TMDs and other layered materials is a crucial consideration.

8.3.4 Assessment of substrate-induced experimental artifacts

So far we have seen that, in order to extract an intrinsic thermal conductivity κ of atomically thin suspended crystals, it is crucial to perform the measurements under vacuum conditions (see Fig. 8.8**a**). Now, we show how substrate properties can also affect the extracted κ leading to a non-intrinsic, apparent thermal conductivity κ_{app} (see Figure 8.8**b,c**). We asses the influence of substrate-induced experimental artifacts on our measurements by using Si_3N_4 substrates without the gold-coating, and coated substrates with smaller holes sizes (with hole radii of 2.5 and 5 μm).

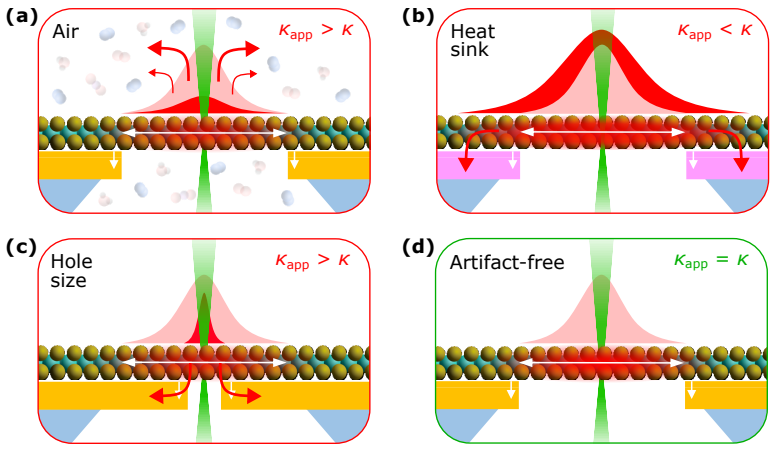

FIGURE 8.8: **Artifact identification and elimination.** **(a)** Side-view schematic of measurements performed in air, where out-of-plane heat dissipation occurs. **(b)** Substrate-induced artifacts due to inefficient heat sinking, leading to heat accumulation. **(c)** Substrate-induced artifacts due to small hole sizes. **(d)** Artifact-free measurements under vacuum conditions, using gold-coated substrates with large holes. The Gaussian profiles represent the expected (*pink*) and observed (*red*) temperature distribution.

Inefficient heat sinking

In **Figure 8.9** we show the impact of inefficient heat sinking. We first compare the results for two suspended flakes with a thickness of 17L placed on Si_3N_4 substrates with and without the 50 nm gold coating. We observe a much higher ΔT for the sample transferred on a holey substrate without gold coating (see Figure 8.9**a**),

which we ascribe to less efficient heat sinking (see Fig. 8.8**b**). We confirm this difference in heat sinking efficiency by measuring Raman spectra, with relatively high incident power, on the substrate-supported regions of a bilayer $MoSe_2$ flake, where ΔT is larger for the flake on non-coated substrate (Si_3N_4) than for that on the gold-coated substrate (see Figure 8.9**b**). The main reason for this is likely that the thermal conductivity of gold is larger than that of thin Si_3N_4 films [189]. Note that, on the substrate-supported region of a 2L sample with efficient heat sinking (*i.e.*, using gold-coated substrates), incident laser powers >1 mW are required to produce a temperature increase of 100 K (see Fig. 8.9**b**). In contrast, the incident power needed to increase the temperature on the suspended region by the same amount is more than an order of magnitude smaller (∼100 μW).

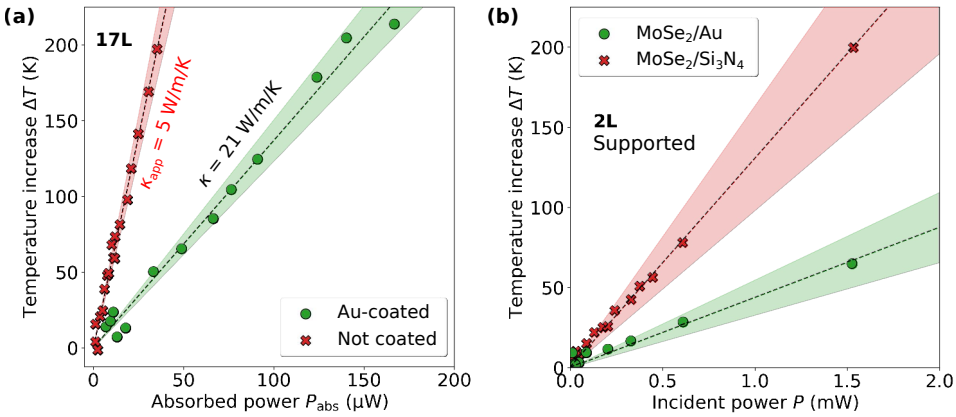

FIGURE 8.9: **Substrate-induced artifacts due to inefficient heat sinking.** **(a)** Temperature increase for suspended 17L $MoSe_2$ flakes using gold-coated (*green circles*) and substrates without gold-coating (*red crosses*). **(b)** Temperature increase on substrate-supported regions of 2L $MoSe_2$ on gold (*green circles*) and on Si_3N_4 (*red crosses*). Dashed lines are linear fits to the data, and shaded areas show the fitting error.

We conclude that heat sinking to the gold-coated substrate is efficient, implying that the requirements for using Equation 8.3 are met, and thus we obtain the intrinsic thermal conductivity κ. The less efficient heat sinking of the non-coated substrate leads to more heat accumulation on the suspended region of the flake and therefore a reduced apparent thermal conductivity κ_{app} when using Equation 8.3. Since in this case the boundary conditions used to arrive at Eq. 8.3 are not fulfilled, one should use a modified version of Eq. 8.3, taking into account, for example, the thermal boundary conductance between $MoSe_2$ and the substrate material, and the substrate's thermal conductivity. However, this requires accurate knowledge of such material parameters, which likely introduces additional

uncertainty and, possibly, errors in the obtained conductivity. We conclude that it is crucial to use gold-coated substrates, as this leads to efficient heat sinking, such that Equation 8.3 is valid.

Insufficiently large hole size

To study possible substrate-induced artifacts related to hole size, we fabricated monolayer $MoSe_2$ flakes suspended over holes with a radius of 2.5 and 5 µm on gold-coated substrates (see Figure 8.1**b**), in addition to the monolayer flakes suspended over holes with a radius of 7.5 µm. **Figure 8.10** shows the temperature increase for these suspended monolayer flakes, where we normalize to the $\ln(R/r_0)$-factor, such that the slope is (inversely) proportional to κ (see Equation 8.3). We find comparable results for holes with a radius of 5 and 7.5 µm, while the sample with the 2.5-µm hole gives rise to a lower ΔT, and therefore a higher κ_{app}.

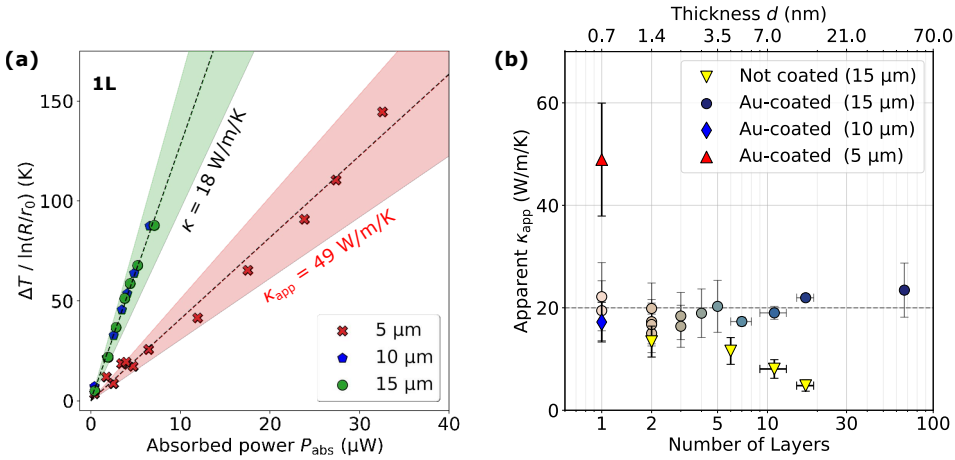

FIGURE 8.10: **Substrate-induced artifacts due to small hole size. (a)** The temperature increase ΔT, normalized to the $\ln(R/r_0)$-factor, for suspended monolayer $MoSe_2$ flakes on gold-coated substrates with hole diameters of 5 µm (*red crosses*), 10 µm (*blue pentagons*) and 15 µm (*green circles*). **(b)** Summary of the apparent thermal conductivity κ_{app} obtained using substrates with artifacts related to hole size (*blue and red scatters*) and to inefficient heat sinking (*yellow scatters*), as compared to the intrinsic κ obtained using artefact-minimized substrates (*circles*)

Raman thermometry measurements on crystals suspended over small holes are prone to several experimental artifacts. It is possible that phonons with a relatively long mean free path are restricted by the size of the suspended region, which would lead to an underestimation of κ. For small hole sizes, any non-ideal heat sinking of the substrate-supported region of the crystal will also have a larger

effect, because the smaller circumference implies a smaller region at the edge of the suspended crystal for heat sinking, leading to an underestimation of κ. Finally, laser absorption by the suspended crystal can be overestimated, as part of the incident light can be clipped by the small hole, leading to an overestimation of κ. Since we find an apparent thermal conductivity for the 2.5-μm hole that is more than two times larger than the intrinsic κ we find using the larger holes, we attribute the artifact we observe for small holes to an error in determining P_{abs} (see Figure 8.8**c**). A possible way to overcome this problem is to use a smaller laser spot size. However, this can introduce additional complications, such as non-diffusive heat transport [190], and does not resolve the other possible artifacts induced by small holes. We conclude that it is crucial to use substrates with an efficient heat sink and relatively large holes, with a radius of at least 5 μm (see Figure 8.8**d**)

8.4 Conclusions

In this chapter, we have combined Raman thermometry with *ab initio* simulations to explore the impact of thickness on the thermal conductivity of suspended $MoSe_2$ crystals. Our experimental measurements showed excellent agreement with the computed in-plane lattice thermal conductivity, confirming the reliability of both approaches. Notably, both methods revealed that the influence of crystal thickness on lattice thermal conductivity κ is relatively weak, within a factor of two from monolayer to bulk $MoSe_2$. We explained this weak thickness influence as the result of competing effects in the phonon contribution to the thermal conductivity. In contrast, we identified a pronounced effect of the surrounding environment on thermal transport, particularly in monolayer $MoSe_2$. This sensitivity arises from significant out-of-plane heat dissipation, characterized by an unexpectedly large heat transfer coefficient. Overall, our findings offer valuable insights for the thermal characterization of other TMDs, and layered materials in general, and establish a foundation for tailoring thermal transport in a broad range of materials, with potential applications in flexible (opto-)electronic devices.

Contributions

Sebin Varghese and I fabricated the suspended $MoSe_2$ samples. I performed the Raman thermometry measurements with help from Sebin Varghese, using the Raman setup of Prof. Clivia Sotomayor Torres. I analyzed the experimental data with inputs from Sebin Varghese, Dr. Jake D. Mehew and Dr. Alexander Block. I performed the optical absorption measurements. Dr. Roberta Farris (theory) and I (experiment) wrote the original manuscript. I sincerely thank Andrea Pitillas Martínez for bringing the concept of the Raman thermometry experiment to life through her 3D representation (see Fig. 8.2**c,d**).

Chapter 9

Summary and Outlook

The increasing demand for improved thermal management in electronics, photonics, and energy harvesting has driven extensive research into nanoscale heat transport. To unravel the fundamentals of thermal conduction at the nanoscale, and overcome the limitations of conventional 3D-bonded materials, a wide range of low- and 2-dimensional van der Waals materials have been explored using both experimental and computational approaches. These studies aim to clarify how reduced dimensionality, confinement, and interfaces reshape phonon dynamics and thermal transport, providing key insights needed for the rational design of next-generation materials and devices.

In this thesis, we designed a dry-transfer setup to manipulate 2D vdW materials enabling the deterministic transfer of flakes onto arbitrary substrates, the fabrication of thickness-controlled suspended samples, encapsulation, assembly and even device integration [Chapter 3]. We have used this setup to fabricate both thickness-controlled MoS_2 flakes supported on standard SiO_2/Si substrates, and thickness-controlled $MoSe_2$ flakes suspended over substrates with large (several micrometers in diameter) circular holes. We have exploited our suspended $MoSe_2$ flakes to perform a thorough characterization of the structural and optical properties of these flakes. Our optical measurements on suspended $MoSe_2$ flakes enabled, for the first time, direct measurements of their thickness-dependent optical absorption at 532 nm wavelengths.

We then built a pump-probe optothermal setup, specifically designed to explore thermal transport properties at the nanoscale with high spatial and temporal resolutions [Chapter 4]. We extensively reviewed the time-domain thermoreflectance theory and implemented a thermal model —based on Fourier heat transport— using Python to simulate the signals we obtained using our lock-in amplifier-based

optothermal setup, with the aim of studying out-of-plane heat transport across our substrate-supported MoS_2 flakes [Chapter 5]. We used a bare substrate and thick MoS_2 flakes as control samples to validate our optothermal setup and thermal model, with which we obtained out-of-plane thermal conductivity (for the thick flakes) and interfacial thermal conductance (for the bare substrate) values in agreement with previous experimental and theoretical works [Chapter 6].

We extracted the total interfacial thermal resistance provided by our substrate-supported thin MoS_2 flakes, and retrieved increased thermal resistance values for flakes with intermediate flake thicknesses of a few nanometers compared to previous experimental works [Chapter 7]. We attributed these discrepancies to multiple unexpected observations, such as an oscillatory behavior of the TDTR signal magnitude with flake thickness, with a strong suppression of the thermoreflectance signal at specific thickness values. We hypothesized that coherent heat conduction and phonon heat interference could be responsible for these observations, and confirmed with temperature-dependent TDTR measurements (down to 120 K) that these effects are tunable by the specific thickness-temperature conditions. Additionally, we explored the possibility of our signals being also influenced by (optical) photon interference, by using the transfer matrix method to estimate the effective thermoreflectance coefficient of our gold transducer layers within our multilayer structure. Our results suggest that both, thermal and optical effects could be responsible for our findings. Moreover, we performed additional measurements with increased sampling at early time delays to further understand how the presence of thin MoS_2 flakes alters the heat generation mechanisms in our experiments, providing a rich landscape of optical, thermal and optothermal information.

Finally, we exploited our thickness-controlled $MoSe_2$ flakes suspended over circular holes to study in-plane heat transport using a standard Raman thermometry setup [Chapter 8]. Our experiments benefited from a suspended sample geometry (exempt of substrate interactions) and direct optical absorption measurements to retrieve the intrinsic, in-plane thermal conductivity κ_r of our samples. We obtained similar κ_r independent of the thickness, which is only a factor of two smaller for monolayer $MoSe_2$ (with sub-nanometer thickness) compared to bulk $MoSe_2$. This is in strong contrast to the ever degrading thermal properties of conventional 3D-bonded materials, like silicon, when approaching the nanometer scales. We explain our results thanks to the insights obtained from *ab initio* simulations using density functional theory and temperature-dependent effective potentials (importantly, at finite temperatures). For bulk $MoSe_2$, most contribution

to heat transport comes from phonons centered around 1 THz frequencies, while the contribution from these modes decreases with flake thickness. For thin flakes, however, the reduction in κ_r is compensated by the appearance of low-frequency (long mean free path) flexural phonon modes thus maintaining a large thermal conductivity value, larger than that of silicon membranes ten times thicker than our flakes [4].

Last, we explored the effects of (*i*) the surrounding environment, (*ii*) heat sinking material and (*iii*) hole size on the apparent in-plane thermal conductivity $\kappa_{r,\text{app}}$ we retrieved from our experiments. On the one hand, mono- and bilayer $MoSe_2$ flakes exhibit enhanced heat dissipation capabilities in air —because of their large surface-to-volume ratio— given the additional cooling channels introduced by direct heat transfer to environmental molecules. On the other hand, decreasing the heat sinking efficiency led to a reduced $\kappa_{r,\text{app}}$; and using hole sizes that are too small ($\leq$ 5 μm) resulted in an artificially larger $\kappa_{r,\text{app}}$. The main reason to use an apparent κ_r is the deviations from strictly diffusive, in-plane heat transport with perfect heat sinking in these conditions.

9.1 Outlook and Conclusions

Our findings provide useful insights for the thermal characterization of few-layer 2D vdW materials, and contribute to the understanding and control ability of heat flow at the nanoscale. Many applications could benefit from the knowledge we have developed, which advance our ability to engineer thermal properties in low-dimensional systems. This progress is particularly relevant for next-generation electronics, optoelectronics, and energy technologies, where efficient thermal management is crucial for performance and reliability. At the same time, our results highlight current challenges in modeling and measuring anisotropic heat transport at the atomic scale, suggesting that future efforts should focus on integrating advanced optical techniques, improved sample design, and extended (opto)thermal simulations. Together, these directions pave the way toward a more complete control of heat in emerging quantum and nanoscale devices.

Importantly, our experimental investigation of coherent phonon heat and coherent phonon interference within a single 2D vdW material calls for further explorations of these effects, and highlights the need to systematically probe their role across different material platforms and device geometries. Such studies could help clarify the extent to which coherence can be harnessed to manipulate heat

flow, potentially enabling new strategies for phonon engineering beyond conventional diffusive transport. In particular, combining ultrafast optical techniques with advanced sample design may allow thermal transport to be actively tuned through interference effects, opening prospects for applications in thermal logic, phononic devices, and quantum technologies.

While coherent heat conduction effects remain an open frontier requiring deeper exploration, our work investigating in-plane heat transport arrives at a consistent and comprehensive understanding of in-plane heat conduction in 2D vdW materials. Our work benefits from a systematic and reproducible fabrication of clean and atomically flat $MoSe_2$ flakes suspended over circular holes, using artifact-minimized substrates, and importantly explores the effects of the environment on the retrieved thermal properties of our samples. In combination with state-of-the-art *ab initio* simulations, we provide a unifying physical picture of in-plane heat flow in TMDs. Our findings reveal crucial knowledge for applications ranging from next-generation electronics and optoelectronics to thermal management and energy technologies, and establish a solid foundation for future efforts aiming to control heat at the atomic scale.

Bibliography

[1] G. E. Moore, "Cramming more components onto integrated circuits", *Electronics* **38**(8), 114–117 (1965).

[2] IEEE International Roadmap for Devices and Systems (IRDS), *IRDS 2021: executive summary*, tech. rep., Accessed 2025-09-14 (Institute of Electrical and Electronics Engineers (IEEE), 2021).

[3] C. J. Lockhart de la Rosa and K. Gouri Sankar, 2D-material based devices in the logic scaling roadmap, Accessed: 2025-08-18, IMEC, (2025)

[4] E. Chávez-Ángel, J. S. Reparaz, J. Gomis-Bresco, M. R. Wagner, J. Cuffe, B. Graczykowski, A. Shchepetov, H. Jiang, M. Prunnila, J. Ahopelto, F. Alzina, and C. M. Sotomayor Torres, "Reduction of the thermal conductivity in free-standing silicon nano-membranes investigated by non-invasive Raman thermometry", *APL Materials* **2**(1), 012113 (2014).

[5] D. Akinwande, C. Huyghebaert, C.-H. Wang, M. I. Serna, S. Goossens, L.-J. Li, H.-S. P. Wong, and F. H. L. Koppens, "Graphene and two-dimensional materials for silicon technology", *Nature* **573**(7775), 507–518 (2019).

[6] M. C. Lemme, D. Akinwande, C. Huyghebaert, and C. Stampfer, "2D materials for future heterogeneous electronics", *Nature Communications* **13**(1), 1392 (2022).

[7] C. Wu, S. Brems, D. Yudistira, D. Cott, A. Milenin, K. Vandersmissen, A. Maestre, A. Centeno, A. Zurutuza, J. Van Campenhout, C. Huyghebaert, D. Van Thourhout, and M. Pantouvaki, "Wafer-scale integration of single layer graphene electroabsorption modulators in a 300 mm CMOS pilot line", *Laser & Photonics Reviews* **17**(6), 2200789 (2023).

[8] X. Zou, Y. Xu, and W. Duan, "2D materials: rising star for future applications", *The Innovation* **2**(2), 100115 (2021).

[9] Y. Zhao, Y. Cai, L. Zhang, B. Li, G. Zhang, and J. T. L. Thong, "Thermal transport in 2D semiconductors—considerations for device applications", *Advanced Functional Materials* **30**(8), 1903929 (2020).

[10] K. S. Novoselov, A. K. Geim, S. V. Morozov, D.-e. Jiang, Y. Zhang, S. V. Dubonos, I. V. Grigorieva, and A. A. Firsov, "Electric field effect in atomically thin carbon films", *Science* **306**(5696), 666–669 (2004).

[11] R. Frisenda, Y. Niu, P. Gant, M. Muñoz, and A. Castellanos-Gómez, "Naturally occurring van der Waals materials", *npj 2D Materials and Applications* **4**(1), 38 (2020).

[12] K. S. Kim, D. Lee, C. S. Chang, S. Seo, Y. Hu, S. Cha, H. Kim, J. Shin, J.-H. Lee, S. Lee, J. S. Kim, K. H. Kim, J. M. Suh, Y. Meng, B.-I. Park, J.-H. Lee, H.-S. Park, H. S. Kum, M.-H. Jo, G. Y. Yeom, K. Cho, J.-H. Park, S.-H. Bae, and J. Kim, "Non-epitaxial

single-crystal 2D material growth by geometric confinement", *Nature* **614**(7946), 88–94 (2023).

[13] D. Moon, W. Lee, C. Lim, J. Kim, J. Kim, Y. Jung, H.-Y. Choi, W. S. Choi, H. Kim, J.-H. Baek, et al., "Hypotaxy of wafer-scale single-crystal transition metal dichalcogenides", *Nature* **638**(8052), 957–964 (2025).

[14] J.-H. Chen, C. Jang, S. Xiao, M. Ishigami, and M. S. Fuhrer, "Intrinsic and extrinsic performance limits of graphene devices on SiO_2", *Nature Nanotechnology* **3**(4), 206–209 (2008).

[15] D. Berman, S. A. Deshmukh, S. K. R. S. Sankaranarayanan, A. Erdemir, and A. V. Sumant, "Macroscale superlubricity enabled by graphene nanoscroll formation", *Science* **348**(6239), 1118–1122 (2015).

[16] D. Scarano and F. Cesano, "Graphene and other 2D layered nanomaterials and hybrid structures: synthesis, properties and applications", *Materials* **14**(23), 7108 (2021).

[17] F. Schwierz, "Graphene transistors", *Nature Nanotechnology* **5**(7), 487–496 (2010).

[18] T. Das, B. K. Sharma, A. K. Katiyar, and J.-H. Ahn, "Graphene-based flexible and wearable electronics", *Journal of Semiconductors* **39**(1), 011007 (2018).

[19] S. Pang, Y. Hernandez, X. Feng, and K. Müllen, "Graphene as transparent electrode material for organic electronics", *Advanced Materials* **23**(25), 2779–2795 (2011).

[20] M. D. Stoller, S. Park, Y. Zhu, J. An, and R. S. Ruoff, "Graphene-based ultracapacitors", *Nano Letters* **8**(10), 3498–3502 (2008).

[21] K. F. Mak, C. Lee, J. Hone, J. Shan, and T. F. Heinz, "Atomically thin MoS_2: a new direct-gap semiconductor", *Physical Review Letters* **105**(13), 136805 (2010).

[22] J. Guo, D. Xie, B. Yang, and J. Jiang, "Low-power logic computing realized in a single electric-double-layer MoS_2 transistor gated with polymer electrolyte", *Solid-State Electronics* **144**, 1–6 (2018).

[23] A. Daus, S. Vaziri, V. Chen, Ç. Köroğlu, R. W. Grady, C. S. Bailey, H. R. Lee, K. Schauble, K. Brenner, and E. Pop, "High-performance flexible nanoscale transistors based on transition metal dichalcogenides", *Nature Electronics* **4**(7), 495–501 (2021).

[24] D. Jariwala, A. R. Davoyan, G. Tagliabue, M. C. Sherrott, J. Wong, and H. A. Atwater, "Near-unity absorption in van der Waals semiconductors for ultrathin optoelectronics", *Nano Letters* **16**(9), 5482–5487 (2016).

[25] M. Amani, D.-H. Lien, D. Kiriya, J. Xiao, A. Azcatl, J. Noh, S. R. Madhvapathy, R. Addou, S. KC, M. Dubey, K. Cho, R. M. Wallace, S.-C. Lee, J.-H. He, J. W. Ager, X. Zhang, E. Yablonovitch, and A. Javey, "Near-unity photoluminescence quantum yield in MoS_2", *Science* **350**(6264), 1065–1068 (2015).

[26] Y. Wang, F. Iyikanat, X. Bai, X. Hu, S. Das, Y. Dai, Y. Zhang, L. Du, S. Li, H. Lipsanen, F. J. García de Abajo, and Z. Sun, "Optical control of high-harmonic generation at the atomic thickness", *Nano Letters* **22**(21), 8455–8462 (2022).

[27] C. Liu, J. Guo, L. Yu, J. Li, M. Zhang, H. Li, Y. Shi, and D. Dai, "Silicon/2D-material photodetectors: from near-infrared to mid-infrared", *Light: Science & Applications* **10**(1), 123 (2021).

[28] M. Abdullah, M. Younis, M. T. Sohail, S. Wu, X. Zhang, K. Khan, M. Asif, and P. Yan, "Recent progress of 2D materials-based photodetectors from UV to THz waves: principles, materials, and applications", *Small* **20**(47), 2402668 (2024).

[29] A. G. Ricciardulli and P. W. M. Blom, "Solution-processable 2D materials applied in light-emitting diodes and solar cells", *Advanced Materials Technologies* **5**(8), 1900972 (2020).

[30] S. Larentis, B. Fallahazad, and E. Tutuc, "Field-effect transistors and intrinsic mobility in ultra-thin $MoSe_2$ layers", *Applied Physics Letters* **101**(22), 223104 (2012).

[31] Y. Cao, V. Fatemi, S. Fang, K. Watanabe, T. Taniguchi, E. Kaxiras, and P. Jarillo-Herrero, "Unconventional superconductivity in magic-angle graphene superlattices", *Nature* **556**(7699), 43–50 (2018).

[32] K. P. Nuckolls, M. Oh, D. Wong, B. Lian, K. Watanabe, T. Taniguchi, B. A. Bernevig, and A. Yazdani, "Strongly correlated Chern insulators in magic-angle twisted bilayer graphene", *Nature* **588**(7839), 610–615 (2020).

[33] X. Xie, Q. Li, C. Liu, Y. Liu, C. Lee, K. Sun, and H. Deng, "2D material exciton-polariton transport on 2D photonic crystals", *Science Advances* **11**(21), eads0231 (2025).

[34] C. Heide, Y. Kobayashi, A. C. Johnson, T. F. Heinz, D. A. Reis, F. Liu, and S. Ghimire, "High-harmonic generation from artificially stacked 2D crystals", *Nanophotonics* **12**(2), 255–261 (2023).

[35] S. Ghosh, W. Bao, D. L. Nika, S. Subrina, E. P. Pokatilov, C. N. Lau, and A. A. Balandin, "Dimensional crossover of thermal transport in few-layer graphene", *Nature Materials* **9**(7), 555–558 (2010).

[36] X. Gu, B. Li, and R. Yang, "Layer thickness-dependent phonon properties and thermal conductivity of MoS_2", *Journal of Applied Physics* **119**(8), 085106 (2016).

[37] M. Goni, J. Yang, and A. J. Schmidt, "Enhanced thermal transport across monolayer MoS_2", *Nano Research* **11**(4), 2173–2180 (2018).

[38] P. Yuan, R. Wang, T. Wang, X. Wang, and Y. Xie, "Nonmonotonic thickness-dependence of in-plane thermal conductivity of few-layered MoS_2: 2.4 to 37.8 nm", *Physical Chemistry Chemical Physics* **20**(40), 25752–25761 (2018).

[39] A. Sood, F. Xiong, S. Chen, R. Cheaito, F. Lian, M. Asheghi, Y. Cui, D. Donadio, K. E. Goodson, and E. Pop, "Quasi-ballistic thermal transport across MoS_2 thin films", *Nano Letters* **19**(4), 2434–2442 (2019).

[40] E. Easy, Y. Gao, Y. Wang, D. Yan, S. M. Goushehgir, E.-H. Yang, B. Xu, and X. Zhang, "Experimental and computational investigation of layer-dependent thermal conductivities and interfacial thermal conductance of one- to three-layer WSe_2", *ACS Applied Materials & Interfaces* **13**(11), 13063–13071 (2021).

[41] M.-J. Lee, J.-H. Ahn, J. H. Sung, H. Heo, S. G. Jeon, W. Lee, J. Y. Song, K.-H. Hong, B. Choi, S.-H. Lee, and M.-H. Jo, "Thermoelectric materials by using two-dimensional materials with negative correlation between electrical and thermal conductivity", *Nature Communications* **7**(1), 12011 (2016).

[42] M. N. Luckyanova, J. Garg, K. Esfarjani, A. Jandl, M. T. Bulsara, A. J. Schmidt, A. J. Minnich, S. Chen, M. S. Dresselhaus, Z. Ren, E. A. Fitzgerald, and G. Chen, "Coherent phonon heat conduction in superlattices", *Science* **338**(6109), 936–939 (2012).

[43] M. Maldovan, "Phonon wave interference and thermal bandgap materials", *Nature Materials* **14**(7), 667–674 (2015).

[44] L. A. Walsh and C. L. Hinkle, "Van der waals epitaxy: 2D materials and topological insulators", *Applied Materials Today* **9**(1), 504–515 (2017).

[45] X. Wu and Q. Han, "Transition from incoherent to coherent phonon thermal transport across graphene/h-BN van der Waals superlattices", *International Journal of Heat and Mass Transfer* **184**, 122390 (2022).

[46] A. Sood, C. Sievers, Y. C. Shin, V. Chen, S. Chen, K. K. H. Smithe, S. Chatterjee, D. Donadio, K. E. Goodson, and E. Pop, "Engineering thermal transport across layered graphene-MoS_2 superlattices", *ACS Nano* **15**(12), 19503–19512 (2021).

[47] L. Zhao, L. Zhang, H. Song, H. Du, J. Wu, F. Kang, and B. Sun, "Incoherent phonon transport dominates heat conduction across van der Waals superlattices", *Applied Physics Letters* **121**(2), 022201 (2022).

[48] S. Vaziri, E. Yalon, M. M. Rojo, S. V. Suryavanshi, H. Zhang, C. J. McClellan, C. S. Bailey, K. K. H. Smithe, A. J. Gabourie, V. Chen, S. Deshmukh, L. Bendersky, A. V. Davydov, and E. Pop, "Ultrahigh thermal isolation across heterogeneously layered two-dimensional materials", *Science Advances* **5**(8), eaax1325 (2019).

[49] S. E. Kim, F. Mujid, A. Rai, F. Eriksson, J. Suh, P. Poddar, A. Ray, C. Park, E. Fransson, Y. Zhong, et al., "Extremely anisotropic van der Waals thermal conductors", *Nature* **597**(7878), 660–665 (2021).

[50] X. Li, X. Shi, D. Marian, D. Soriano, T. Cusati, G. Iannaccone, G. Fiori, Q. Guo, W. Zhao, and Y. Wu, "Rhombohedral-stacked bilayer transition metal dichalcogenides for high-performance atomically thin CMOS devices", *Science Advances* **9**(7), eade5706 (2023).

[51] M. I. Aroyo, ed., *International Tables for Crystallography, Volume A: Space-group symmetry*, 2nd Online Edition (International Union of Crystallography, Chester, England, 2016).

[52] R. Suzuki, M. Sakano, Y. J. Zhang, R. Akashi, D. Morikawa, A. Harasawa, K. Yaji, K. Kuroda, K. Miyamoto, T. Okuda, K. Ishizaka, R. Arita, and Y. Iwasa, "Valley-dependent spin polarization in bulk MoS_2 with broken inversion symmetry", *Nature Nanotechnology* **9**(8), 611–617 (2014).

[53] Y. Zhang, T.-R. Chang, B. Zhou, Y.-T. Cui, H. Yan, Z. Liu, F. Schmitt, J. Lee, R. Moore, Y. Chen, et al., "Direct observation of the transition from indirect to direct bandgap in atomically thin epitaxial $MoSe_2$", *Nature Nanotechnology* **9**(2), 111–115 (2014).

[54] S. Tongay, J. Zhou, C. Ataca, K. Lo, T. S. Matthews, J. Li, J. C. Grossman, and J. Wu, "Thermally driven crossover from indirect toward direct bandgap in 2D semiconductors: $MoSe_2$ versus MoS_2", *Nano Letters* **12**(11), 5576–5580 (2012).

[55] P. Tonndorf, R. Schmidt, P. Böttger, X. Zhang, J. Börner, A. Liebig, M. Albrecht, C. Kloc, O. Gordan, D. R. T. Zahn, S. M. de Vasconcellos, and R. Bratschitsch, "Photoluminescence emission and Raman response of monolayer MoS_2, $MoSe_2$, and WSe_2", *Optics Express* **21**(4), 4908–4916 (2013).

[56] W. Cai, A. L. Moore, Y. Zhu, X. Li, S. Chen, L. Shi, and R. S. Ruoff, "Thermal transport in suspended and supported monolayer graphene grown by chemical vapor deposition", *Nano Letters* **10**(5), 1645–1651 (2010).

[57] J.-U. Lee, D. Yoon, H. Kim, S. W. Lee, and H. Cheong, "Thermal conductivity of suspended pristine graphene measured by Raman spectroscopy", *Physical Review B* **83**, 081419 (2011).

[58] Q. Cai, D. Scullion, W. Gan, A. Falin, S. Zhang, K. Watanabe, T. Taniguchi, Y. Chen, E. J. G. Santos, and L. H. Li, "High thermal conductivity of high-quality monolayer boron nitride and its thermal expansion", *Science Advances* **5**(6), eaav0129 (2019).

[59] P. Jiang, X. Qian, X. Gu, and R. Yang, "Probing anisotropic thermal conductivity of transition metal dichalcogenides MX_2 (M = Mo, W and X = S, Se) using time-domain thermoreflectance", *Advanced Materials* **29**(36), 1701068 (2017).

[60] S. Huberman, R. A. Duncan, K. Chen, B. Song, V. Chiloyan, Z. Ding, A. A. Maznev, G. Chen, and K. A. Nelson, "Observation of second sound in graphite at temperatures above 100 K", *Science* **364**(6438), 375–379 (2019).

[61] T. Luo, J. Garg, J. Shiomi, K. Esfarjani, and G. Chen, "Gallium arsenide thermal conductivity and optical phonon relaxation times from first-principles calculations", *Europhysics Letters* **101**(1), 16001 (2013).

[62] K. T. Regner, D. P. Sellan, Z. Su, C. H. Amon, A. J. H. McGaughey, and J. A. Malen, "Broadband phonon mean free path contributions to thermal conductivity measured using frequency domain thermoreflectance", *Nature Communications* **4**(1), 1640 (2013).

[63] Z. Yan and S. Kumar, "Phonon mode contributions to thermal conductivity of pristine and defective β-Ga_2O_3", *Physical Chemistry Chemical Physics* **20**(43), 29236–29244 (2018).

[64] G. Romano, K. Esfarjani, D. A. Strubbe, D. Broido, and A. M. Kolpak, "Temperature-dependent thermal conductivity in silicon nanostructured materials studied by the Boltzmann transport equation", *Physical Review B* **93**, 035408 (2016).

[65] M. Sledzinska, B. Graczykowski, M. Placidi, **D. Saleta Reig**, A. E. Sachat, J. S. Reparaz, F. Alzina, B. Mortazavi, R. Quey, L. Colombo, S. Roche, and C. M. Sotomayor Torres, "Thermal conductivity of MoS_2 polycrystalline nanomembranes", *2D Materials* **3**(3), 035016 (2016).

[66] M. Sledzinska, R. Quey, B. Mortazavi, B. Graczykowski, M. Placidi, **D. Saleta Reig**, D. Navarro-Urrios, F. Alzina, L. Colombo, S. Roche, and C. M. Sotomayor Torres, "Record low thermal conductivity of polycrystalline MoS_2 films: tuning the thermal conductivity by grain orientation", *ACS Applied Materials & Interfaces* **9**(43), 37905–37911 (2017).

[67] E. Yalon, C. J. McClellan, K. K. H. Smithe, M. Muñoz Rojo, R. L. Xu, S. V. Suryavanshi, A. J. Gabourie, C. M. Neumann, F. Xiong, A. B. Farimani, and E. Pop, "Energy dissipation in monolayer MoS_2 electronics", *Nano Letters* **17**(6), 3429–3433 (2017).

[68] W. Zheng, C. Shao, Q. Wang, G. Li, and H. Li, "Understanding and engineering interfacial thermal conductance of two-dimensional materials", *Surfaces and Interfaces* **43**, 103538 (2023).

[69] H. Zobeiri, R. Wang, T. Wang, H. Lin, C. Deng, and X. Wang, "Frequency-domain energy transport state-resolved Raman for measuring the thermal conductivity of suspended nm-thick $MoSe_2$", *International Journal of Heat and Mass Transfer* **133**(1), 1074–1085 (2019).

[70] X. Zhang, D. Sun, Y. Li, G.-H. Lee, X. Cui, D. Chenet, Y. You, T. F. Heinz, and J. C. Hone, "Measurement of lateral and interfacial thermal conductivity of single-and bilayer MoS_2 and $MoSe_2$ using refined optothermal Raman technique", *ACS Applied Materials & Interfaces* **7**(46), 25923–25929 (2015).

[71] J. J. Bae, H. Y. Jeong, G. H. Han, J. Kim, H. Kim, M. S. Kim, B. H. Moon, S. C. Lim, and Y. H. Lee, "Thickness-dependent in-plane thermal conductivity of suspended MoS_2 grown by chemical vapor deposition", *Nanoscale* **9**(7), 2541–2547 (2017).

[72] B. Peng, H. Zhang, H. Shao, Y. Xu, X. Zhang, and H. Zhu, "Thermal conductivity of monolayer MoS_2, $MoSe_2$, and WS_2: interplay of mass effect, interatomic bonding and anharmonicity", *RSC Advances* **6**(7), 5767–5773 (2016).

[73] X. Gu and R. Yang, "Phonon transport in single-layer transition metal dichalcogenides: a first-principles study", *Applied Physics Letters* **105**(13), 131903 (2014).

[74] S. Chen, A. L. Moore, W. Cai, J. W. Suk, J. An, C. Mishra, C. Amos, C. W. Magnuson, J. Kang, L. Shi, et al., "Raman measurements of thermal transport in suspended monolayer graphene of variable sizes in vacuum and gaseous environments", *ACS Nano* **5**(1), 321–328 (2011).

[75] R. M. Costescu, M. A. Wall, and D. G. Cahill, "Thermal conductance of epitaxial interfaces", *Physical Review B* **67**(5), 054302 (2003).

[76] H. Casimir, "Note on the conduction of heat in crystals", *Physica* **5**(6), 495–500 (1938).

[77] J.-K. Yu, S. Mitrovic, D. Tham, J. Varghese, and J. R. Heath, "Reduction of thermal conductivity in phononic nanomesh structures", *Nature Nanotechnology* **5**(10), 718–721 (2010).

[78] C. W. Chang, D. Okawa, A. Majumdar, and A. Zettl, "Solid-state thermal rectifier", *Science* **314**(5802), 1121–1124 (2006).

[79] M. N. Luckyanova, J. Mendoza, H. Lu, B. Song, S. Huang, J. Zhou, M. Li, Y. Dong, H. Zhou, J. Garlow, L. Wu, B. J. Kirby, A. J. Grutter, A. A. Puretzky, Y. Zhu, M. S. Dresselhaus, A. Gossard, and G. Chen, "Phonon localization in heat conduction", *Science Advances* **4**(12), eaat9460 (2018).

[80] K. S. Novoselov, A. Mishchenko, A. Carvalho, and A. H. C. Neto, "2D materials and van der Waals heterostructures", *Science* **353**(6298), aac9439 (2016).

[81] R. Guo, Y.-D. Jho, and A. J. Minnich, "Coherent control of thermal phonon transport in van der Waals superlattices", *Nanoscale* **10**(30), 14432–14440 (2018).

[82] Y. Yoon, Z. Lu, C. Uzundal, R. Qi, W. Zhao, S. Chen, Q. Feng, W. Kim, M. H. Naik, K. Watanabe, T. Taniguchi, S. G. Louie, M. F. Crommie, and F. Wang, "Terahertz phonon engineering with van der Waals heterostructures", *Nature* **631**(8022), 771–776 (2024).

[83] Z. Shi, X. Wang, Y. Sun, Y. Li, and L. Zhang, "Interlayer coupling in two-dimensional semiconductor materials", *Semiconductor Science and Technology* **33**(9), 093001 (2018).

[84] J. Ravichandran, A. K. Yadav, R. Cheaito, P. B. Rossen, A. Soukiassian, S. Suresha, J. C. Duda, B. M. Foley, C.-H. Lee, Y. Zhu, et al., "Crossover from incoherent to coherent phonon scattering in epitaxial oxide superlattices", *Nature Materials* **13**(2), 168–172 (2014).

[85] C. Perez, L. Avazpour, M. K. Eryilmaz, T. Earles, S. Ruder, V. Gopalan, D. Botez, I. Knezevic, B. Ramos-Alvarado, B. M. Foley, and L. J. Mawst, "Incoherent-to-coherent crossover in thermal transport through III–V alloy superlattices", *Applied Physics Letters* **121**(23), 232201 (2022).

[86] H. Kwon, A. I. Khan, C. Perez, M. Asheghi, E. Pop, and K. E. Goodson, "Uncovering thermal and electrical properties of Sb_2Te_3/GeTe superlattice films", *Nano Letters* **21**(14), 5984–5990 (2021).

[87] V. Mishra, C. L. Hardin, J. E. Garay, and C. Dames, "A 3 omega method to measure an arbitrary anisotropic thermal conductivity tensor", *Review of Scientific Instruments* **86**(5), 054902 (2015).

[88] L. Yang, S. Yue, Y. Tao, S. Qiao, H. Li, Z. Dai, B. Song, Y. Chen, J. Du, D. Li, and P. Gao, "Suppressed thermal transport in silicon nanoribbons by inhomogeneous strain", *Nature* **629**(8014), 1021–1026 (2024).

[89] W. Jeong, S. Hur, E. Meyhofer, and P. Reddy, "Scanning probe microscopy for thermal transport measurements", *Nanoscale and Microscale Thermophysical Engineering* **19**(4), 279–302 (2015).

[90] S. Sandell, E. Chávez-Ángel, A. El Sachat, J. He, C. M. Sotomayor Torres, and J. Maire, "Thermoreflectance techniques and Raman thermometry for thermal property characterization of nanostructures", *Journal of Applied Physics* **128**(13), 131101 (2020).

[91] F. Hofmann, M. P. Short, and C. A. Dennett, "Transient grating spectroscopy: an ultrarapid, nondestructive materials evaluation technique", *Mrs Bulletin* **44**(5), 392–402 (2019).

[92] S. Varghese, J. D. Mehew, A. Block, **D. Saleta Reig**, P. Woźniak, R. Farris, Z. Zanolli, P. Ordejón, M. J. Verstraete, N. F. van Hulst, and K.-J. Tielrooij, "A pre-time-zero spatiotemporal microscopy technique for the ultrasensitive determination of the thermal diffusivity of thin films", *Review of Scientific Instruments* **94**(3), 034903 (2023).

[93] S. Varghese, Heat transport in layered semiconductors, PhD thesis (Universitat Autònoma de Barcelona, 2024).

[94] S. Varghese, J. Tur-Prats, J. D. Mehew, **D. Saleta Reig**, R. Farris, J. Camacho, J. A. Haibeh, A. Sokolov, P. Ordejón, S. Huberman, A. Beardo, F. X. Alvarez, and K.-J. Tielrooij, "Controllable hydro-thermoelastic heat transport in 2D semiconductors at room temperature", *Under review* (2025).

[95] F. Vialla and N. D. Fatti, "Time-domain investigations of coherent phonons in van der Waals thin films", *Nanomaterials* **10**(12), 2543 (2020).

[96] S. Varghese[†], **D. Saleta Reig**[†], J. D. Mehew, A. Block, A. El Sachat, E. Chávez-Ángel, M. Sledzinska, B. Ballesteros, C. M. S. Torres, and K.-J. Tielrooij, "Fabrication and characterization of large-area suspended $MoSe_2$ crystals down to the monolayer", *Journal of Physics: Materials* **4**(4), 046001 (2021), see Chapter 3.
[†]Equally contributing authors.

[97] S. Adam, E. Hwang, and S. D. Sarma, "Scattering mechanisms and Boltzmann transport in graphene", *Physica E: Low-dimensional Systems and Nanostructures* **40**(5), 1022–1025 (2008).

[98] M. L. Trolle, T. G. Pedersen, and V. Véniard, "Model dielectric function for 2D semiconductors including substrate screening", *Scientific Reports* **7**(1), 39844 (2017).

[99] A. J. Gabourie, S. V. Suryavanshi, A. B. Farimani, and E. Pop, "Reduced thermal conductivity of supported and encased monolayer and bilayer MoS_2", *2D Materials* **8**(1), 011001 (2020).

[100] A. Principi, M. B. Lundeberg, N. C. Hesp, K.-J. Tielrooij, F. H. Koppens, and M. Polini, "Super-Planckian electron cooling in a van der Waals stack", *Physical Review Letters* **118**(12), 126804 (2017).

[101] P. Xiao, Layered materials for thermal management and sensing applications, PhD thesis (Universitat Autònoma de Barcelona, 2022).

[102] R. Frisenda, E. Navarro-Moratalla, P. Gant, D. P. De Lara, P. Jarillo-Herrero, R. V. Gorbachev, and A. Castellanos-Gómez, "Recent progress in the assembly of nanodevices and van der Waals heterostructures by deterministic placement of 2D materials", *Chemical Society Reviews* **47**(1), 53–68 (2018).

[103] A. Castellanos-Gómez, M. Buscema, R. Molenaar, V. Singh, L. Janssen, H. S. Van Der Zant, and G. A. Steele, "Deterministic transfer of two-dimensional materials by all-dry viscoelastic stamping", *2D Materials* **1**(1), 011002 (2014).

[104] N. S. Taghavi, P. Gant, P. Huang, I. Niehues, R. Schmidt, S. Michaelis de Vasconcellos, R. Bratschitsch, M. García-Hernández, R. Frisenda, and A. Castellanos-Gómez, "Thickness determination of MoS_2, $MoSe_2$, WS_2 and WSe_2 on transparent stamps used for deterministic transfer of 2D materials", *Nano Research* **12**(7), 1691–1695 (2019).

[105] S. B. Desai, S. R. Madhvapathy, M. Amani, D. Kiriya, M. Hettick, M. Tosun, Y. Zhou, M. Dubey, J. W. Ager III, D. Chrzan, and A. Javey, "Gold-mediated exfoliation of ultralarge optoelectronically-perfect monolayers", *Advanced Materials* **28**(21), 4053–4058 (2016).

[106] F. Pizzocchero, L. Gammelgaard, B. S. Jessen, J. M. Caridad, L. Wang, J. Hone, P. Bøggild, and T. J. Booth, "The hot pick-up technique for batch assembly of van der Waals heterostructures", *Nature Communications* **7**(1), 11894 (2016).

[107] P. J. Zomer, M. H. D. Guimarães, J. C. Brant, N. Tombros, and B. J. van Wees, "Fast pick up technique for high quality heterostructures of bilayer graphene and hexagonal boron nitride", *Applied Physics Letters* **105**(1), 013101 (2014).

[108] Y. Wakafuji, R. Moriya, S. Masubuchi, K. Watanabe, T. Taniguchi, and T. Machida, "3D manipulation of 2D materials using microdome polymer", *Nano Letters* **20**(4), 2486–2492 (2020).

[109] V. Babacic, **D. Saleta Reig**, S. Varghese, T. Vasileiadis, E. Coy, K.-J. Tielrooij, and B. Graczykowski, "Thickness-dependent elastic softening of few-layer free-standing $MoSe_2$", *Advanced Materials* **33**(23), 2008614 (2021).

[110] G. Lo Gerfo Morganti, R. Rosati, G. D. Brinatti Vazquez, S. Varghese, **D. Saleta Reig**, E. Malic, N. F. van Hulst, and K.-J. Tielrooij, "Transient ultrafast and negative diffusion of charge carriers in suspended $MoSe_2$ from multilayer to monolayer", *Nature Communications* **16**(1), 5184 (2025).

[111] C. J. Brennan, J. Nguyen, E. T. Yu, and N. Lu, "Interface adhesion between 2D materials and elastomers measured by buckle delaminations", *Advanced Materials Interfaces* **2**(16), 1500176 (2015).

[112] J. Torres, Y. Zhu, P. Liu, S. C. Lim, and M. Yun, "Adhesion energies of 2D graphene and MoS_2 to silicon and metal substrates", *Physica Status Solidi (A)* **215**(1), 1700512 (2018).

[113] J. C. Shaw, H. Zhou, Y. Chen, N. O. Weiss, Y. Liu, Y. Huang, and X. Duan, "Chemical vapor deposition growth of monolayer $MoSe_2$ nanosheets", *Nano Research* **7**(4), 511–517 (2014).

[114] Y. Sun, D. Wang, and Z. Shuai, "Indirect-to-direct band gap crossover in few-layer transition metal dichalcogenides: a theoretical prediction", *The Journal of Physical Chemistry C* **120**(38), 21866–21870 (2016).

[115] X.-L. Li, W.-P. Han, J.-B. Wu, X.-F. Qiao, J. Zhang, and P.-H. Tan, "Layer-number dependent optical properties of 2D materials and their application for thickness determination", *Advanced Functional Materials* **27**(19), 1604468 (2017).

[116] J. S. Reparaz, E. Chávez-Ángel, M. R. Wagner, B. Graczykowski, J. Gomis-Bresco, F. Alzina, and C. M. Sotomayor Torres, "A novel contactless technique for thermal field mapping and thermal conductivity determination: two-laser Raman thermometry", *Review of Scientific Instruments* **85**(3), 034901 (2014).

[117] S. J. Cartamil-Bueno, M. Cavalieri, R. Wang, S. Houri, S. Hofmann, and H. S. van der Zant, "Mechanical characterization and cleaning of CVD single-layer h-BN resonators", *npj 2D Materials and Applications* **1**(1), 16 (2017).

[118] C. Palacios-Berraquero, D. M. Kara, A. R.-P. Montblanch, M. Barbone, P. Latawiec, D. Yoon, A. K. Ott, M. Loncar, A. C. Ferrari, and M. Atatüre, "Large-scale quantum-emitter arrays in atomically thin semiconductors", *Nature Communications* **8**(1), 15093 (2017).

[119] Z. Chen, H. Liu, X. Chen, G. Chu, S. Chu, and H. Zhang, "Wafer-size and single-crystal $MoSe_2$ atomically thin films grown on GaN substrate for light emission and harvesting", *ACS Applied Materials & Interfaces* **8**(31), 20267–20273 (2016).

[120] Y. Niu, S. Gonzalez-Abad, R. Frisenda, P. Marauhn, M. Drüppel, P. Gant, R. Schmidt, N. S. Taghavi, D. Barcons, A. J. Molina-Mendoza, et al., "Thickness-dependent differential reflectance spectra of monolayer and few-layer MoS_2, $MoSe_2$, WS_2 and WSe_2", *Nanomaterials* **8**(9), 725 (2018).

[121] A. Beal and H. Hughes, "Kramers-Kronig analysis of the reflectivity spectra of 2H-MoS_2, 2H-$MoSe_2$ and 2H-$MoTe_2$", *Journal of Physics C: Solid State Physics* **12**(5), 881 (1979).

[122] A. R. Beal, J. C. Knights, and W. Y. Liang, "Transmission spectra of some transition metal dichalcogenides. II. Group VIA: trigonal prismatic coordination", *Journal of Physics C: Solid State Physics* **5**(24), 3540 (1972).

[123] R. A. Bromley, R. B. Murray, and A. D. Yoffe, "The band structures of some transition metal dichalcogenides. III. Group VIA: trigonal prism materials", *Journal of Physics C: Solid State Physics* **5**(7), 759 (1972).

[124] N. Dong, Y. Li, Y. Feng, S. Zhang, X. Zhang, C. Chang, J. Fan, L. Zhang, and J. Wang, "Optical limiting and theoretical modelling of layered transition metal dichalcogenide nanosheets", *Scientific Reports* **5**(1), 14646 (2015).

[125] W. Zhao, Z. Ghorannevis, L. Chu, M. Toh, C. Kloc, P.-H. Tan, and G. Eda, "Evolution of electronic structure in atomically thin sheets of WS_2 and WSe_2", *ACS Nano* **7**(1), 791–797 (2013).

[126] R. Frisenda, Y. Niu, P. Gant, A. J. Molina-Mendoza, R. Schmidt, R. Bratschitsch, J. Liu, L. Fu, D. Dumcenco, A. Kis, et al., "Micro-reflectance and transmittance spectroscopy: a versatile and powerful tool to characterize 2D materials", *Journal of Physics D: Applied Physics* **50**(7), 074002 (2017).

[127] **D. Saleta Reig**, S. Varghese, R. Farris, A. Block, J. D. Mehew, O. Hellman, P. Woźniak, M. Sledzinska, A. El Sachat, E. Chávez-Ángel, S. O. Valenzuela, N. F. van Hulst, P. Ordejón, Z. Zanolli, C. M. Sotomayor Torres, M. J. Verstraete, and K.-J. Tielrooij, "Unraveling heat transport and dissipation in suspended $MoSe_2$ from bulk to monolayer", *Advanced Materials* **34**(10), 2108352 (2022), see Chapter 8.

[128] A. V. Oppenheim, R. W. Schafer, and J. R. Buck, *Discrete-Time Signal Processing*, 3rd (Pearson, Upper Saddle River, NJ, 2010).

[129] E. Hecht, *Optics*, 5th (Pearson, New York, 2017).

[130] D. G. Cahill, "Analysis of heat flow in layered structures for time-domain thermoreflectance", *Review of Scientific Instruments* **75**(12), 5119–5122 (2004).

[131] P. Jiang, X. Qian, and R. Yang, "Tutorial: time-domain thermoreflectance (TDTR) for thermal property characterization of bulk and thin film materials", *Journal of Applied Physics* **124**(16), 161103 (2018).

[132] A. J. Schmidt, Optical characterization of thermal transport from the nanoscale to the macroscale, PhD thesis (Massachusetts Institute of Technology, 2008).

[133] A. J. Schmidt, X. Chen, and G. Chen, "Pulse accumulation, radial heat conduction, and anisotropic thermal conductivity in pump-probe transient thermoreflectance", *Review of Scientific Instruments* **79**(11), 114902 (2008).

[134] A. Rosencwaig, "Thermal-wave imaging", *Science* **218**(4569), 223–228 (1982).

[135] C. A. Paddock and G. L. Eesley, "Transient thermoreflectance from thin metal films", *Journal of Applied Physics* **60**(1), 285–290 (1986).

[136] C. Thomsen, H. Maris, and J. Tauc, "Picosecond acoustics as a non-destructive tool for the characterization of very thin films", *Thin Solid Films* **154**(1), 217–223 (1987).

[137] J. P. Feser and D. G. Cahill, "Probing anisotropic heat transport using time-domain thermoreflectance with offset laser spots", *Review of Scientific Instruments* **83**(10), 104901 (2012).

[138] R. Wilson and D. G. Cahill, "Anisotropic failure of fourier theory in time-domain thermoreflectance experiments", *Nature Communications* **5**(1), 5075 (2014).

[139] P. Jiang, X. Qian, and R. Yang, "Time-domain thermoreflectance (TDTR) measurements of anisotropic thermal conductivity using a variable spot size approach", *Review of Scientific Instruments* **88**(7), 074901 (2017).

[140] Y. K. Koh and D. G. Cahill, "Frequency dependence of the thermal conductivity of semiconductor alloys", *Physical Review B* **76**(7), 075207 (2007).

[141] A. J. Minnich, J. A. Johnson, A. J. Schmidt, K. Esfarjani, M. S. Dresselhaus, K. A. Nelson, and G. Chen, "Thermal conductivity spectroscopy technique to measure phonon mean free paths", *Physical Review Letters* **107**(9), 095901 (2011).

[142] R. B. Wilson, B. A. Apgar, L. W. Martin, and D. G. Cahill, "Thermoreflectance of metal transducers for optical pump-probe studies of thermal properties", *Optics Express* **20**(27), 28829–28838 (2012).

[143] P. E. Raad, Thermo-reflectance thermography for submicron temperature measurements, Accessed: 2025-08-18, Electronics Cooling, (2008)

[144] A. Giri, J. T. Gaskins, B. F. Donovan, C. Szwejkowski, R. J. Warzoha, M. A. Rodriguez, J. Ihlefeld, and P. E. Hopkins, "Mechanisms of nonequilibrium electron-phonon coupling and thermal conductance at interfaces", *Journal of Applied Physics* **117**(10), 105105 (2015).

[145] H. S. Carslaw and J. C. Jaeger, *Conduction of Heat in Solids*, 2nd (Clarendon Press, Oxford, 1959).

[146] A. Feldman et al., "Algorithm for solutions of the thermal diffusion equation in a stratified medium with a modulated heating source", *High Temperatures-High Pressures* **31**(3), 293–298 (1999).

[147] J. H. Kim, A. Feldman, and D. Novotny, "Application of the three omega thermal conductivity measurement method to a film on a substrate of finite thickness", *Journal of Applied Physics* **86**(7), 3959–3963 (1999).

[148] D. Maillet, S. André, J.-C. Batsale, A. Degiovanni, and C. Moyne, *Thermal Quadrupoles: Solving the Heat Equation through Integral Transforms*, 1st (John Wiley & Sons, Chichester, 2000).

[149] J. Yang, E. Ziade, and A. J. Schmidt, "Uncertainty analysis of thermoreflectance measurements", *Review of Scientific Instruments* **87**(1), 014901 (2016).

[150] J. Liu, J. Zhu, M. Tian, X. Gu, A. Schmidt, and R. Yang, "Simultaneous measurement of thermal conductivity and heat capacity of bulk and thin film materials using frequency-dependent transient thermoreflectance method", *Review of Scientific Instruments* **84**(3), 034902 (2013).

[151] P. Jiang, B. Huang, and Y. K. Koh, "Accurate measurements of cross-plane thermal conductivity of thin films by dual-frequency time-domain thermoreflectance (TDTR)", *Review of Scientific Instruments* **87**(7), 075101 (2016).

[152] P. Jiang, L. Lindsay, and Y. K. Koh, "Role of low-energy phonons with mean-free-paths >0.8 μm in heat conduction in silicon", *Journal of Applied Physics* **119**(24), 245705 (2016).

[153] M. Efremov, E. Olson, M. Zhang, S. Lai, F. Schiettekatte, Z. Zhang, and L. Allen, "Thin-film differential scanning nanocalorimetry: heat capacity analysis", *Thermochimica Acta* **412**(1), 13–23 (2004).

[154] K. E. O'Hara, X. Hu, and D. G. Cahill, "Characterization of nanostructured metal films by picosecond acoustics and interferometry", *Journal of Applied Physics* **90**(9), 4852–4858 (2001).

[155] L. J. van der Pauw, "A method of measuring specific resistivity and Hall effect of discs of arbitrary shape", *Philips Research Reports* **13**(1), 1–9 (1958).

[156] N. W. Ashcroft and N. D. Mermin, *Solid State Physics*, 1st (Holt, Rinehart and Winston, New York, 1976).

[157] R. J. Stoner, H. J. Maris, T. R. Anthony, and W. F. Banholzer, "Measurements of the Kapitza conductance between diamond and several metals", *Physical Review Letters* **68**(10), 1563–1566 (1992).

[158] S. M. Hatam-Lee, F. Jabbari, and A. Rajabpour, "Interfacial thermal conductance between gold and SiO_2: a molecular dynamics study", *Nanoscale and Microscale Thermophysical Engineering* **26**(1), 40–51 (2022).

[159] J. El Hajj, C. Adessi, M. de San Feliciano, G. Ledoux, and S. Merabia, "Enhanced thermal conductance at interfaces between gold and amorphous silicon and between gold and amorphous silica", *Physical Review B* **110**(11), 115437 (2024).

[160] W. M. Haynes, *CRC Handbook of Chemistry and Physics*, 97th (CRC Press, Boca Raton, FL, 2016).

[161] J. Kimling, A. Philippi-Kobs, J. Jacobsohn, H. P. Oepen, and D. G. Cahill, "Thermal conductance of interfaces with amorphous SiO_2 measured by time-resolved magneto-optic Kerr-effect thermometry", *Physical Review B* **95**(18), 184305 (2017).

[162] K. Gordiz, M. G. Muraleedharan, and A. Henry, "Interface conductance modal analysis of a crystalline Si-amorphous SiO_2 interface", *Journal of Applied Physics* **125**(13), 135102 (2019).

[163] G. Cordoba and C. R. Brooks, "The heat capacity of gold from 300 to 1200 K: experimental data and analysis of contributions", *Physica Status Solidi (A)* **6**(2), 581–595 (1971).

[164] K. Yu, T. Devkota, G. Beane, G. P. Wang, and G. V. Hartland, "Brillouin oscillations from single Au nanoplate opto-acoustic transducers", *ACS Nano* **11**(8), 8064–8071 (2017).

[165] C. Y. Ho, R. W. Powell, and P. E. Liley, *Thermal Conductivity of the Elements: A Comprehensive Review*, Vol. 8, National Standard Reference Data Series (National Bureau of Standards, Washington, D.C., 1972).

[166] X. Fan, Z. Zhang, J. Zhu, K. Yuan, J. Zhou, X. Zhang, and D. Tang, "Systematic investigations on doping dependent thermal transport properties of single crystal silicon by time-domain thermoreflectance measurements", *International Journal of Thermal Sciences* **177**(1), 107558 (2022).

[167] K. M. Freedy, D. H. Olson, P. E. Hopkins, and S. J. McDonnell, "Titanium contacts to MoS_2 with interfacial oxide: interface chemistry and thermal transport", *Physical Review Materials* **3**(10), 104001 (2019).

[168] E. Yalon, B. Aslan, K. K. H. Smithe, C. J. McClellan, S. V. Suryavanshi, F. Xiong, A. Sood, C. M. Neumann, X. Xu, K. E. Goodson, T. F. Heinz, and E. Pop, "Temperature-dependent thermal boundary conductance of monolayer MoS_2 by Raman thermometry", *ACS Applied Materials & Interfaces* **9**(49), 43013–43020 (2017).

[169] S. V. Suryavanshi, A. J. Gabourie, A. Barati Farimani, and E. Pop, "Thermal boundary conductance of two-dimensional MoS_2 interfaces", *Journal of Applied Physics* **126**(5), 055107 (2019).

[170] Z. Chea, X. Wang, C. Guo, and F. Sun, "A complex signal fitting method for thermal property determination of TDTR measurement", *ES Energy & Environment* **11**(2), 58–64 (2021).

[171] C. Hua, X. Chen, N. K. Ravichandran, and A. J. Minnich, "Experimental metrology to obtain thermal phonon transmission coefficients at solid interfaces", *Physical Review B* **95**(20), 205423 (2017).

[172] Y. Pang, P. Jiang, and R. Yang, "Machine learning-based data processing technique for time-domain thermoreflectance (TDTR) measurements", *Journal of Applied Physics* **130**(8), 084901 (2021).

[173] S. McDonnell, C. Smyth, C. L. Hinkle, and R. M. Wallace, "MoS_2-titanium contact interface reactions", *ACS Applied Materials & Interfaces* **8**(12), 8289–8294 (2016).

[174] M. K. Zalalutdinov, J. T. Robinson, J. J. Fonseca, S. W. LaGasse, T. Pandey, L. R. Lindsay, T. L. Reinecke, D. M. Photiadis, J. C. Culbertson, C. D. Cress, and B. H. Houston, "Acoustic cavities in 2D heterostructures", *Nature Communications* **12**(1), 3267 (2021).

[175] P. Soubelet, A. A. Reynoso, A. Fainstein, K. Nogajewski, M. Potemski, C. Faugeras, and A. E. Bruchhausen, "The lifetime of interlayer breathing modes of few-layer 2H-$MoSe_2$ membranes", *Nanoscale* **11**(21), 10446–10453 (2019).

[176] P. B. Johnson and R. W. Christy, "Optical constants of the noble metals", *Physical Review B* **6**, 4370–4379 (1972).

[177] A. Zenji, J. M. Rampnoux, S. Grauby, and S. Dilhaire, "Ultimate-resolution thermal spectroscopy in time domain thermoreflectance (TDTR)", *Journal of Applied Physics* **128**(6), 065106 (2020).

[178] S. Ge, X. Liu, X. Qiao, Q. Wang, Z. Xu, J. Qiu, P.-H. Tan, J. Zhao, and D. Sun, "Coherent longitudinal acoustic phonon approaching THz frequency in multilayer molybdenum disulphide", *Scientific reports* **4**(1), 5722 (2014).

[179] B. Liu[‡], **D. Saleta Reig**[‡], et al., "Ultrafast thermalization dynamics of gold superstrates using adhesion layers and interfacial MoS_2", *In preparation* (2025), see Chapters 6 and 7.
[‡]Equally contributing authors.

[180] J. M. Soler, E. Artacho, J. D. Gale, A. García, J. Junquera, P. Ordejón, and D. Sánchez-Portal, "The SIESTA method for *ab initio* order-*N* materials simulation", *Journal of Physics: Condensed Matter* **14**(11), 2745 (2002).

[181] A. García, N. Papior, A. Akhtar, E. Artacho, V. Blum, E. Bosoni, P. Brandimarte, M. Brandbyge, J. I. Cerdá, F. Corsetti, et al., "SIESTA: recent developments and applications", *The Journal of Chemical Physics* **152**(20), 204108 (2020).

[182] O. Hellman, I. A. Abrikosov, and S. I. Simak, "Lattice dynamics of anharmonic solids from first principles", *Physical Review B* **84**(18), 180301 (2011).

[183] O. Hellman, P. Steneteg, I. A. Abrikosov, and S. I. Simak, "Temperature dependent effective potential method for accurate free energy calculations of solids", *Physical Review B* **87**(10), 104111 (2013).

[184] K. Lee, É. D. Murray, L. Kong, B. I. Lundqvist, and D. C. Langreth, "Higher-accuracy van der Waals density functional", *Physical Review B* **82**(8), 081101 (2010).

[185] R. Farris, O. Hellman, Z. Zanolli, **D. Saleta Reig**, S. Varghese, P. Ordejón, K.-J. Tielrooij, and M. J. Verstraete, "Microscopic understanding of the in-plane thermal transport properties of 2H transition metal dichalcogenides", *Physical Review B* **109**(12), 125422 (2024).

[186] R. Wang, T. Wang, H. Zobeiri, P. Yuan, C. Deng, Y. Yue, S. Xu, and X. Wang, "Measurement of the thermal conductivities of suspended MoS_2 and $MoSe_2$ by nanosecond ET-Raman without temperature calibration and laser absorption evaluation", *Nanoscale* **10**(48), 23087–23102 (2018).

[187] F. P. Incropera, D. P. DeWitt, T. L. Bergman, and A. S. Lavine, *Fundamentals of Heat and Mass Transfer*, 4th (John Wiley & Sons, New York, 1996).

[188] D. Mann, E. Pop, J. Cao, Q. Wang, K. Goodson, and H. Dai, "Thermally and molecularly stimulated relaxation of hot phonons in suspended carbon nanotubes", *The Journal of Physical Chemistry B* **110**(4), 1502–1505 (2006).

[189] X. Zhang and C. P. Grigoropoulos, "Thermal conductivity and diffusivity of free-standing silicon nitride thin films", *Review of Scientific Instruments* **66**(2), 1115–1120 (1995).

[190] V. Chiloyan, S. Huberman, A. A. Maznev, K. A. Nelson, and G. Chen, "Thermal transport exceeding bulk heat conduction due to nonthermal micro/nanoscale phonon populations", *Applied Physics Letters* **116**(16), 163102 (2020).

[191] M. Malyj and J. E. Griffiths, "Stokes/anti-Stokes Raman vibrational temperatures: reference materials, standard lamps, and spectrophotometric calibrations", *Applied Spectroscopy* **37**(4), 315–333 (1983).

[192] H. Hamaguchi and K. Iwata, "Time-Resolved Raman Spectroscopy", in *Encyclopedia of Spectroscopy and Spectrometry*, edited by J. C. Lindon, G. E. Tranter, and D. W. Koppenaal, 3rd (Academic Press, Oxford, 2017), pp. 463–468.

[193] J.-A. Yang, S. Parham, D. Dessau, and D. Reznik, "Novel electron-phonon relaxation pathway in graphite revealed by time-resolved Raman scattering and angle-resolved photoemission spectroscopy", *Scientific Reports* **7**(1), 40876 (2017).

[194] S. Han, C. Boguschewski, Y. Gao, L. Xiao, J. Zhu, and P. H. M. van Loosdrecht, "Incoherent phonon population and exciton-exciton annihilation dynamics in monolayer WS_2 revealed by time-resolved resonance Raman scattering", *Optics Express* **27**(21), 29949–29961 (2019).

[195] A. Block, Quantifying nanoscale carrier diffusion with ultrafast optical and photocurrent microscopy, PhD thesis (Universitat Politècnica de Catalunya, 2019).

Appendix A

Fabrication and Characterization of Suspended $MoSe_2$ Flakes

A.1 Components of our Dry-Transfer Setup

In Table A.1 we detail the components used to build the dry-transfer setup described in Chapter 3.

TABLE A.1: Summary of the different components needed to assemble our highly mechanically stable transfer stage whose cost is 12 000 €, including the anti-vibration table. The probe station functionality can be added for 3 000 €.

Component	Description	Part Number	Distributor	Price (€)
Optomechanical components	Optical breadboard	B3045A	Thorlabs	598.79
	Stainless steel post	39353	Edmund optics	57.00
	Rack and pinion	03609	Edmund optics	260.00
Zoom lens	2X F-mount Adapter tube	1-62922	Delta optics	487.00
	2X Lens Attachment	1-50015	Delta optics	253.00
	12X zoom motorized	1-51200	Delta optics	3953.00
	10 mm ø fiber input for 12X	2-50751	Delta optics	260.00
	Phase Desktop Enclosure	40234	Delta optics	1260.00
Stages	Linear translational stage (x2)	XR25C/M	Thorlabs	769.72
	Vertical translational stage	MVS005/M	Thorlabs	609.28
	Continuous rotational stage	CR1/M	Thorlabs	306.55
	Translational stage w/ diff. adjuster (x2)	MT1A/M	Thorlabs	748.72
	Dual-thread adapter M4-M6 screw (x4)	AE4M6M	Thorlabs	16.00
	Tilt stage	AIS-60B	OptoSigma	160.30
Illumination	LED point light	ML02221212	Boli optics	152.49
	Adapter plug	EC02411201	Boli optics	9.86
Camera	Canon EOS 6D	—	FotoK	825.62
	Continuous power supply	—	FotoK	171.90
	F-mount to Canon EF/E	—	Gobe	26.00
Temperature control	Thermocouple, K type	405-000	TC direct	15.00
	Temperature Controller	309-103	TC direct	81.00
	Mini transformer	714-1388	RS	15.32
	Solid state relay	102-5544	RS	15.28
	Mini vacuum pumps (x2)	ROB-10398	Electan electrónica	33.56
Table	Anti-vibration table	AZ-104008036	Biogen científica	925.00
Probe station	Magnetic base (x3)	MB175/M	Thorlabs	140.40
	Solid post (x3)	P100/M	Thorlabs	115.08
	Micro positioner (x2)	XYZ 300 TR	Quarter research	984.815
	Micro positioner	XYZ 300 TL	Quarter research	492.41
	Cable BNC to straight pin (x3)	—	Quarter research	118.18
	Test needle – Beryllium copper	H-20242-C	Quarter research	45.28
	Source measure unit	P2005A2-EU	Ossilia	1100.00
Total				**15 006.56**

A.2 The Transfer Matrix Method

The transfer matrix method (TMM) provides a rigorous framework to calculate the optical response of multilayer structures at normal incidence, accounting for the multiple internal reflections at the different interfaces. For a stack of $j = N$ layers, each characterized by a complex refractive index n_j and thickness L_j, the

propagation of the electric field is described by a transfer matrix for each layer:

$$\mathbf{M}_j = \begin{pmatrix} \cos\delta_j & \frac{i}{\eta_j}\sin\delta_j \\ i\eta_j \sin\delta_j & \cos\delta_j \end{pmatrix} \tag{A.1}$$

where $\delta_j = 2\pi n_j d_j/\lambda$ is the phase thickness and $\eta_j = n_j$ is the normal-incidence optical impedance. The overall transfer matrix for the full stack is the ordered product:

$$\mathbf{M}_{\text{total}} = \prod_{j=1}^{N} \mathbf{M}_j \tag{A.2}$$

The complex reflection coefficient at the interface between the stack and the substrate is then

$$r = \frac{m_{11} + m_{12}\eta_s - m_{21} - m_{22}\eta_0}{m_{11} + m_{12}\eta_s + m_{21} + m_{22}\eta_0} \tag{A.3}$$

where m_{ij} are the elements of $\mathbf{M}_{\text{total}}$, η_0 is the impedance of the incident medium (air), and η_s is that of the substrate.

The reflectivity is given by

$$R = |r|^2 \tag{A.4}$$

To quantify the temperature sensitivity of the reflectivity, we numerically compute the derivative dR/dT via a finite difference:

$$\frac{dR}{dT} \approx \frac{R(T_0 + \Delta T) - R(T_0)}{\Delta T} \tag{A.5}$$

where the temperature dependence of the optical constants $n_j(T)$ and $k_j(T)$ is incorporated for each layer.

We also use the TMM method in Chapter 7 to simulate our TDTR sample geometry —consisting of a Au/Ti transducer, MoS_2 spacers with varying thickness and a SiO_2/Si substrate— and compute the reflectance and thermoreflectance coefficients shown in Figure 7.8. As boundary conditions we use the fact that there are no back-reflected waves from the bottom surface of the semi-infinite Si slab.

Analytical solution for a single slab in air

For a single thin film of thickness L and complex refractive index n_1, surrounded by air ($n_0 = n_2 = 1$), the transfer matrix method admits an analytical solution.

The total transfer matrix for the system is simply that of the single slab:

$$\mathbf{M}_{\text{total}} = \mathbf{M}_1 \tag{A.6}$$

with

$$\mathbf{M}_1 = \begin{pmatrix} \cos\delta & \frac{i}{n_1}\sin\delta \\ in_1\sin\delta & \cos\delta \end{pmatrix} \tag{A.7}$$

where $\delta = \frac{2\pi n_1 d}{\lambda}$ is the phase accumulated in the slab.

The reflection coefficient at normal incidence is then

$$r = \frac{(n_0^2 - n_1^2)\sin\delta}{2in_0n_1\cos\delta + (n_1^2 + n_0^2)\sin\delta}, \tag{A.8}$$

and the reflectivity is again $R = |r|^2$.

This single-layer solution offers clear physical insight into the effects of interference and absorption in thin films and provides a useful reference for validating multilayer computations. We use the TMM method to calculate the reflection, transmission and absorption values as a function of slab thickness using arbitrary n_1 values to fit our experimental laser absorption data for $MoSe_2$ (see Figure 3.10) of Section 3.3.3.

Appendix B

Multifunctional Optothermal Pump-Probe Setup

B.1 Predicting the TDTR Signal Magnitude from a Si Photodetector

In this section, we describe how to estimate the expected TDTR signal magnitude we will obtain from our photodetector, which will then be read by the lock-in amplifier. The photodetector essentially converts an optical signal into an electrical current, with a given responsivity (in A/W). This current flows through the terminating resistor of the lock-in amplifier, producing a measurable voltage. Taking into account the probe power, the reflectivity of the sample and that of the optical elements interacting with the reflected probe, while making some assumptions, we estimate the signal magnitude (in volts) we expect to read with our lock-in amplifier.

Let us consider a probe beam power of $P_{\text{probe}} = 1$ mW, which reflects off a gold transducer (for which we assume $R_{\text{gold}} \simeq 0.9$) with a thermoreflectance coefficient $\chi_{\text{gold}} \equiv dR/dT \simeq 3 \times 10^{-4}$ K^{-1}. The total reflected power collected at the photodiode is given by the losses introduced by the objective lens and beamsplitters in the collection path (the collection efficiency is $\xi \approx 50\%$). The probe power at the photodiode $P_{\text{probe,PD}}$ is then:

$$P_{\text{probe,PD}} = \xi \cdot R_{\text{gold}} \cdot P_{\text{probe}} \simeq 0.45 \text{ mW} \tag{B.1}$$

However, we are interested in the transient reflectivity changes created by the

pump-induced temperature fluctuations at the sample surface. If we would assume temperature fluctuations of 1 K, the reflectivity of a gold transducer would change $\Delta R = \chi_{\text{gold}} \cdot \Delta T \simeq 3 \times 10^{-4}$ and the detected probe power fluctuations would be:

$$\Delta P_{\text{probe,PD}} = \Delta R \cdot P_{\text{probe,PD}} \simeq 135 \text{ nW} \tag{B.2}$$

The Si photodiode converts these few-hundred nW power fluctuations in a fluctuating current, given by its responsivity of $S = 0.24$ A/W at the 515 nm probe wavelength:

$$\Delta I = S \cdot \Delta P_{\text{probe,PD}} \simeq 32.4 \text{ nA} \tag{B.3}$$

The TDTR signal after the 50 Ω terminating resistor of the lock-in amplifier will be $\Delta V = \Delta I \cdot R_{\Omega} \simeq 1.62$ μV, which is well above the noise floor of our lock-in amplifier (∼50 nV). We note that this signal magnitude is still quite small, and it would be recommended to use a low-noise, high-speed current preamplifier to operate in the few-hundred microvolt regime. For this, the operational speed of the current preamplifier should be, at least, as high as the modulation frequency of the pump beam. The TDTR signals reported in Chapters 6 and 7 are in the same order of magnitude as our predicted signal magnitude, and, without using a current pre-amplifier, we still obtain a large signal-to-noise ratio.

B.2 Additional Setup Configurations

In this section, we review the additional setup configurations other than the standard time-domain thermoreflectance that our setup is capable of performing.

Additional TDTR configurations enabled by the front- and back-objective lenses

The second viewport at the back of the sample space enables the use of a second (back-)objective lens (10X Plan Apo NIR Infinity Corrected, Mitutoyo) to perform transmission measurements or to pump the sample from the back. In the latter case, a flip mirror guides the pump beam towards the back-objective, which also sits on RT *xyz*-nanopositioners. This configuration further enhances the versatility of our setup by enabling precise alignment of the two objectives ensuring collinearity, while also allowing controlled scanning of one beam relative to the other. Then, our optothermal setup is also be capable of performing beam-offset TDTR measurements when using samples on transparent substrates. Here, the

pump heats the transducer and the probe senses the reflectivity changes of the transducer through the transparent substrate, while it is spatially scanned over the area heated by the pump beam.

For all experiments reported in this thesis, we only use the front-objective to focus both beams on our sample (see Fig. 4.2), and we set our beam-offset to zero. However, the possibility to pump the sample from the back side introduces four distinct TDTR configurations given the relative incidence of the pump and probe beams and orientation of the sample. This is basically given by the two pump-probe configurations (*i.e.*, both beams from the front, or one beam from each side) and the two sample orientations (*i.e.*, mounted right-side up, or upside-down):

1. **Front-probe, front-pump:** representing the standard-TDTR configuration where both, pump and probe, beams illuminate the metal transducer on our sample, which is mounted right-side up. The heat is then dumped at the top surface of the transducer and the temperature is also probed at the surface.
2. **Front-probe, back-pump:** the pump is directed to the back of the sample, through a transparent substrate, heating the transducer/substrate interface. The temperature is probed at the top surface of the metal transducer.
3. **Back-probe, front-pump:** when the sample is mounted upside-down, the pump heats the surface of the transducer. The temperature is probed at the transducer/substrate interface through the transparent substrate.
4. **Back-probe, back-pump:** representing the inverted standard-TDTR configuration where the sample is mounted upside-down, and both beams illuminate the back of the transducer through the transparent substrate. Heat is then dumped and probed at the transducer/substrate interface.

Time-resolved Raman scattering

As introduced in Chapter 2, several methods have been developed to measure temperature using Raman scattering [90]. Most commonly using temperature-calibrated Raman shift, as in Raman thermometry experiments, or measuring the intensity ratios between the Stokes and anti-Stokes lines, which are temperature-dependent as these rely on the available phonon populations [191]. Typical trRS measurements are not suitable for measuring Raman shifts, as there is a compromise between the bandwidth of the excitation and the pulse duration. Therefore, most trRS experiments use intensity ratios to measure optical phonon temperature as a function of time delay [192], as is our case.

Figure B.1 shows our time-resolved Raman scattering setup designed to precisely track transient lattice temperatures dynamics by monitoring optical phonons in 2D materials. The probe beam is generated by a non-linear periodically polled lithium niobate crystal (AC-Y191202-22-01, Stuttgart Instruments) that produces the second harmonic of our fundamental laser while compressing its bandwidth to $<$0.1 nm, which is crucial for resolving the narrow linewidths of Raman modes. Note that the bandwidth compression provided by the PPLN crystal comes at the cost of extending the pulse duration from $\sim$100 fs to $\sim$3 ps. The periodic polling allows for generating a 514.5 nm line, and a home-built temperature stabilizer ensures minimal wavelength shifts during experiments. The probe beam is cleaned from undesired frequencies using a short-pass and a clean-up filters before reaching the sample. The probe light scattered from the sample (both elastically and inelastically) is collected by a drop-in beamsplitter and guided in an enclosed cage-system towards the spectrometer. In practice, for the detection path of the trRS setup we use an enclosed periscope to raise the beam height to the entrance of the spectrometer, which is around 10 cm higher than the rest of the setup. Spatial and spectral filtering is achieved using a confocal module and a Notch filter. The confocal module consists of two lenses in a telescope arrangement that focus the reflected light through a 50 µm pinhole. The Notch filter (514.5-12NNF, Iridian Spectral Technologies) blocks the undesired elastically scattered light which is orders of magnitude more intense than the inelastic scattering from optical phonons. Additional filters might be used for specific Raman experiments. Our spectrometer (Kymera 328i, Andor) is equipped with an electron-multiplying CCD camera and three gratings with 300, 600 and 1200 l/mm allowing for measuring both photoluminescence and Raman spectra.

By using samples on transparent substrates and a back-pump that heats up a metal transducer layer, we can directly probe the Raman modes of 2D materials through the transparent substrate. In this case, the phonon dynamics are exclusively affected by the thermal exchange between the transducer and sample in picosecond to nanosecond timescales. Note that trRS is commonly used to study phonon dynamics up to $\sim$100 ps [193, 194]. This enables the study thermally driven processes, such as energy dissipation pathways and heat transport mechanisms with high spatial and temporal resolution. These measurements could potentially allow for tracking heat layer-by-layer within 2D material heterostructures. This is, with sub-nm spatial information along the stacking direction given the material specificity of Raman spectroscopy.

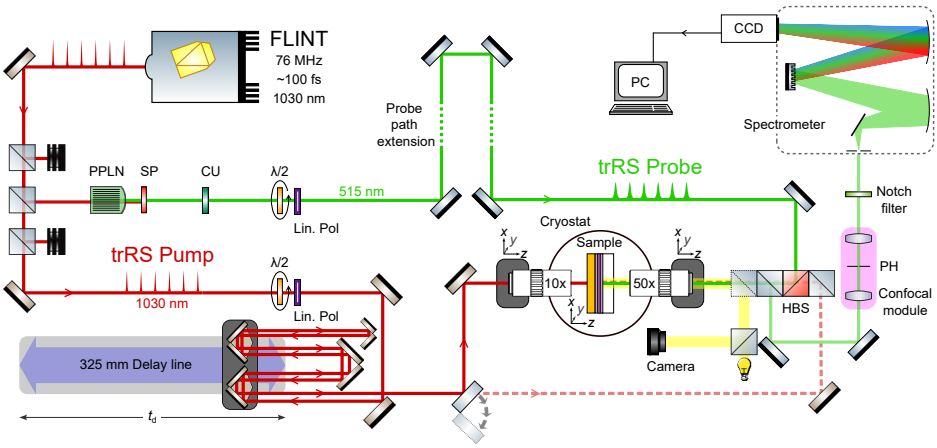

FIGURE B.1: **Detailed schematic of the time-resolved Raman scattering setup.** PPLN: periodically polled lithium niobate, SP: short-pass filter, CU: clean-up filter $\lambda/2$: half-waveplate, Lin. Pol: linear polarizer, HBS: harmonic beamsplitter, PH: pinhole, CCD: charged-coupled device.

Time-resolved photocurrent

Photocurrent is generated when a material absorbs light, creating charge carriers that generate an electrical current. For photocurrent to be generated, the material must be subject to an electric field, which can be internal (*e.g.*, via broken inversion symmetry) or external (*e.g.*, using a junction or bias), to separate the charges resulting in a net current. Pump-probe trPC measurements add a dynamic element, allowing us to track how the photocurrent evolves after a light pulse excites the material. Time-resolved photocurrent offers a practical way to track how 2D materials dissipate heat, revealing details of carrier–phonon coupling, energy transfer pathways, and ultimately how these atomically thin structures handle thermal energy in practical devices.

Figure B.2 shows our trPC setup, where both the pump and probe (in this case, a second pump) maintain the same wavelength as our fundamental laser source ($\lambda = 1030$ nm). A chopper blade (MC2F57B, Thorlabs) differentially modulates the two beams at few-hundred Hz, and the photo-generated current signal is demodulated by our lock-in amplifier at any of the relevant experimental frequencies (*i.e.*, the frequency of one or the other beam, their sum or difference frequencies). The reflected light can also be collected by a biased InGaAs photodiode to perform simultaneous reflectivity and photocurrent maps, which give spatial information about where on the sample the photocurrent is generated.

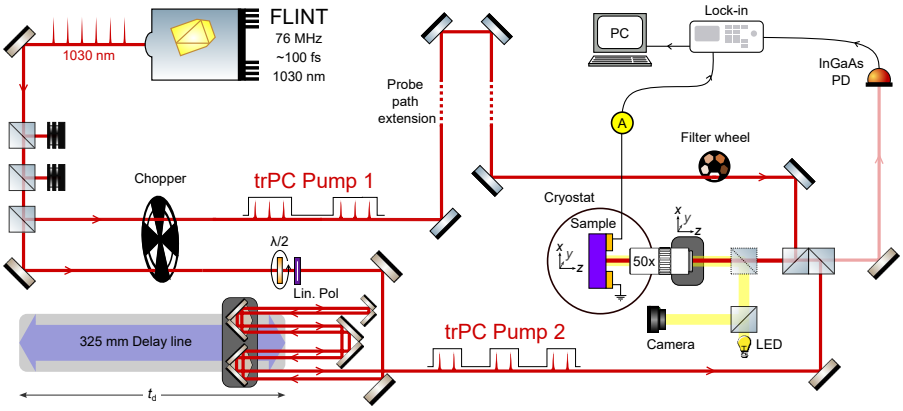

FIGURE B.2: **Detailed schematic of the time-resolved photocurrent setup.** $\lambda/2$: half-waveplate, Lin. Pol: linear polarizer, LED: white light-emitting diode.

In a typical trPC experiment, two pump pulses are focused on the sample at a controlled delay time while the current is monitored at one of the relevant frequencies in the excitation. The first pump pulse initially excites carriers (electrons and holes), while the second pump pulse arrives at a variable time delay exciting more carriers. While scanning the time delay between the laser pulses, a pronounced dip in the measured photocurrent is typically observed when the pulses coincide in time. Note that this is only valid when looking at the single modulation frequency of one of the two beams. When looking at the sum/difference photocurrent (*i.e.*, by monitoring the sum or difference frequency) a peak would be observed instead, and the signal would be zero when they do not coincide in time. The dip (peak) in photocurrent signal arises due to the non-linear nature of the electron temperature with laser power. As a result, when the two pulses arrive at the same time, they produce less time-averaged photocurrent as compared to the situation when they arrive at the sample at different times, separated by more than the electron cooling time. By monitoring how this dip (peak) recovers over time, it is possible to extract information about carrier lifetimes, recombination rates, and other ultrafast processes that govern how the material responds to photoexcitation (for more details, see Ref. [195]).

Appendix C

Time-Domain Thermoreflectance

C.1 Background and Theory

Mathematical tools for TDTR

Fourier Transforms. A Fourier transform $\mathcal{F}$ is an integral transform that decomposes a function into its constituent frequencies, providing a representation in the frequency domain:

$$\mathcal{F}\{y(t)\} = \hat{Y}(f) \equiv \int_{-\infty}^{\infty} y(t) e^{-i2\pi ft} dt$$

with $y(t)$ the original function in time domain, $\hat{Y}(f)$ its Fourier transform in frequency domain, and $2\pi f$ the angular frequency in radians per second.

The use of Fourier transforms simplifies the analysis in the time domain because convolutions are easier to manipulate in the frequency domain.[1] Some properties of Fourier transforms relevant in the TDTR theory are listed below:

- One-to-one correspondence between $\hat{Y}(f)$ and the original function $y(t)$ via the inverse Fourier transform $\mathcal{F}^{-1}$:

$$y(t) = \mathcal{F}^{-1}\{\hat{Y}(f)\} \equiv \frac{1}{2\pi} \int_{-\infty}^{\infty} \hat{Y}(f) e^{i2\pi ft} df$$

[1] Convolutions appear in TDTR experiments because the temperature profile on the surface is essentially the sum of all the responses from the inputs that occurred at different times.

- Linearity:

$$\mathcal{F}\{y(t) = \alpha p(t) + \beta g(t)\} \Longleftrightarrow \hat{Y}(f) = \alpha \hat{P}(f) + \beta \hat{G}(f)$$

- Both the original function $y(t)$ and its Fourier transform $\hat{Y}(f)$ are defined over infinite extents:

$$-\infty < t < \infty \Longleftrightarrow -\infty < f < \infty$$

- The Fourier transform of a product between two functions is the convolution of their Fourier transforms:

$$\mathcal{F}\{p(t) \cdot g(t)\} = \hat{P}(f) * \hat{G}(f) \equiv \int_{-\infty}^{\infty} \hat{P}(\xi)\hat{G}(f-\xi)d\xi$$

- Similarly, a Fourier transform of the convolution between two functions is just the multiplication of their Fourier transforms:

$$\mathcal{F}\left\{(p * g)(t)\right\} \equiv \mathcal{F}\left\{\int_{-\infty}^{\infty} p(t-\xi)g(\xi)d\xi\right\} = \hat{P}(f)\hat{G}(f)$$

Hankel Transforms. The Hankel transform $\mathcal{H}_\nu$ of order ν is a type integral transform that expresses a function in terms of its radial Bessel components.[2] The Hankel transform of order 0 for a function $g(r)$ is especially useful in problems involving systems with radial symmetry, and is defined as:

$$\mathcal{H}_0\{g(r)\} = \hat{G}(k) = 2\pi \int_0^{\infty} g(r)J_0(2\pi kr)rdr$$

with $J_0(2\pi kr)$ the Bessel function of order 0. Similarly to Fourier transforms, the TDTR theory benefits from some of the properties of Hankel transforms, namely:

- One-to-one correspondence between $\hat{G}(k)$ and $g(r)$ via the inverse Hankel transform $\mathcal{H}^{-1}$:

$$g(r) = \mathcal{H}^{-1}\{\hat{G}(k)\} = 2\pi \int_0^{\infty} \hat{G}(r)J_0(2\pi kr)kdk$$

[2] The Hankel transform decomposes a radially symmetric function into components associated with Bessel functions J_ν, just as the Fourier Transform decomposes a function into sine and cosine waves. A Hankel transform can be viewed as a simplification of the 2D axisymmetric Fourier transform.

- The convolution of a real space function corresponds to the inverse Hankel transform of the two Hankel transforms being convoluted:

$$p(r) * g(r) = \mathcal{H}^{-1}\{\hat{P}(k)\hat{G}(k)\} = 2\pi \int_0^\infty \hat{P}(k)\hat{G}(k)J_0(2\pi kr)kdk$$

In TDTR, each of the Gaussian pump pulses $p(r)$ generates a spatial temperature profile as a point response function $g(r)$. In other words, the real space surface temperature is a convolution (in space) of the intensity of the pump beam $\hat{P}$ and the point response function $\hat{G}$ (see details in Section 5.2.2):

$$\begin{aligned} \hat{T}(r,f) &= \hat{P}(r,f) * \hat{G}(r,f) \\ &= 2\pi \int_0^\infty \hat{\hat{P}}(k,f)\hat{\hat{G}}(k,f)J_0(2\pi kr)kdk \end{aligned} \tag{C.1}$$

where $\hat{\hat{G}}(k,f)$ is the Green's function, the calculation of which is the main goal of Section 5.2.1.

Nyquist Sampling Theorem. The theory of time-domain thermoreflectance is based on the Nyquist sampling theorem. In a TDTR experiment, the modulated pump beam induces temperature modulations on the transducer's surface, referred to as transient temperature. The probe beam, a train of laser pulses regularly spaced over the period of sampling T_{rep} (given by the repetition rate of the probe laser $T_{\text{rep}} = 1/f_{\text{rep}}$), samples the surface temperature at those instants in time. The sensor, typically a photodiode that collects the reflected probe light, does not measure the average temperature at the surface but the surface temperature at those discrete times. The sampled signal $x_S(t)$ is basically the multiplication of the signal $x(t)$ and the discrete sampling $s(t)$, which can be described as an infinite series of Delta functions δ where each of them may be time delayed by t_d:[3]

$$\begin{aligned} x_S(t) &= x(t) \cdot s(t) \\ &= x(t) \cdot \sum_{n=-\infty}^{\infty} \delta\left(t - nT_{\text{rep}} - t_d\right) \end{aligned}$$

The Nyquist sampling theorem describes the Fourier transform of the sampled

[3] In practice, a mechanical delay line controls the time delay t_d varying the optical path difference between the pump and probe beams.

signal $\hat{X}_S(f)$, which is exactly what a lock-in amplifier detects in a TDTR experiment.[4] The Fourier transform of the sensed signal is an infinite series that involves the Fourier transform of the continuous signal times an exponential term involving the time delay:[5]

$$\hat{X}_S(f) = \sum_{n=-\infty}^{\infty} \hat{X}\left(f - \frac{n}{T_{rep}}\right) \exp\left[-i2\pi \frac{n}{T_{rep}} t_d\right]$$

In a TDTR experiment, as the reflectance of the metal transducer changes linearly with temperature when the temperature rise is small, the sampled detector signal $x_S(t)$ is proportional to the sensed average temperature $T_S^{avg}(t)$, which is the continuous average surface temperature $T^{avg}(t)$ sampled by the probe beam. Then, the signal that would be picked up by a lock-in amplifier is given by Equation C.2:[6]

$$\hat{T}_S^{avg}(f) = \sum_{n=-\infty}^{\infty} \hat{T}^{avg}\left(f - \frac{n}{T_{rep}}\right) \exp\left[-i2\pi \frac{n}{T_{rep}} t_d\right] \tag{C.2}$$

Considering the Gaussian shape of the pump laser, the average surface temperature $T^{avg}(r,t)$ is a function of space and time, so the average surface temperature sampled by the probe beam $T_S^{avg}(t)$ is exactly in the form of the Nyquist theorem:

$$\begin{aligned} T_S^{avg}(t) &= \int_A T(r,t) s_0(r) \sum_{n=-\infty}^{\infty} \delta\left(t - nT_{rep} - t_d\right) dA \\ &= \underbrace{\left(\int_A T(r,t) s_0(r) dA\right)}_{T^{avg}(t)} \underbrace{\sum_{n=-\infty}^{\infty} \delta\left(t - nT_{rep} - t_d\right)}_{s(t)} \end{aligned} \tag{C.3}$$

where $T^{avg}(t) = \int_A T(r,t) s_0(r) dA$ is the weighted average of the surface temperature $T(r,t)$ sampled by a probe laser with a Gaussian profile $s_0(r)$, normalized

[4] The lock-in amplifier demodulates the signal at a particular frequency, *i.e.* the modulation frequency of the pump beam.

[5] Proof:

$$\begin{aligned} \mathcal{F}\{x_S(t)\} &= \mathcal{F}\{x(t) \cdot s(t)\} \\ \hat{X}_S(f) &= \hat{X}(f) * \hat{S}(f) \\ &= \int_{-\infty}^{\infty} \hat{X}(\xi) \hat{S}(f - \xi) d\xi \\ &= \int_{-\infty}^{\infty} \hat{X}(\xi) \left(\sum_{n=-\infty}^{\infty} \delta\left(f - \xi - \frac{n}{T}\right) \exp\left[-i2\pi (f - \xi) t_d\right] \right) d\xi \end{aligned}$$

[6] In the original derivation of Ref. [130], Cahill writes this in terms of reflectivity with real and imaginary parts as the in- and out-of-phase signals from the lock-in amplifier. We will reach that point in Section 5.2.2.

so that the integral $\int_A s_0(r)dA = 1$.

In essence, modelling the signals acquired in TDTR using a lock-in amplifier requires prior knowledge of the Fourier transformed average surface temperature $\mathcal{F}\{T^{\text{avg}}(t)\}$ to compute Equation C.2 (more details in Section 5.2.2).

Thermoreflectance coefficients of various metal films

Figure C.1 summarizes the wavelength dependence of the thermoreflectance coefficient χ for some metal films typically used as transducers in TDTR and FDTR. Conventional TDTR setups utilize a Ti:Sapphire laser, centered at around 800 nm, making aluminum the most common choice of transducer material. This is because its thermoreflectance coefficient χ_{Al} peaks around this wavelength.

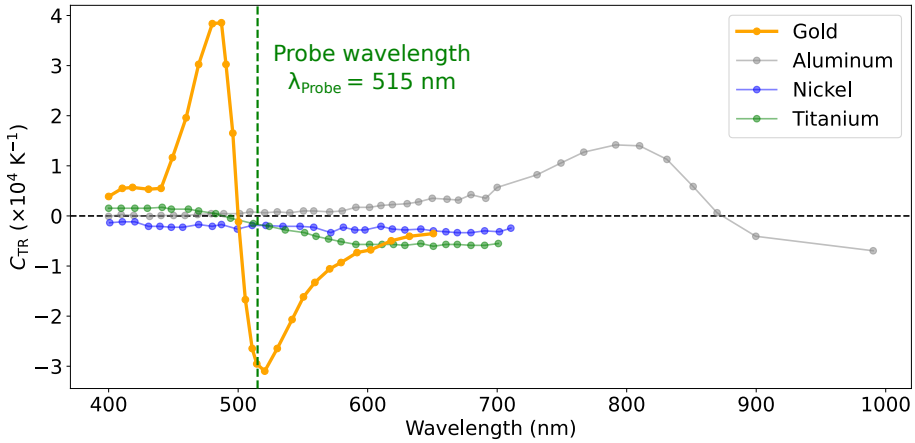

FIGURE C.1: **Thermoreflectance coefficient vs wavelength for various materials.** Data replotted from Ref. [143].

In our setup (see Chapter 4), we use a fundamental laser centered at 1030 nm, which we frequency-double (515 nm) using a second harmonic crystal. We notice that gold has a very large thermoreflectance coefficient around 515 nm of $\chi_{\text{Au}} = -3 \cdot 10^{-4}\ \text{K}^{-1}$, which justifies our choice of using gold transducers to probe the transient reflectivity using the green, frequency-doubled beam (515 nm).

C.2 Data Post-Processing and Setup Validation

Radiative pick-up of signals at high modulation frequencies

In our setup, when using large modulation frequencies we detect a non-zero signal even when the pump beam is blocked and does not reach the sample (nor the detector). This frequency actually radiates from our power amplifier (VBA-100-30, Vectawave) and is picked up by the BNC cables that connect to the lock-in amplifier. This signal is not stable, and therefore we measure it for each TDTR signal we acquire. This is, we acquire a signal, block the pump beam using an automated shutter at the beginning of its path, and measure the background signal. At the time of data processing, we subtract the background from the signal (see Section 6.2.2). **Figure C.2** shows a frequency sweep of the lock-in amplifier output that feeds the power amplifier, while we record the in- and out-of-phase background signals. These background signals become larger with increasing modulation frequency, but are absent when the frequency is below ∼3 MHz.

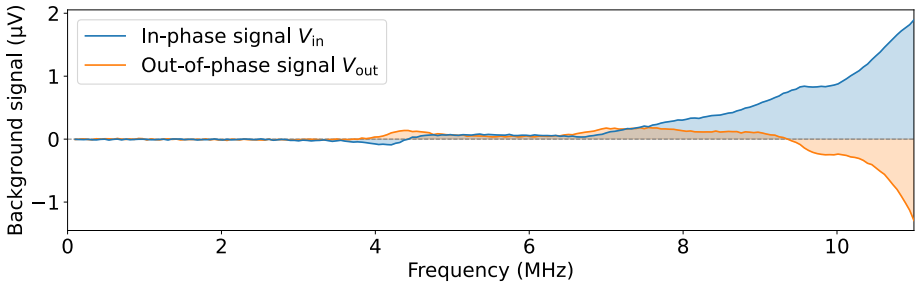

FIGURE C.2: **Background signals measured with pump OFF as a function of frequency.** The pump beam is blocked from reaching the sample, and thus, the photodiode. We sweep the output frequency of the lock-in amplifier while recording the in-phase (*blue*) and out-of-phase (*orange*) signals. Above ∼3 MHz, the signals are non-zero and need to be subtracted from actual measurements that include the presence of the pump.

Sensitivity analysis for our control experiments

To understand which parameters have a stronger influence on our measured signals, we perform a sensitivity analysis on a $Au/SiO_2/Si$ system simulating all our experimental conditions. **Figure C.3** shows our sensitivity analysis results, from which is clear that the V_{in} signals [Fig. C.3**a**] are weakly affected by κ_{SiO_2}, G_{Au/SiO_2} and w_0. The only parameter with significant influence on V_{in} is κ_{SiO_2} when using a large spot size. The ratio $-V_{in}/V_{out}$ signals are strongly affected by the averaged

laser spot size, particularly when tight focusing the beams. This sensitivity to w_0 decreases to almost zero when using a large spot size and a large modulation frequency. Our sensitivity to the first interface is almost zero in all our experimental conditions, leaving κ_{SiO_2} the only parameter that can be extracted with confidence, particularly when using low modulation frequencies and large spot sizes.

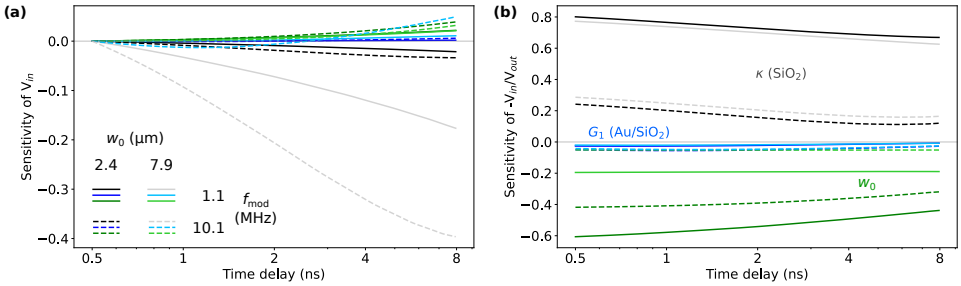

FIGURE C.3: **Sensitivity analysis for the control experiments on bare substrate.** Sensitivity of **(a)** V_{in} and **(b)** ratio $-V_{in}/V_{out}$ signals to G_{Au/SiO_2} (*blue*), κ_{SiO_2} (*black*), and w_0 (*green*); at $f_{mod} = 1.1$ (*solid lines*) and 10.1 MHz (*dashed lines*); while using $w_0 = 2.4$ (*dark colors*) and 7.9 μm (*light colors*).

We notice that the sensitivity to G_1 is extremely small, because the interfacial conductance of the Au/SiO_2 is large. However, we expect that the introduction of thin MoS_2 interlayers between transducer and substrate will result in smaller values of G_1. In **Figure C.4** we perform a sensitivity analysis where we verify that the sensitivity of V_{in} [Fig. C.4**a**] and ratio $-V_{in}/V_{out}$ [Fig. C.4**b**] signals to G_1 are strongly dependent on the parameter magnitude. For values of G_1 bellow 20 MW m^{-2} K^{-1}, our sensitivity to this parameter would suddenly increase as heat transport becomes limited by this interface, even when using low modulation frequencies (1.11 MHz) and small spot sizes (2.2 μm).

We now perform a sensitivity analysis for our second control experiment, using a $Au/MoS_2/SiO_2/Si$ geometry (see **Figure C.5**). We observe a small sensitivity to $G_2 = G_{MoS_2/SiO_2}$, which is the reason we fixed its value to 18 MW m^{-2} K^{-1}, within the range reported in the literature. The κ_{MoS_2} shows the strongest sensitivity at short time delays, while the sensitivity to $G_1 = G_{Au/MoS_2}$ is smaller, but maximum at long time delays. Note that the sensitivities shown here for G_1 were calculated using its best fit value of ∼35 MW m^{-2} K^{-1}, but using smaller values, as expected from the literature for this interface, would result in larger sensitivities to this parameter.

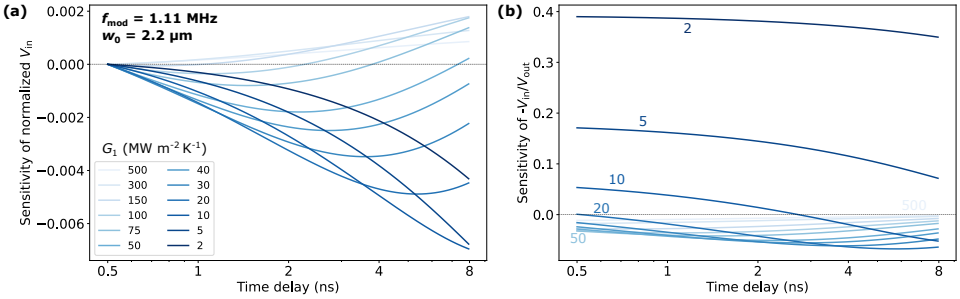

FIGURE C.4: **Sensitivity to G_1 depending on its value.** Sensitivity of **(a)** V_{in} and **(b)** ratio $-V_{\text{in}}/V_{\text{out}}$ signals to G_1 at $f_{\text{mod}} = 1$ MHz and $w_0 = 2.2$ µm for different values of G_1 from 2 to 500 MW m^{-2} K^{-1}.

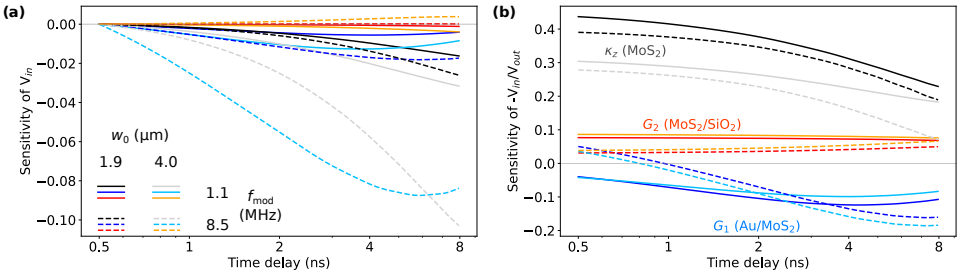

FIGURE C.5: **Sensitivity analysis for the control experiments on thick MoS_2.** Sensitivity of **(a)** V_{in} and **(b)** ratio $-V_{\text{in}}/V_{\text{out}}$ signals to $G_{\text{Au/MoS}_2}$ (*blue*), κ_{z,MoS_2} (*black*), and $G_{\text{MoS}_2/\text{SiO}_2}$ (*red*); at $f_{\text{mod}} = 1.1$ (*solid lines*) and 8.5 MHz (*dashed lines*); while using $w_0 = 1.9$ (*dark colors*) and 4.0 µm (*light colors*).

Fitting routine and minimization process

Our fitting routine starts with a brute step minimization, where we systematically explore the parameter space for our two variables. We globally fit all our experimental data sets obtained at various spot sizes and modulation frequencies. We obtain the best fit parameters from the configuration that produces the smallest residuals across all data sets. **Figure C.6** summarizes our fitting routine results for the thick MoS_2 control sample.

We first scan the interfacial thermal conductance $G_{\text{Au/MoS}_2}$ and out-of-plane thermal conductivity κ_{z,MoS_2} [Fig. C.2**a**] while monitoring the sum squared residuals [Fig. C.6**b**] of all data sets. We observe two superimposed minimizations for both parameters suggesting that the fit converged to a global minimum when $G_{\text{Au/MoS}_2} \approx 35$ MW m^{-2} K^{-1} and $\kappa_{z,\text{MoS}_2} \approx 2.4$ W m^{-1} K^{-1}. Finally, we recompute the model at the best values found in this brute minimization step, which we

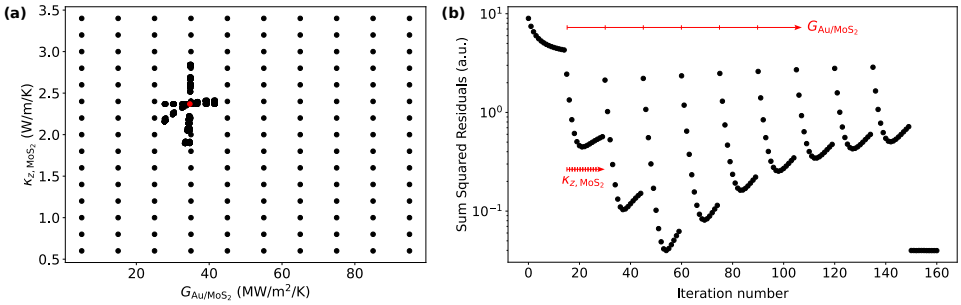

FIGURE C.6: **Parameter space and minimization routine in TDTR fitting. (a)** The brute minimization step allows for systematically exploring the parameter space in a simultaneous fit of two variables: κ_{z,MoS_2} and G_{Au/MoS_2}. **(b)** The resulting sum squared residuals shows two superimposed minimizations while varying both parameters. The best value for G_{Au/MoS_2} changes with the value of κ_{z,MoS_2}. This is particularly noticeable at extreme values of κ_{z,MoS_2}.

will use as initial guess values in the least-squares minimization step. We obtain $G_{Au/MoS_2} = 34.7 \pm 1.9$ MW m^{-2} K^{-1} and $\kappa_{z,MoS_2} = 2.37 \pm 0.22$ W m^{-1} K^{-1}. We obtain the 95% confidence intervals by simultaneously varying both parameters, as depicted by the explored configurations around the best fit parameter values in Fig. C.6**a**. The residuals for the least-squares minimization step and determination of the confidence interval are not shown here for clarity. The red data point indicates the best fit values for both parameters.

C.3 Thermoreflectance of Thermally Thin MoS_2

In this section first show the optical and TDTR imaging performed in the main studied regions of three samples [**Figure C.7**], and an example of a less-ideal flake [**Figure C.8**]. We show the summary of thickness-dependent TDTR data and simulations varying G_{eff} at 1.11 and 5.11 MHz [**Figure C.9**]. Then, we show the fits performed to the 1.11 MHz TDTR data at room temperature [**Figures C.10** and **C.11**], using our thermal model described in Chapter 5; and the fits performed to the TDTR signal magnitudes at long time delays for varying temperatures [**Figure C.12**], using an Airy transmission function (see Eq. 7.1). Finally, we show the parameters [**Table C.1**] we used in the transfer matrix method simulations, aimed at understanding the effects of introducing few-layer MoS_2 flakes under our optically-thin transducer layer [**Figure C.13**]; and provide a summary of the loss of thermoreflectance signal obtained for 3L, 4L and 5L MoS_2 at 300, 210 and 120 K, respectively [**Figure C.14**].

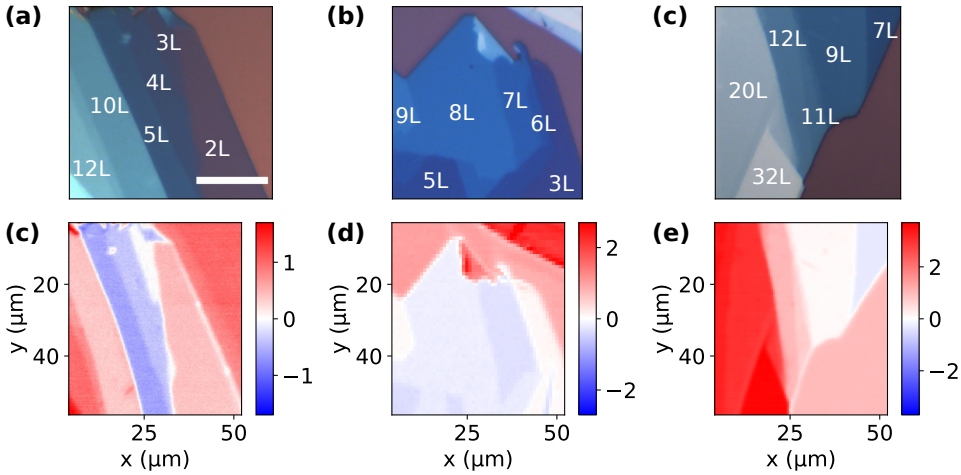

FIGURE C.7: **Optical and TDTR imaging on terraced-like MoS_2 flakes. (a,b,c)** Optical images of three terraced-like MoS_2 flakes showing thickness regions between 1L and 12L. The scale bar of 20 μm in panel (a) is also valid for panels (b,c). **(d,e,f)** Their corresponding TDTR maps obtained at 1.11 MHz and $w_0 \approx 2.2$ μm. Flakes between 3L and 9L show a sign change with 3L and 9L flakes exhibit minimum in-phase signal magnitudes. Here, we only show the in-phase V_{in} signals normalized to the substrate's value, but we find the same exact trends for V_{out}.

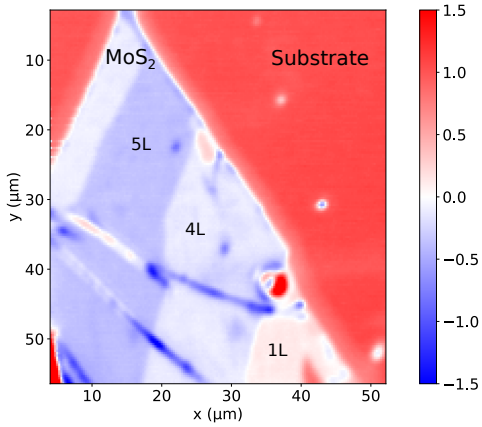

FIGURE C.8: **Example of TDTR imaging on a less-ideal flake**. The TDTR signals show a strong dependence of whatever is underneath the gold transducer, providing a remarkable ability to spot defective regions in our flakes, such as cracks, wrinkles, particles or residues.

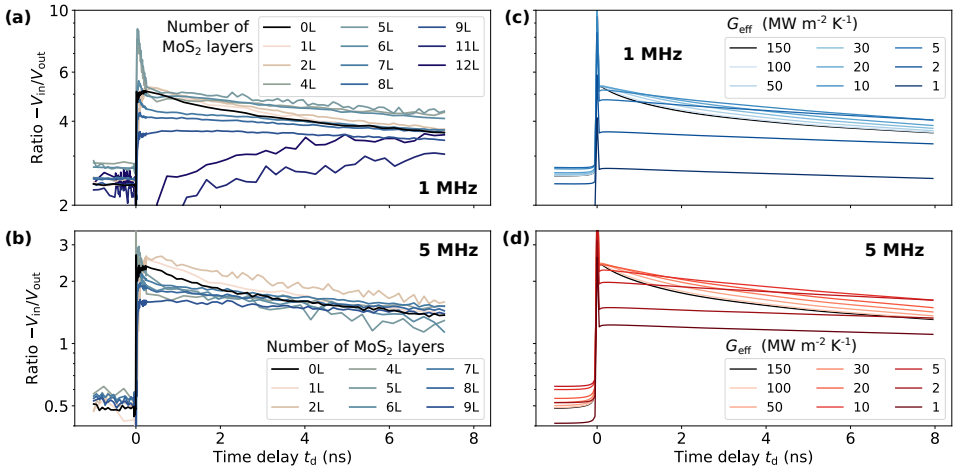

FIGURE C.9: **Ratio signals for few-layer MoS_2 at room temperature. (a,b)** Experimental and **(c,d)** simulated ratio $-V_{\text{in}}/V_{\text{out}}$ signals using a spot size of $w_0 = 2.2$ μm at **(a,c)** 1.11 MHz and **(b,d)** 5.11 MHz. The experimental traces correspond to MoS_2 flake thicknesses ranging from 1L to 9L (3L data is not shown here, see Section 7.5). The simulated traces correspond to an $Au/SiO_2/Si$ sample geometry using $G_1 \equiv G_{\text{eff}}$ in range $2 - 150$ MW m^{-2} K^{-1}.

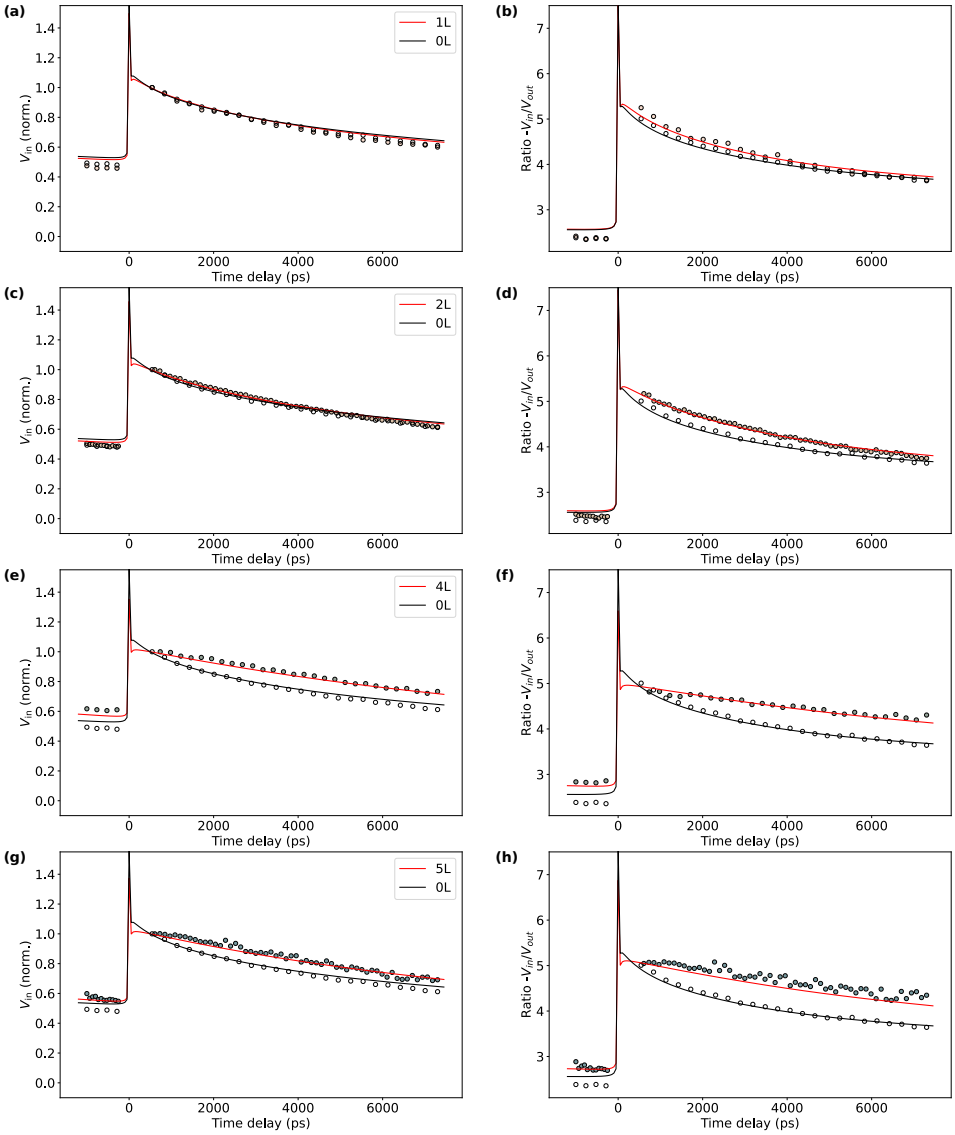

FIGURE C.10: **TDTR fits for 1L to 5L MoS_2.** Experimental (*scatters*) and fitted (*lines*) **(a,c,e,g)** normalized V_{in} and **(b,d,f,h)** ratio signals obtained at 1.11 MHz and $w_0 = 2.2$ µm corresponding to the bare substrate (*empty scatters*) and MoS_2 flakes of **(a,b)** 1L, **(c,d)** 2L, **(e,f)** 4L and **(g,h)** 5L.

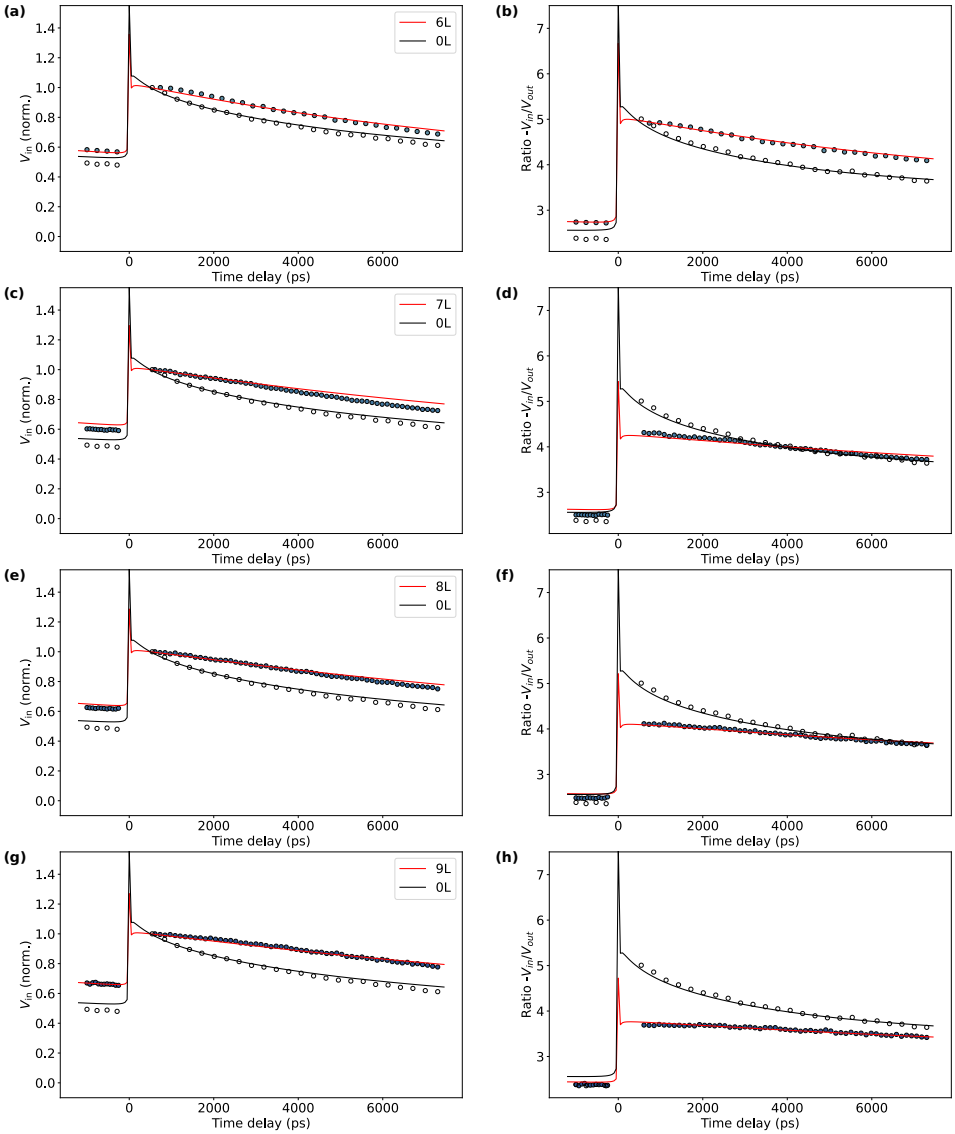

FIGURE C.11: **TDTR fits for 6L to 9L MoS_2.** Experimental (*scatters*) and fitted (*lines*) **(a,c,e,g)** normalized V_{in} and **(b,d,f,h)** ratio signals obtained at 1.11 MHz and $w_0 = 2.2$ µm corresponding to the bare substrate (*empty scatters*) and MoS_2 flakes of **(a,b)** 6L, **(c,d)** 7L, **(e,f)** 8L and **(g,h)** 9L.

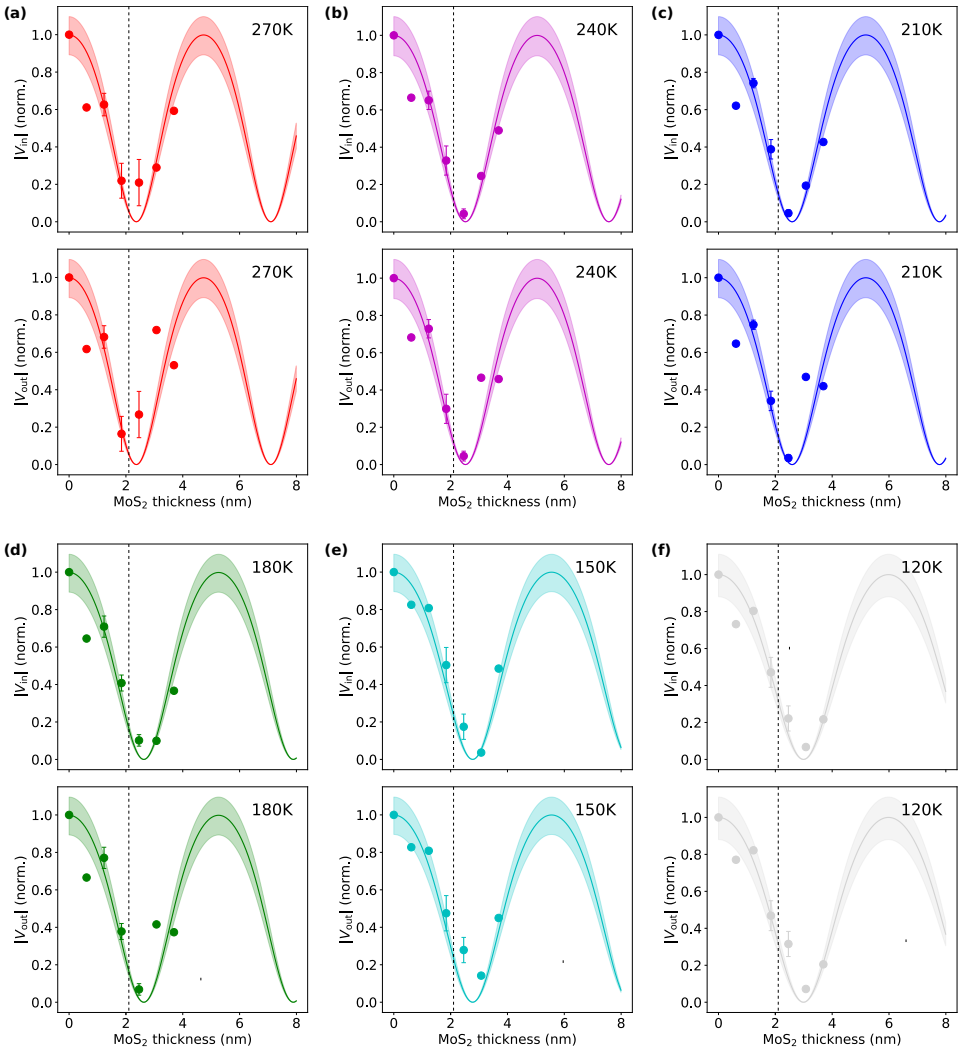

FIGURE C.12: **Airy fitting of TDTR signal magnitudes as a function of temperature.** Absolute TDTR signal magnitudes at $t_d \geq 4$ ns obtained at **(a)** 270 K, **(b)** 240 K, **(c)** 210 K, **(d)** 180 K, **(e)** 150 K and **(f)** 120 K. For each temperature, the V_{in} (*top panel*) and V_{out} (*bottom panel*) experimental signal magnitudes (*scatters*) for few-layer MoS_2 is used to extract the wavelength λ and finesse $\mathfrak{F}$ via a least-squares minimization of Eq. 7.1. The vertical dashed line corresponds to the thickness found for the first resonance at 300 K.

TABLE C.1: **Summary of optical parameters for various materials.** The refractive indexes n_j, extinction coefficients k_j are obtained from the literature, with $\mathrm{d}n/\mathrm{d}T$ and $\mathrm{d}k/\mathrm{d}T$ the assumed temperature-dependencies considered only for gold and MoS_2. For MoS_2 we use the bulk values of n and k for all thicknesses L.

j	L_j (nm)	n_j	k_j	$\mathrm{d}n_j/\mathrm{d}T$ ($\times 10^4$)	$\mathrm{d}k_j/\mathrm{d}T$ ($\times 10^4$)
Au	50	0.72	2.02	-1.0	-2.0
Ti	2	2.90	3.27	0.0	0.0
MoS_2	$0-10$	6.75	1.36	-2.0	1.0
SiO_2	285	1.46	0.00	0.0	0.0
Si	semi-∞	4.22	0.06	0.0	0.0

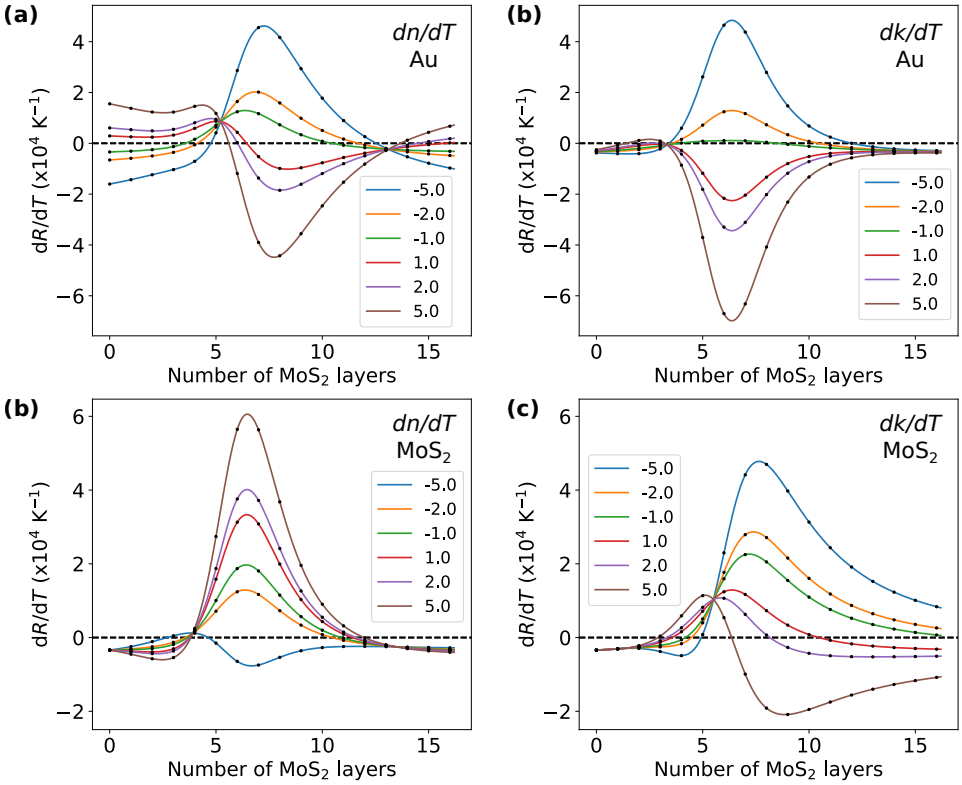

FIGURE C.13: **Influence of temperature-dependent optical parameters on calculated thermoreflectance.** Effects of varying **(a,c)** dn/dT and **(b,d)** dk/dT of **(a,b)** gold and **(c,d)** MoS_2 using the values of Table C.1.

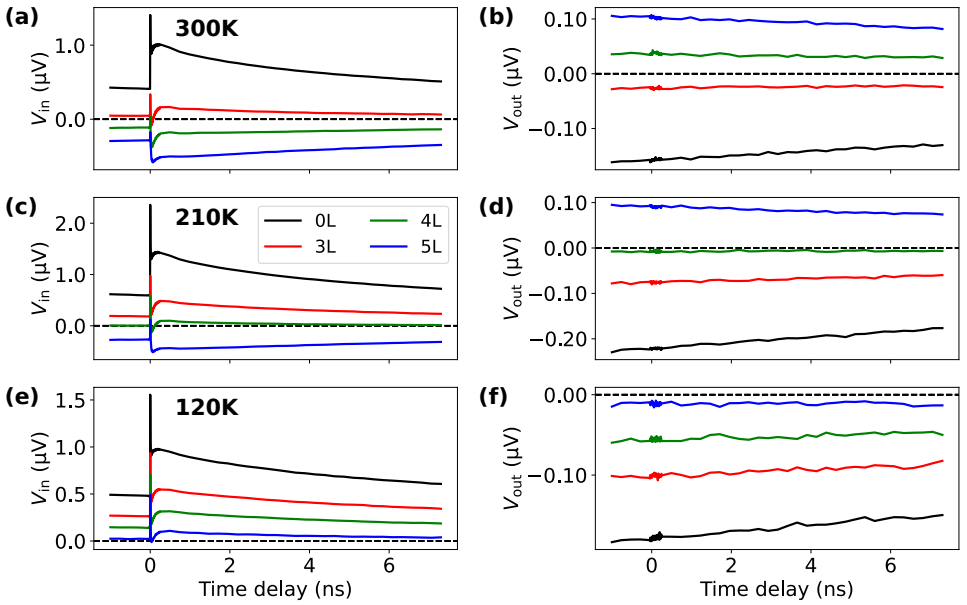

FIGURE C.14: **On-demand suppression of the thermoreflectance coefficient. (a,c,e)** In-phase V_{in} and **(b,d,f)** out-of-phase V_{out} signals for 0L, 3L, 4L and 5L MoS_2 obtained at **(a,b)** 300 K, **(c,d)** 210 K, and **(e,f)** 120 K. Note that the thermoreflectance of 4L MoS_2 at 210 K is efficiently suppressed at all time delays. The TDTR signals for few-layer MoS_2 smoothly cross zero signal for changing temperature. The ratio signals for these measurements are shown in Figure 7.7.